Structure of Resistive Magnetohydrodynamic Shocks

Stephen George McAndrew BSc MA DipEd *Syd.*, MSc *N.S.W.*

Department of Physics and Astronomy, Macquarie University, Sydney, Australia

June 14, 2021

Statement of Originality

This work has not previously been submitted for a degree or diploma in any university. To the best on my knowledge and belief, the thesis contains no material previously published or written by another person except where due reference is made in the thesis itself.

Stephen McAndrew, 30th October 2020

Dedication

To Catherine, who was as happy when I finished as when I started.

Acknowledgement

With thanks to Professor Mark Wardle for suggesting the topic and providing supervision of this research.

Contents

List of Figures

List of Tables

a	speed of sound at a point in the transition
a_1	upstream speed of sound
a_2	downstream speed of sound
$\mathbf{B}$	magnetic field vector at a point in the flow
B_1	magnitude of upstream (undisturbed) magnetic field vector taken to be in the x-y plane
B_2	magnitude of downstream (disturbed) magnetic field vector in the x-y plane
$\lvert B_T \rvert$	magnitude of transverse magnetic field component in a switch-on shock
B_x	magnetic field component in the direction normal to the upstream plane of the shock
B_y	magnetic field component in the y direction at a point in the shock transition
B_{y1}	upstream y magnetic field component
B_{y2}	downstream y magnetic field component
B_z	magnetic field component in the z direction at a point in the shock transition
b_1	upstream Alfven speed
c	speed of light in a vacuum
c_v	specific heat at a constant volume
D	downstream stationary point in the $B_y - B_z$ phase plane
$D12$	downstream point for a fast shock
$D13$	downstream point for an intermediate $1 \rightarrow 3$ shock
$D14$	downstream point for an intermediate $1 \rightarrow 4$ shock
$D23$	downstream point for an intermediate $2 \rightarrow 3$ shock
$D24$	downstream point for an intermediate $2 \rightarrow 4$ shock
$D34$	downstream point for a slow shock
f_1	constant mass flux per unit area through the shock
f_2	constant momentum flux per unit area in the x direction through the shock
f_3	constant momentum flux per unit area in the y direction through the shock
f_4	constant momentum flux per unit area in the z direction through the shock
f_5	constant proportional to the electric field component in the y direction through the shock
f_6	constant proportional to the electric field component in the z direction through the shock
f_7	constant of energy flux per unit area through the shock
k_{ij}	coefficients of cubic equation for downstream sound speed
l_{ij}	coefficients of sextic equation for downstream flow speed
m_i	coefficients for calculation of Jouget speed
p	fluid pressure at a point in the shock transition
p_1	upstream fluid pressure
p_2	downstream fluid pressure
q	ratio of downstream fluid pressure to upstream fluid pressure
R	radicand in the ODEs, the locus of points on the supersonic/subsonic boundary; rotational discontinuity
r	ratio of downstream mass density to upstream mass density, called the compression ratio
Δs	change in entropy per unit mass, called change in specific entropy
U	upstream stationary point in the $B_y - B_z$ phase plane
$\mathbf{u}$	fluid velocity vector at a point in the flow
u_x	fluid velocity component normal to the upstream plane of the shock in the x direction
u_{x1}	upstream x velocity flow component, called upstream normal flow velocity or upstream shock speed
u_{x2}	downstream x velocity flow component
u_y	fluid velocity component in the y direction
u_{y2}	downstream y velocity flow component

u_z	fluid velocity component in the x direction
v_{ef1}	upstream speed for equisonic downstream speeds for a fast shock
v_{ei1}	upstream speed for equisonic downstream speeds for an intermediate shock
v_{f1}	upstream fast magnetohydrodynamic wave speed, called upstream fast speed
v_{f2}	downstream fast magnetohydrodynamic wave speed, called downstream fast speed
v_{i1}	upstream intermediate magnetohydrodynamic wave speed, called upstream intermediate speed
v_{i2}	downstream intermediate magnetohydrodynamic wave speed
v_{j1}	upstream Jouget speed, maximum value of u_{x1} to produce an intermediate shock
v_{s1}	upstream slow magnetohydrodynamic wave speed, called upstream slow speed
v_{s2}	downstream slow magnetohydrodynamic wave speed
w	geometric mean of upstream and downstream normal flow speeds, called the parametric speed
X	direction perpendicular to the upstream shock plane making an angle θ_1 with the upstream magnetic field
x	position along x axis taken as positive from upstream point towards the downstream point
x_η	x divided by η
Y	direction perpendicular to X such that upstream and downstream fields are in the $X-Y$ plane
Z	direction perpendicular to both X and Y directions according to the right hand convention
α	ratio of normal velocity component of shock to the speed of sound
β	plasma beta, ratio of gas pressure to magnetic pressure
β_1	upstream value of plasma beta
γ	ratio of specific heats at a constant pressure to a constant volume, also called the adiabatic index
η	magnetic diffusivity
θ_1	angle between the normal to the plane of the shock (x direction) and the upstream magnetic field direction
ν	kinematic viscosity
ξ	ratio of magnetic diffusivity to kinematic viscosity, reciprocal of the magnetic Prandtl number
ρ	mass density at a point in the shock transition
ρ_1	upstream mass density
ρ_2	downstream mass density
ϕ	step-off angle into $B_y - B_z$ phase plane measured from positive B_y axis, allowing a degree of freedom

Abstract

This thesis presents results of a study of the steady state structure of slow, intermediate and fast magnetohydrodynamic (MHD) shocks in the case where energy dissipation is due to resistive heating of the fluid and the upstream Alfven speed is greater than the sound speed. A new parametric solution of the jump conditions is given and the various shock families are shown to be determined by the presence and number of stationary points in the magnetic field phase plane and the speed of sound. It is shown that there are 14 types of MHD shock structure contained in 12 families with the "switch-on" shock being the limiting case of a fast and intermediate shock combination. The thesis proceeds as follows. First, the background to the MHD shock structure problem is given. The equations for resistive MHD are then presented in the normal incidence frame for the steady state and the jump conditions relating the upstream and downstream states are then given in conventional and parametric form. The classification of shocks in terms of the MHD signal speeds is then described. The MHD equations yield a pair of ODEs in the transverse components of B, allowing the shock transition to be represented as a trajectory in the B_y-B_z plane. The magnetic field phase plane is then used to show the emergence of families of shocks, with different families of intermediate shocks found to have 0, 1 or 2 degrees of freedom in their internal structure. The multiplicity arises due to the possibility of an entropy increasing gas dynamic jump inside them from a supersonic to subsonic state across which the magnetic field components do not change. An original analysis is presented of the smooth passage of an intermediate shock from a supersonic to a subsonic state at a special point known as the transonic transition point. The final chapter gives a table of the shocks possible in resistive MHD, presents a calculation of the effect of fluid viscosity on the structure of a shock and gives details of a preliminary study of shock stability using an eigenvalue analysis. The calculations in this thesis confirm that intermediate shocks have the requisite number of degrees of freedom in their structure to be stable according to the hypothesis of Wu (*J. Geophys. Res.*, 95: 8149, 1990) which had cast doubt on the original view that intermediate shocks are structurally unstable.

1 Introduction

Magnetic fields and conducting fluids pervade the Universe. Violent disturbances abound in the Universe. The combination of violent disturbances, conducting fluids and magnetic fields produces magnetohydrodynamic shock waves which carry energy through the local region. Whether on a star or in the region of influence of a star the coupling of magnetic fields and hydrodynamic fields via magnetotohydrodynamics (MHD) determines the physical processes occurring. Examples include the dynamics of solar flares, the Earth's bow shock, the solar wind termination shock and supernova shock waves.

Roberts [1] states that the study of magnetohydrodynmics began with the prediction by Hannes Alfven of the waves now carrying his name. Electromagnetism and hydrodynamics developed separately and the concept of an Alfven wave, at first predicted in an incompressible perfectly conducting fluid, was met with suspicion. Falthamar [2] states that Enrico Fermi said "of course such waves could exist" and Alfven said "the next day everybody in the physics community said of course". The application of MHD to a compressible conducting fluid and the deduction of three characteristic disturbance speeds, the slow, intermediate and fast speeds was first done by Herlofson [3].

The application of the laws of physics to shock waves in a conducting fluid in a magnetic field began with the work of de Hoffmann and Teller [4] who applied the conservation of mass, momentum, energy and magnetic flux to connect the fluid properties on each side of a discontinuity in a magnetised fluid in the case where the fluid is a perfect conductor. Relative to the undisturbed magnetic field, parallel, perpendicular and oblique disturbances were considered. In this model, ideal MHD, dissipative processes in the fluid were not explicitly considered and so the spatial transition of the flow variables between the undisturbed and disturbed states, i.e. the structure of the shock, was not considered. The study of MHD shocks with reference to possible astrophysical applications began with Helfer [5] who applied the condition of infinite conductivity to the problem of calculating the magnetic field and velocity distributions in a gas modelled on the Sun's chromosphere and inner corona and found results that matched observed values in prominence studies.

Two sections follow. The first presents the relevance of the magnetohydrodynamic (MHD) shock structure problem in physics and the second section outlines previous studies of MHD shock structure.

1.1 Motivation

The purpose of this research is to present stationary shock structures in the case where the upstream Alfven speed is greater than the sound speed. There are two reasons for doing this. Firstly, to determine the possible transitions produced by a given set of upstream parameters to determine if degrees of freedom are possible in the shock transition or if the transition is unique. Secondly, to provide a basis for the future examination of the stability of each shock structure to small perturbations as the degrees of freedom in a structure will have a crucial role in determining stability.

A MHD shock is the transition between two states in a conducting fluid in which a magnetic field is present when the fluid is subjected to a disturbance travelling at a speed greater than one of the characteristic speeds in the fluid. In a magnetised fluid these are the slow and fast magneto-acoustic speeds, commonly called the fast and slow speeds, and the intermediate speed. This thesis determines the possible variation in the flow variables through an MHD shock between the steady upstream (undisturbed) state to a second steady state, the downstream state. There are three types of MHD shocks, fast, slow and intermediate shocks. Emphasis will be placed on intermediate shocks, these being shocks that occur when a multiplicity of shock transitions are possible for given pre-shock conditions, either two intermediate shocks alone or two intermediate shocks and a fast shock. In this case of multiplicity two or three downstream steady states are possible respectively from the same upstream state.

Roberts [6] comments that "recent research has led to an amusing reversal of ideas" with regards to the physical nature of MHD shocks. This refers to a possible change in viewpoint from the earlier idea proposed by Russian authors [7] and [8] of intermediate shocks being "non-evolutionary" meaning non-surviving due to them being unstable to small perturbations. This was prompted by the works of Wu [9] who found surviving intermediate shocks in numerical simulations and the reported observations of intermediate shocks in *Voyager I* data by Chao et al. [10] and *Voyager 2* data by Feng [11]. Feng et. al. [12] reported an intermediate shock in data recorded by *Wind* and the *Advanced Composition Explorer* (*ACE*). Steinolfson and Hundhausen [13] demonstrated the formation of both types of intermediate shocks in numerical simulations in idealised conditions expected to occur in coronal mass ejections. This motivates an examination of the nature of MHD shocks.

1.2 Previous Studies of MHD Shock Structure

The literature on MHD shocks is extensive and in this section an outline of some previous works on MHD shock structure will be given.

The first work to determine a shock structure in MHD was that of Marshall [14] who calculated shock structures for a perpendicular shock, this being the case when the upstream magnetic field and velocity vectors are parallel and perpendicular to the shock plane respectively. Shock profiles were calculated by numerical integration of first order ODEs for the cases of high and low electrical conductivity the transition width being calculated in each case.

Whitham [15] gave the structure equations for a perpendicular shock with dissipation due to finite electrical conductivity and included the cases where the downstream flow speed is equal to and less than the speed of sound. The passage to the subsonic state in these cases causes the shock velocity to have a discontinuous first spatial derivative as viscosity was not included in the ODE to smooth the transition. Shock profiles were sketched in each case. The gas dynamic jump in velocity to the subsonic state is described in §4.2.

The monograph of Anderson [16] provided the first analysis of shock structure allowing for dissipation coefficients in viscosity, electrical conductivity and thermal conductivity. Properties of integral curves coming from singular points of the ODEs in the solution plane were determined using an eigenvector approach allowing their general features to be sketched. The ODEs were not integrated numerically, instead the shock structure was described qualitatively. The conclusion was that only fast and slow shocks exist independently of the dissipation coefficients with intermediate shocks having steady structures only for certain values of the three dissipation coefficients and being unstable to small perturbations.

Bickerton et al. [17] provide an analysis giving shock profiles with dissipation due to viscosity and electrical resistivity. The method of solution of their coupled ODEs is not given and it is stated that fast, slow, switch-on and intermediate shocks $2 \rightarrow 3$ shocks have a unique structure, a result in accord with the calculations presented later in later chapters. Their approach uses critical Mach numbers to designate the condition for occurrence of each shock type and it is stated that non-unique shock structures are structurally unstable. Justification of the stability assertion is not given. The authors quote a result attributed to Anderson that the $1 \rightarrow 3$ shock structure is at first expansive, meaning undergoing a decline in mass density after leaving the upstream state, and then becoming compressive for the remainder of the transition. The calculations presented in this thesis find that initial density expansions are possible in both $1 \rightarrow 3$ and $1 \rightarrow 4$ shocks with $1 \rightarrow 4$ shocks sometimes exhibiting an expansion just before the downstream point.

Dixon and Woods [18] integrated a system of ODEs for a fast oblique shock including both viscosity and electrical and thermal conductivities. The aim was to compare their numerical profiles with experimental results. The dissipative coefficients were adjusted in an attempt to match a laboratory experimental profile of a fast perpendicular shock obtained by Robson and Sheffield [19]. Increasing the dissipation coefficients tended to dampen the magnetic field components more than observed experimentally, the authors considering that the mismatch of theory and experiment being due to a paucity of experimental data.

The next stage in the study of MHD shock structure was concerned with the study of intermediate shocks, these being shocks where the downstream transverse magnetic field is in the opposite direction

to its upstream direction. For reference purposes, the magnetic field vectors in an intermediate shock are shown in Figure 1 in §2.1. Fast and slow shocks, where the downstream magnetic field strength is respectively greater and less than the upstream value, both have their upstream and downstream transverse magnetic field components in the same direction. Intermediate shocks were considered to be unphysical or non-evolutionary due to them being unstable to small perturbations. Akhiezer et al. [20] used a wave counting argument to determine survivability of the shock. In brief, in ideal MHD 6 outgoing characteristic waves were needed to carry applied perturbations away from the shock, this allowing "evolutionarity" of the shock.

C. C. Wu in [21] and subsequent works started a new approach to the understanding of the nature and stability of intermediate shocks following the detection of a surviving one-dimensional intermediate shock structure in a one-dimensional Navier-Stokes MHD code. Previous thinking, based on the evolutionarity arguments of Russian authors using the hyperbolic nature of the MHD equations, predicted that most intermediate shocks were unphysical as all but one of these crossed two characteristic MHD propagation speeds. After calculating intermediate shock trajectories Wu subsequently suggested that intermediate shocks have free parameters, or degrees of freedom, in their structure. The degrees of freedom allow an intermediate shock transition to reach the downstream state by a number of routes and Wu stated that effectively this allows an intermediate shock to absorb small perturbations by adjusting its internal structure. Wu provided a number of numerical examples of the structure of intermediate shocks determined using a simplified set of equations based on the CKB (Cohen-Kulsrud-Burgers) equation as first proposed by Kennel et al. [22]. The CKB equation applies in the limit of weak nonlinearity and weak dissipation. This thesis calculates the structure of an intermediate shock in every possible case where the upstream Alfven speed is greater than the sound speed, this being the case that is most astrophysically relevant and supports a greater variety of shock types. It will be shown in Chapter 3 that intermediate shock formation is extremely limited when the upstream speed of sound is greater than the Alfven speed.

Coppi et. al. [23] further raised the question of the physical reality of intermediate shocks. They proposed that the equations of ideal MHD are not hyperbolic in nature as previously thought and this might allow shocks to cross more than one characteristic speeds in the flow allowing the possibility of intermediate shocks. They also stated that without dissipative terms the structure of the shock, meaning the spatial transition from the upstream to the downstream state, is not known and stability arguments "remain conjectures". To provide groundwork for future studies the authors provided graphical solutions using cubic equations for the jump conditions in several cases where multiple downstream shock states are possible. A more comprehensive analysis of the calculation of jump conditions is presented in §2.3.1 and a new method is given in §2.4 known as the parametric solution that allows multivalued plots to be drawn with greater computational ease than in the conventional approach of following the roots of a cubic.

Hau and Sonnerup [24] presented a detailed analysis of intermediate shock structure using three magnetic field hodograms. Hodograms are plots of B_z versus B_y through a shock, these being the transverse magnetic field components. The values of B_y and B_z were determined by numerically solving two first order ODEs for a range of initial conditions. The transition from a supersonic upstream state to a downstream subsonic state was stated to be achieved by a gas dynamic jump or by a purely smooth resistive transition through a transonic point. The conditions for the latter transition were not given. In this thesis the conditions for the smooth transition through the transonic point are described in §4.3 and are shown graphically in §3.2 with numerical integration through the transonic point giving the

smooth shock structures presented in §7.2.2 and §7.6.3.

Hada [25] stated that questions of evolutionarity and structure cannot be separated in the case of intermediate shocks and gave reasoning for the survivability of intermediate shocks to small perturbations. Shock structures were not calculated. It was stated that conventional arguments for the break up of intermediate shocks were based on an ideal MHD system and that when dissipation is included due to ohmic heating resistive wave modes appear which have no counterpart in ideal MHD. A perturbation given to the shock can be expressed as a sum of the resistive modes. To produce a uniquely defined system, and thus allow the amplitude of the outgoing wave modes to be determined, a constraint was introduced involving minimising the rate of entropy production, this principle being justified as the resistive wave modes dampen completely over the shock transition scale length.

Falle and Komarissov [26] stated that it was "well known" that intermediate shocks were unphysical and stated that another solution could arise in the original calculations of Wu [21] in which the intermediate shock was replaced by a slow shock and an Alfven wave. It was stated that the intermediate shock solution only arose due to the 180° rotation of the direction of the upstream transverse magnetic field component through the shock.

Inoue and Inutsuka [27] furthered the use of resistive modes near the shock approach of Hada [25] by proposing a method in which a small perturbation was added to the steady state shock structure and the resulting differential equations were linearised giving 13 first order differential equations for the spatial variations of the perturbed quantities. The presence of resistive modes, a feature absent in ideal MHD, allowed a unique determination of the perturbed solutions suggesting that intermediate shocks may appear in physical systems. In Chapter 9 of this thesis the approach of Inoue and Inutsuka is used in a preliminary analysis of the stability of an intermediate shock.

Takahashi and Yamada in two papers [28] and [29] present details of the solutions of the equations of ideal MHD in several situations using a specially written solver. In the first paper the "regular" and "non-regular" solutions of the ideal MHD problem are presented. These are slow and fast shocks and intermediate shocks respectively. Attention is given to a non-regular case previously noted by Brio and Wu [30] that was always realised in numerical simulations. The jump conditions of ideal MHD are given with plots included showing the downstream values in terms of the Mach number. As dissipative processes are not included in the calculations shock structures from the upstream to the downstream state are not given. The second paper presents the equations for the jump conditions with plots with $\gamma = \frac{5}{3}$ of the downstream values versus the Mach number. Details of the solver are presented and its use in searching for downstream solutions of the MHD shock problem is given. It is indicated that the solver is a powerful tool for finding shock solutions that may be "missed" by conventional approaches and these could have a role in the overall stability problem for MHD shocks. As in the first paper dissipative terms are not included and structures giving the transition in the flow variables between the disturbed and undisturbed states are not given. The phase plane and its role in showing the presence of degrees of freedom in shock structures is not given. The non-regular surviving shock observed in simulations corresponds to an intermediate shock with one degree of freedom in its structure. A detailed analysis of intermediate shock structures, including the effects of Ohmic heating, is presented in Chapter 7 of this thesis.

In summary, the nature of MHD intermediate shocks has had a mixed history. Initially thought to be unphysical due to arguments based on ideal MHD systems with no dissipative mechanisms such

as ohmic heating, a number of arguments were proposed for the physical nature of intermediate shocks, the turning point being the work of Wu [21] who found that intermediate shocks have internal degrees of freedom, Hau and Sonnerup [24] who gave a study using phase plane analysis and Inoue and Inutsuka [27] who provided a formulation to test shock stability in terms of ODEs.

To determine the physical reality of intermediate shocks it is necessary to determine their steady state structure and apply a perturbation to this structure. This thesis sets out to determine the steady state structure of each possible type of intermediate shock in the case where the upstream Alfven speed is greater than the upstream sound speed and energy dissipation is due to ohmic heating. This is done using a phase plane analysis to map out possible shock transitions and numerical integration of two first order ODEs to determine the shock structure. These computed structures lay the groundwork for further analysis on the stability of each shock structure, a preliminary example of which is given in Chapter 9.

2 The Equations of Resistive MHD

This chapter presents the equations of resistive MHD that describe the structure of shock fronts. In general three dissipative processes may occur in MHD due to the fluid's viscosity, thermal conductivity and electrical conductivity. The coefficients for these processes determine the structure of the shock. In this thesis structure will be analysed taking electrical resistance as the sole dissipative process. The starting point are the fundamental MHD equations given by, for example, Landau et al.[31] .

A possible overarching question is why the dissipative effects due to electrical heating are discussed at length in this thesis and not those due to fluid viscosity. The dilute interstellar medium is characterised by a small resistivity and a large viscosity. The MHD equations for the resistivity-viscosity case consist of five coupled ODEs in five variables whereas the resistivity case involves two variables. The two variable case is suitable for analysis using the phase plane method described in Chapter 4. A five variable problem in the general case would require additional dimensions in the phase analysis, adding considerable complexity to the problem. The final chapter presents a two variable case where viscosity is included, this being a perpendicular shock. In this case the results show that the presence of fluid viscosity does not have a major effect on the shock profile, its presence allowing a continuous passage of the fluid from a supersonic to subsonic state. In the absence of viscosity this passage is allowed by an entropy increasing gasdynamic jump.

To set the scene for a study of resistive MHD shocks it is timely to first mention gasdynamic shocks, often called hydrodynamic shocks. The theory of these shocks is given in Zel'dovich and Raizer [32] . When a large disturbance travels through a fluid in the absence of a magnetic field at a speed greater than that of sound the transition between the initial and final fluid states is known as a gas dynamic shock. In the absence of a magnetic field there is only one characteristic speed at which small vibrations can be transmitted through the fluid, this being the speed of sound. The speed of small vibrations of fluid particles is independent of any reference direction and so there is only one possible "type" of gas dynamic shock regardless of the speed of the shock. The strength of a gasdynamic shock depends on the ratio of the specific heats of the fluid and the ratio of the shocked to unshocked densities of the fluid. In a gasdynamic shock the gas enters the reference frame of the shock with a supersonic speed and leaves it subsonically. When a magnetic field is present there are three characteristic speeds in the fluid each depending on the angle between the magnetic field and the normal to the plane of the shock. In this situation there are three "types" of shock that can occur and both supersonic to supersonic and subsonic to subsonic transitions can occur for certain parameter ranges.

2.1 Resistive MHD

The MHD equations express conservation of mass, momentum, magnetic flux and energy. The first of these is the equation of continuity, expressing conservation of mass

$$\nabla \cdot (\rho \mathbf{u}) + \frac{\partial \rho}{\partial t} = 0. \tag{1}$$

The next equation is the Navier-Stokes equation for a magneto-fluid, which in Gaussian units is

$$\rho \left(\frac{\partial \mathbf{u}}{\partial t} + \mathbf{u} \cdot \nabla \mathbf{u} \right) = -\nabla p + \frac{\mathbf{J} \times \mathbf{B}}{c}. \tag{2}$$

On neglecting the displacement current density term in the Ampere-Maxwell equation this becomes

$$\rho\left(\frac{\partial \mathbf{u}}{\partial t}+\mathbf{u}\cdot\nabla\mathbf{u}\right)=-\nabla p+\frac{1}{4\pi}\left(\nabla\times\mathbf{B}\right)\times\mathbf{B}. \tag{3}$$

The equation expressing conservation of magnetic flux, expressed through the induction equation, is

$$\frac{\partial \mathbf{B}}{\partial t}=\eta\nabla^2\mathbf{B}+\nabla\times\left(\mathbf{u}\times\mathbf{B}\right). \tag{4}$$

In the last equation η is the magnetic diffusivity

$$\eta=\frac{c^2}{4\pi\sigma}, \tag{5}$$

where σ is the electrical conductivity of the fluid, which is assumed to be constant.

The equation expressing conservation of energy is [31]

$$\frac{\partial}{\partial t}\left(\frac{1}{2}\varrho\left|\mathbf{u}\right|^2+\frac{p}{\gamma-1}+\frac{1}{8\pi}\left|\mathbf{B}\right|^2\right)=-\nabla\cdot\left[(\frac{1}{2}\rho\left|\mathbf{u}\right|^2+\frac{\gamma p}{\gamma-1})\mathbf{u}+\frac{1}{4\pi}\mathbf{B}\times(\mathbf{u}\times\mathbf{B})-\frac{\eta}{4\pi}\mathbf{B}\times(\nabla\times\mathbf{B})\right]. \tag{6}$$

Here γ is the adiabatic index for the gas, being the ratio of the specific heat of the gas at constant pressure to the specific heat at constant volume. For a monatomic gas $\gamma=\frac{5}{3}$ and for a diatomic gas $\gamma=\frac{7}{5}$.

The unshocked fluid state is referred to as the upstream state and the shocked fluid state is termed the downstream state. A shock is the transition of the flow variables from the upstream to the downstream states. In the calculations that follow the upstream state is taken to be to the left and the downstream state is on the right. The direction of increasing x is from the upstream state towards the downstream state. As viewed from the unshocked fluid, the disturbance is coming from the right towards the left. In order to calculate the shock structure it is convenient to use a reference frame, called the shock reference frame, in which the shock is stationary and the unshocked gas approaches from the left. The normal incidence frame will be employed with the axes chosen such that the upstream shock front lies in the $y-z$ plane with the upstream fluid velocity perpendicular to this plane and directed along the positive x axis. The y axis is aligned such that the upstream magnetic field lies in the $x-y$ plane. Values of the flow variables can later be found in the rest reference frame by a Galilean transformations. The normal incidence frame has the advantage that only one upstream velocity component is used, producing a slight simplification of the flow equations. The upstream state fluid velocity has the symbol u_{x1}, with by choice u_{y1} and u_{z1} both being zero in this reference system. The downstream state fluid velocity components are u_{x2} and u_{y2} , with u_{z2} being zero as it will later be seen that u_{z2} is proportional to B_{z2} which is zero as the magnetic field components remain in the $x-y$ plane at the downstream state. This is shown in Figure 1.

2.2 The Plane Parallel Steady State Equations

The steady shock structure equations are found by putting all derivatives with respect to t, y and z equal to zero. The magnetic field components B_y and B_z are then functions of x. Since $\nabla\cdot\mathbf{B}=0$, the magnetic field component perpendicular to the shock plane, B_x, is unchanged through the shock.

In the stationary state all flow quantities only depend on x and the equations representing conservation of mass, momentum, magnetic flux and energy become respectively

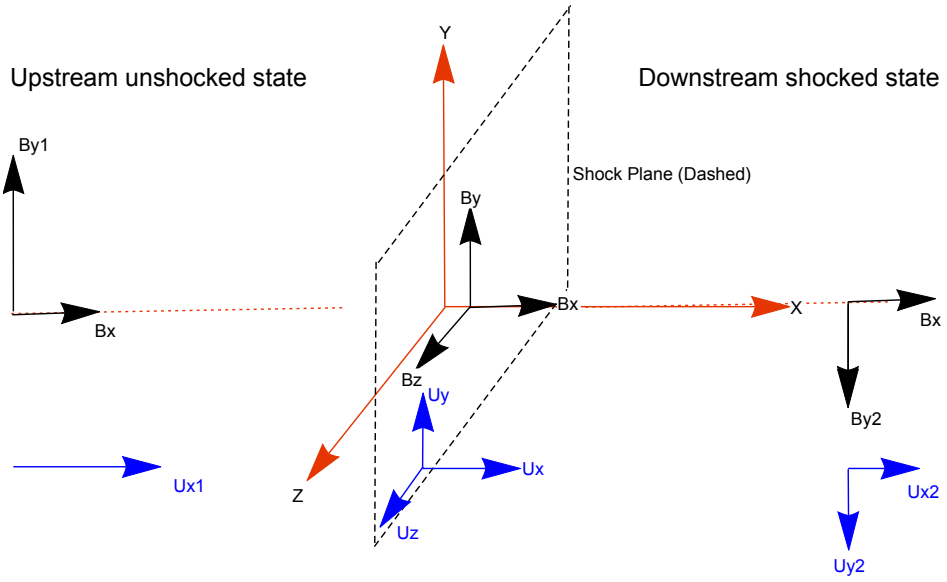

Figure 1: Magnetic field and fluid flow velocity vectors for a MHD shock. Vectors are shown for an intermediate shock where B_y and u_y reverse direction; for fast and slow shocks these vectors do not change direction.

$$\frac{d}{dx}(\rho u_x) = 0, \tag{7}$$

$$\rho u_x \frac{du_x}{dx} = -\frac{dp}{dx} - \frac{1}{8\pi}\frac{d}{dx}\left(B_y^2 + B_z^2\right), \tag{8}$$

$$\rho u_x \frac{du_y}{dx} = B_x \frac{dB_y}{dx}, \tag{9}$$

$$\rho u_x \frac{du_z}{dx} = B_x \frac{dB_z}{dx}, \tag{10}$$

$$\eta \frac{d^2 B_y}{dx^2} = \frac{d}{dx}\left(B_x u_y - B_y u_x\right), \tag{11}$$

$$\eta \frac{d^2 B_z}{dx^2} = \frac{d}{dx}\left(B_x u_z - B_z u_x\right), \tag{12}$$

and

$$0 = \frac{d}{dx}\{\ u_x\left[\frac{1}{2}\rho\left(u_x^2+u_y^2+u_z^2\right)+\frac{\gamma p}{\gamma-1}\right]+\frac{1}{4\pi}u_x\left(B_x^2+B_y^2+B_z^2\right)$$
$$-\frac{1}{4\pi}B_x\left(B_xu_x+B_yu_y+B_zu_z\right)-\frac{\eta}{4\pi}\left(B_y\frac{dB_y}{dx}+B_z\frac{dB_z}{dx}\right)\ \}. \tag{13}$$

The equations (7)-(13) are integrated once with respect to x to obtain the following conserved quantities:

$$\rho u_x = f_1, \tag{14}$$

$$\frac{B_y^2+B_z^2}{8\pi}+p+f_1u_x = f_2, \tag{15}$$

$$-\frac{B_xB_y}{4\pi}+f_1u_y = f_3, \tag{16}$$

$$-\frac{B_xB_z}{4\pi}+f_1u_z = f_4, \tag{17}$$

$$B_yu_x-B_xu_y-\eta\frac{dB_y}{dx} = f_5, \tag{18}$$

$$B_zu_x-B_xu_z-\eta\frac{dB_z}{dx} = f_6, \tag{19}$$

and

$$\frac{1}{2}f_1\left(u_x^2+u_y^2+u_z^2\right)+\frac{\gamma pu_x}{\gamma-1}+\frac{u_x\left(B_y^2+B_z^2\right)}{4\pi}-\frac{B_x\left(B_yu_y+B_zu_z\right)}{4\pi}-\frac{\eta}{4\pi}\left(B_y\frac{dB_y}{dx}+B_z\frac{dB_z}{dx}\right) = f_7. \tag{20}$$

In equations (14)-(20) f_1, f_2, f_3, f_4, f_5, f_6 and f_7 are determined by the upstream conditions and are constant through the shock. These respectively express conservation of mass flux, momentum flux, the y and z components of the electric field and energy flux through the shock. Together with the component of the magnetic field perpendicular to the plane of the shock, B_x, these 8 constants determine the transition from the upstream to the downstream state. In this chapter the seven constants are used for notational convenience to avoid equations becoming too cluttered. The constants will be related to specific properties of the fluid in Chapter 3. As the magnetic field and flow velocity components in the upstream state lie in the $x-y$ plane, the constants f_4 and f_6 are both zero.

We now show that the equations (14)-(20) can be reduced to a pair of coupled ODEs in B_y and B_z.

Equations (15), (16) and (17) can be used to determine p, u_y and u_z in terms of the magnetic field components and the normal flow velocity component u_x:

$$p = f_2 - f_1 u_x - \frac{B_y^2 + B_z^2}{8\pi}, \tag{21}$$

$$u_y = \frac{1}{f_1}\left(f_3 + \frac{B_x B_y}{4\pi}\right), \tag{22}$$

$$u_z = \frac{B_x B_z}{4\pi f_1}. \tag{23}$$

Equations (18)-(20) become

$$\eta \frac{dB_y}{dx} = B_y u_x - \frac{B_x}{f_1}\left(f_3 + \frac{B_x B_y}{4\pi}\right) - f_5, \tag{24}$$

$$\eta \frac{dB_z}{dx} = B_z u_x - \frac{B_x^2 B_z}{4\pi f_1}, \tag{25}$$

and u_x is given by

$$\begin{aligned} \frac{1}{2} f_1 u_x^2 \left(1 - \frac{2\gamma}{\gamma - 1}\right) &+ \frac{u_x}{\gamma - 1}\left[\gamma f_2 - (2-\gamma)\frac{\left(B_y^2 + B_z^2\right)}{8\pi}\right] + \frac{1}{2f_1}\left[f_3^2 - \frac{B_x^2}{16\pi^2}\left(B_y^2 + B_z^2\right)\right] \\ &- \frac{\eta}{4\pi}\left(B_y \frac{dB_y}{dx} + B_z \frac{dB_z}{dx}\right) = f_7 \end{aligned} \tag{26}$$

respectively.

Equations (24), (25), (26) become on eliminating u_x and solving for $\frac{dB_y}{dx}$ and $\frac{dB_z}{dx}$

$$\begin{aligned} 8\pi\eta\left(\gamma+1\right) f_1 \frac{dB_y}{dx} = &-8\pi\left(\gamma+1\right)\left(f_3 B_x + f_1 f_5\right) - B_y\left\{\gamma\left(B_y^2 + B_z^2\right) + 2\left[\left(\gamma+1\right)B_x^2 - 4\pi\gamma f_2\right]\right\} \\ &\pm B_y\{\ \gamma^2\left(B_y^4 + B_z^4\right) + 4[\left(\gamma^2-1\right)B_x^2 - 4\pi\gamma^2 f_2](B_y^2 + B_z^2) + 2\gamma^2 B_y^2 B_z^2 \\ &+ 32\pi\left(\gamma^2-1\right)\left(f_3 B_x + f_1 f_5\right) B_y + 64\pi^2[\gamma^2 f_2^2 + (\gamma^2-1)(f_3^2 - 2f_1 f_7)]\ \}^{\frac{1}{2}}, \end{aligned} \tag{27}$$

and

$$\begin{aligned} 8\pi\eta\left(\gamma+1\right) f_1 \frac{dB_z}{dx} = &-B_z\left\{\gamma\left(B_y^2 + B_z^2\right) + 2\left[\left(\gamma+1\right)B_x^2 - 4\pi\gamma f_2\right]\right\} \\ &\pm B_z\{\ \gamma^2\left(B_y^4 + B_z^4\right) + 4[\left(\gamma^2-1\right)B_x^2 - 4\pi\gamma^2 f_2](B_y^2 + B_z^2) + 2\gamma^2 B_y^2 B_z^2 \\ &+ 32\pi\left(\gamma^2-1\right)\left(f_3 B_x + f_1 f_5\right) B_y + 64\pi^2[\gamma^2 f_2^2 + (\gamma^2-1)(f_3^2 - 2f_1 f_7)]\ \}^{\frac{1}{2}}. \end{aligned} \tag{28}$$

Equations (24), (25) and (26) become on eliminating $\frac{dB_y}{dx}$ and $\frac{dB_z}{dx}$

$$\frac{16\pi^2\left(\gamma+1\right)f_1^2}{\left(\gamma-1\right)}u_x^2+\frac{4\pi\gamma f_1}{\left(\gamma-1\right)}\left(B_y^2+B_z^2-8\pi f_2\right)u_x-B_x^2\left(B_y^2+B_z^2\right)-8\pi B_y(B_xf_3+f_1f_5)-16\pi^2\left(f_3^2-2f_1f_7\right)=0. \tag{29}$$

The simultaneous numerical solution of equations (27) and (28), using the upstream conditions, gives the variation of B_y and B_z through the shock. Equation (29) then determines the flow velocity u_x at each particular point in the shock and the fluid density and pressure can be found using equations (14) and (21) respectively.

Equation (29) defines a cubic surface in B_y - B_z - u_x space. For given values of B_y and B_z there are at most two different values of u_x due to the quadratic form of (29) in u_x . It will be shown in §4.1 that the two values of u_x correspond to supersonic ($u_x > a$) and subsonic ($u_x < a$) flow, where a is the speed of sound in the fluid for the particular values of B_y and B_z and the upstream conditions, given by $a=\sqrt{\frac{\gamma p}{\rho}}$. This allows the insertion of a gasdynamic jump within the shock, the location of the jump being a degree of freedom in the structure of the shock.

Derivatives of $\mathbf{u_x}$

In §4.3 it will be shown that a continuous shock structure between supersonic and subsonic states is possible for certain upstream parameter ranges. This type of transition requires analysis of the higher order spatial derivatives of the normal shock velocity component, up to the fourth order. The first derivative, $\frac{du_x}{dx}$, is obtained by differentiating (29) with respect to x.

$$\frac{4\pi f_1}{\left(\gamma-1\right)}\left[8\pi(\gamma+1)f_1u_x+\gamma\left(B_y^2+B_z^2-8\pi f_2\right)\right]\frac{du_x}{dx}-2\{B_y[B_x^2-\frac{4\pi\gamma f_1}{(\gamma-1)}u_x]+4\pi(B_xf_3+f_1f_5)\}\frac{dB_y}{dx}$$
$$-\,2B_z[B_x^2-\frac{4\pi\gamma f_1}{(\gamma-1)}u_x]\frac{dB_z}{dx}=0. \tag{30}$$

Replacing the magnetic field derivatives in (30) using equations (24) and (25) gives

$$\frac{4\pi f_1}{\left(\gamma-1\right)}\left\{\gamma\left(B_y^2+B_z^2\right)+8\pi\left[\left(\gamma+1\right)f_1u_x-\gamma f_2\right]\right\}\frac{du_x}{dx}+\frac{1}{2\pi\eta\left(\gamma-1\right)f_1}\left(B_y^2+B_z^2\right)\left(B_x^2-4\pi f_1u_x\right)\left[\left(\gamma-1\right)B_x^2-4\pi\gamma f_1u_x\right]$$
$$+\,\frac{4}{\eta\left(\gamma-1\right)f_1}\left(B_xf_3+f_1f_5\right)B_y\left[\left(\gamma-1\right)B_x^2-2\pi\left(2\gamma-1\right)f_1u_x\right]+\frac{8\pi}{\eta f_1}\left(B_xf_3+f_1f_5\right)^2=0. \tag{31}$$

Equation (31) can be written as with $\frac{du_x}{dx}$ as the subject

$$8\eta\pi^2f_1^2\left[8\pi\left(\gamma+1\right)f_1u_x+\gamma\left(B_y^2+B_z^2-8\pi f_2\right)\right]\frac{du_x}{dx}=\left(B_y^2+B_z^2\right)\left(B_x^2-4\pi f_1u_x\right)\left[4\pi\gamma f_1u_x-\left(\gamma-1\right)B_x^2\right]$$
$$+8\pi\left(B_xf_3+f_1f_5\right)\left[2\pi\left(2\gamma-1\right)f_1u_x-\left(\gamma-1\right)B_x^2\right]B_y-16\pi^2\left(\gamma-1\right)\left(B_xf_3+f_1f_5\right)^2. \tag{32}$$

Taking the speed of sound to be given by $a=\sqrt{\frac{\gamma p}{\rho}}$, equations (14) and (15) allow equation (32) to be

written as

$$64\eta\pi^3 f_1^3 \frac{\left(a^2-u_x^2\right)}{u_x}\frac{du_x}{dx} = \left(B_y^2+B_z^2\right)\left(B_x^2-4\pi f_1 u_x\right)\left[\left(\gamma-1\right)B_x^2-4\pi\gamma f_1 u_x\right]$$
$$+8\pi\left(B_x f_3+f_1 f_5\right)\left[\left(\gamma-1\right)B_x^2-2\pi\left(2\gamma-1\right)f_1 u_x\right]B_y+16\pi^2\left(\gamma-1\right)\left(B_x f_3+f_1 f_5\right)^2. \qquad (33)$$

The second derivative of the normal shock velocity component is obtained by differentiating equation (29) twice with respect to x and replacing the first and second derivatives of the magnetic field components using equations (24) and (25),

$$16\eta^2\pi^3 f_1^3\left[8\pi(\gamma+1)f_1 u_x+\gamma\left(B_y^2+B_z^2-8\pi f_2\right)\right]\frac{d^2u_x}{dx^2} = -128\left(\gamma+1\right)\eta^2\pi^4 f_1^4\left(\frac{du_x}{dx}\right)^2$$
$$+\ 8\eta\pi^2 f_1^2\left\{\left(B_y^2+B_z^2\right)\left[\left(3\gamma-1\right)B_x^2-12\pi\gamma f_1 u_x\right]+4\pi\left(3\gamma-1\right)\left(B_x f_3+f_1 f_5\right)B_y\right\}\frac{du_x}{dx}$$
$$+\left(B_y^2+B_z^2\right)\left(B_x^2-4\pi f_1 u_x\right)^2\left[\left(\gamma-1\right)B_x^2-4\pi\gamma f_1 u_x\right]+8\pi\left(B_x f_3+f_1 f_5\right)\left(B_x^2-4\pi f_1 u_x\right)$$
$$\times\left[\left(\gamma-1\right)B_x^2-\left(4\gamma-1\right)\pi f_1 u_x\right]B_y+16\pi^2\left(B_x f_3+f_1 f_5\right)^2\left[\left(\gamma-1\right)B_x^2-2\left(2\gamma-1\right)\pi f_1 u_x\right]. \qquad (34)$$

The third derivative of the shock velocity is found by differentiating equation (29) three times with respect to x and replacing the first, second and third derivatives of the magnetic field components using equations (24) and (25),

$$32\pi^4\eta^3 f_1^4\left[8\pi(\gamma+1)f_1 u_x+\gamma\left(B_y^2+B_z^2-8\pi f_2\right)\right]\frac{d^3u_x}{dx^3} = -16\pi^3\eta^2 f_1^3\{\ 48\pi^2\eta f_1^2\left(\gamma+1\right)\frac{du_x}{dx}$$
$$-\left[\left(4\gamma-1\right)B_x^2-16\pi\gamma f_1 u_x\right]\left(B_y^2+B_z^2\right)-4\pi\left(4\gamma-1\right)\left(B_x f_3+f_1 f_5\right)B_y\ \}\frac{d^2u_x}{dx^2}$$
$$-\ 192\pi^4\eta^2\gamma f_1^4\left(B_y^2+B_z^2\right)\left(\frac{du_x}{dx}\right)^2-8\pi^2\eta f_1^2\{\ 3\left(B_x^2-4\pi f_1 u_x\right)\left[\left(2\gamma-1\right)B_x^2-8\pi\gamma f_1 u_x\right]\left(B_y^2+B_z^2\right)$$
$$+\ 2\pi(B_x f_3+f_1 f_5)\left[\left(17\gamma-8\right)B_x^2-4\pi\left(17\gamma-3\right)f_1 u_x\right]B_y+8\pi^2\left(5\gamma-2\right)\left(B_x f_3+f_1 f_5\right)^2\ \}\frac{du_x}{dx}$$
$$-\left(B_x^2-4\pi f_1 u_x\right)\{\ \left(B_y^2+B_z^2\right)\left(B_x^2-4\pi f_1 u_x\right)^2\left[\left(\gamma-1\right)B_x^2-4\pi\gamma f_1 u_x\right]+4\pi(B_x f_3+f_1 f_5)\{\left(B_x^2-4\pi f_1 u_x\right)$$
$$\times\left[2\left(\gamma-1\right)B_x^2-\pi f_1\left(8\gamma-1\right)u_x\right]B_y+4\pi(B_x f_3+f_1 f_5)\left[\left(\gamma-1\right)B_x^2-\pi f_1\left(4\gamma-1\right)u_x\right]\}\ \}. \qquad (35)$$

The fourth derivative, found in a similar manner, is

$$64\pi^5\eta^4 f_1^5\left[8\pi(\gamma+1)f_1 u_x+\gamma\left(B_y^2+B_z^2-8\pi f_2\right)\right]\frac{d^4u_x}{dx^4} = 32\pi^4\eta^3 f_1^4\{\ \left(B_y^2+B_z^2\right)\left[\left(5\gamma-1\right)B_x^2-20\pi\gamma f_1 u_x\right]$$
$$+4\pi\left(5\gamma-1\right)\left(B_x f_3+f_1 f_5\right)B_y-64\pi^2\left(\gamma+1\right)\eta f_1^2\frac{du_x}{dx}\ \}\frac{d^3u_x}{dx^3}-1536\pi^6\eta^4\left(\gamma+1\right)f_1^6\left(\frac{d^2u_x}{dx^2}\right)^2$$
$$-32\pi^3\eta^2 f_1^3\{\left(B_y^2+B_z^2\right)\{\left(B_x^2-4\pi f_1 u_x\right)\left[\left(5\gamma-2\right)B_x^2-20\pi\gamma f_1 u_x\right]+40\pi^2\gamma\eta f_1^2\frac{du_x}{dx}\}+\pi(B_x f_3+f_1 f_5)$$
$$\times[\left(29\gamma-11\right)B_x^2-4\pi\left(29\gamma-4\right)f_1 u_x]B_y+12\pi^2\left(3\gamma-1\right)\left(B_x f_3+f_1 f_5\right)^2\}\frac{d^2u_x}{dx^2}$$
$$+64\pi^4\eta^2 f_1^4\{3\left(B_y^2+B_z^2\right)\left[\left(5\gamma-1\right)B_x^2-20\pi\gamma f_1 u_x\right]+2\pi\left(23\gamma-3\right)\left(B_x f_3+f_1 f_5\right)B_y\}\left(\frac{du_x}{dx}\right)^2$$
$$-8\pi^2\eta f_1^2\{-2\left(B_y^2+B_z^2\right)\left(B_x^2-4\pi f_1 u_x\right)^2\left[\left(5\gamma-3\right)B_x^2-20\pi\gamma f_1 u_x\right]-\pi(B_x f_3+f_1 f_5)\left(B_x^2-4\pi f_1 u_x\right)$$
$$\times[\left(65\gamma-37\right)B_x^2-4\pi\left(65\gamma-6\right)f_1 u_x]B_y-4\pi^2(B_x f_3+f_1 f_5)^2[\left(25\gamma-13\right)B_x^2-20\pi\left(5\gamma-1\right)f_1 u_x]\}\frac{du_x}{dx}$$

$$+\left(B_x^2-4\pi f_1 u_x\right)^2\left\{\left(B_y^2+B_z^2\right)\left(B_x^2-4\pi f_1 u_x\right)^2\left[\left(\gamma-1\right)B_x^2-4\pi\gamma f_1 u_x\right]+2\pi(B_x f_3+f_1 f_5)\left(B_x^2-4\pi f_1 u_x\right)\right.$$
$$\left.\times[4\left(\gamma-1\right)B_x^2-\pi\left(16\gamma-1\right)f_1 u_x]B_y+8\pi^2(B_x f_3+f_1 f_5)^2[2\left(\gamma-1\right)B_x^2-\pi\left(8\gamma-1\right)f_1 u_x]\right\}. \quad (36)$$

2.3 The Jump Conditions

Jump conditions relate the upstream and downstream values of the flow variables. In this section the conventional approach is presented where the downstream mass density, flow speed and magnetic field are related to the upstream properties by cubic equations. Two special cases must be considered separately: the parallel shock, where the upstream magnetic field is parallel to the velocity vector, and the perpendicular shock, where the upstream magnetic field is perpendicular to the velocity vector. For a parallel shock, $B_x = B_1$, $B_{y1} = 0$ with $\theta_1 = 0°$, for a perpendicular shock, $B_x = 0$, $B_{y1} = B_1$ with $\theta_1 = 90°$, where θ_1 is the angle between the normal to the plane of the shock and the upstream magnetic field vector given by $B_x = B_1 \cos\theta_1$. This section is therefore divided into subsections presenting the oblique, parallel and perpendicular jump conditions.

2.3.1 Oblique Shock

This subsection derives the jump conditions for the case where the upstream magnetic field is neither parallel nor perpendicular to the shock normal. The distinction is necessary to avoid division in the algebraic manipulation by the term $\left(rB_x^2-4\pi\rho_1 u_{x1}^2\right)$ that is zero in the case of a parallel shock and $(B_{y2}-B_{y1}r)$ that is zero in the case of a perpendicular shock.
At the upstream and downstream states in the steady state the MHD flow variables are all constant. The relationships between the upstream and downstream values of the flow variables denoted by $B_{y1}, u_{x1}, \rho_1, p_1$ and $B_{y2}, u_{x2}, u_{y2}, \rho_2, p_2$ are found by putting $\frac{dB_y}{dx}=0$, $\frac{dB_z}{dx}=0$, $B_{z1}=0$, $B_{z2}=0$, $u_{z1}=0$ and $u_{z2}=0$ with $u_{y1}=0$ in equations (14) to (20):

$$\rho_1 u_{x1} = \rho_2 u_{x2}, \quad (37)$$

$$\frac{B_{y1}^2}{8\pi}+p_1+\rho_1 u_{x1}^2 = \frac{B_{y2}^2}{8\pi}+p_2+\rho_2 u_{x2}^2, \quad (38)$$

$$-\frac{B_x B_{y1}}{4\pi} = -\frac{B_x B_{y2}}{4\pi}+\rho_2 u_{x2} u_{y2}, \quad (39)$$

$$B_{y1}u_{x1} = B_{y2}u_{x2}-B_x u_{y2}, \quad (40)$$

$$\frac{1}{2}\rho_1 u_{x1}^3+\frac{\gamma}{\gamma-1}p_1 u_{x1}+\frac{B_{y1}^2}{4\pi}u_{x1} = \frac{1}{2}\rho_2 u_{x2}\left(u_{x2}^2+u_{y2}^2\right)+\frac{\gamma}{\gamma-1}p_2 u_{x2}+\frac{B_{y2}^2}{4\pi}u_{x2}-\frac{B_x B_{y2}}{4\pi}u_{y2}. \quad (41)$$

Equations (37) to (41) are known as the jump conditions and can be used to predict the possible downstream values produced by a shock transition for a given set of upstream values $B_{y1}, u_{x1}, \rho_1, p_1$ and γ (assumed constant). The magnetic diffusivity η does not affect the downstream values as it enters the equations as a multiplier of the magnetic field derivatives and so only determines the length scale of the transition.

The first relationship is the connection between the upstream values and the downstream to upstream mass density ratio r, defined by $r = \frac{\rho_2}{\rho_1}$,

$$B_x^2\left[\rho_1(\gamma-1)\left(B_x^2+B_{y1}^2\right)u_{x1}^2+2\gamma p_1 B_x^2\right]r^3-\rho_1 u_{x1}^2\{\ B_x^2\left[16\pi\gamma p_1+(\gamma+1)\left(B_x^2+B_{y1}^2\right)\right]$$
$$+\ 4\pi\rho_1 u_{x1}^2\left[(\gamma-2)B_{y1}^2+2(\gamma-1)B_x^2\right]\ \}r^2+4\pi\rho_1^2u_{x1}^4[2(\gamma+1)B_x^2\ +\gamma\left(B_{y1}^2+8\pi p_1\right)$$
$$+\ 4\pi\rho_1(\gamma-1)u_{x1}^2\ ]r-16\pi^2(\gamma+1)\rho_1^3u_{x1}^6=0. \tag{42}$$

Equation (42) is a cubic equation in r and so may have one real solution or three real solutions. Each value of r corresponds to a particular type of shock depending on its transverse downstream magnetic field component B_{y2} which is found from the upstream values from

$$B_{y2}^3+(\gamma-1)B_{y1}B_{y2}^2+\left\{B_x^2+\gamma\left[B_x^2-B_{y1}^2-8\pi\left(p_1+\rho_1u_{x1}^2\right)\right]\right\}B_{y2}-(\gamma+1)\left(B_x^2-8\pi\rho_1u_{x1}^2\right)B_{y1}=0. \tag{43}$$

This can be expressed using the integration constants f_1 and f_2 as

$$B_{y2}^3+(\gamma-1)B_{y1}B_{y2}^2+\left[(\gamma+1)B_x^2-8\pi f_2\right]B_{y2}-(\gamma+1)\left(B_x^2-8\pi f_1u_{x1}\right)B_{y1}=0. \tag{44}$$

The relationship between B_{y1}, r, u_{x1}, ρ_1 and B_{y2} is

$$B_{y2}=B_{y1}\frac{\left(B_x^2-4\pi\rho_1u_{x1}^2\right)}{\left(rB_x^2-4\pi\rho_1u_{x1}^2\right)}r. \tag{45}$$

The downstream normal flow speed u_{x2} in terms of the upstream values can be found from

$$16\pi^2(\gamma+1)\rho_1^3u_{x1}^3u_{x2}^3-4\pi\rho_1^2u_{x1}^2\left[2(\gamma+1)B_x^2+\gamma\left(B_{y1}^2+8\pi p_1\right)+4\pi\rho_1(\gamma-1)u_{x1}^2\right]u_{x2}^2$$
$$+\ \rho_1u_{x1}\left\{B_x^2\left[16\pi\gamma p_1+(\gamma+1)\left(B_x^2+B_{y1}^2\right)\right]+4\pi\rho_1u_{x1}^2\left[(\gamma-2)B_{y1}^2+2(\gamma-1)B_x^2\right]\right\}u_{x2}$$
$$-\ B_x^2[2\gamma p_1B_x^2+(\gamma-1)\rho_1\left(B_x^2+B_{y1}^2\right)u_{x1}^2]=0. \tag{46}$$

The relationship between u_{x1}, r and u_{x2} is

$$u_{x2}=\frac{u_{x1}}{r}. \tag{47}$$

The relationship between the downstream fluid pressure, p_2 and the upstream fluid pressure p_1 is found by eliminating u_{x1}, u_{x2} and u_{y2} from equations (37)-(40),

$$p_2=p_1-\frac{(B_{y2}-B_{y1})}{8\pi}\left[B_{y2}+B_{y1}-\frac{2(r-1)B_x^2}{(B_{y2}-B_{y1}r)}\right]. \tag{48}$$

The relationship between the upstream and downstream pressures, densities and transverse magnetic field components is found by eliminating u_{x1}, u_{x2},u_{y2} and B_x from equations (37)-(41)

$$\frac{p_2}{p_1}=\frac{\frac{\gamma+1}{\gamma-1}r+\frac{(B_{y2}-B_{y1})^2}{8\pi p_1}(r-1)-1}{\frac{\gamma+1}{\gamma-1}-r}. \tag{49}$$

Equation(49) indicates that the maximum value of the density ratio of the downstream and upstream states is $\dfrac{\gamma+1}{\gamma-1}$, since $\gamma > 1$, $r > 1$ and $\frac{p_2}{p_1} > 1$. The pressure ratio of the downstream to upstream states is not limited in value due to its dependence on the square of the difference of the downstream and upstream transverse magnetic field components. Equations (48)-(49) are suitable for the numerical computation of the pressure ratio. Equation (49) can be expressed in a form that separates the gas dynamic and magnetic terms. This form has been given names such as the shock adiabatic or the Hugoniot relationship,

$$\frac{\left(B_{y2}-B_{y1}\right)^2}{8\pi} = 2\frac{p_2 - rp_1}{\left(\gamma-1\right)\left(r-1\right)} - p_2 - p_1. \tag{50}$$

The relationship between the downstream speed of sound and the upstream values, found by eliminating ρ_2, u_{y2} and B_{y2} from (37)-(41) and using $a_2 = \sqrt{\frac{\gamma p_2}{\rho_2}}$ is a cubic equation in a_2^2, the coefficients k_i being listed in Table 2 given in Appendix A,

$$k_6 a_2^6 + k_4 a_2^4 + k_2 a_2^2 + k_0 = 0. \tag{51}$$

The relationship between the downstream flow speed and the downstream sound speed is a sextic equation in u_{x2}^2, the coefficients l_i being listed in Table 3 given in Appendix B,

$$l_{12}u_{x2}^{12} + l_{10}u_{x2}^{10} + l_8 u_{x2}^8 + l_6 u_{x2}^6 + l_4 u_{x2}^4 + l_2 u_{x2}^2 + l_0 = 0. \tag{52}$$

Equation (52) can be used to find when $u_{x2} = a_2$. This is of significance as an increase in the upstream flow speed may cause the downstream flow to change from supersonic to subsonic and (46) can be used to determine the upstream shock speed where this change occurs. In this thesis points where the downstream sound and normal shock speed points are equal will be called equisonic points, the upstream shock speed at these points having the symbols v_{ei1} and v_{ef1}, the first of these applying to an intermediate shock, the second to a fast shock. In general, in an oblique shock model that only includes dissipation due to electrical heating through the introduction of a resistivity factor into the equations a continuous shock structure in both transverse magnetic field and flow velocity components is only possible when the upstream and downstream states are both supersonic or subsonic, otherwise a hydrodynamic jump must occur at some point in the flow. The exception to this rule is flow through a unique transonic flow point, where the sound speed equals the normal shock velocity and the normal shock velocity derivatives of first and higher orders are the same on the supersonic and subsonic sides of the transition point. The domain of upstream normal flow speeds for which a smooth transonic flow point exists depends on the values of the equisonic points. For a given set of upstream conditions, two unique transonic points can exist provided $v_{ei1} < u_{x1} < v_{ef1}$. Appendix B also contains plots of a_2 versus u_{x2} obtained using (52) with the numerical value of the equisonic speed being determined by a root finding method and the associated upstream speed being found by solving the cubic (46) for u_{x1} with (51) being used to select the correct solution. The upstream parameters used in the plots are those considered in shock structure calculations in Chapters 5, 6 and 7.

The Jouget Point

Another important point in the shock transition is the Jouget point as designated by Kulikovskii et al.[33], where the upstream flow speed has a local maximum turning point with respect to the downstream normal flow speed, so that $\frac{du_{x1}}{du_{x2}} = 0$. The upstream flow speed at the Jouget point will be given the symbol v_{j1}. Differentiating (46) with respect to u_{x2}, placing the derivative equal to zero and then eliminating u_{x2} using (46) gives the following quartic equation in v_{j1}^2

$$m_8 v_{j1}^8 + m_6 v_{j1}^6 + m_4 v_{j1}^4 + m_2 v_{j1}^2 + m_0 = 0, \tag{53}$$

where

$$\begin{aligned}
m_8 &= 256\pi^4 (\gamma-1)^2 \rho_1^4 \left[4(\gamma-1) B_x^2 - (\gamma-2)^2 B_{y1}^2\right], \\
m_6 &= 1024\pi^4 \gamma (\gamma-1) \rho_1^3 p_1 \left[6(\gamma-1) B_x^2 - (\gamma-2)^2 B_{y1}^2\right] - 128\pi^3 \rho_1^3 [\,4(2\gamma+1)(\gamma-1)^2 B_x^4 \\
&\quad -2(\gamma-1)(\gamma+1)\left(\gamma^2-6\gamma+10\right) B_x^2 B_{y1}^2 - (\gamma-2)^2\left(\gamma^2-\gamma-4\right) B_{y1}^4\,], \\
m_4 &= 1024\pi^4 \gamma^2 \rho_1^2 p_1^2 \left[12(\gamma-1) B_x^2 - (\gamma-2)^2 B_{y1}^2\right] - 256\pi^3 \gamma \rho_1^2 p_1 [\,6(\gamma-1)(3\gamma+1) B_x^4 \\
&\quad -(\gamma+1)\left(3\gamma^2-11\gamma+18\right) B_x^2 B_{y1}^2 + \gamma(\gamma-2)^2 B_{y1}^4\,] + 16\pi^2 \rho_1^2 [\,24\gamma\left(\gamma^2-1\right) B_x^6 \\
&\quad -2\left(3\gamma^4-18\gamma^3+5\gamma^2+18\gamma-24\right) B_{y1}^2 B_x^4 - 2\left(3\gamma^4-10\gamma^3+5\gamma^2+6\gamma-24\right) B_x^2 B_{y1}^4 \\
&\quad -\gamma^2(\gamma-2)^2 B_{y1}^6\,], \\
m_2 &= 8192\pi^4 \gamma^3 \rho_1 B_x^2 p_1^3 - 512\pi^3 \gamma^2 \rho_1 B_x^2 p_1^2 \left[12\gamma B_x^2 - (\gamma+1)(\gamma+2) B_{y1}^2\right] + 64\pi^2 \gamma \rho_1 p_1 B_x^2 \\
&\quad \times \left[6(\gamma+1)(3\gamma-1) B_x^4 + \left(-3\gamma^3+\gamma^2-10\gamma-30\right) B_x^2 B_{y1}^2 + 2\gamma\left(\gamma^2+2\right) B_{y1}^4\right] \\
&\quad -8\pi\rho_1 B_x^2\left(B_x^2+B_{y1}^2\right)[\,4(2\gamma-1)(\gamma+1)^2 B_x^4 - 2(\gamma+1)\left(\gamma^3-3\gamma^2-6\right) B_x^2 B_{y1}^2 + \gamma^2\left(-\gamma^2+\gamma-2\right) B_{y1}^4], \\
m_0 &= -2048\pi^3 \gamma^3 p_1^3 B_x^4 + 64\pi^2 \gamma^2 p_1^2 B_x^4 \left[12(\gamma+1) B_x^2 - \left(\gamma^2+10\gamma+1\right) B_{y1}^2\right] \\
&\quad -16\pi\gamma p_1 B_x^4 \left[6(\gamma+1)^2 B_x^4 - (\gamma+1)\left(\gamma^2+\gamma+10\right) B_x^2 B_{y1}^2 + \gamma\left(\gamma^2+4\gamma+1\right) B_{y1}^4\right] \\
&\quad +(\gamma+1)^2 B_x^4 \left[4(\gamma+1) B_x^2 - \gamma^2 B_{y1}^2\right]\left(B_x^2+B_{y1}^2\right)^2.
\end{aligned}$$

The Jouget point is of significance as, given a set of upstream conditions a_1, b_1, γ, ρ_1 and θ_1, it is the maximum velocity point in the upstream flow domain where intermediate shocks can be produced. At the Jouget point the downstream slow MHD wave speed equals the downstream normal flow speed and it is the point in the intermediate shock domain where the maximum increase in specific entropy occurs measured from the upstream state. The upstream flow speed at the Jouget point is the largest positive solution of (53).

Entropy

To determine if a shock transition can occur between two states the entropy change of the fluid per unit mass is examined. Across the shock there is an increase in entropy due to the increase in internal energy per unit mass of the fluid. The jump in entropy per unit mass between the upstream and downstream states is given by Jones [34] as

$$\Delta s = c_v \ln\left[\frac{p_2}{p_1}\left(\frac{\rho_1}{\rho_2}\right)^{\gamma}\right], \tag{54}$$

where c_v is the specific heat of the fluid at a constant volume. The pressure and density ratios can be expressed in terms of the upstream and downstream transverse magnetic field components using (48) so that (54) can be written in terms of the upstream variables and B_{y2}

$$\frac{\Delta s}{c_v} = \ln\left\{1 + \frac{1}{8\pi p_1}\left[B_{y1}^2 - B_{y2}^2 + \left(\frac{B_{y1}}{B_{y2}} - 2\right)\left(B_x^2 - 4\pi\rho_1 u_{x1}^2\right)\right]\right\} - \gamma \ln\left[\frac{4\pi\rho_1 B_{y2} u_{x1}^2}{B_x^2(B_{y2} - B_{y1}) + 4\pi\rho_1 B_{y1} u_{x1}^2}\right]. \tag{55}$$

Replacing B_{y2} using (45) allows (54) to be expressed in terms of the upstream variables and ρ_2

$$\frac{\Delta s}{c_v} = \ln\left\{\frac{1}{\rho_2 p_1(\rho_2 B_x^2 - 4\pi\rho_1^2 u_{x1}^2)^2}\left[\,[\rho_1 B_{y1}^2 u_{x1}^2(B_x^2 - 2\pi\rho_1 u_{x1}^2) + B_x^4(p_1 + \rho_1 u_{x1}^2)]\rho_2^3 + \rho_1^2 B_x^2 u_{x1}^2\right.\right.$$
$$\left.\left.\times\,[B_x^2 + B_{y1}^2 + 8\pi(p_1 + \rho_1 u_{x1}^2)]\rho_2^2 + 2\pi\rho_1^4 u_{x1}^4[4B_x^2 + B_{y1}^2 + 8\pi(p_1 + \rho_1 u_{x1}^2)]\rho_2 - 16\pi^2\rho_1^6 u_{x1}^6\right]\,\right\} - \gamma \ln\left(\frac{\rho_2}{\rho_1}\right). \tag{56}$$

Equations (55) and (56) can be expanded in terms of ΔB_y and $\Delta\rho$ where $\Delta B_y = B_{y2} - B_{y1}$ and $\Delta\rho = \rho_2 - \rho_1$. The results to the second order are

$$\frac{\Delta s}{c_v} = \frac{\gamma\left[a_1^2\frac{B_x^2}{4\pi\rho_1} - u_{x1}^2\left(a_1^2 + \frac{B_1^2}{4\pi\rho_1} - u_{x1}^2\right)\right]}{a_1^2 u_{x1}^2}\frac{\Delta B_y}{B_{y1}} - \frac{\gamma}{8\pi\rho_1 a_1^4 u_{x1}^4}\left\{B_{y1}^2 u_{x1}^4\left[\gamma\left(\frac{B_1^2}{4\pi\rho_1} + \frac{B_x^2}{4\pi\rho_1} - 2u_{x1}^2\right) + a_1^2\right]\right.$$
$$\left. + 4\pi\rho_1\left(\frac{B_x^2}{4\pi\rho_1} - u_{x1}^2\right)\left[\frac{B_x^2}{4\pi\rho_1}\left(a_1^4 + \gamma u_{x1}^4\right) + u_{x1}^2\left(a_1^4 - 2a_1^2 u_{x1}^2 - \gamma u_{x1}^4\right)\right]\right\}\frac{\Delta B_y^2}{B_{y1}^2}, \tag{57}$$

$$\frac{\Delta s}{c_v} = \frac{\gamma}{a_1^2}\left[\frac{u_{x1}^2\left(\frac{B_1^2}{4\pi\rho_1} - u_{x1}^2\right)}{\left(\frac{B_x^2}{4\pi\rho_1} - u_{x1}^2\right)} - a_1^2\right]\frac{\Delta\rho}{\rho_1} + \frac{\gamma}{2a_1^4}\left\{\frac{\gamma u_{x1}^2}{16\pi^2\rho_1^2\left(\frac{B_x^2}{4\pi\rho_1} - u_{x1}^2\right)^2}\{8\pi\rho_1 B_{y1}^2[u_{x1}^2\left(u_{x1}^2 - \frac{a_1^2}{2\gamma}\right)\right.$$
$$\left. - \frac{B_x^2}{4\pi\rho_1}\left(\frac{a_1^2}{\gamma} + u_{x1}^2\right)] - 16\pi^2\rho_1^2\left(\frac{B_x^2}{4\pi\rho_1} - u_{x1}^2\right)^2\left(\frac{2a_1^2}{\gamma} + u_{x1}^2\right) - u_{x1}^2 B_{y1}^4\} + a_1^4\right\}\frac{\Delta\rho^2}{\rho_1^2}. \tag{58}$$

Although of limited computational use due to the slow convergence of the logarithmic expansion, the series expansions can be applied for small changes to determine the entropy increase. The expansion in terms of $\Delta\rho$ is valid provided $u_{x1}^2 \neq \frac{B_x^2}{4\pi\rho_1}$, this being the square of the upstream intermediate speed.

Entropy increase is a necessary condition for a shock between two states, whether upstream and downstream or along the internal structure of a shock, and can be expressed as

$$\left(\frac{\rho_2}{\rho_1}\right)^\gamma < \frac{p_2}{p_1}. \tag{59}$$

Pressure and Density Ratios for Shocks

The combination of the jump conditions (37) to (41) and (59) determines the region in the $q-r$ plane, where q is the pressure ratio and r is the density ratio, allowing a shock transition. Figure 2 shows the allowable values for q and r according to each of the equations of MHD and entropy increase. Figure 2a shows the allowable region for transitions according to the jump conditions alone as expressed in (50), traditionally this equation being known as the MHD Hugoniot, for $\gamma = \frac{5}{3}$ being the adiabatic index of a monatomic gas. Using these conditions alone it is seen that transitions could be in an area with $r < 1$. Figure 2b shows the allowable region for transitions according to (59). Figure 2c shows the combination of the entropy and MHD jump conditions. Points within the shaded region R represent a shock transition. The last diagram shows that MHD shocks have a mass density ratio increase between their upstream and downstream states, $\frac{\rho_2}{\rho_1} > 1$, with an accompanying increase in gas pressure, $\frac{p_2}{p_1} > 1$.

Eliminating u_{y2}, u_{x2} and u_{x1} from the jump conditions (37) to (41) gives two equations in terms of γ, θ_1, p_1, q and r for B_x and B_{y2} provided $\theta_1 \neq 90°$:

$$\begin{aligned}\tan\theta_1\left[-2+r\left(2+\tan^2\theta_1\right)\right]B_x^3 - B_{y2}\left(-2+2r+\tan^2\theta_1\right)B_x^2 - r\tan\theta_1\left[B_{y2}^2+8\pi p_1\left(q-1\right)\right]B_x \\ +B_{y2}\left[B_{y2}^2+8\pi p_1\left(q-1\right)\right]=0, \qquad (60)\\ (\gamma-1)\tan\theta_1\sec^2\theta_1\left[1-2r^2+\cos 2\theta_1\right]B_x^3 - (\gamma-1)\sec^2\theta_1\left[1-2r^2+\cos 2\theta_1\right]B_{y2}B_x^2 \\ +2\tan\theta_1\left[(\gamma-1)B_{y2}^2+8\pi\gamma p_1 r\left(q-r\right)\right]B_x - 2B_{y2}\left[(\gamma-1)B_{y2}^2+8\pi\gamma p_1\left(q-r\right)\right]=0. \qquad (61)\end{aligned}$$

Eliminating B_{y2} from (60) and (61) gives a quadratic equation in B_x^2

$$\begin{aligned}&\left\{1-\gamma-q\left(\gamma+1\right)+r\left[\gamma+1+q\left(\gamma-1\right)\right]\right\}\left(\gamma-1\right)^2\left(r-1\right)^4\sec^4\theta_1 B_x^4 + 4\pi p_1\left(\gamma-1\right)\left(r-1\right)\sec^2\theta_1 \\ &\quad\times\left\{\left[\gamma q-\left(\gamma-2\right)\left(q-1\right)r-\gamma r^2\right]^2-\left[2-q\left(2+\gamma-\gamma r\right)-\gamma\left(r-1\right)\left(r-2\right)\right]^2\cos 2\theta_1\right\}B_x^2 \\ &\quad+64\pi^2 p_1^2\left\{1-\gamma-q\left(\gamma+1\right)+r\left[\gamma+1+q\left(\gamma-1\right)\right]\right\}\left[1-q+\gamma\left(r-1\right)\right]^2=0. \qquad (62)\end{aligned}$$

Values of B_x and B_{y2} can be found by determining the points of intersection of the contours in (60) and (61) using a root finding method or by solving the quadratic equation (62) to find B_x and then using (50) to determine two possible values of B_{y2} due to the $\left(B_{y2}-B_{y1}\right)^2$ term in the Hugoniot equation. Equation (45) is then used to determine u_{x1} for each B_x, B_{y2} combination. The jump conditions (38) to (41) are then used to determine the consistent set of solutions $\{B_x, u_{x1}, B_{y2}\}$.

The presence of equal roots in the quadratic equation (62) is found by setting its discriminant equal to zero. This gives two equations

$$q = \frac{\gamma\left(r-1\right)\left(r-2\right)-2}{\gamma\left(r-1\right)-2}, \qquad (63)$$

$$4\left(r-1\right)\left[-1+q-\gamma\left(r-1\right)\right]\left[2\left(q-r\right)-\left(\gamma-1\right)\left(q+1\right)\left(r-1\right)\right]+\left[r\left(\gamma-2\right)\left(q-1\right)+\gamma\left(r^2-q\right)\right]^2\tan^2\theta_1=0. \qquad (64)$$

Equation (63) is the curve C_1 inside the shaded region in Figure 2c, which has the asymptote $r = 1 + \frac{2}{\gamma}$. When (63) is placed in the jump conditions (37) to (41) after eliminating u_{y2}, u_{x2}, u_{x1} and B_{y2} we obtain $B_1 = \sqrt{\dfrac{8\pi\gamma p_1}{\gamma\,(1-r)+2}}$. This indicates that at each point on C_1 there is one value of the upstream magnetic field depending on γ, p_1 and r alone.

Equation (64) describes a curve to the right of the shaded region in Figure 2c for $\theta_1 > 0°$. For $\theta_1 = 0°$ the locus described by (64) is C_2. Each point on C_2 has one value of B_x associated with it, the values of B_{y1} and B_{y2} both being zero at each point. Points on C_2 are found by placing $\theta_1 = 0°$ in (64). The first square bracket when placed equal to zero gives (r, q) points outside of R. When the second square bracket is placed equal to zero it represents the gas dynamic Hugoniot relationship, found by placing B_{y1} and B_{y2} both zero in (50). The equation of the gas dynamic dashed boundary is $r = \frac{q(\gamma+1)+\gamma-1}{q(\gamma-1)+\gamma+1}$, this being the gas dynamic Hugoniot curve. As $q \to \infty$, $r \to \frac{\gamma+1}{\gamma-1}$. For $\theta_1 = 0°$, $B_{y1} = 0$ and the solution of (60) and (61) in this case gives rise to a non zero solution for B_{y2} within R known as a switch-on shock. Specific details of the gas dynamic shock and MHD switch-on shock are given in the next subsection.

For the case of $\theta_1 = 90°$, placing $B_x = 0$ in the jump conditions (37) to (41) and eliminating u_{x1} and B_{y2} gives

$$B_{y1}^2 = 8\pi p_1 \frac{[(q-1)\,(r+1) - \gamma\,(q+1)\,(r-1)]}{(\gamma-1)\,(r-1)^3}. \tag{65}$$

Equation (65) has a right hand side that is positive for values of q and r that are in R on Figure 2c and so a perpendicular shock is possible at each point in this region for given values of γ and p_1.

The presence of a magnetic field allows shock transitions to occur in the region R of Figure 2c, in the absence of a magnetic field the transitions are confined to C_2.

Given the upstream adiabatic index, sound speed, mass density and shock angle, a point in the shaded blue region of Figure 2c not on the dashed line corresponds to two different upstream values of B_x, (provided $\theta_1 \neq 0°\&90°$) each having different downstream u_{x2} and B_{y2} values but the same density and pressure ratios. One transition is a fast shock with $B_{y2} > B_{y1}$ and both fields having the same sign, the other being an intermediate or slow shock with $B_{y2} < B_{y1}$. Associated with each value of B_x is a value for u_{x1}, the larger value of u_{x1} is with the fast shock and the smaller value is with the intermediate or slow shock.

At the point $(2, 6)$ on C_1 in Figure 2c, with the upstream conditions as $a_1 = 1$, $\gamma = \frac{5}{3}$, $\rho_1 = 1$, the solutions $\{B_x, B_{y1}, B_1, b_1, u_{x1}, B_{y2}\}$, to the jump conditions, where b_1 is the upstream Alfven speed given by $b_1 = \dfrac{B_x}{\sqrt{4\pi\rho_1}\cos\theta_1}$, are at four angles that will be used later to illustrate shock structure:

$\theta_1 = 0°, \{8.68322, 0, 8.68322, 2.44949, 3.4641, 8.68322\}, \{8.68322, 0, 8.68322, 2.44949, 3.4641, -8.68322\}$
$\theta_1 = 15°, \{8.38734, 2.24738, 8.68322, 2.44949, 3.88662, 10.9306\}, \{8.38734, 2.24738, 8.68322, 2.44949, 2.98231, -6.43583\}$
$\theta_1 = 37°, \{6.93472, 5.22569, 8.68322, 2.44949, 4.38427, 13.9089\}, \{6.93472, 5.22569, 8.68322, 2.44949, 2.18591, -3.45753\}$
$\theta_1 = 90°, \{0, 8.68322, 8.68322, 2.44949, 4.89898, 17.3664\}, \{0, -8.68322, 8.68322, 2.44949, 4.89898, -17.3664\}$

The first example shows that the switched on magnetic field component B_{y2} can be in either the positive or negative y direction. At points on C_1 the switched-on B_{y2} field equals in magnitude the B_x field. The second and third examples have a fast shock as their first solution and an intermediate shock as their second. The last example indicates that a perpendicular shock can have its B_{y1} vector along the positive or negative y axis.

At the point $(2.306, 6.0574)$ in R in Figure 2c, with the upstream conditions as $a_1 = 1$, $\gamma = \frac{5}{3}$, $\rho_1 = 1$, the solutions $\{B_x, B_{y1}, B_1, b_1, u_{x1}, B_{y2}\}$ to the jump conditions are at these angles:
$\theta_1 = 0°, \{6.18087, 0, 6.18087, 1.74359, 2.64773, 4.85003\}, \{6.18087, 0, 6.18087, 1.74359, 2.64773, -4.85003\}$
$\theta_1 = 15°, \{5.20485, 1.39463, 5.38845, 1.52005, 2.82151, 6.24467\}, \{6.84824, 1.83498, 7.08982, 2, 2.4, -3.01505\}$
$\theta_1 = 37°, \{3.60315, 2.71517, 4.51163, 1.27271, 2.97671, 7.5652\}, \{6.7626, 5.09599, 8.4677, 2.38869, 1.88088, 0.245956\}$
$\theta_1 = 90°, \{0, 3.71365, 3.71365, 1.0476, 3.08889, 8.56369\}, \{0, -3.71365, 3.71365, 1.0476, 3.08889, -8.56369\}$

The second example in the last group shows a fast and an intermediate shock. The structure of this particular intermediate shock will be studied in Chapter 7. The third example shows a fast and a slow shock. These examples show that a given point on the (r, q) plane can be associated with all shock types depending on the given values a_1, ρ_1, γ and θ_1.

In the above examples non-dimensionalised units are used for the magnetic field components. The magnetic field components are proportional to the Alfven speed. By choosing an upstream sound speed of 1 the Alfven speed relative to the speed of sound is determined at a given point in the $q - r$ plane.

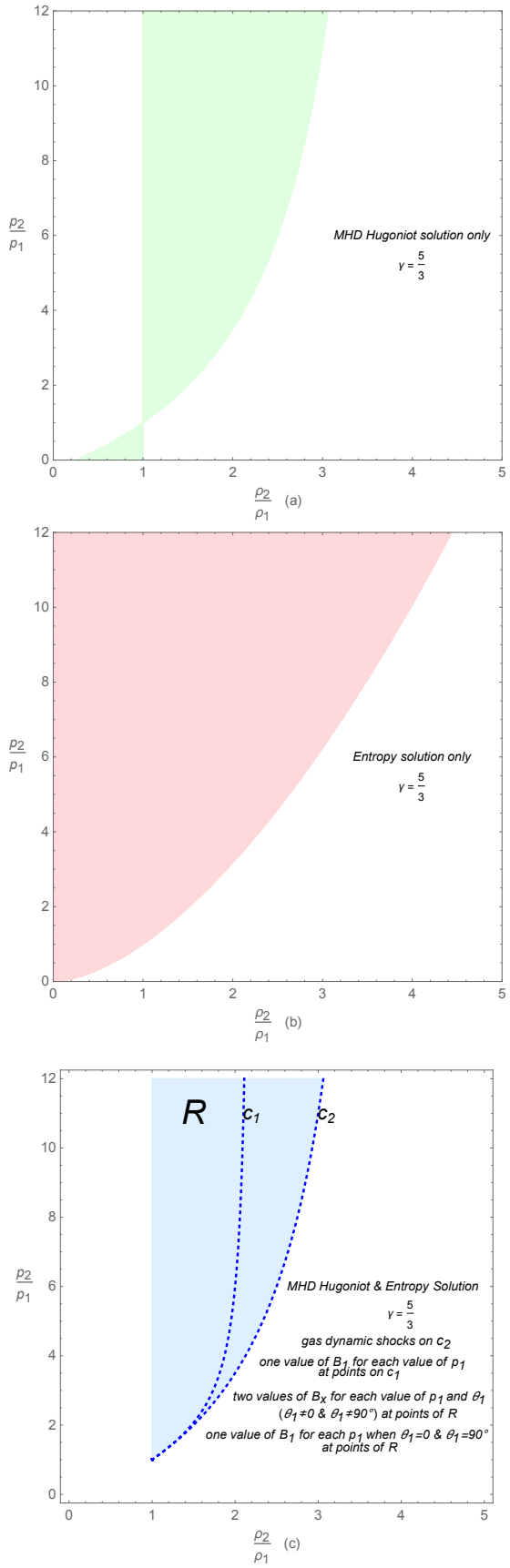

Figure 2: Pressure and density ratio allowed region (shown in blue) for the formation of MHD shocks in a monatomic gas according to fluid dynamical, electromagnetic and entropy considerations.

2.3.2 Parallel Shock

Placing $B_{y1} = 0$ in equations (37) to (41) and solving gives the following two solutions for the upstream normal flow velocity in terms of the mass density ratio,

$$u_{x1} = \sqrt{r} b_1, \tag{66}$$

$$u_{x1} = \frac{\sqrt{2r} a_1}{\sqrt{1 + \gamma - r\,(\gamma - 1)}}, \tag{67}$$

where b_1 is the upstream Alfven speed defined by $b_1 = \dfrac{B_1}{\sqrt{4\pi\rho_1}}$. Equation (66) gives the speed of a MHD shock, which is determined by the upstream magnetic field strength and density. Equation (67) gives the speed of a gas dynamic shock, its speed being independent of the upstream magnetic field strength. The MHD shock is called a "switch-on" shock as the downstream state gains a transverse magnetic field component given by

$$\frac{B_{y2}^2}{B_x^2} = \frac{\left(u_{x1}^2 - b_1^2\right)\left(-2a_1^2 + (\gamma + 1)\, b_1^2 - (\gamma - 1)\, u_{x1}^2\right)}{b_1^4}. \tag{68}$$

For $b_1 > a_1$ the condition $B_{y2}^2 > 0$ for a switch-on magnetic field gives the mass density ratio

$$1 < r < \frac{(\gamma + 1)\, b_1^2 - 2a_1^2}{(\gamma - 1)\, b_1^2}, \tag{69}$$

for the the range of upstream speeds given by

$$b_1 < u_{x1} < \sqrt{\frac{(\gamma + 1)\, b_1^2 - 2a_1^2}{\gamma - 1}}. \tag{70}$$

For $b_1 < a_1$ the condition $B_{y2}^2 > 0$ does not allow a switch-on transition as the corresponding mass density ratio r satisfies

$$\frac{(\gamma + 1)\, b_1^2 - 2a_1^2}{(\gamma - 1)\, b_1^2} < r < 1 \tag{71}$$

and does not give rise to an increase in entropy across the transition as it is less than 1.

For $b_1 = a_1$ the condition $B_{y2}^2 > 0$ does not allow a real solution for r and so a switch-on shock is not possible.

By placing the maximum value of r given in (69) in (67) it is seen that the maximum switch on shock compression ratio occurs when the switch-on shock speed equals the gas dynamic shock speed. By placing the maximum value of u_{x1} given in (70) in $u_{x2} = \dfrac{b_1^2}{u_{x1}}$ it is found that the MHD switch-on shock has the same downstream speed as the gas dynamic shock at this value of u_{x1}. This is of significance as this is a "break point" in the formation of intermediate and fast shocks that are produced as the angle θ_1 increases from 0. The MHD switch-on shock can be considered as both an intermediate and a fast shock. This switch-on shock structure will be given in Chapter 8.

The downstream speed of sound in the fluid due to the passage of the MHD switch-on shock is found by combining (38) and (68)

$$a_2^2 = \frac{\gamma\left(\gamma-1\right)\left(b_1^2-u_{x1}^2\right)^2 - 2a_1^2\left[\left(\gamma-1\right)b_1^2-\gamma u_{x1}^2\right]}{2u_{x1}^2}. \tag{72}$$

The gas dynamic shock exists for all values of u_{x1} greater than the upstream slow MHD wave speed. Below this speed the mass density ratio r would be less than 1 causing a decrease in entropy across the shock meaning that the transition is not physically possible. The downstream speed of sound in the fluid due to the passage of a gas dynamic shock is found by combining (38) and (67)

$$a_2^2 = \frac{\left(2a_1^2+\left(\gamma-1\right)u_{x1}^2\right)\left[\left(1-\gamma\right)a_1^2+2\gamma u_{x1}^2\right]}{\left(\gamma+1\right)^2 u_{x1}^2}. \tag{73}$$

The upstream shock speed when the downstream MHD switch-on shock speed equals the downstream sound speed is found by using (66) and (72)

$$u_{x1}^2 = \frac{\gamma\left[\left(\gamma-1\right)b_1^2-a_1^2\right]+\sqrt{\gamma\left[\gamma a_1^4+2\left(\gamma-1\right)b_1^2\left(b_1^2-a_1^2\right)\right]}}{\gamma\left(\gamma-1\right)}. \tag{74}$$

Equation (74) is of importance as it gives the upstream shock speed at the transition from a supersonic to a subsonic downstream state.

2.3.3 Perpendicular Shock

The downstream values for a perpendicular shock are found by placing $B_x = 0$ and $B_{y1} = \sqrt{4\pi\rho_1}b_1$ in equations (37) to (41) . The mass density ratio is given by

$$\left(\gamma-2\right)b_1^2r^3 - \left[\left(\gamma-1\right)\left(2b_1^2+u_{x1}^2\right)+2a_1^2\right]r^2 + \left[2a_1^2+\gamma\left(b_1^2+2u_{x1}^2\right)\right]r - \left(\gamma+1\right)u_{x1}^2 = 0. \tag{75}$$

Equation (75) has a common factor of $(r-1)$ that after cancelling reduces to

$$\left(\gamma-2\right)b_1^2r^2 - \left[2a_1^2+\gamma b_1^2+\left(\gamma-1\right)u_{x1}^2\right]r + \left(\gamma+1\right)u_{x1}^2 = 0. \tag{76}$$

Equation (76) has a discriminant that is greater than zero for all values of a_1, b_1 and u_{x1} when $\gamma = \frac{5}{3}$ or $\frac{7}{5}$. The two real solutions for r are opposite in sign and the perpendicular MHD shock corresponds to the solution greater than 1 that occurs for all values of u_{x1} greater than the fast MHD wave speed, which when $\theta = 90°$ is given by $v_{f1} = \sqrt{a_1^2+b_1^2}$. Below this speed the positive solution is less than 1, corresponding to a decrease in entropy, and so the transition is not physically possible. When $b_1 = 0$, (76) predicts the same speed as (67), the shock being purely hydrodynamic in this case.

The MHD shock mass density ratio and its reciprocal are given by (76)

$$r = \frac{1}{2(2-\gamma)b_1^2}\left(-2a_1^2 - \gamma b_1^2 - (\gamma-1)\,u_{x1}^2 + \sqrt{\left[2a_1^2 + \gamma b_1^2 + (\gamma-1)\,u_{x1}^2\right]^2 + 4\,(\gamma+1)\,(2-\gamma)\,b_1^2 u_{x1}^2}\right), \tag{77}$$

$$\frac{1}{r} = \frac{1}{2(\gamma+1)u_{x1}^2}\left(2a_1^2 + \gamma b_1^2 + (\gamma-1)\,u_{x1}^2 + \sqrt{\left[2a_1^2 + \gamma b_1^2 + (\gamma-1)\,u_{x1}^2\right]^2 + 4\,(\gamma+1)\,(2-\gamma)\,b_1^2 u_{x1}^2}\right). \tag{78}$$

The downstream normal flow speed u_{x2} is the positive root of the equation

$$(\gamma+1)\,u_{x1}u_{x2}^2 - \left[2a_1^2 + \gamma b_1^2 + (\gamma-1)\,u_{x1}^2\right]u_{x2} + (\gamma-2)\,b_1^2 u_{x1} = 0. \tag{79}$$

The transverse downstream magnetic field component is given by

$$B_{y2} = rB_{y1}, \tag{80}$$

showing that B_{y2} is greater than B_{y1} and has the same sign as B_{y1}.

The downstream sound speed is found from equation (38) using $p_2 = \dfrac{\rho_1 r a_2^2}{\gamma}$

$$a_2 = \sqrt{\frac{1}{r}\left[a_1^2 - \frac{\gamma b_1^2}{2}\,(r^2-1) + \gamma\left(1 - \frac{1}{r}\right)u_{x1}^2\right]}. \tag{81}$$

When the downstream normal flow speed and sound speeds are equal the flow speed is given by the positive real root u_{x2} in the equation

$$(\gamma+1)^2\,u_{x2}^6 - (\gamma+1)\left[(\gamma+1)\,a_1^2 + 2\,(2\gamma-1)\,b_1^2\right]u_{x2}^4 + \gamma b_1^2\left[2\,(\gamma+1)\,a_1^2 + (5\gamma-4)\,b_1^2\right]u_{x2}^2 - \gamma b_1^4\left[\gamma a_1^2 + 2\,(\gamma-1)\,b_1^2\right] = 0. \tag{82}$$

When expressed in terms of u_{x2}^2 the discriminant of the cubic equation formed from (82) is negative, indicating the presence of one real solution. When $u_{x2} = 0$ the left hand side of the cubic equation formed from (82) is negative and as $u_{x2} \to \infty$ the left hand side $\to \infty$ showing that the root of the cubic is positive. The associated value of u_{x1} and r are found by solving (79) for u_{x1} and (47) for r. The values obtained for u_{x1} and r are greater than $\sqrt{a_1^2 + b_1^2}$ and 1 respectively showing that this equal speed point is present in all perpendicular shocks. This particular value u_{x1} is significant in the study of shock structure as it marks the transition from a supersonic to a subsonic downstream state.

Due to the comparative simplicity of the MHD equations in the case of a perpendicular shock, the first order ODEs can be integrated through the shock in each of transverse magnetic field component, normal flow velocity component and temperature to produce continuous structures in each of these variables by the introduction of coefficients of resistivity, viscosity and thermal conductivity into the equations. Continuous structures are produced whether the flow is from upstream supersonic to downstream supsersonic, supersonic to subsonic or equisonic.

2.4 A Parametric Solution of the Jump Conditions

The traditional solution of the jump conditions to determine the downstream values involves the solution of a cubic equation such as (43). Wardle [unpublished] proposed a parametric solution of the jump conditions involving a parameter w that is defined to be the geometric mean of the upstream and downstream speeds. The introduction of this parameter has the advantage that it avoids the solution of a cubic equation and in general the plots of the flow variables appear as single valued functions of w^2, (the exception being for the switch-on shocks that occur for a range of upstream speeds in the case when the normal to the shock is parallel to the upstream magnetic field, $\theta_1 = 0$, which have $w^2 = b_1^2$ for each value of u_{x1}) rather than multivalued functions as when u_{x1} is chosen as the independent variable, aiding the visualisation of the change from one shock type to another. The parametric speed is given by

$$w = \sqrt{u_{x1}u_{x2}} \tag{83}$$

Equations (37) to (41) are rewritten replacing u_{x2} using (83) and eliminating the downstream pressure p_2, the magnetic field component B_{y2} and the flow velocity component v_{y2}. The upstream pressure p_1 and magnetic field components B_x, B_{y1} are expressed in terms of the upstream sound speed a_1, and Alfven speed b_1 respectively by

$$p_1 = \frac{\rho_1 a_1^2}{\gamma}, \tag{84}$$

$$B_x = \sqrt{4\pi\rho_1}\, b_1 \cos\theta_1, \tag{85}$$

$$B_{y1} = \sqrt{4\pi\rho_1}\, b_1 \sin\theta_1. \tag{86}$$

The relationship obtained is

$$u_{x1}^2 = w^2 + 2\frac{\left(w^2 - b_1^2\cos^2\theta_1\right)\left[w^4 - w^2\left(a_1^2 + b_1^2\right) + a_1^2 b_1^2\cos^2\theta_1\right]}{(\gamma-1)\left(w^2 - b_1^2\right)\left(w^2 - b_1^2\cos^2\theta_1\right) + w^2 b_1^2\sin^2\theta_1}. \tag{87}$$

The sum of the squares of the sound and Alfven speeds and the product of their squares can be expressed in terms of the upstream fast MHD wave speed, v_{f1}, and the upstream slow MHD wave speed v_{s1}. Since

$$v_{f1}^2 = \frac{1}{2}\left[a_1^2 + b_1^2 + \sqrt{\left(a_1^2 + b_1^2\right)^2 - 4a_1^2 b_1^2\cos^2\theta_1}\right], \tag{88}$$

$$v_{s1}^2 = \frac{1}{2}\left[a_1^2 + b_1^2 - \sqrt{\left(a_1^2 + b_1^2\right)^2 - 4a_1^2 b_1^2\cos^2\theta_1}\right], \tag{89}$$

therefore

$$v_{f1}^2 + v_{s1}^2 = a_1^2 + b_1^2, \tag{90}$$

$$v_{f1}^2 v_{s1}^2 = a_1^2 b_1^2\cos^2\theta_1. \tag{91}$$

The third solution of the dispersion relation for the speed of small amplitude waves in ideal MHD is

the upstream intermediate speed v_{i1},

$$v_{i1} = b_1 \cos\theta_1. \tag{92}$$

Equation (87) can be written in terms of the three upstream signal speeds v_{s1}, v_{i1} and v_{f1} as

$$u_{x1}^2 = w^2 + 2\frac{\left(w^2 - v_{s1}^2\right)\left(w^2 - v_{i1}^2\right)\left(w^2 - v_{f1}^2\right)}{(\gamma - 1)\left(w^2 - b_1^2\right)\left(w^2 - v_{i1}^2\right) + w^2 b_1^2 \sin^2\theta_1}. \tag{93}$$

The downstream transverse magnetic field component given by (45) can be expressed in terms of w

$$B_{y2} = \frac{\left(u_{x1}^2 - v_{i1}^2\right)}{\left(w^2 - v_{i1}^2\right)} B_{y1}. \tag{94}$$

For a value of the parameter w, (87) or (93) allows the determination of u_{x1} for a given set of upstream conditions. The downstream values of the other flow variables can then be determined using the jump conditions. In this thesis plots of the downstream flow variables are determined using (87) to determine u_{x1} for values of w with the set of upstream values $\{a_1, b_1, \gamma, \rho_1, \theta_1\}$. Equation (83) is then used to determine u_{x2} with (94), (37), (48) and (54) being used to determine B_{y2}, ρ_2, p_2 and Δs respectively. Chapter 3 presents a panorama of downstream states for the set of shocks with upstream values $\{a_1$, b_1, γ, $\rho_1, \theta_1\} = \{1,\ 2,\ \frac{5}{3}, 1,\ \theta_1\}$ with the shock angle θ_1 taking the values $\{0°, 5°, 15°, 37°, 63°, 90°\}$. These angles show the range of downstream states possible for the given upstream state.

2.5 Numerical Solution of the ODEs

The structure of a shock is normally shown as a plot of a flow variable versus x_η showing the transition from the upstream to downstream state. The transverse magnetic field components through a shock are found by solving the autonomous ODEs (27) and (28) numerically. The normal shock velocity component u_x, mass density ρ, fluid pressure p and change in specific entropy Δs at a point in the transition are found using the magnetic field components obtained from the numerical integration.

The numerical integration method employed for the solution of the first order ODEs in this thesis is the Dormand-Prince Runge-Kutta 8th order variable step size method [35]. A high order variable step size method, rather than a low order fixed step size method, was used as some applications such as integration towards a transonic point require high accuracy. These applications are described in Chapter 7. The code for this method was first written by the author in Fortran and this integrator has been tested extensively over a number of years by the author in many applications in dynamical astronomy such as numerical integration of asteroid and comet orbits using full planetary perturbations, relativistic corrections and non-gravitational terms in the case of comet orbits, the accuracy of these calculations being assessed by comparing results obtained with other integrators such as Bulirsch-Stoer extrapolation, Gauss-Jackson and Adams multistep or with published ephemerides, agreement being to the 6th decimal place when astronomical units are used for the distance scale. These integrations were used to produce ephemerides of minor planets and comets for subsequent CCD astrometric observation and report to the Minor Planet Center from 1993-2021 under the IAU station code 423 North Ryde [36].

Shock structure integrations, in most situations, start from a stationary point in the $B_y - B_z$ phase plane. The starting point is determined from examination of the phase plane vectors given in Chapter 4. As the sign convention employed in this thesis has the positive x direction from the upstream to the downstream point, a numerical integration out of the upstream stationary point is only possible in the direction of an outwards vector and integration out of the downstream point is only possible in the directions of an inwards vector. For the numerical integration to leave a stationary point in the phase plane a small step-off in $|\mathbf{B}|$ in the intended direction of integration is needed. The size of the step-off is indicated with each integration. The step size was chosen to allow the profile to be proportionately positioned in the plot. The size of the step-off does not affect the gradient of the $B_y - x$ or $B_z - x$ profiles, a smaller step-off translating the profile in the x direction. For parametric plots, such as $B_y - u_x$, the magnitude of the step-off does not affect the plot.

3 Shock Classification

In this chapter the classification of MHD shocks in terms of their speed relative to the MHD signal speeds and plots of the downstream values of the shock variables obtained using the parametric solution will be given.

The upstream state of the gas is determined by six quantities: the sound speed a_1, Alfven speed b_1, ratio of specific heats γ, mass density ρ_1, angle between the normal to the plane of the shock and the upstream magnetic field θ_1 and the upstream shock speed u_{x1}. In set form these six will be called the upstream parameters, $\{a_1, b_1, \gamma, \rho_1, \theta_1, u_{x1}\}$.

The use of the five non-zero constants, f_1, f_2, f_3, f_5 and f_7 allows the equations of resistive MHD to be written in a compact form. For computational purposes, it is necessary to express the integration constants in terms of the parameters describing the upstream state. Using $p_1 = \frac{\rho_1 a_1^2}{\gamma}$, $B_x = \sqrt{4\pi\rho_1}\cos\theta_1$, $B_{y1} = \sqrt{4\pi\rho_1}\sin\theta_1, B_z = 0$, $\frac{dB_y}{dx} = 0$ and $\frac{dB_z}{dx} = 0$ in (14) to (20) gives

$$f_1 = \rho_1 u_{x1}, \tag{95}$$

$$f_2 = \frac{1}{2}\rho_1 b_1^2 \sin^2\theta_1 + \frac{\rho_1 a_1^2}{\gamma} + \rho_1 u_{x1}^2, \tag{96}$$

$$f_3 = -\rho_1 b_1^2 \cos\theta_1 \sin\theta_1, \tag{97}$$

$$f_5 = \sqrt{4\pi\rho_1} b_1 u_{x1} \sin\theta_1, \tag{98}$$

$$f_7 = \frac{1}{2}\rho_1 u_{x1}^3 + \frac{1}{\gamma - 1}\rho_1 a_1^2 u_{x1} + \rho_1 b_1^2 u_{x1} \sin^2\theta_1. \tag{99}$$

The essential problem encountered in this chapter is that a given upstream shock speed can produce zero, one, two or three possible downstream states.

Chapter Overview

The downstream shock speed u_{x2} is found by solving the cubic equation (46). For a given upstream speed u_{x1} there can be three possible values of u_{x2}. The number of solutions for u_{x2} that have an associated density increase will be the number of possible downstream states. As a general overview, to highlight the multiplicity of downstream states produced by a given upstream shock speed and angle, Figure 3 gives a colour-coded polar representation of the number of solutions of (46) for u_{x2} that have an associated increase in entropy from the upstream state for the case where the upstream Alfven speed is greater the upstream sound speed, $b_1 > a_1$.

The grey zone indicates that there are no possible downstream states, meaning that a shock transition cannot take place at these particular "upstream" values. The blue zone indicates that only one downstream solution is possible at the given value of (u_{x1}, θ_1), transitions within the inner blue zone being a slow shock, those in the outer blue zone being a fast shock. A point in the yellow zone allows two possible downstream shocked states, both of these being intermediate shocks. A point in the green zone has three possible downstream states, two intermediate shocks and a fast shock. For labelling purposes, fast and slow shocks are identified by the symbols $1 \to 2$ and $3 \to 4$ respectively. Intermediate shocks are identified by the symbols $2 \to 3$, $2 \to 4$ and $1 \to 3$, $1 \to 4$. The superscripts designate

the ratio of the normal shock speed to the sound speed, + indicating that a state is supersonic with $u_{x2} > a_2$ and − indicating that a state is subsonic, $u_{x2} < a_2$. The shock nomenclature is fully described in §3.1.

In Figure 3 the red curve is the locus of equisonic points, where the downstream sound speed equals the downstream normal flow speed, $a_2 = u_x$. The upstream shock speed at points on the red equisonic curves are designated as v_{ei1} and v_{ef1} with $v_{ei1} < v_{ef1}$ for an oblique shock. The v_{ei1} curve extends between $\theta_1 = 0$ and $\theta_1 = \arccos \frac{a_1}{b_1}$, the upper limit being when the upstream sound and intermediate speeds are equal. The v_{ef1} curve extends from $\theta_1 = 0$ to $\theta_1 = 90°$.

Transonic flow points, where $u_x = a$ and $\frac{du_x}{dx}$ has a finite value, play a role in allowing a shock transition to pass smoothly from a supersonic to a subsonic state, are found for upstream shock speeds in the region between the two red curves provided $u_{x1} > a_1$. Details of these points will be given in §4.3.

In Figure 3 the blue curves a_1, v_{f1}, v_{i1}, v_{j1} and v_{s1} are the locus of upstream sound, fast, intermediate, Jouget and slow speeds respectively for each angle in the polar plot.

The dashed lines at the magnetic field angles of 5°, 15°, 37° and 63° through a blue, yellow or green region indicate that a shock transition can occur at the given point in the coloured region. The black disks on the dotted lines, placed at positions to show different types of shock transitions, indicate the upstream values setting up the $B_y - B_z$ phase plane where the shock transition between the upstream and downstream points will be computed in later chapters of this thesis using numerical integration.

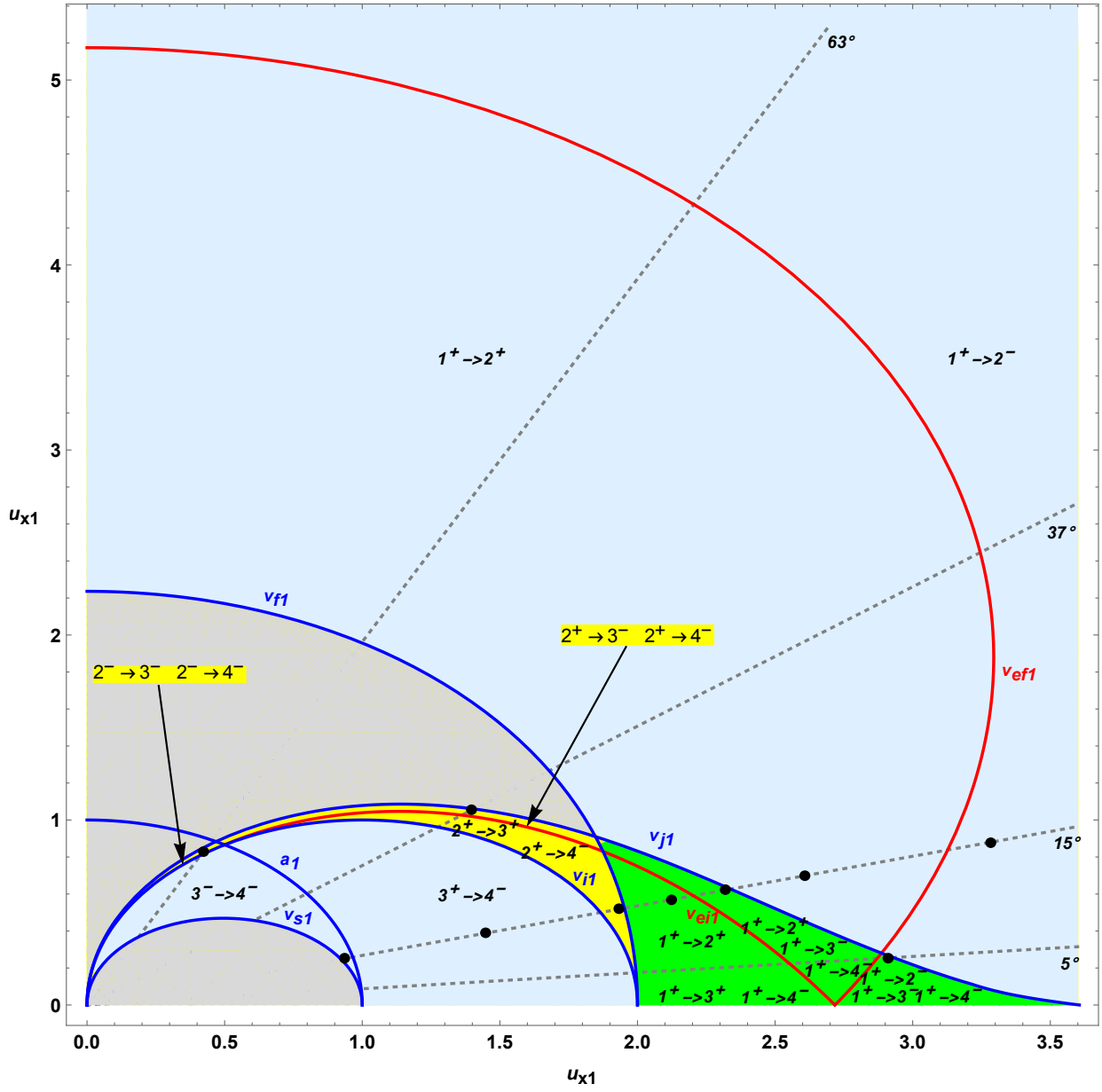

Figure 3: Polar plot with shading colour indicating the number of downstream states in terms of the upstream speed and shock angle in a monatomic gas when $a_1 < b_1$; grey shows that a shock transition is not possible, blue shows one downstream state only is possible, yellow that two downstream states are possible and green that three downstream states can form at the particular upstream speed value; $\frac{b_1}{a_1} = 2$, see text.

For the case when the upstream Alfven speed is less that the upstream sound speed, $b_1 < a_1$, a much limited variety of downstream state possibilities is produced. Figure 4(a) shows the number of downstream states when the upstream Alfven speed is one-half the upstream sound speed. Figure 4(b) shows an enlarged portion of (a) showing the narrow yellow region where two downstream states are possible. Three downstream shock solutions are not possible in the case where $b_1 < a_1$. The reason for this is that a switch-on shock as given by (69) cannot form when $b_1 < a_1$ and the switch-on structure becomes the three downstream solution region as the shock angle is increased from zero. This will be seen in Figures 7 and 8 in §3.2.

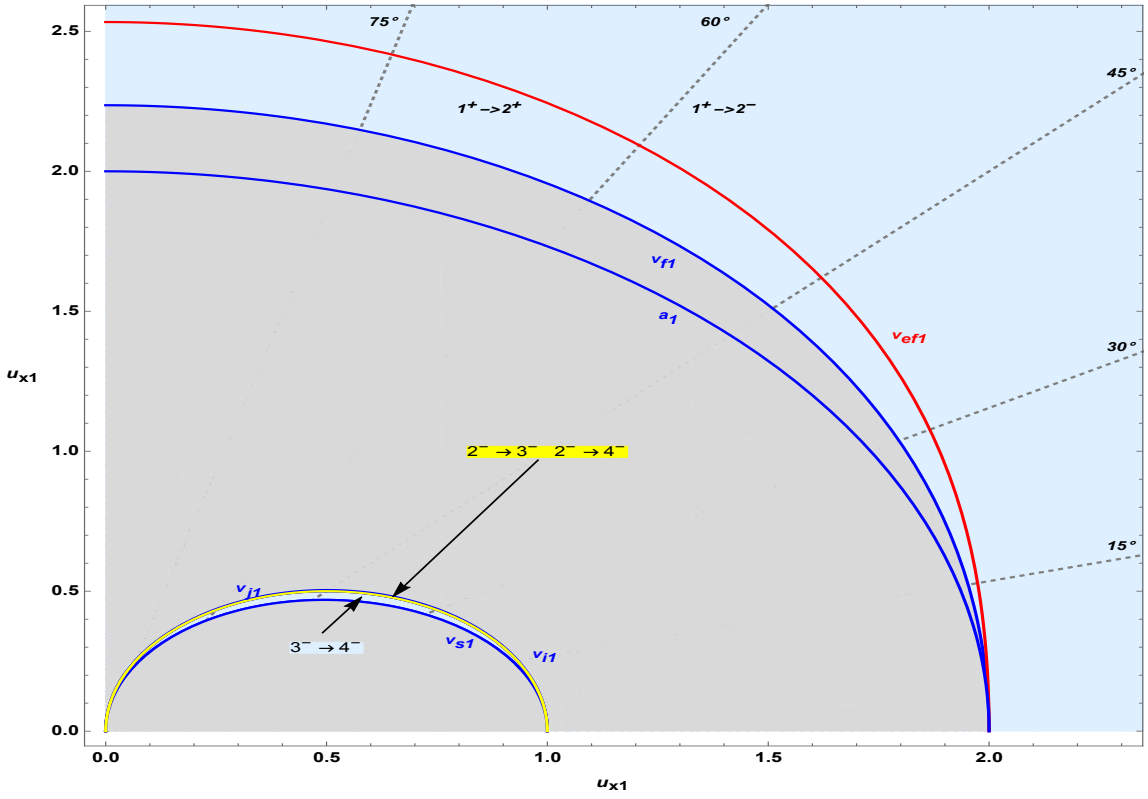

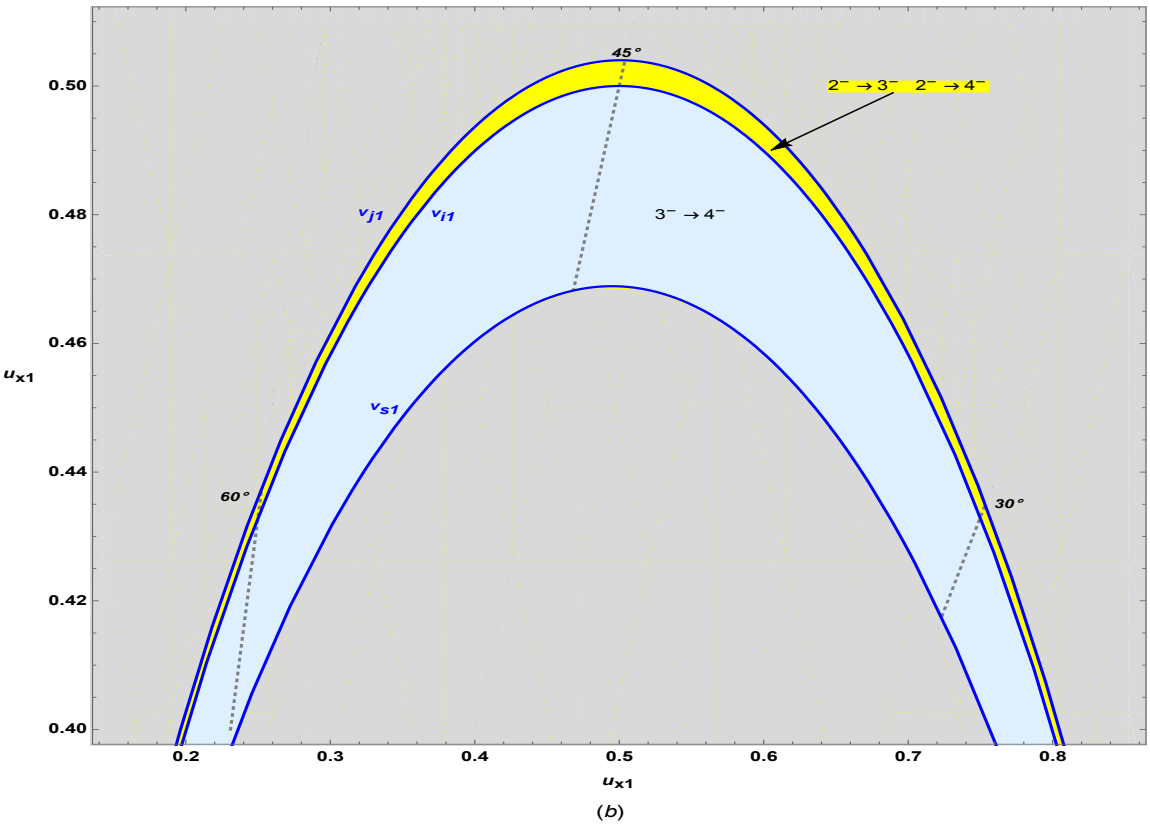

Figure 4: Polar plots with shading colour indicating the number of downstream states in terms of the upstream speed and shock angle in a monatomic gas when $a_1 > b_1$; grey shows that a shock transition is not possible, blue shows only one downstream state only is possible, yellow that two downstream states are possible; (b) shows a close up view of part of the narrow two solution domain; $\frac{b_1}{a_1} = \frac{1}{2}$, see text.

As the variety of shocks possible is greater when $b_1 > a_1$ than when $b_1 < a_1$, calculations in this thesis, unless otherwise specified, take $\frac{b_1}{a_1} = 2$ with u_{x1} being measured as a multiple of the upstream sound speed. The upstream mass density will be taken as 1, unless otherwise specified, and the gas as monatomic both upstream and downstream having $\gamma = \frac{5}{3}$. For plot labelling purposes the upstream properties will be written in a reduced three value form of $\frac{b_1}{a_1}$, θ_1, $\frac{u_{x1}}{a_1}$ with γ and ρ_1 having the assumed values of $\frac{5}{3}$ and 1 respectively.

3.1 Shock Nomenclature in Terms of Characteristic Speeds

The shock classification nomenclature that is shown on Figures 3 and 4 was first used by Shercliff [37]. This terminology is based on the relationship between the flow speed and the three MHD signal speeds. Upstream states are designated $1, 2, 3$ or 4 depending if $u_{x1} > v_{f1}$, $v_{i1} < u_{x1} < v_{f1}$, $v_{s1} < u_{x1} < v_{i1}$ and $u_{x1} < v_{s1}$ respectively, similarly the downstream states are designated 1, 2, 3 and 4 when $u_{x2} > v_{f2}$, $v_{i2} < u_{x2} < v_{f2}$, $v_{s2} < u_{x2} < v_{i2}$ and $u_{x2} < v_{s2}$ respectively. Here the subscripts f, i and s indicate fast, intermediate and slow signal speeds respectively.

Figures 5 and 6, produced using the parametric solution (83), show the downstream fast, intermediate, slow and normal shock speeds in orange, yellow, grey and blue respectively for the upstream shock angles used as examples in this thesis. The upstream values of the fast, intermediate and slow speeds are the dashed orange, green and grey vertical lines respectively.

For example, shock transitions from an upstream state with normal flow speed greater than the fast speed to a downstream state with normal flow speed greater than the intermediate speed are termed fast shocks as they "cross" the downstream fast speed. In Figures 5 and 6 fast shocks are the part of the blue curve in the region to the right of the upstream fast speed, giving the first zone as 1, below the orange downstream fast speed and above the green downstream intermediate speed, giving the second zone as 2. Fast shocks are designated as $1 \to 2$ shocks.

Similarly, slow shocks have shock speeds greater than the slow speed but less than the intermediate speed, with a downstream normal flow speed less than the slow speed. In Figures 5 and 6 slow shocks are the part of the blue curve in the region between the upstream slow and intermediate speeds, giving the first zone as 3, below the grey downstream slow speed curve, giving the second zone as 4. Slow shocks are designated as $3 \to 4$ shocks.

Shocks whose normal velocity component "crosses" the downstream intermediate speed are called intermediate shocks. In this situation there are four possibilities; the downstream intermediate signal speed alone is crossed (a one zone crossing), the downstream intermediate speed and the downstream slow speed are crossed (a two zone crossing), the downstream fast and intermediate speeds are crossed (a two zone crossing) or the downstream fast, intermediate and slow speeds are crossed (a three zone crossing. The respective designations for these intermediate shocks are $2 \to 3$, $2 \to 4$, $1 \to 3$ and $1 \to 4$. This classification is possible as Figures 5 and 6 show that when the upstream shock speed is equal to the Jouget speed the downstream slow speed has the same value. This means that $2 \to 4$ and $1 \to 4$ shocks are on the lower portion of the blue flow speed curve and $2 \to 3$ and $1 \to 3$ shocks are on the corresponding higher portion of the blue curve in the intermediate shock domain.

To summarise, fast and slow shocks are designated as $1 \to 2$ and $3 \to 4$ respectively. Intermediate shocks can be classified as $1 \to 3$, $1 \to 4$, $2 \to 3$ and $2 \to 4$. We also denote whether the flow in each state is supersonic or subsonic by adding a superscript $+$ or $-$ respectively.

Plots of the downstream sound and normal shock speed versus upstream shock speed for the representative shock angles, with each shock type classified using labels, are given in the next section.

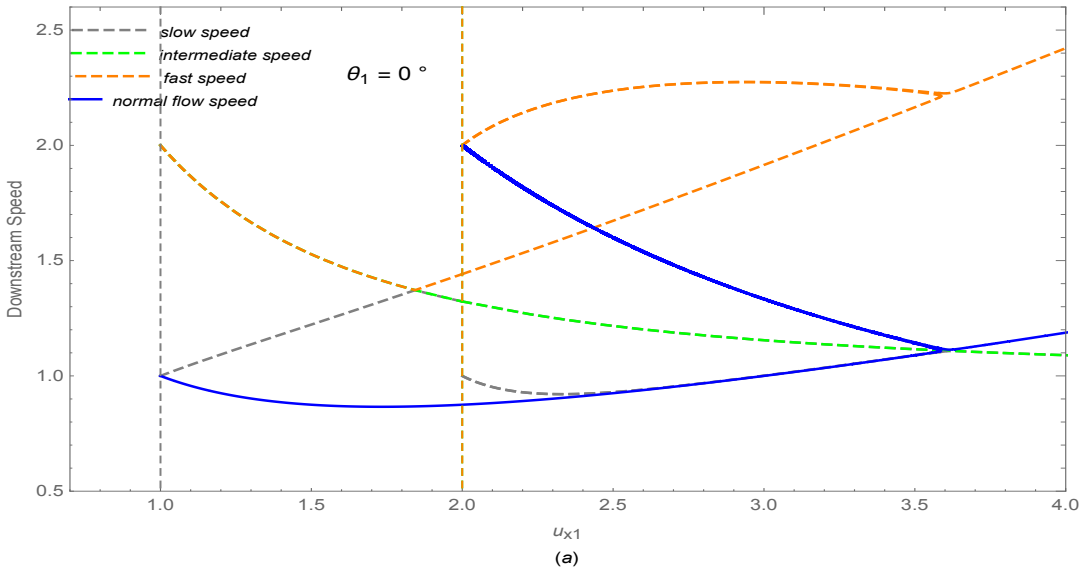

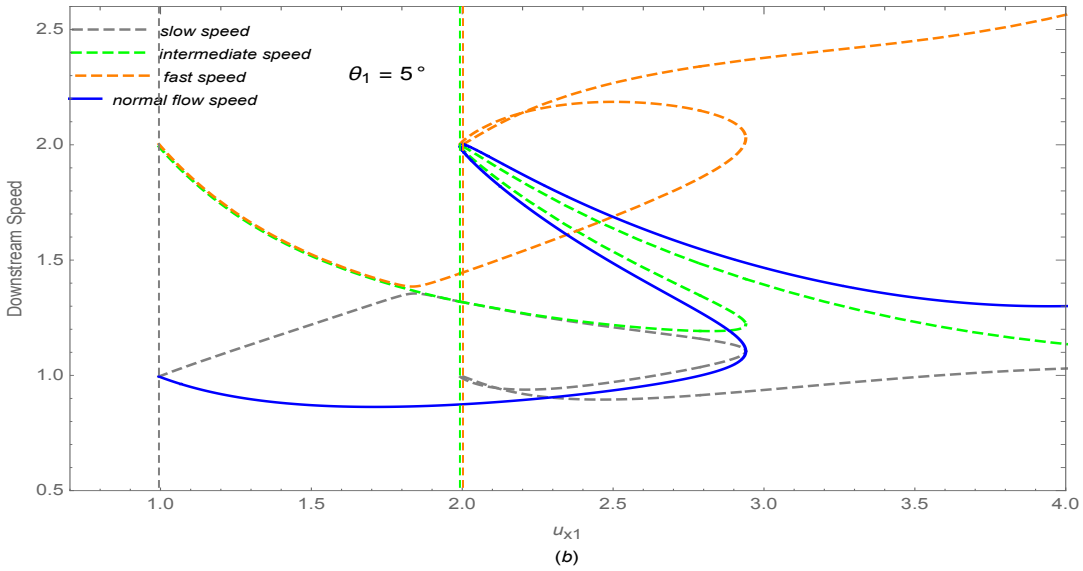

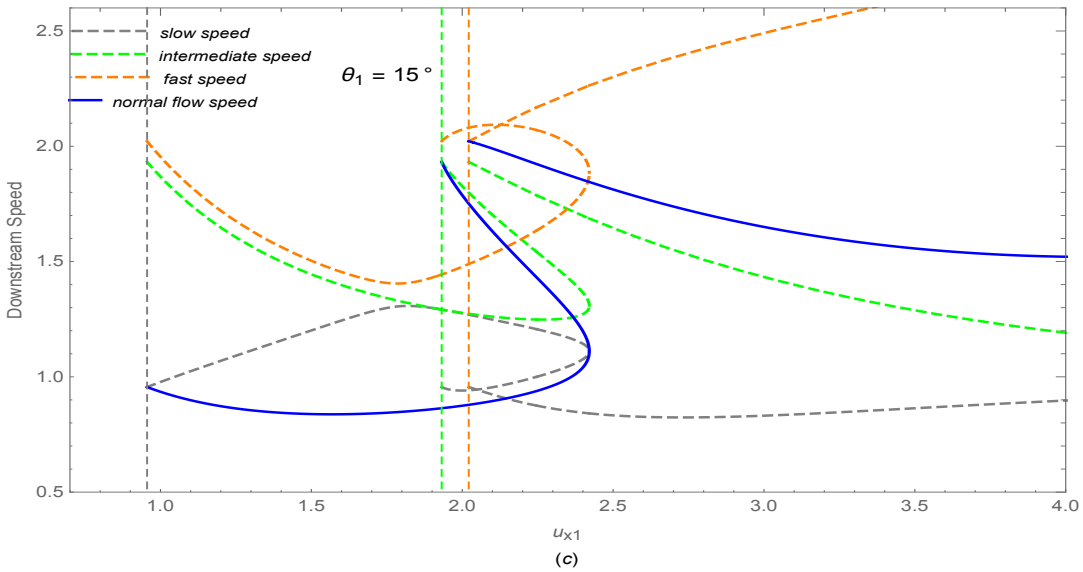

Figure 5: Downstream fluid normal flow speed u_{x2} and MHD signal speeds when a maximum of three downstream states are possible. Speed units are multiples of the upstream sound speed; $\frac{b_1}{a_1} = 2$, $\theta_1 = 0°, 5°, 15°$

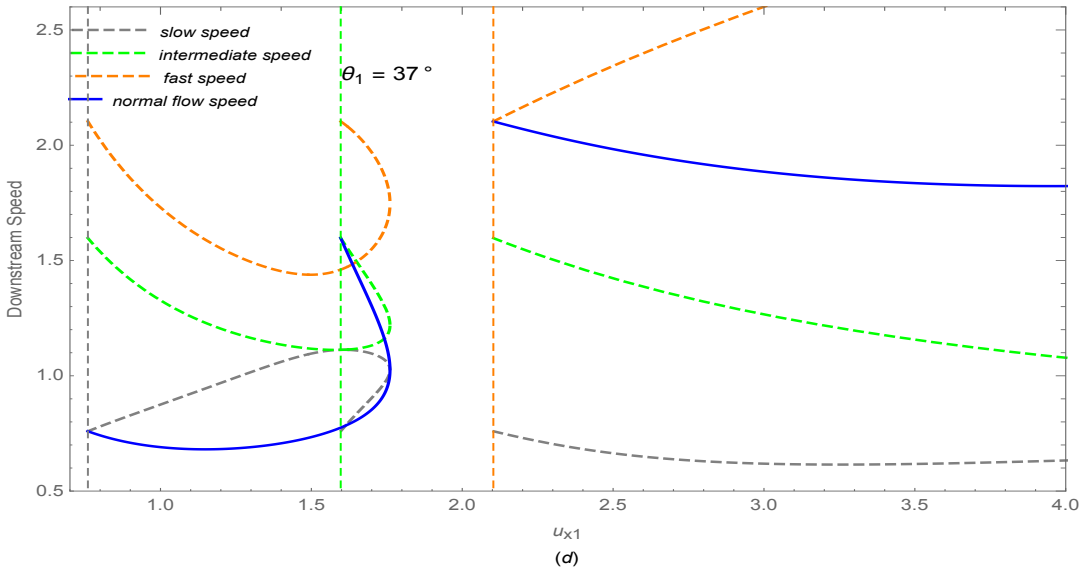

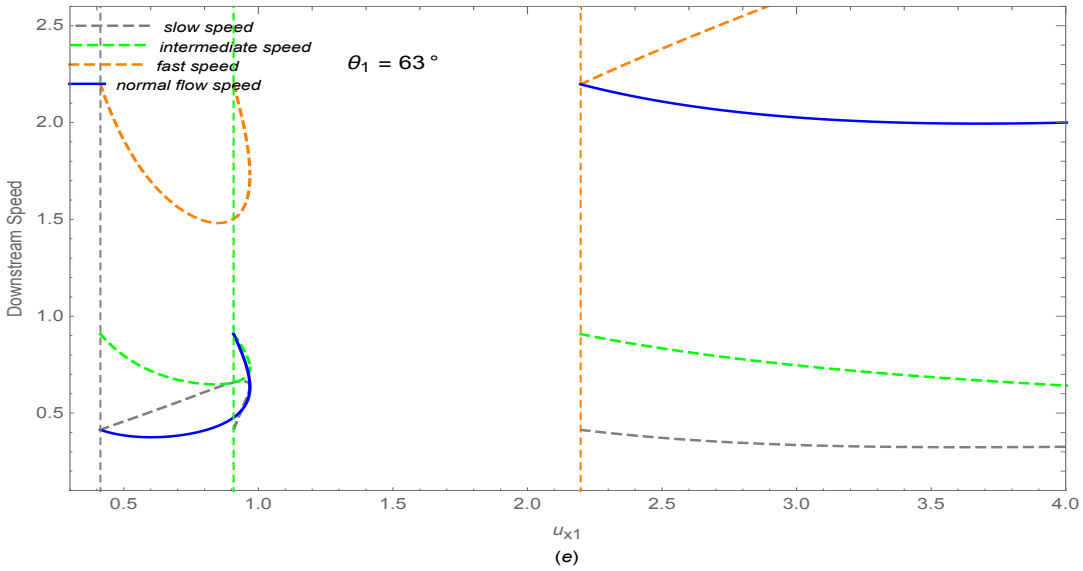

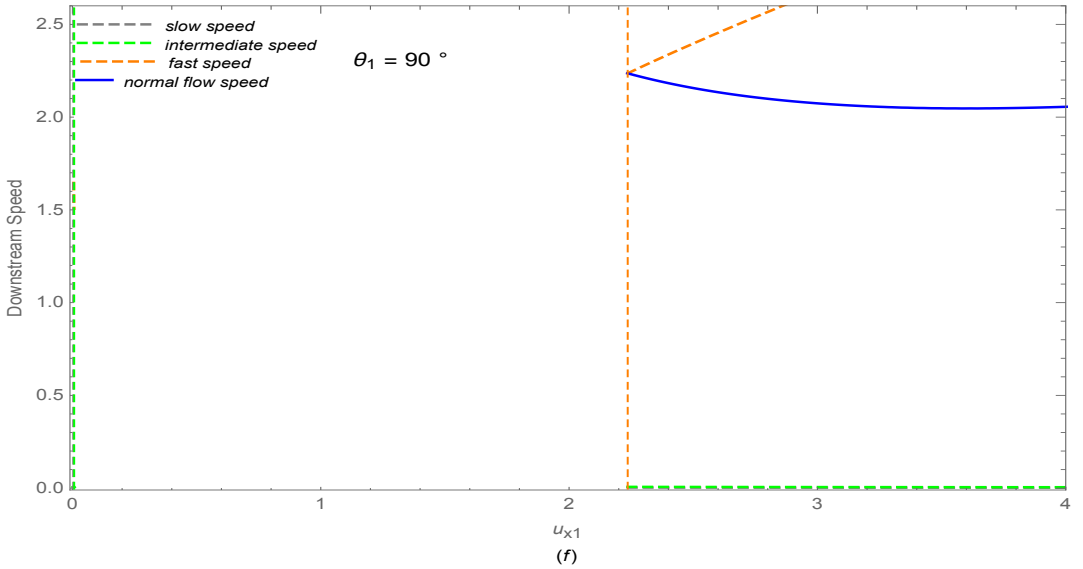

Figure 6: Downstream normal fluid speed u_{x2} shock speed and MHD signal speeds when a maximum of two downstream states are possible. Speed units are multiples of the upstream sound speed; $\frac{b_1}{a_1} = 2$, $\theta_1 = 37°$,$63°$,$90°$

3.2 Shock Taxonomy in Terms of the Upstream Shock Speed

In this section the parametric solution of the jump conditions given in §2.4 will be used to generate plots showing the downstream normal flow speed and downstream sound speed in terms of the upstream shock speed. The parametric solution allows considerable computational simplicity, especially in the determination of the downstream sound speed, compared to a method based on solving a cubic as in (51). The shock angles given are 0°,1°,5°,15°,37°,63° and 90°. The 1° shock angle plot is given to show the emergence of the intermediate and fast shock structure as the upstream shock angle increases from 0°.

Each plot shows the downstream sound speed a_2 in red and the downstream normal shock velocity component u_{x2} in blue in terms of the upstream shock speed u_{x1}. The dashed vertical lines indicate the upstream MHD signal speeds as in §3.1. Along a vertical line on each plot, the red and blue curve intercepts representing the respective downstream sound and normal shock speeds for a given upstream shock speed, f_1,f_2,f_3,f_5 and f_7 are constants. Each upstream speed gives a set of upstream conditions producing a magnetic phase plane on which the f_i are constant. The phase plane concept is introduced in Chapter 4.

Dashed curved lines on the plots denote unphysical transitions where the compression ratio is less than 1 or equivalently, as shown in §2.3.1, a decrease in specific entropy would occur across the transition making it not physically possible. The filled points indicate a change from one shock type to another. Filled points at the intersection of the red and blue curves are the equisonic points where $u_{x2} = a_2$. Open points bracket the regions in which transonic transition points form in the magnetic phase plane, the theory of these points being presented in §4.3.

For classification purposes, each shock type is labelled with its name, the change in the sonic nature of the transition, the signs of the respective (B_y, B_z) eigenvalues of the solutions to the linearised ODEs near the upstream and downstream stationary points and a statement of the uniqueness of the particular shock transition. The eigenvalue signs indicate the nature of the stationary point in the phase plane. The combination $(+,+)$ indicating a source point, $(-,-)$ a sink and $(+,-)$ or $(-,+)$ a saddle point. In some situations it is possible to connect the upstream and downstream states using different paths in the numerical integration linking them so a statement of the uniqueness of its shock transition is given at the end of the label. The phase plane is described in Chapter 4.

The plots follow the change from one shock type to the next with increasing upstream speed and the occurrence of possible multiple downstream states to be seen. For example, when the upstream shock speed first exceeds the slow speed a $3 \rightarrow 4$ slow shock can be formed (provided $\theta_1 \neq 90°$) as the downstream to upstream mass density ratio is now greater than 1, or equivalently an increase in specific entropy has occurred across the transition. When the upstream shock speed crosses the intermediate speed two possible downstream states can form (provided $\theta_1 \neq 90°$), these transitions being intermediate $2 \rightarrow 3$ and $2 \rightarrow 4$ shocks, both belonging to the same family as they arise from the same upstream conditions. When the upstream fast speed is crossed one or three downstream states can form depending on the upstream shock angle θ_1. The single downstream state in this case is produced by a $1 \rightarrow 2$ fast shock with three states being produced by a $1 \rightarrow 2$ fast, $1 \rightarrow 3$ and $1 \rightarrow 4$ intermediate family of shocks.

Important Features Shown in the Plots

Figure 7 shows the case of a parallel shock where for a certain range of upstream speeds a switch-on downstream transverse magnetic field component is produced. For shock speeds less than the sound speed a shock transition is not produced. For shock speeds greater than the sound speed a gas dynamic shock is produced and for a limited range of shock speeds starting at the Alfven speed two downstream states are produced, the second being the switch-on MHD state. Particular details are shown on the annotations on Figure 7.

Figures 8 and 9 show the effect on the downstream normal fluid velocity component and sound speed of increasing the angle between the normal to the plane of the shock and the magnetic field. The former switch-on shock separates into a fast and intermediate component and the former gas dynamic shock becomes a slow MHD shock or at higher speeds a fast MHD shock. Detailed annotations are given on Figures 8 and 9.

Figure 10 shows the effect of an increased upstream shock angle on the downstream normal flow speed and sound speed for a case when the Jouget speed is less than the fast equisonic speed. Three downstream states are still possible for shock speeds between the fast and Jouget speeds. The emerging presence of a shock speed range where the downstream normal flow curve is not continuous appears in the vicinity of the interval between the upstream intermediate and fast speeds. A shock is not possible on the dashed curve as the density ratio is less than one, or equivalently, a decrease in entropy would occur. Phase plane diagrams showing the absence of shocks on dashed curve are given in §6.2.1 and §7.1. Details of each shock type are given in the annotations on Figure 10.

Figure 11 shows the downstream normal flow velocity component and sound speed when for a certain upstream shock speed range no downstream shocked states can be produced. In this situation the maximum possible number of downstream states for a given upstream speed is 2. The change from three downstream states to two occurs when $\theta_1 = 26.2325°$. Details of the shock types present are given on the plot.

Figure 12 shows the effect of increasing the upstream shock angle further until all downstream shock speeds become subsonic. This effect first occurs when $\theta_1 = 60°$. The plot shows the increasing region having no shocks and the shrinking of the shock speed range producing intermediate shocks. Further details are given on the plot.

Figure 13 shows the case of a perpendicular shock. Only fast shocks are present as in this case the MHD slow and intermediate speeds are both equal to zero. Details are given on the plot.

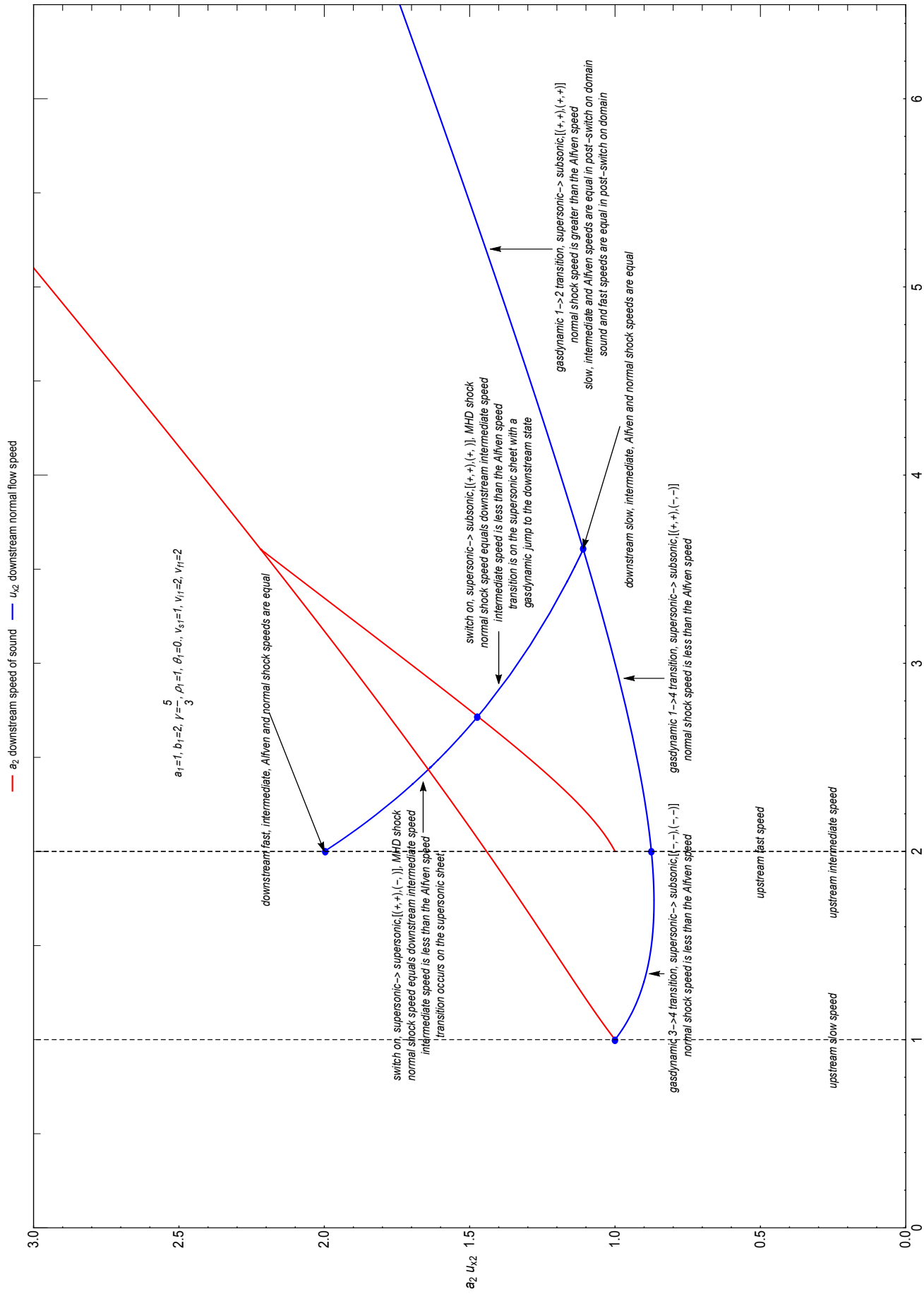

Figure 7: Relationship between upstream shock speed u_{x1} and the resulting downstream fluid normal flow speed u_{x2} and sound speed a_2 for a parallel shock. All speed units are relative to the upstream sound speed in this and subsequent plots; $\frac{b_1}{a_1} = 2, \theta_1 = 0°$ (see text)

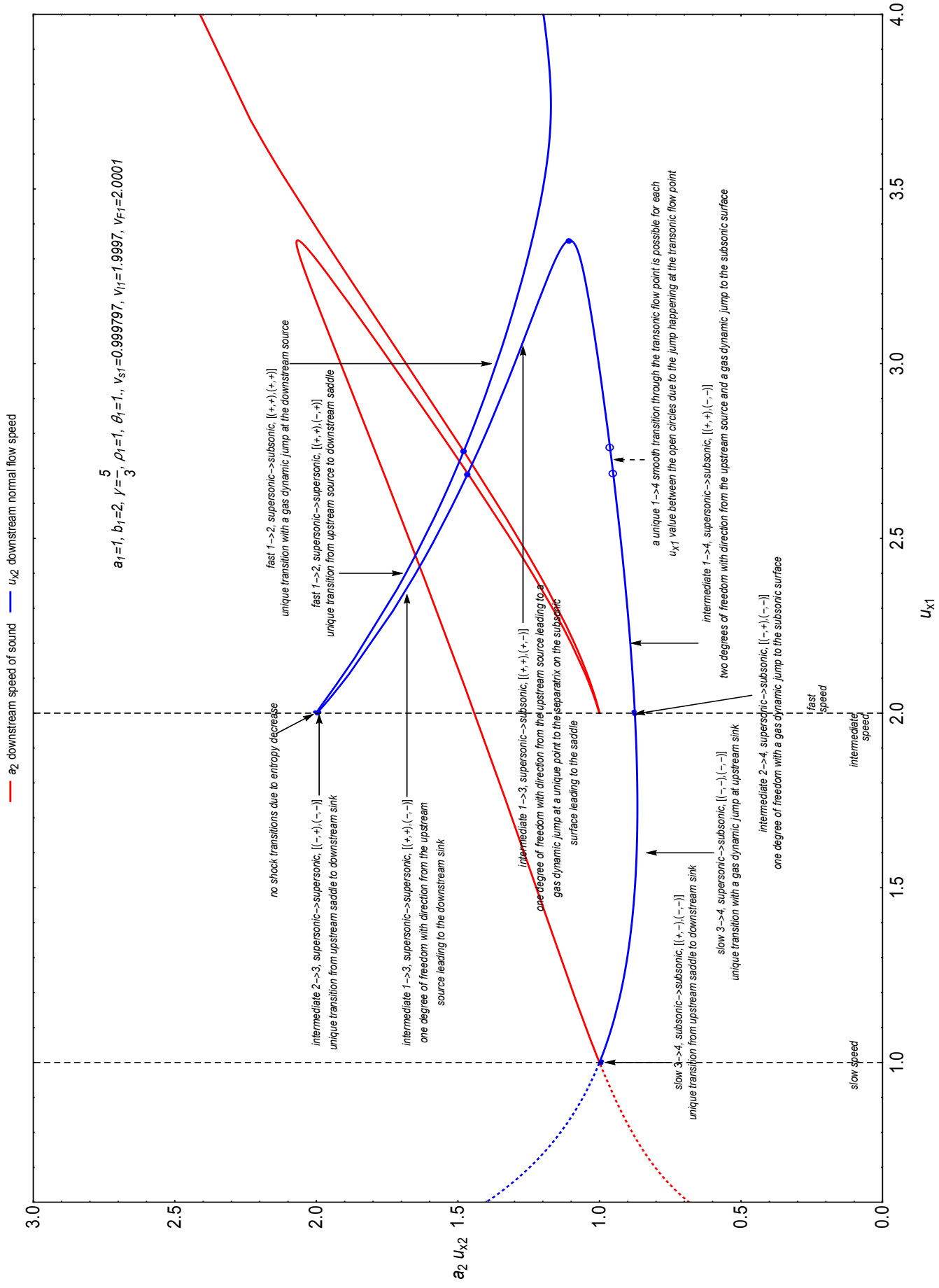

Figure 8: As for Fig 7, but for $\theta_1 = 1°$.

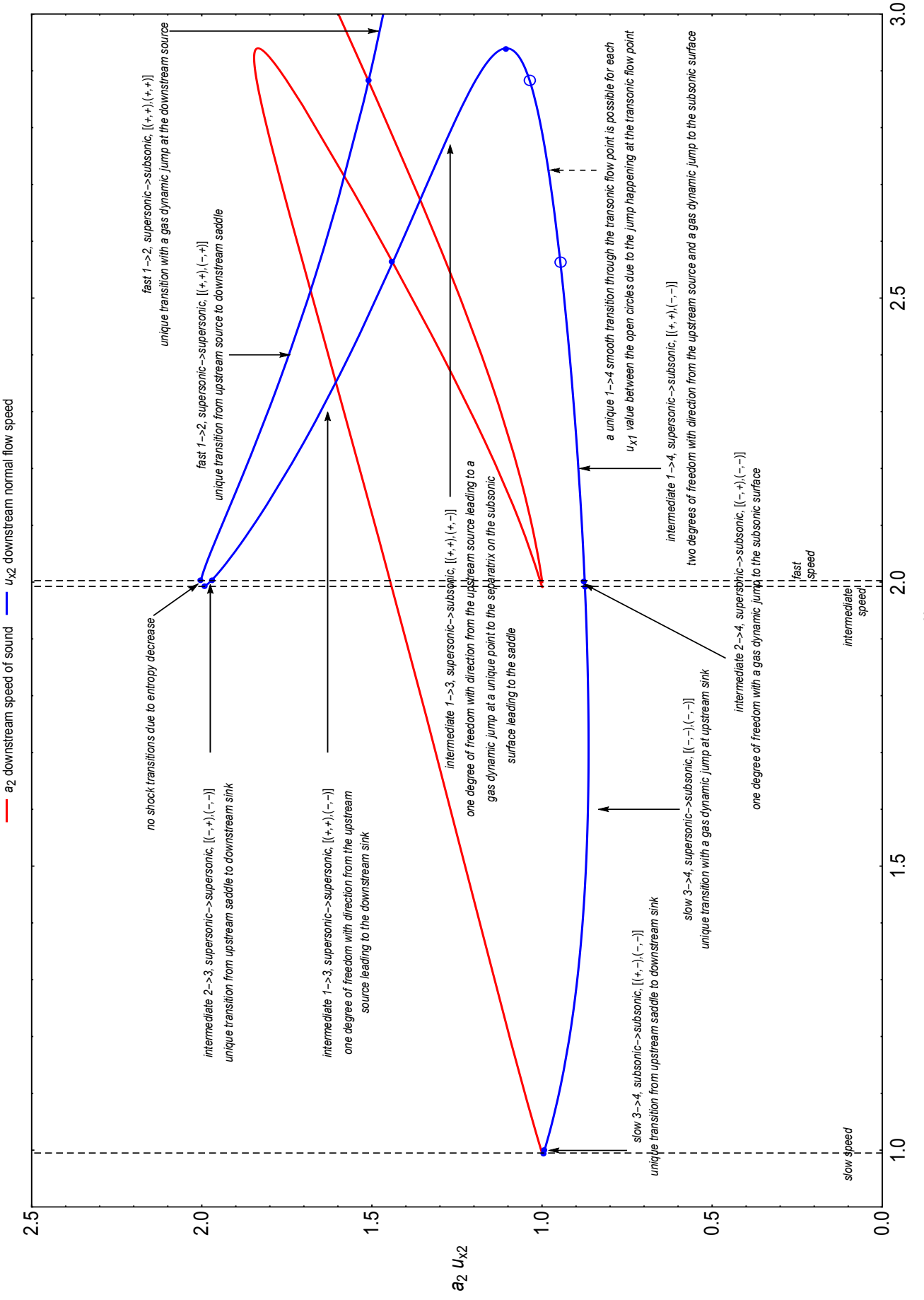

Figure 9: As for Fig 7, but for $\theta_1 = 5°$.

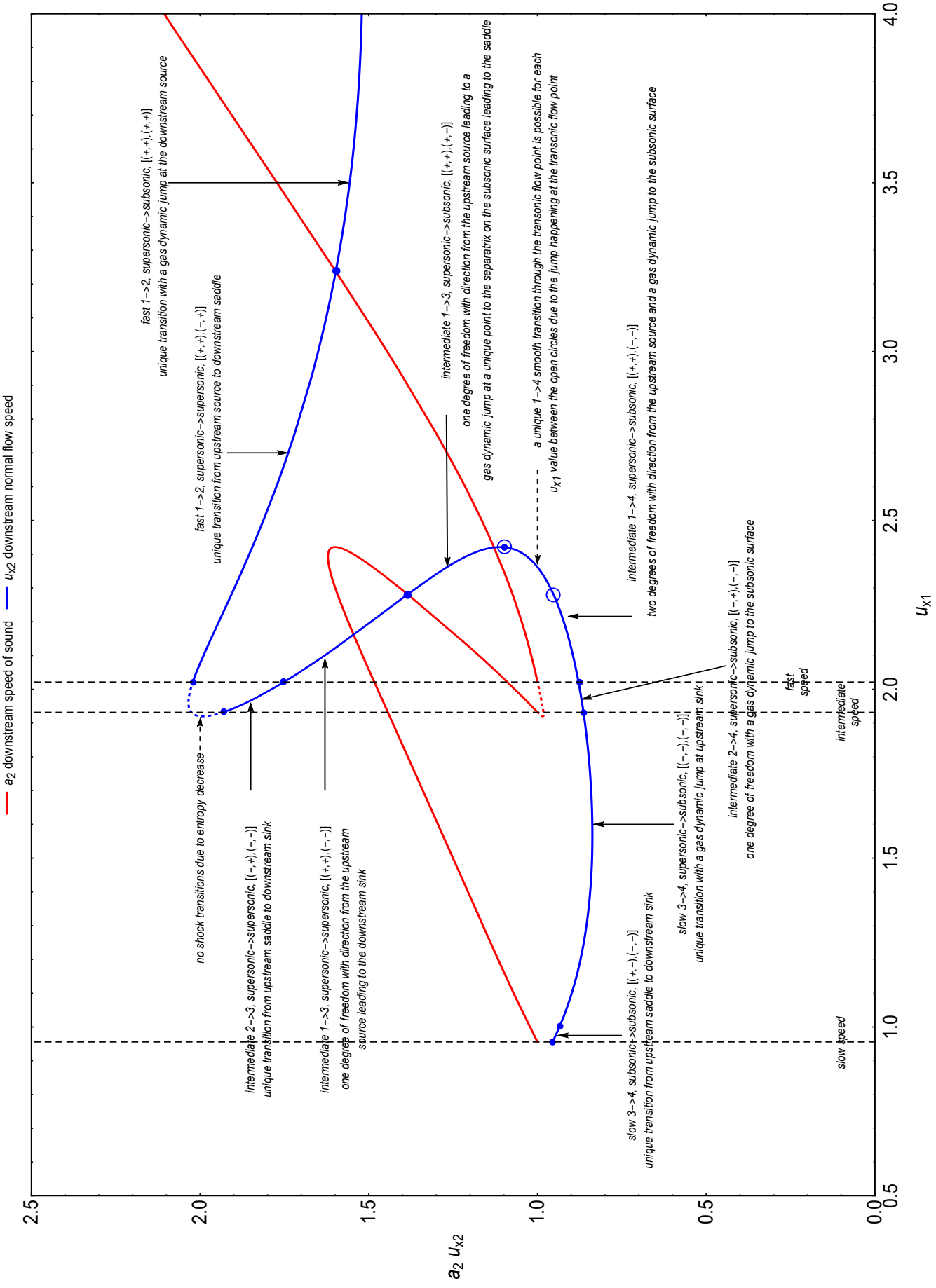

Figure 10: As for Fig 7, but for $\theta_1 = 15°$.

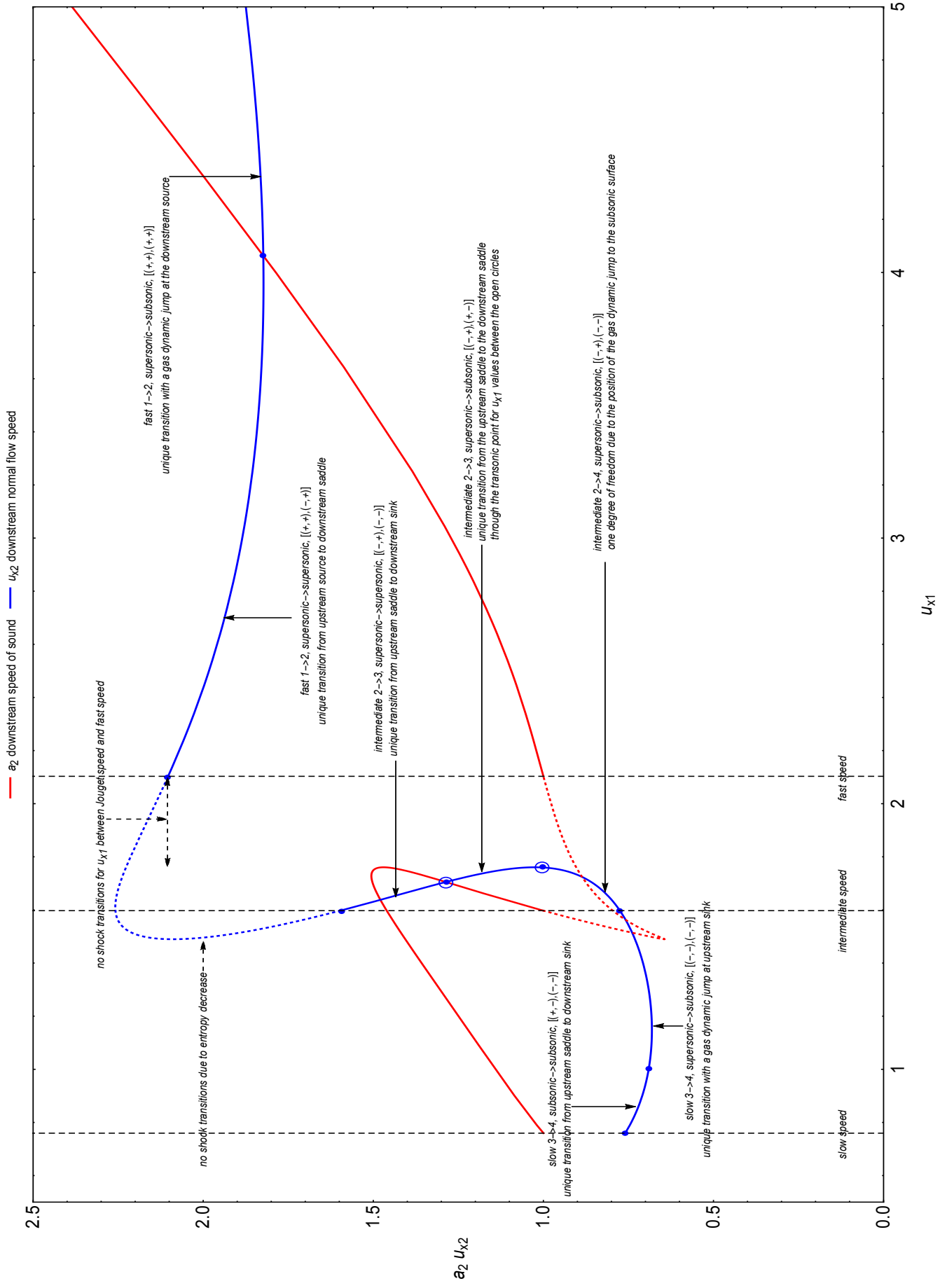

Figure 11: As for Fig 7, but for $\theta_1 = 37°$.

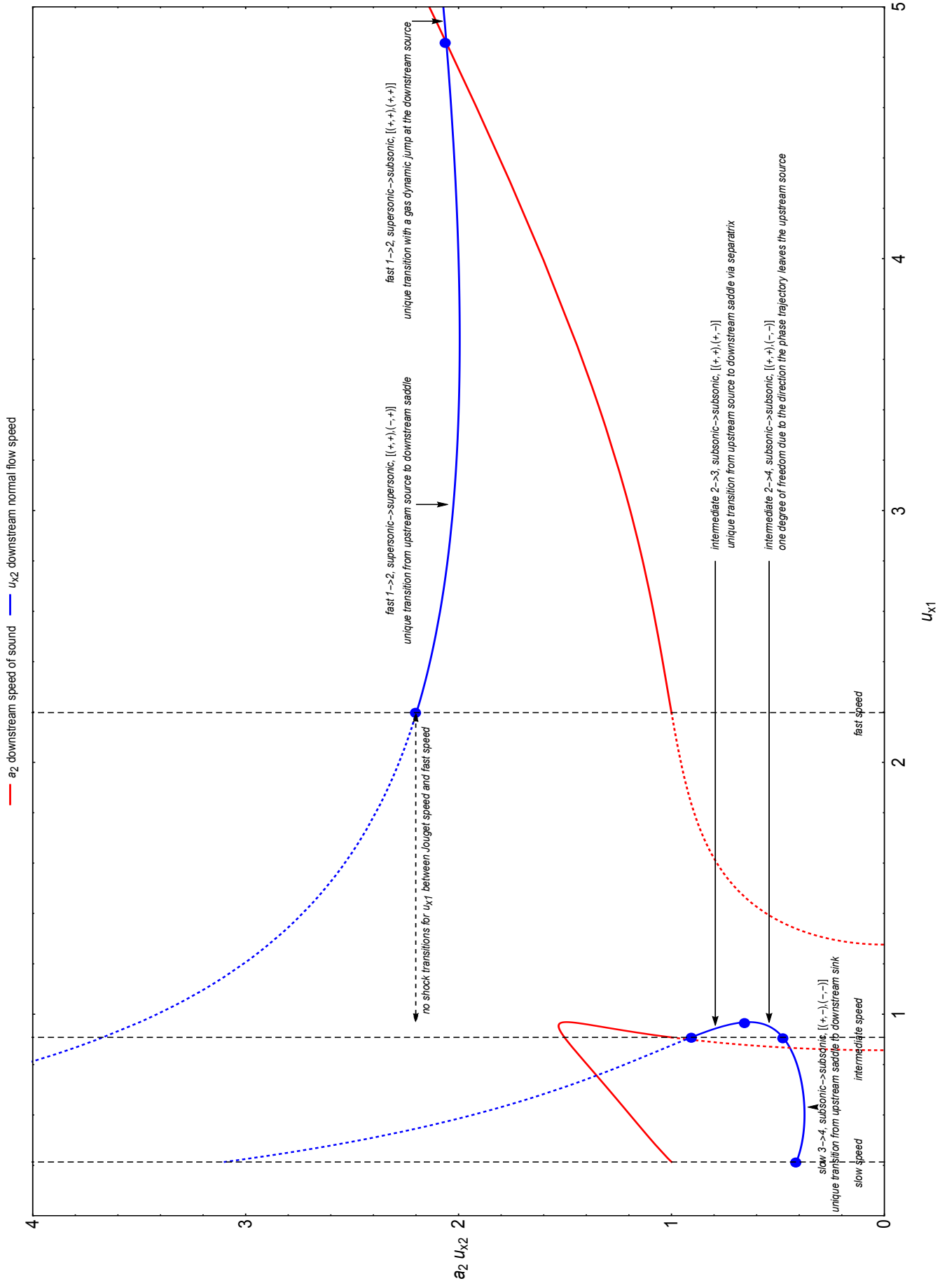

Figure 12: As for Fig 7, but for $\theta_1 = 63°$.

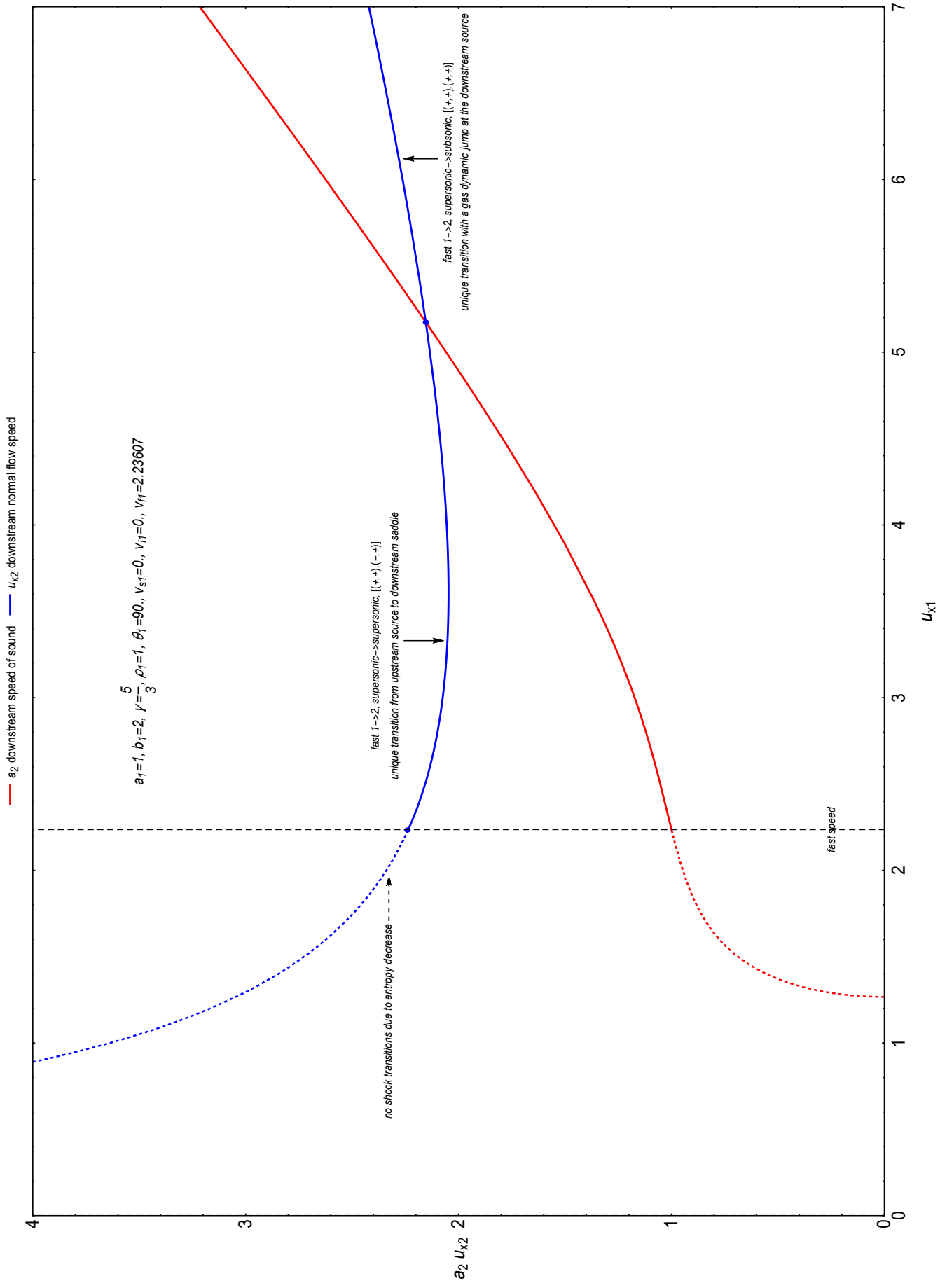

Figure 13: As for Fig 7, but for $\theta_1 = 90°$.

3.3 Downstream Values in terms of the Parametric Speed Squared

By using the parametric speed squared w^2 (83) as the independent variable the shock quantities u_{x1}, u_{x2}, a_2, r, B_{y2}, β and $\frac{\Delta s}{c_v}$ can be displayed as single valued functions, with one exception. The use of w^2 as the independent variable is computationally easier to program to produce plots than the traditional method of solving the cubic (42) for r for a given value of u_{x1} and then configuring the correct ordering of the roots in the branches on a multi-valued plot.

Figures 14 to 19 give the upstream shock speed, downstream x-velocity component, sound speed, mass density ratio, transverse magnetic field component, ratio of gas pressure to magnetic pressure and increase in specific entropy as functions of the square of the parametric speed for the upstream conditions and shock angles studied in this thesis. The various shock types are given a colour code. The colour coding used to display the various types of shocks is slow in grey, intermediate $2 \to 4$ in yellow, intermediate $1 \to 4$ in brown, intermediate $1 \to 3$ in green, intermediate $2 \to 3$ in magenta and fast shocks in orange. The values plotted are the "end values" of the transition from the starting upstream state. The internal structure of the shock representing the transition from the upstream to the downstream state is determined using numerical integration and is given in Chapters 5-8.

The $\theta_1 = 0°$ plot in Figures 14-19 are for a parallel shock, this being the case where the upstream plane of the shock is perpendicular to the upstream shock velocity direction, this being along the X axis. For upstream shock speeds greater than the sound speed a gas dynamic shock is produced, this being shown by the continuous cyan-pink-dark yellow curve. This curve gives the upstream speeds according to (67). Placing the upstream magnetic field dependent upstream speed (66) in the equation defining the parametric speed, $w^2 = u_{x1}u_{x2}$, gives $w^2 = b_1^2$. This means that the upstream speed domain given by (70) for the production of switch-on shocks has the common parametric speed b_1. The switch-on values are represented by the vertical purple line in the $\theta_1 = 0$ plots.

As the upstream shock angle θ_1 increases the vertical purple line "opens" to form intermediate $1 \to 3$, intermediate $2 \to 3$ and fast shocks. The gas dynamic cyan-pink-dark yellow curve becomes MHD slow, intermediate $2 \to 4$, intermediate $1 \to 4$ and fast shocks due to the gain in an initial upstream B_y component as the angle θ_1 increases.

Figure 14 allows the conversion between parametric and upstream speed. Figure 15 allows the comparison of downstream sound and shock speeds, this being of use as it allows the location of the equisonic points, where $u_{x2} = a_2$, to be seen. Figure 16 gives the mass density ratio across the shock, showing speeds where a shock cannot form when $\frac{\rho_2}{\rho_1} < 1$. Figure 17 gives the downstream transverse magnetic field component B_{y2} in terms of the parametric speed squared. Taking B_{y1} to be positive in sign, the diagrams display the reversal in the direction of the downstream B_{y2} vector for intermediate shocks and its non-reversal for slow and fast shocks. Analytically, the reversal and non-reversal can be shown using (133) in Chapter 7. Figure 18 displays the relative value of the gas pressure p and the magnetic pressure $\frac{B^2}{8\pi}$ for the range of parametric speeds at each shock angle. Figure 19 displays the increase in specific entropy across a shock, with a local maximum being present at the Jouget point, this being at the meeting of the brown and green curves for 5° and 15° or the yellow and magenta curves for 37° and 63°.

In summary, the parametric approach allows all shock properties to be graphically displayed as single valued functions. A disadvantage of this method is that a switch-on shock is displayed as a vertical line. As the upstream shock speed increases the switch-on shock plot opens into a fast and intermediate shock.

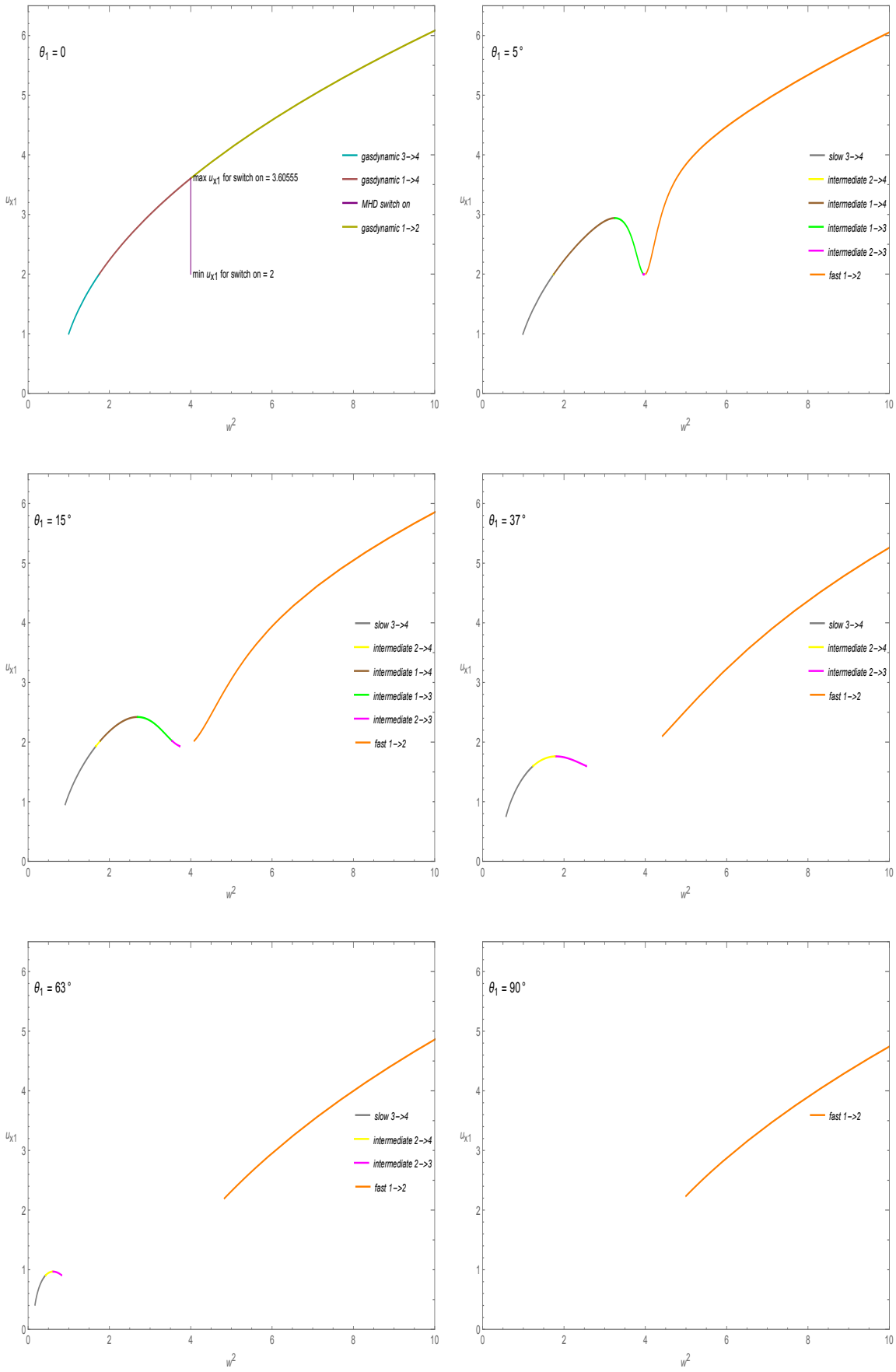

Figure 14: Upstream shock speed in terms of parametric speed squared for $\frac{b_1}{a_1} = 2$ and $\theta_1 = 0$,5,15,37,63 and 90°. Speeds in this and subsequent plots are relative to the upstream sound speed. Colour indicates the type of shock transition (see text).

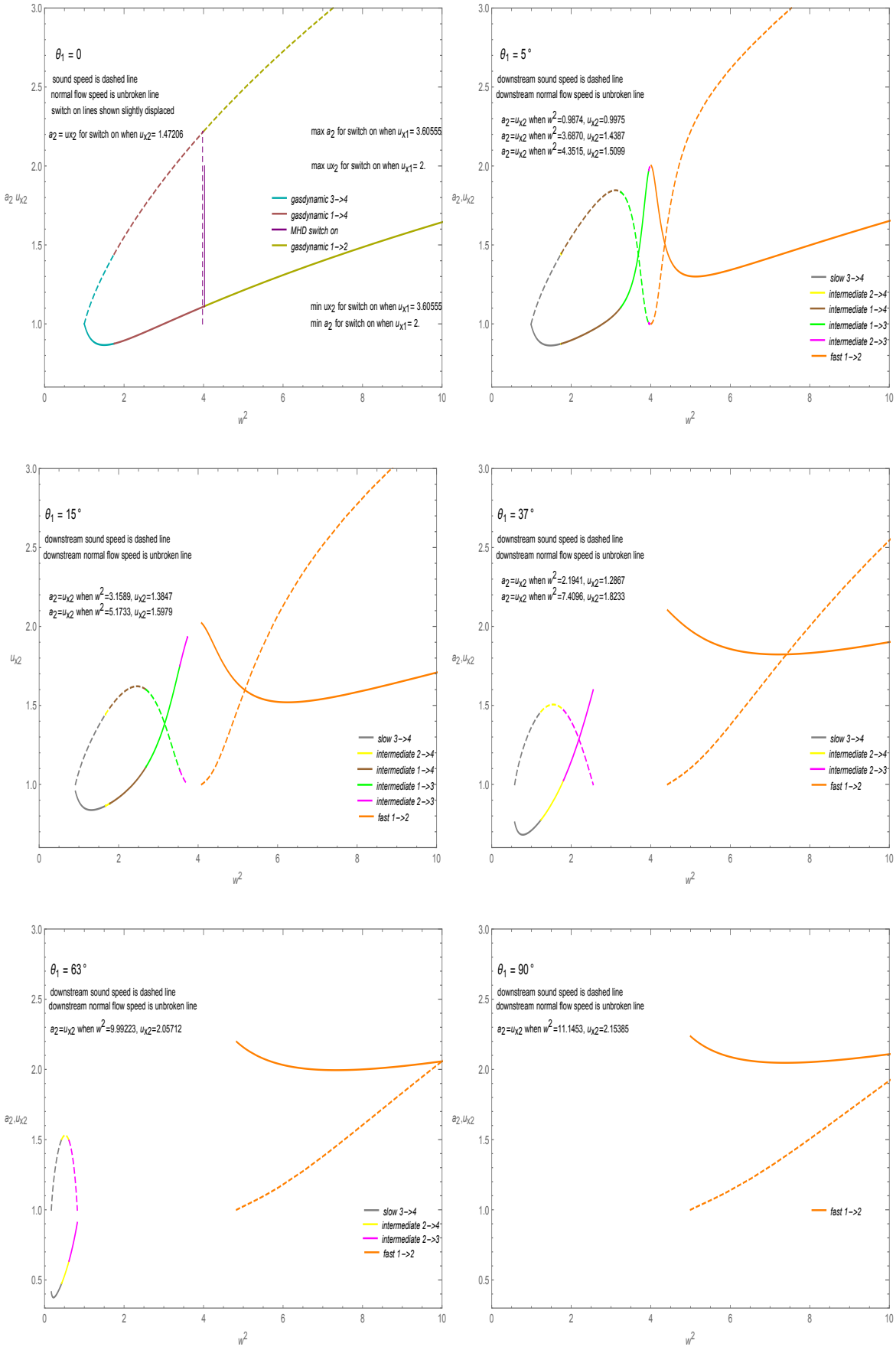

Figure 15: As for Fig 14, but showing downstream normal shock and sound speeds in terms of parametric speed squared; $\frac{b_1}{a_1} = 2$

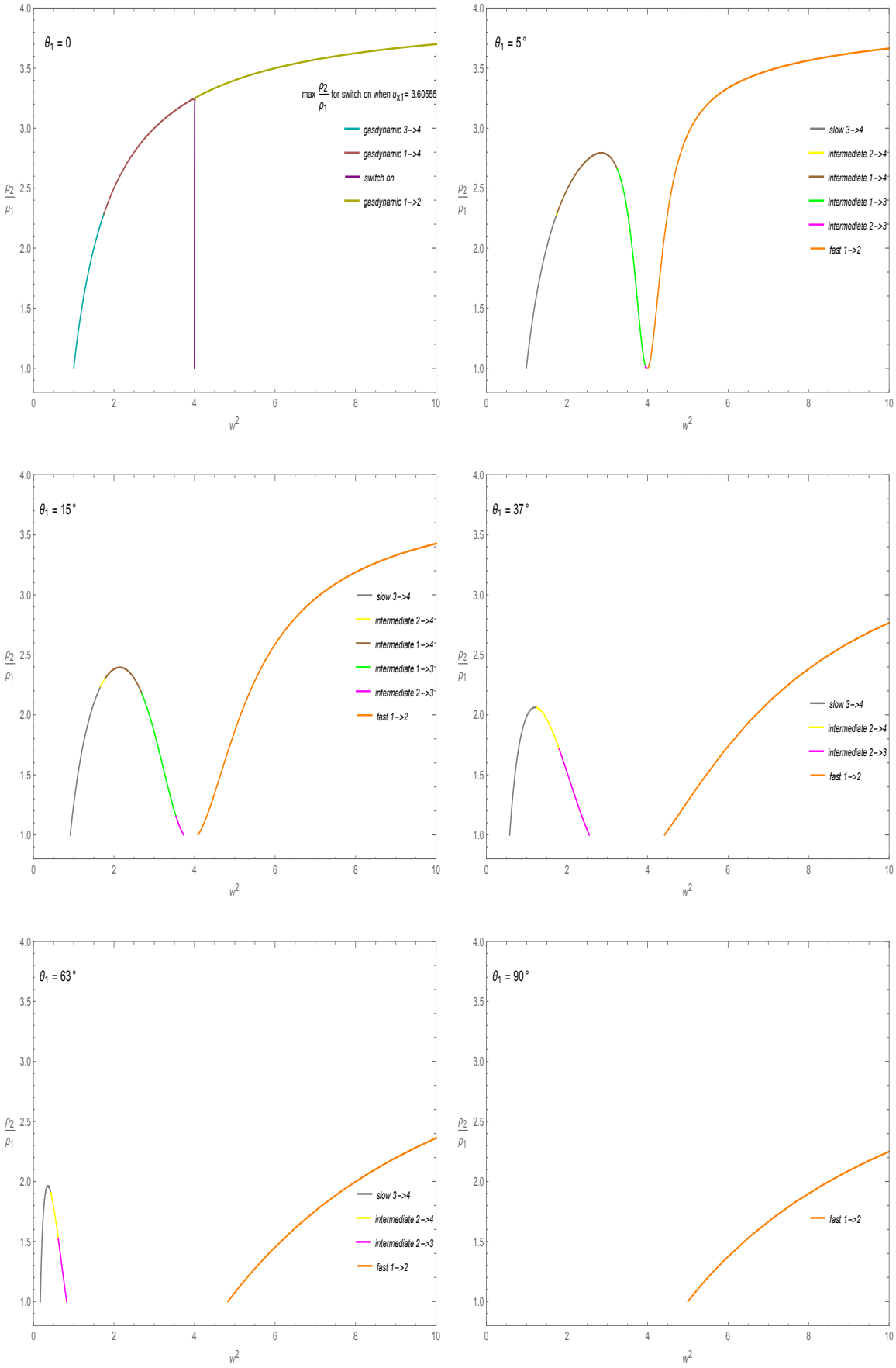

Figure 16: As for Fig 14, but showing mass density ratio in terms of parametric speed squared; $\frac{b_1}{a_1} = 2$

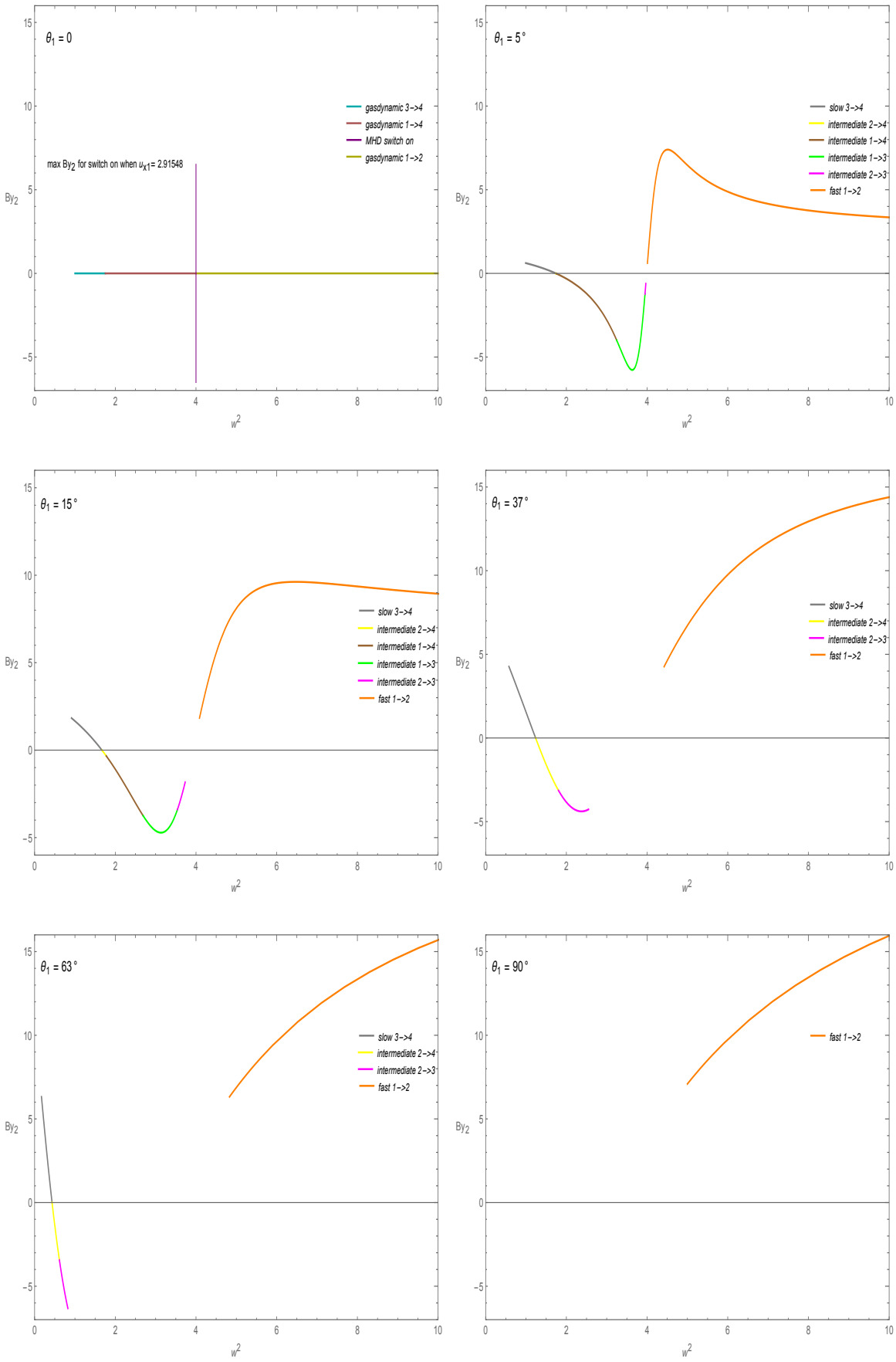

Figure 17: As for Fig 14, but showing downstream transverse magnetic field component versus parametric speed squared. Upstream density is taken as 1; $\frac{b_1}{a_1} = 2$

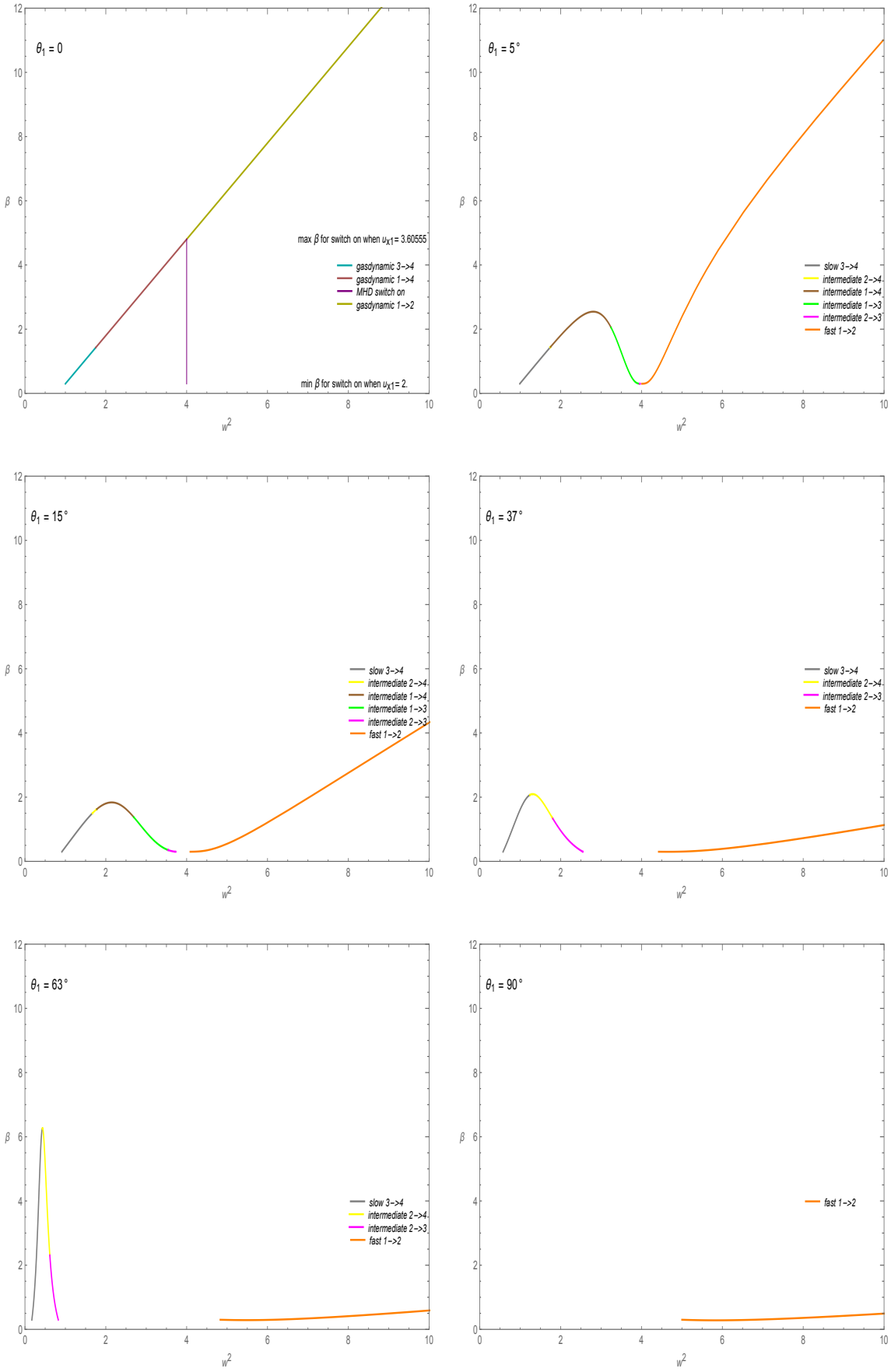

Figure 18: As for Fig 14, but showing downstream ratio of gas pressure to magnetic pressure in terms of parametric speed squared; $\frac{b_1}{a_1} = 2$

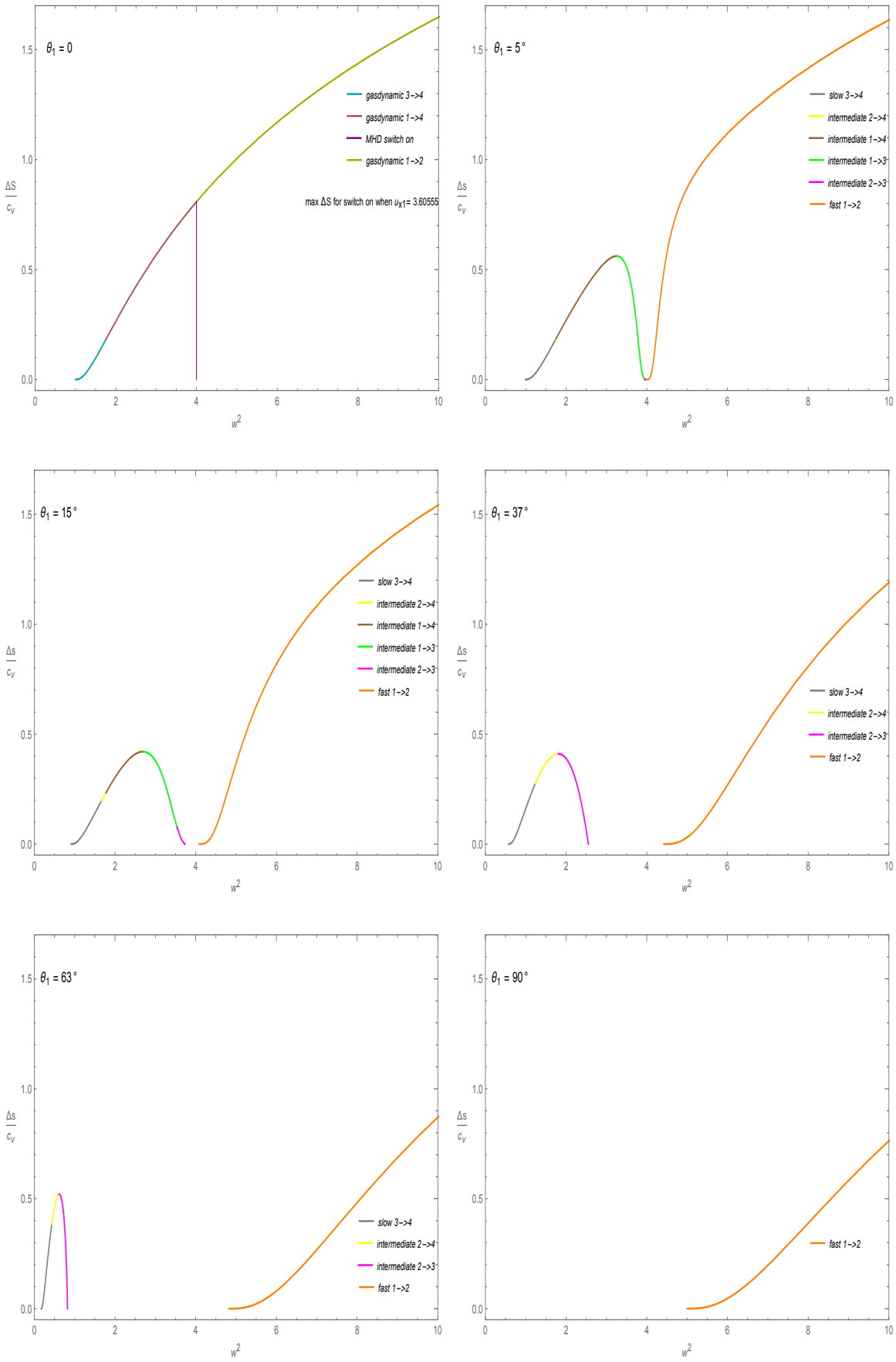

Figure 19: As for Fig 14, but showing downstream increase in specific entropy versus parametric speed squared; $\frac{b_1}{a_1} = 2$

3.4 Downstream Values in terms of the Mass Density Ratio

By using the mass density ratio $\frac{\rho_2}{\rho_1}$ as the independent variable the domain on each plot is given by $1 < \frac{\rho_2}{\rho_1} < \frac{\gamma+1}{\gamma-1}$, this inequality being predicted by (49). For $\gamma = \frac{5}{3}$ this becomes $1 < \frac{\rho_2}{\rho_1} < 4$. This is useful in showing the gas pressure ratio across the shock and the downstream transverse magnetic field component.

The plot of $\frac{p_2}{p_1}$ versus $\frac{\rho_2}{\rho_1}$ was used in §2.3.1 to establish the compressive nature of a shock between its downstream and upstream states. The placement of the various shock types on this diagram will now be shown for given upstream conditions, the upstream shock speed u_{x1} varying along the curves. Figure 20 shows the gas dynamic, switch-on, slow, intermediate and fast shocks present for the upstream shock angles 0°, 5°, 15°, 37°, 63° and 90° for the upstream values of $\frac{b_1}{a_1} = 2$, $\gamma = \frac{5}{3}$ and $\rho_1 = 1$. The colour codes for the shocks are the same as in §3.3. The plots show that at a given upstream angle $2 \rightarrow 4$ intermediate shocks always have a greater value of $\frac{\rho_2}{\rho_1}$ and $\frac{p_2}{p_1}$ than $2 \rightarrow 3$ intermediate shocks. At a given upstream shock angle and speed $1 \rightarrow 4$ intermediate shocks have a greater value of $\frac{\rho_2}{\rho_1}$ and $\frac{p_2}{p_1}$ than $1 \rightarrow 3$ intermediate shocks. The intersection of the orange locus of points representing fast shocks with another shock locus indicates that for a given set of upstream parameters a common downstream density and pressure ratio can be produced by two different shock transitions, provided $\theta_1 \neq 90°$, each having the same increase in specific entropy.

Figure 21 shows the relationship between the downstream transverse magnetic field component and the mass density ratio for the selected shock angles. The plots display that at a given upstream angle fast shocks have a greater value of B_{y2} than slow shocks, $2 \rightarrow 3$ intermediate shocks always have a greater value of $|B_{y2}|$ than $2 \rightarrow 4$ intermediate shocks. For a given upstream shock angle and speed, $|B_{y2}|$ is greater for $1 \rightarrow 3$ shocks than $1 \rightarrow 4$ intermediate shocks. For the case of $\theta_1 = 90°$ the relationship is linear as predicted by (80).

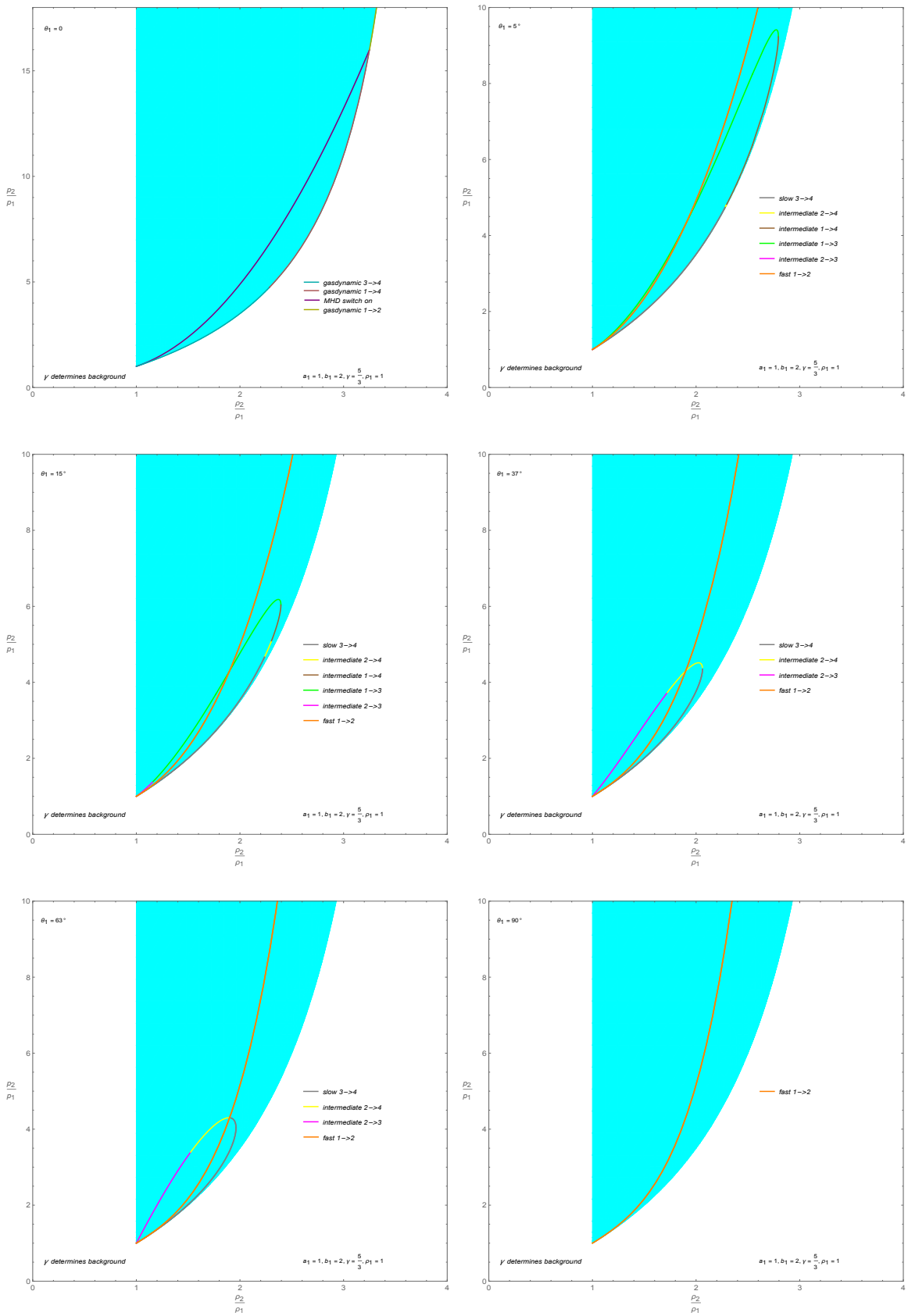

Figure 20: Gas pressure versus mass density ratio for shocks with $\frac{b_1}{a_1} = 2$ and $\theta_1 = 0$, 5, 15, 37, 63 and 90° . Speeds in this and subsequent plots are in terms of the upstream sound speed. The curve colour indicates the shock type and the blue shaded region shows the region of entropy increase. (see text)

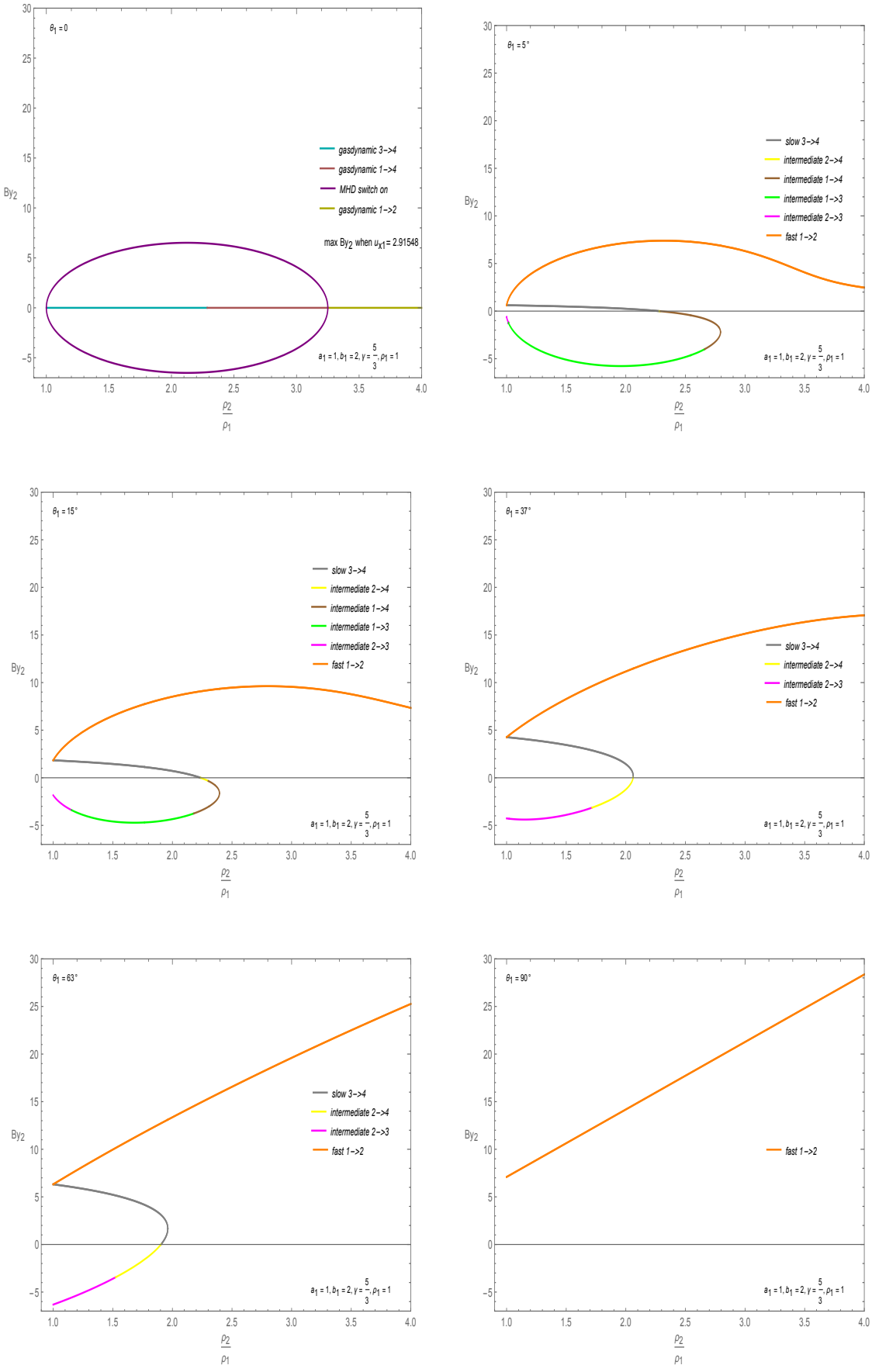

Figure 21: As for Fig 20, but showing the downstream transverse magnetic field component versus mass density ratio. Upstream density is taken as 1; $\frac{b_1}{a_1} = 2$

4 The B_y - B_z Phase Plane

Shocks can be represented as trajectories $B_y(x)$ versus $B_z(x)$ and this provides an efficient overview of the relationship between shock classes. The resistive MHD structure equations are the first order ODEs (27) and (28) with derivatives on the left only. The derivatives are functions of B_y and B_z and the equations do not have an explicit dependence on the independent variable x. This allows the derivatives at each point of the $B_z - B_y$ phase plane for a given set of upstream parameters to be determined. The stationary points in the phase plane represent the upstream (undisturbed or pre-shock) and possible downstream (disturbed or post-shock) states. MHD shocks are the transitions between stationary points in the $B_y - B_z$ plane where the first derivatives are zero. Once these are found the phase plane can be "mapped out" by determining the possible trajectories between the stationary points. The presence, location and nature of the stationary points is determined by the set of upstream parameters $\{a_1, b_1, \gamma, \rho_1, \theta_1, u_{x1}\}$. In later chapters the ODEs (27) and (28) will be numerically integrated, using the upstream parameters as initial conditions, to determine the trajectory in the phase plane connecting the stationary points. For given values of B_y and B_z, the quadratic nature of (29) indicates that there are two possible values of u_x and it will be shown that these values lie on supersonic and subsonic sheets.

By way of example, Figure 22 is a sample phase plane with vector fields as arrows indicating the direction of ΔB_y and ΔB_z for increasing values of Δx_η at points in the plane, the positive x direction being from the upstream to the downstream point. The upstream and downstream stationary points are shown as circles on the B_y axis with the upstream state shown as U and the possible downstream states labelled according to the type of shock that can come from the upstream state.

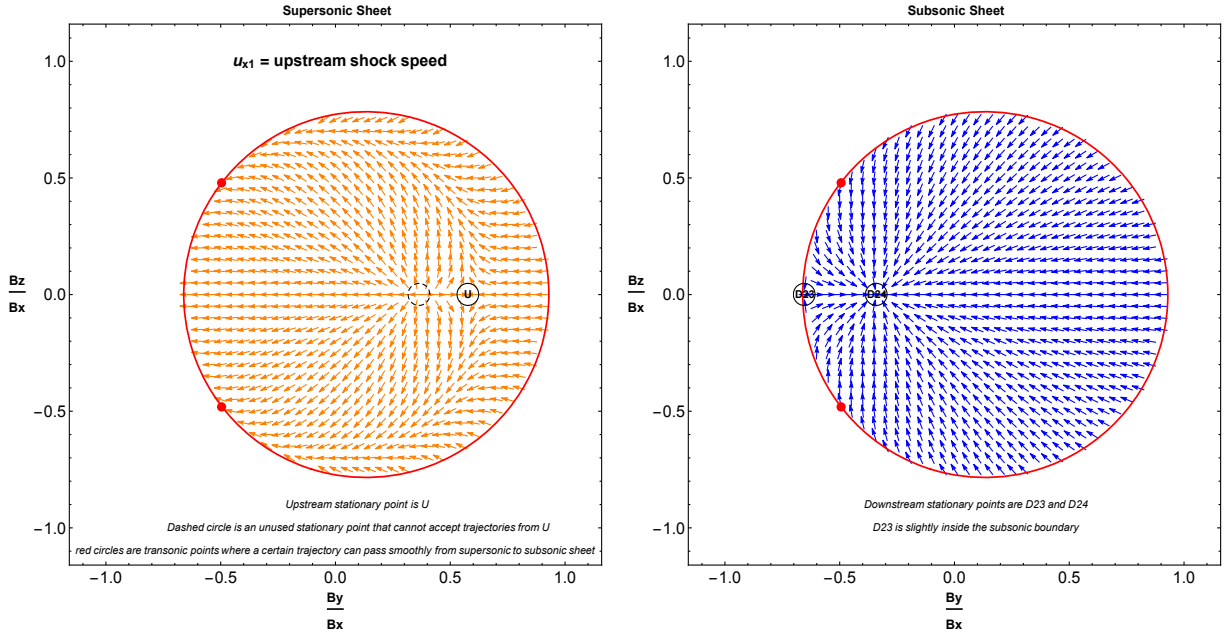

Figure 22: Sample general phase plane vector fields for a shock family with upstream point U. Stationary points shown as small circles are where $\frac{dB_y}{dx_\eta}$ and $\frac{dB_z}{dx_\eta}$ equal zero. Shocks are trajectories connecting stationary points. Dashed circle is unable to accept trajectories from U. On the supersonic sheet (left panel) $u_x > a$, on the subsonic sheet (right panel), $u_x < a$, where a is the local sound speed. On the red boundary $u_x = a$. Sheets overlie each other with connection being by an entropy increasing gas dynamic jump, keeping B_y and B_z constant, from the supersonic to the subsonic sheet or by a particular trajectory passing through a transonic point shown as red circles.

4.1 Supersonic and Subsonic Sheets

The significance of the sound speed in the structure of resistive MHD shocks is in the $\pm$ sign that occurs in the ODEs (27) and (28). To show this let α represent the ratio of the normal velocity component of the shock to the sound speed at a point in the transition from the upstream to the downstream state

$$\alpha = \frac{u_x}{a}. \tag{100}$$

Taking the speed of sound as $a = \sqrt{\frac{\gamma p}{\rho}}$ and using (14), equation (21) becomes

$$\frac{(B_y^2 + B_z^2)}{8\pi} + u_x \left(f_1 + \frac{1}{\gamma \alpha^2} \right) = f_2. \tag{101}$$

Eliminating u_x from (25) and (101) gives

$$\alpha^2 = \frac{2(B_z B_x^2 + 4\pi\eta f_1 \frac{dB_z}{dx})}{\gamma \left[B_z(8\pi f_2 - 2B_x^2 - B_y^2 - B_z^2) - 8\pi\eta f_1 \frac{dB_z}{dx} \right]}. \tag{102}$$

Replacing $\frac{dB_z}{dx}$ in (102) using (28) gives

$$\alpha^2 = \frac{\gamma \left(B_y^2 + B_z^2 - 8\pi f_2 \right) \pm \sqrt{R}}{\gamma \left(B_y^2 + B_z^2 - 8\pi f_2 \mp \sqrt{R} \right)}, \tag{103}$$

where R is the function of B_y and B_z inside the square root term in the ODEs (27) and (28), given by

$$\begin{aligned} R = {} & \gamma^2 \left(B_y^4 + B_z^4 \right) + 4[\left(\gamma^2 - 1 \right) B_x^2 - 4\pi\gamma^2 f_2](B_y^2 + B_z^2) + 2\gamma^2 B_y^2 B_z^2 + 32\pi \left(\gamma^2 - 1 \right) (f_3 B_x + f_1 f_5) B_y \\ & + 64\pi^2[\gamma^2 f_2^2 + (\gamma^2 - 1)(f_3^2 - 2 f_1 f_7)]. \end{aligned} \tag{104}$$

Equation (103) shows that the positive sign before the square root gives $\alpha > 1$ with supersonic values of u_x and that the negative sign before the square root makes $\alpha < 1$ the normal shock velocity being subsonic. This classification allows the $B_y - B_z$ phase plane to be considered as two overlying sheets, the supersonic sheet, on which $u_x > a$ and the subsonic sheet on which $u_x < a$. The common boundary of each sheet is the locus defined by $R = 0$, on which $u_x = a$. In this thesis the locus $R = 0$ (with $u_x = a$) is drawn in red on phase plane plots. When necessary for visual clarity, vector fields and phase trajectories on the supersonic sheet are shown in orange and those in the subsonic sheet are in blue. To aid visualisation in 3-D plots of the variables $B_y - B_z - u_x$ the supersonic surface will be shown in yellow and the subsonic surface in blue.

4.2 Isomagnetic Jumps

In the previous section it was shown that the $B_y - B_z$ phase plane is an overlay of two sheets, supersonic and subsonic, that have the same (B_y, B_z) but different u_x, ρ and p at each overlying point. Thermodynamically, a transition between the two sheets, keeping the magnetic field components constant, is possible provided that the pre-shock state is supersonic. The transition is called by Polovin [38] an isomagnetic jump or gas dynamic jump, the magnetic field components not changing across the jump, the first derivatives changing in the transition according to (27) and (28) in the change from the supersonic to the subsonic state. The non-zero constants f_1,f_2, f_3, f_5 and f_7 are the same on both sheets, these being determined by the upstream conditions, enabling equations (14) to (20) to be applied to the jump. The supersonic and subsonic normal shock speeds at the phase plane point $(B_y$,$B_z)$ are the larger and smaller roots of the quadratic (29)

$$u_x = \frac{\gamma\left(8\pi f_2 - B_y^2 - B_z^2\right) \pm \sqrt{R}}{8\pi(\gamma+1)f_1}, \tag{105}$$

where $R = 0$ is the locus in phase space where $u_x = a$.

For an isomagnetic transition between two states with respective normal shock speeds, pressure and mass density values u_{x1}, p_1, ρ_1 and u_{x2}, p_2, ρ_2 equations (14) to (20) reduce to

$$\rho_1 u_{x1} = \rho_2 u_{x2}, \tag{106}$$

$$p_1 + \rho_1 u_{x1}^2 = p_2 + \rho_2 u_{x2}^2, \tag{107}$$

$$\frac{1}{2}\rho_1 u_{x1}^3 + \frac{\gamma}{\gamma-1} p_1 u_{x1} = \frac{1}{2}\rho_2 u_{x2}^3 + \frac{\gamma}{\gamma-1} p_2 u_{x2}, \tag{108}$$

the magnetic field derivatives in (18) and (19) causing the energy equation (20) to be written without direct magnetic field terms, equations (106) to (108) describing a hydrodynamic shock.

Eliminating the velocity terms in (106) to (108) gives

$$\frac{p_2}{p_1} = \frac{\frac{\gamma+1}{\gamma-1}\frac{\rho_2}{\rho_1} - 1}{\frac{\gamma+1}{\gamma-1} - \frac{\rho_2}{\rho_1}}, \tag{109}$$

this result being the hydrodynamic case of (49).

Equation (107) can be written in terms of $\alpha = \frac{u_{x1}}{a_1}$ as

$$\frac{p_2}{p_1} = 1 + \gamma\alpha^2\left(1 - \frac{\rho_1}{\rho_2}\right). \tag{110}$$

When the initial state is supersonic $\alpha > 1$, $u_{x1} > u_{x2}$, $\rho_2 > \rho_1$ and from (110) $p_2 > p_1$. For $\frac{p_2}{p_1} > 1$ and $\frac{\rho_2}{\rho_1} > 1$ points on the gas dynamic curve C_2 in Figure 2 have an increase in specific entropy in the

transition from a supersonic to subsonic state and so are thermodynamically possible.

The mass density and fluid pressure at the magnetic phase plane point (B_y, B_z) are found by placing (105) in (14) and (21). The pressure and mass density ratios respectively in terms of magnetic field components are

$$\frac{p_2}{p_1} = \frac{8\pi f_2 - B_y^2 - B_z^2 + \sqrt{R}}{8\pi f_2 - B_y^2 - B_z^2 - \sqrt{R}} \tag{111}$$

and

$$\frac{\rho_2}{\rho_1} = \frac{\gamma\left(8\pi f_2 - B_y^2 - B_z^2\right) + \sqrt{R}}{\gamma\left(8\pi f_2 - B_y^2 - B_z^2\right) - \sqrt{R}}. \tag{112}$$

The change in specific entropy across an isomagnetic jump at (B_y, B_z) is deduced using (54)

$$\frac{\Delta s}{c_v} = \ln\left\{\frac{8\pi f_2 - B_y^2 - B_z^2 + \sqrt{R}}{8\pi f_2 - B_y^2 - B_z^2 - \sqrt{R}}\left[\frac{\gamma\left(8\pi f_2 - B_y^2 - B_z^2\right) - \sqrt{R}}{\gamma\left(8\pi f_2 - B_y^2 - B_z^2\right) + \sqrt{R}}\right]^{\gamma}\right\}. \tag{113}$$

Figure 23 shows the increase in specific entropy in a gas dynamic jump from a supersonic state to a subsonic state in terms of the mass density ratio $r = \frac{\rho_2}{\rho_1}$.

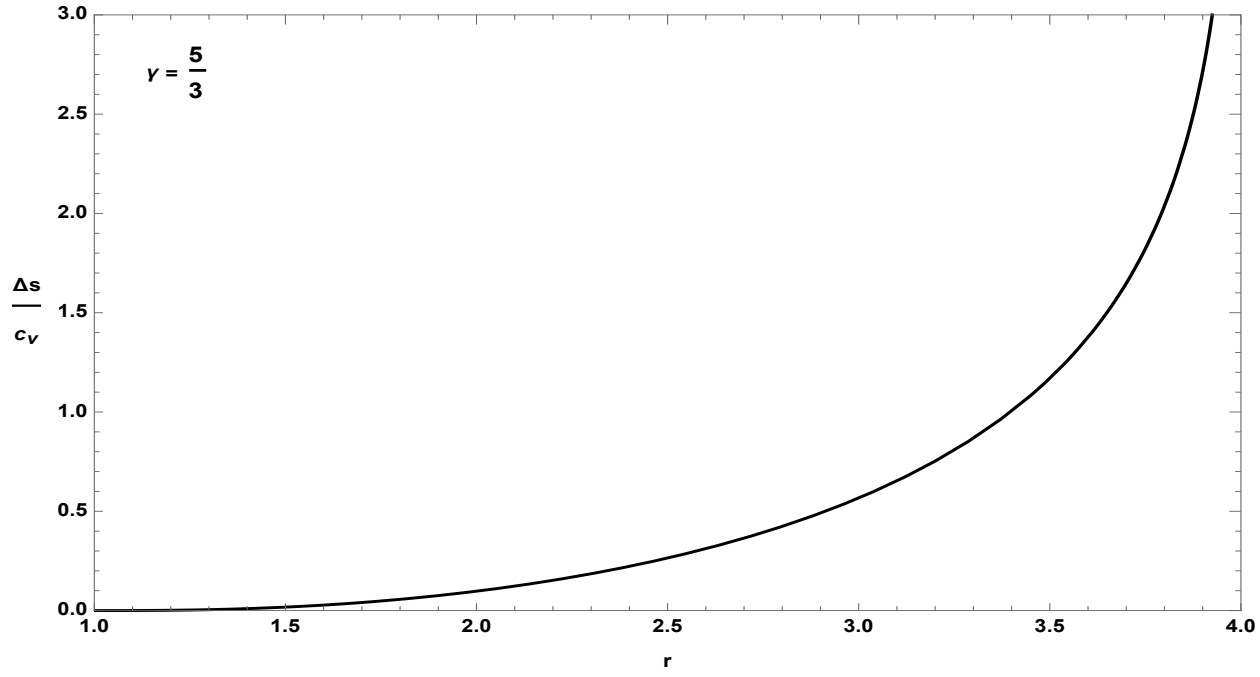

Figure 23: Change in specific entropy across a gas dynamic jump from a supersonic to subsonic state in a monatomic gas.

4.3 Transonic Flow Points

The previous section showed that a shock transition can reach a subsonic state by an isomagnetic jump from the supersonic state. The other possible way to reach the subsonic state is via a smooth transition in terms of B_y, B_z, u_x and their derivatives and this means is only possible for a certain set of upstream shock speeds. When $u_x = a$ the left hand side of equation (33) is equal to zero. For a physical solution at these points the right hand side must also be equal to zero. The locus of such points in the (B_y, B_z) plane is found by placing the left and right hand sides of (32) equal to zero and eliminating u_x to give the following sextic relationship in B_y and B_z

$$\begin{aligned}
&\gamma^3 B_y^6 + \gamma\left[2(\gamma+1)(2\gamma-1)B_x^2 + \gamma^2\left(3B_z^2 - 16\pi f_2\right)\right]B_y^4 + 8\pi\gamma(\gamma+1)(2\gamma-1)(B_x f_3 + f_1 f_5)B_y^3 \\
&+\left\{\gamma^3\left[B_z^2\left(3B_z^2 - 32\pi f_2\right) + 64\pi^2 f_2^2\right] + 4(\gamma+1)^2(\gamma-1)B_x^4 + 4(2\gamma-1)(\gamma+1)B_x^2\left(B_z^2 - 4\pi f_2\right)\right\}B_y^2 \\
&+8\pi(\gamma+1)(B_x f_3 + f_1 f_5)\left[4\left(\gamma^2-1\right)B_x^2 + \gamma(2\gamma-1)\left(B_z^2 - 8\pi f_2\right)\right]B_y \\
&+B_z^2\left[4(\gamma-1)(\gamma+1)^2 B_x^4 + \gamma^3\left(B_z^2 - 8\pi f_2\right)^2\right] + 2(\gamma+1)B_x^2\left[\gamma(2\gamma-1)B_z^2\left(B_z^2 - 8\pi f_2\right) + 32\pi^2\left(\gamma^2-1\right)f_3^2\right] \\
&+64\pi^2 f_1 f_5(\gamma-1)(\gamma+1)^2(2B_x f_3 + f_1 f_5) = 0. \qquad (114)
\end{aligned}$$

Equation (114) gives the points in the (B_y, B_z) plane where $\frac{du_x}{dx}$ is of the indeterminate form $\frac{0}{0}$, the physical value of the derivative being able to be calculated using l'Hopital's rule.

Points on the common boundary of the supersonic and subsonic sheets are given by

$$R = 0. \qquad (115)$$

The points on the boundary given by (115) at which (114) holds are denoted as transonic flow points, these being the only points on the boundary where the u_x derivatives have real values, allowing a possible smooth transition to the subsonic sheet through this point.

As an example to show the determination of the position of the transonic point for a given set of upstream parameters, Figure 24 shows the intersecting contours for the sextic (114) and the quartic (115) for upstream conditions that will be studied in §7.6. A root finding method is used to obtain the (B_y, B_z) values of these transonic transition points and these are shown as red circles on the phase plane. The phase plane (B_y, B_z) coordinates of the transonic transition point are shown at the bottom left of the diagram. Two phase planes are given to show that two sets of upstream parameters can produce the same downstream stationary points and transonic points, the upstream point swapping its position in the $B_y - B_z$ plane in each case. Each upstream point can send a different unique trajectory through the transonic point, these being members of the $1^+ \to 3^-$, $1^+ \to 4^-$ and $1^+ \to 2^+$ shock family and the $2^+ \to 3^-$ and $2^+ \to 4^-$ shock families respectively.

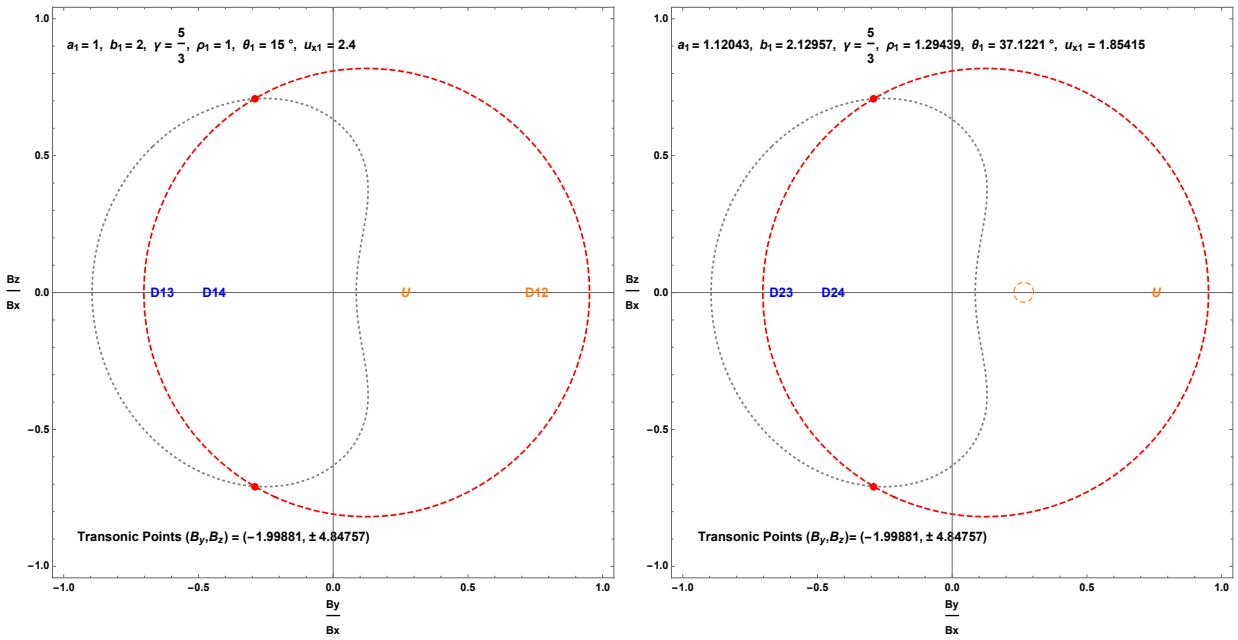

Figure 24: Transonic transition points are red points on the boundary of the supersonic and subsonic sheets (dashed red locus). These are determined numerically by finding the intersection of the sextic dotted curve and the quartic dashed curve, the quartic being the common boundary of the sheets. The value of $\frac{du_x}{dx}$ at each transonic point has two finite values allowing two trajectories to pass to the subsonic sheet. For a given value of γ, an identical phase plane and transonic points can be produced for two sets of upstream parameters, one set producing a $1^+ \to 3^-$& $1^+ \to 4^-$& $1^+ \to 2^+$ family and the other a $2^+ \to 3^-$ & $2^+ \to 4^-$ family. One of the transonic values of $\frac{du_x}{dx}$ belongs to each family. Speeds are in terms of the upstream speed of sound.

Transonic transition points only occur for upstream shock speeds between the red equisonic curves in Figure 3. Figure 25 shows the position of the transonic flow points, displayed as red circles, in the $B_y - B_z$ phase plane for the set of upstream parameters $\left\{1, 2, \frac{5}{3}, 1, 15°, u_{x1}\right\}$ for three values of u_{x1}, allowing the change in the positions of the transonic points with upstream shock speed to be seen. The green coloration represents areas in the phase plane where $\frac{du_x}{dx} < 0$, from (14) the green zone corresponds to $\frac{d\rho}{dx} > 0$ representing a compressive stage if the shock transition passes through these points. The red coloration represents $\frac{du_x}{dx} > 0$, corresponding to $\frac{d\rho}{dx} < 0$, corresponding to an expansive stage of the shock transition. The transonic points first form when the upstream shock speed equals the equisonic intermediate speed and they progress around the boundary disappearing when the upstream shock speed equals the downstream equisonic fast speed. Figure 25a shows an upstream shock speed slightly greater than the equisonic intermediate speed, Figure 25b has an upstream shock speed equal to the Jouget speed and Figure 25c represents an upstream shock speed slightly less than the equisonic fast speed. For these upstream parameters $\{v_{ef1}, v_{j1}, v_{ef1}\}$=$\{2.28129, 2.42108, 3.2375\}$.

Chapter 7 will present examples of intermediate $1^+ \to 3^-$ and intermediate $1^+ \to 4^-$ structure with $u_{x1} = 2.4$. These shock transitions pass through the red zone on the supersonic sheet after leaving the upstream point and so undergo an expansive stage, or may pass through the red zone on the subsonic sheet before reaching the downstream point in the case of a $1^+ \to 4^-$ shock.

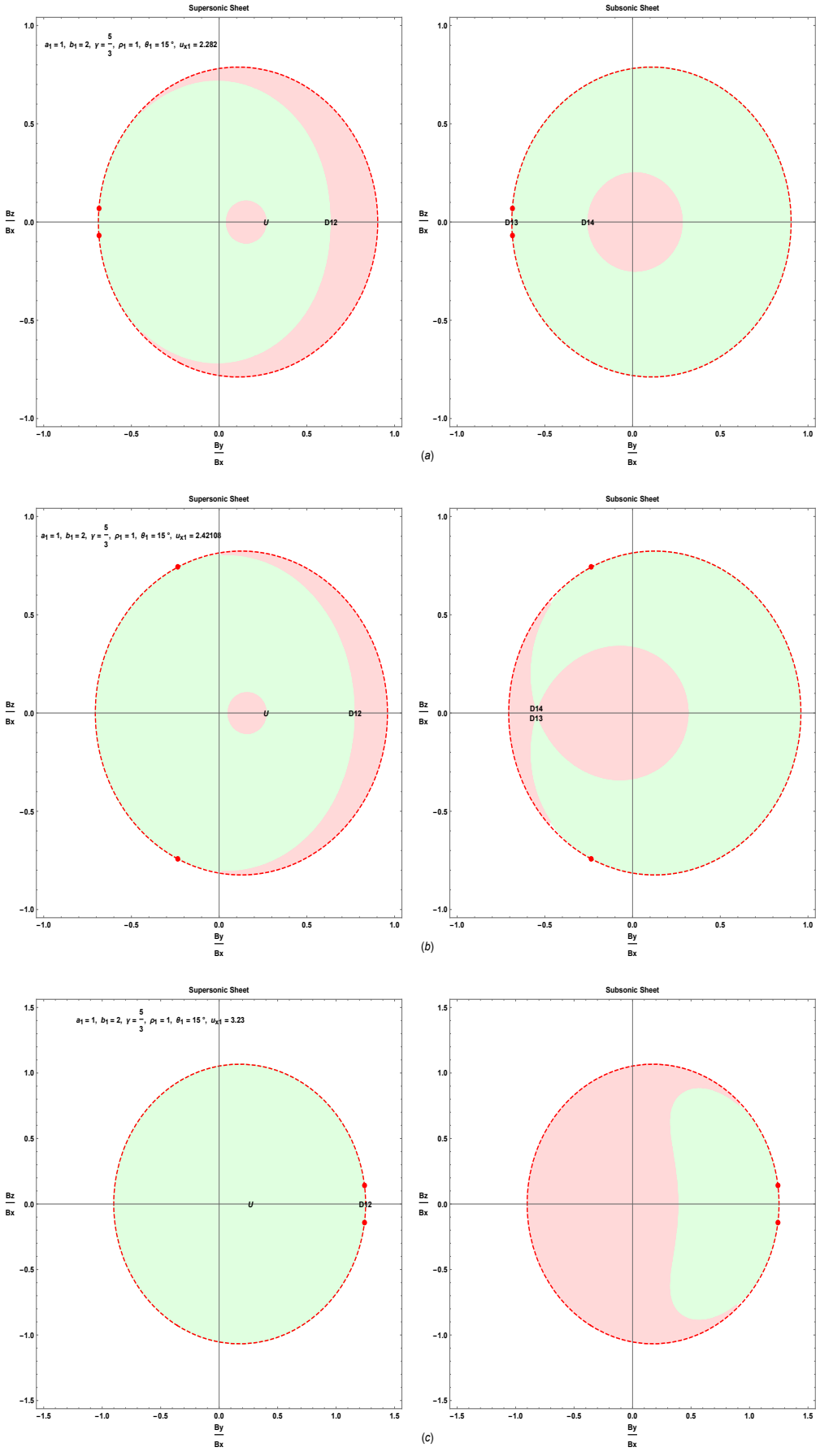

Figure 25: Progression of transonic points in the phase plane with increasing upstream shock speed. Speeds are in terms of the upstream speed of sound. Green represents areas where the passage is compressive, $\frac{d\rho}{dx_\eta} > 0$, red shows where the shock has an expansive stage, $\frac{d\rho}{dx_\eta} < 0$; $\frac{b_1}{a_1} = 2$, $\theta_1 = 15^\circ$

For future reference, the equation for the calculation of the first derivative of the normal shock velocity component at the transonic transition point will now be given. The first and higher derivatives at the transonic transition points are of significance as they allow the determination of the unique shock transition from the supersonic to the subsonic sheets that passes through the transonic point. Numerical values will also be given for the derivatives at the transonic points encountered in §7.2 and §7.6.

To obtain the first derivative of the normal shock velocity component at the transonic transition point l'Hopital's rule is applied to the indeterminate form of (32), using $x_\eta = \frac{x}{\eta}$, giving

$$32\pi^2(\gamma+1)f_1^2\frac{du_x}{dx_\eta} = \left[(2\gamma-1)B_x^2 - 8\pi\gamma f_1 u_x\right]B_y^2 + 4\pi\left[(2\gamma-1)(B_x f_3 + f_1 f_5) - \gamma f_1\frac{dB_y}{dx_\eta}\right]B_y + \left[(2\gamma-1)B_z B_x^2 - 4\pi\gamma f_1\left(2B_z u_x + \frac{dB_z}{dx_\eta}\right)\right]B_z + W, \tag{116}$$

where

$$\begin{aligned}
W^2 = {} & \left[(2\gamma-1)B_x^2 - 8\pi\gamma f_1 u_x\right]^2\left(B_y^4 + B_z^4\right) + 8\pi\left[(2\gamma-1)B_x^2 - 8\pi\gamma f_1 u_x\right]\left[(2\gamma-1)(B_x f_3 + f_1 f_5) - \gamma f_1\frac{dB_y}{dx_\eta}\right]B_y^3 \\
& + 2\left\{B_z\left[(1-2\gamma)B_x^2 + 8\pi\gamma f_1 u_x\right]\left\{\left[(1-2\gamma)B_x^2 + 8\pi\gamma f_1 u_x\right]B_z + 4\pi\gamma f_1\frac{dB_z}{dx_\eta}\right\} + 8\pi^2\left[(2\gamma-1)(B_x f_3 + f_1 f_5) - \gamma f_1\frac{dB_y}{dx_\eta}\right]\right\}B_y^2 \\
& + 8\pi\{f_1\left[-4(\gamma+1)\left(B_x^2 - 4\pi f_1 u_x\right)\left[(\gamma-1)B_x^2 - 4\pi\gamma f_1 u_x\right] + \gamma\left[(1-2\gamma)B_x^2 + 8\pi\gamma f_1 u_x\right]B_z^2 + 4\pi\gamma^2 f_1 B_z\frac{dB_z}{dx_\eta}\right]\frac{dB_y}{dx_\eta} \\
& + (2\gamma-1)(B_x f_3 + f_1 f_5)\left[(2\gamma-1)B_x^2 B_z - 4\pi\gamma f_1\left(2B_z u_x + \frac{dB_z}{dx_\eta}\right)\right]\}B_y \\
& + 8\pi f_1\left\{-4(\gamma+1)\left(B_x^2 - 4\pi f_1 u_x\right)\left[(\gamma-1)B_x^2 - 4\pi\gamma f_1 u_x\right] + \gamma\left[(1-2\gamma)B_x^2 + 8\pi\gamma f_1 u_x\right]B_z^2 + 2\pi\gamma^2 f_1 B_z\frac{dB_z}{dx_\eta}\right\}B_z\frac{dB_z}{dx_\eta} \\
& - 128\pi^2(\gamma+1)f_1(B_x f_3 + f_1 f_5)\left[(\gamma-1)B_x^2 + 2\pi(1-2\gamma)f_1 u_x\right]\frac{dB_y}{dx_\eta}.
\end{aligned} \tag{117}$$

Calculation of the second derivative of u_x at the transonic transition point is obtained differentiating (32) with respect to x_η and applying l'Hopital's rule twice to the indeterminate expression. A similar lengthy procedure is followed for the third derivative.

For the set of upstream parameters $\left\{1, 2, \frac{5}{3}, 1, 15^\circ, 2.4\right\}$ the following two sets of values are obtained for the first three derivatives of the normal shock velocity components at the transonic transition point, $\left\{\frac{du_x}{dx_\eta}, \frac{d^2u_x}{dx_\eta^2}, \frac{d^3u_x}{dx_\eta^3}\right\} = \{-0.3278143194, +0.2826047102, -0.1097200558\}$ and $\left\{\frac{du_x}{dx_\eta}, \frac{d^2u_x}{dx_\eta^2}, \frac{d^3u_x}{dx_\eta^3}\right\} = \{-0.1036405795, -0.01071224205, +0.3488002504\}$. The first set of derivatives will be used in §7.6.3 to show the presence of a continuous $1^+ \to 4^-$ shock structure from the upstream point U on the supersonic sheet through the transonic point to the downstream point D14 on the subsonic sheet. The second set of transonic derivatives is associated with a unique $2^+ \to 3^-$ shock structure in the same phase plane, the upstream point now being the D12 point.

For the set of upstream parameters $\left\{1, 2, \frac{5}{3}, 1, 37^\circ, 1.75\right\}$ the sets of values obtained for the first three derivatives of the normal shock velocity components at the transonic transition point are $\left\{\frac{du_x}{dx_\eta}, \frac{d^2u_x}{dx_\eta^2}, \frac{d^3u_x}{dx_\eta^3}\right\} = \{-0.2900380969, +0.2386489913, -0.09712559249\}$ and $\{-0.08781961392, +0.007298889456, +0.07497447836\}$. The first set is associated with a $1^+ \to 4^-$ shock in the phase plane, its origin being an unused sta-

tionary point in the phase plane, the second set being those of a $2^+ \rightarrow 3^-$ shock in this phase plane starting from U. The second set of derivatives will be used in §7.2.2 to show the presence of a continuous $2^+ \rightarrow 3^-$ shock structure from the upstream point U on the supersonic sheet through the transonic point to the downstream point D24 on the subsonic sheet.

The first derivatives are given to high precision as these are used to calculate in succession the second and then the third derivatives to determine the unique trajectories that pass through the transonic point in §7.2.2 and §7.6.2.

4.4 Stationary Points as Determiners of Shock Families

This section presents plots showing vectors giving the direction of $\frac{dB_z}{dB_y}$ for increasing values of x at points in the $B_y - B_z$ phase plane. These plots map out the supersonic and subsonic sheets allowing integration strategies to be determined in the vicinity of stationary points in the planes. The B_y values of stationary points are found by placing $\frac{dB_y}{dx} = 0$ and $B_z = 0$ in (27)

$$B_x^2 B_y^4 + 4\pi\left(2-\gamma\right)\left(B_x f_3 + f_1 f_5\right) B_y^3 + \left[\left(\gamma+1\right) B_x^4 - 8\pi\gamma f_2 B_x^2 - 16\pi^2\left(\gamma-1\right)\left(f_3^2 - 2 f_1 f_7\right)\right] B_y^2$$
$$+8\pi(B_x f_3 + f_1 f_5)\left[\left(\gamma+1\right) B_x^2 - 4\pi\gamma f_2\right] B_y + 16\pi^2\left(\gamma+1\right)\left(B_x f_3 + f_1 f_5\right)^2 = 0. \tag{118}$$

Expressing the constants in (118) in terms of the upstream density, pressure, shock speed and transverse magnetic field component using (14) to (20) allows the upstream transverse magnetic field component B_{y1} to be factored out of (118)

$$\left(B_y - B_{y1}\right)\{B_x B_y^3 + B_{y1}\left[\left(\gamma-1\right) B_x^2 - 4\pi\rho_1\left(\gamma-2\right) u_{x1}^2\right] B_y^2 + (B_x^2 - 4\pi\rho_1 u_{x1}^2)\{\left(\gamma+1\right) B_x^2 - \gamma B_{y1}^2$$
$$-4\pi\left[2\gamma p_1 + \rho_1\left(\gamma-1\right) u_{x1}^2\right]\} B_y - \left(\gamma+1\right)\left(B_x^2 - 4\pi\rho_1 u_{x1}^2\right)^2 B_{y1}\} = 0. \tag{119}$$

Due to the quartic nature of (119) with real coefficients, as the upstream value of B_y is one solution there can be either one other real solution or three other real solutions. The presence of stationary points in the phase plane does not guarantee that a MHD shock transition can occur from the given upstream state to a particular stationary point. The direction of the vector fields in the vicinity of the stationary point determine whether a numerical integration from the upstream point with a small step-off can reach the stationary point, or in some situations for computational ease, an integration out of the stationary point with a small step-off can proceed in the phase plane to the upstream state. Aside from being a numerical integration indicator, as the positive direction of x in this Thesis is defined to be from the upstream to the downstream state, the arrows in the vector fields point in the direction of entropy increase due to the irreversible nature of a shock.

To gain insight into how the stationary points are determined and the possible shock transitions between them, it is useful to express (119) in terms of $a_1, B_{y1}, \gamma, \rho_1, \theta_1$ and u_{x1} as given by (84)-(86),

$$\left(B_y - B_{y1}\right)\{B_{y1}^2 \cot^2\theta_1 B_y^3 + \left[4\pi\rho_1\left(2-\gamma\right) B_{y1} u_{x1}^2 + \left(\gamma-1\right) B_{y1}^3 \cot^2\theta_1\right] B_y^2 +$$
$$+\left(4\pi\rho_1 u_{x1}^2 - B_{y1}^2\cot^2\theta_1\right)\left\{\gamma B_{y1}^2 + 4\pi\rho_1\left[\left(\gamma-1\right) u_{x1}^2 + 2a_1^2\right] - \left(\gamma+1\right) B_{y1}^2\cot^2\theta_1\right\} B_y$$
$$-\left(\gamma+1\right) B_{y1}\left(4\pi\rho_1 u_{x1}^2 - B_{y1}^2\cot^2\theta_1\right)^2\} = 0. \tag{120}$$

For (120) to have four real solutions for B_y, giving four stationary points in the $B_y - B_z$ plane, the discriminant must be greater than zero. For two real solutions and two stationary points the discriminant is less than zero. The discriminant of (120) is a quartic in u_{x1}^2. The inequality to determine the domain of upstream speeds for each number of stationary points is solved numerically using a root finding method.

Figure 26 shows the solutions to (120) for the upstream values values $a_1 = 1$, $b_1 = 2$, $\gamma = \frac{5}{3}$, $\rho_1 = 1$ for six representative upstream shock angles. Supersonic values are shown in orange, subsonic in blue. The horizontal line in each case represents the upstream transverse magnetic field component B_{y1}. The number of stationary points in the $B_y - B_z$ phase plane at each upstream speed is the number of vertical intercepts. When the upstream speed equals the upstream slow or fast speed a double root occurs, these two stationary points coincident on the B_y axis. When the upstream speed equals the upstream intermediate speed, four real solutions occur, two belonging to a double root. At the upstream Jouget speed the graph has a vertical tangent with four real solutions for B_y, a double root occurring at the point of tangency. At the point of vertical tangency at the lower speed four real solutions for B_y also occur, two being a double root.

A linear analysis about the upstream stationary point shows that B_y and B_z have the following dependence on the upstream sound, slow, intermediate and fast speeds. This was given by Coroniti [39].

$$\frac{d\delta B_y}{dx_\eta} = \frac{\left(u_{x1}^2 - v_{f1}^2\right)\left(u_{x1}^2 - v_{s1}^2\right)}{u_{x1}\left(u_{x1}^2 - a_1^2\right)}\delta B_y, \tag{121}$$

$$\frac{d\delta B_z}{dx_\eta} = \frac{\left(u_{x1}^2 - v_{i1}^2\right)}{u_{x1}}\delta B_z. \tag{122}$$

Equations (121) and (122) predict the nature of the upstream, or downstream stationary point using appropriate downstream values, with the signs of the coefficients of δB_y and δB_z indicating whether B_y and B_z are increasing (+) with phase plane vectors outwards, or decreasing (−) having inwards pointing phase plane vectors, for increasing x_η. In Figures 7-13 the signs in the square brackets in the shock labels designate the nature of the shock transition for the particular upstream and downstream states. The first sign in brackets is that of the B_y eigenvalue and the second that of the B_z eigenvalue.

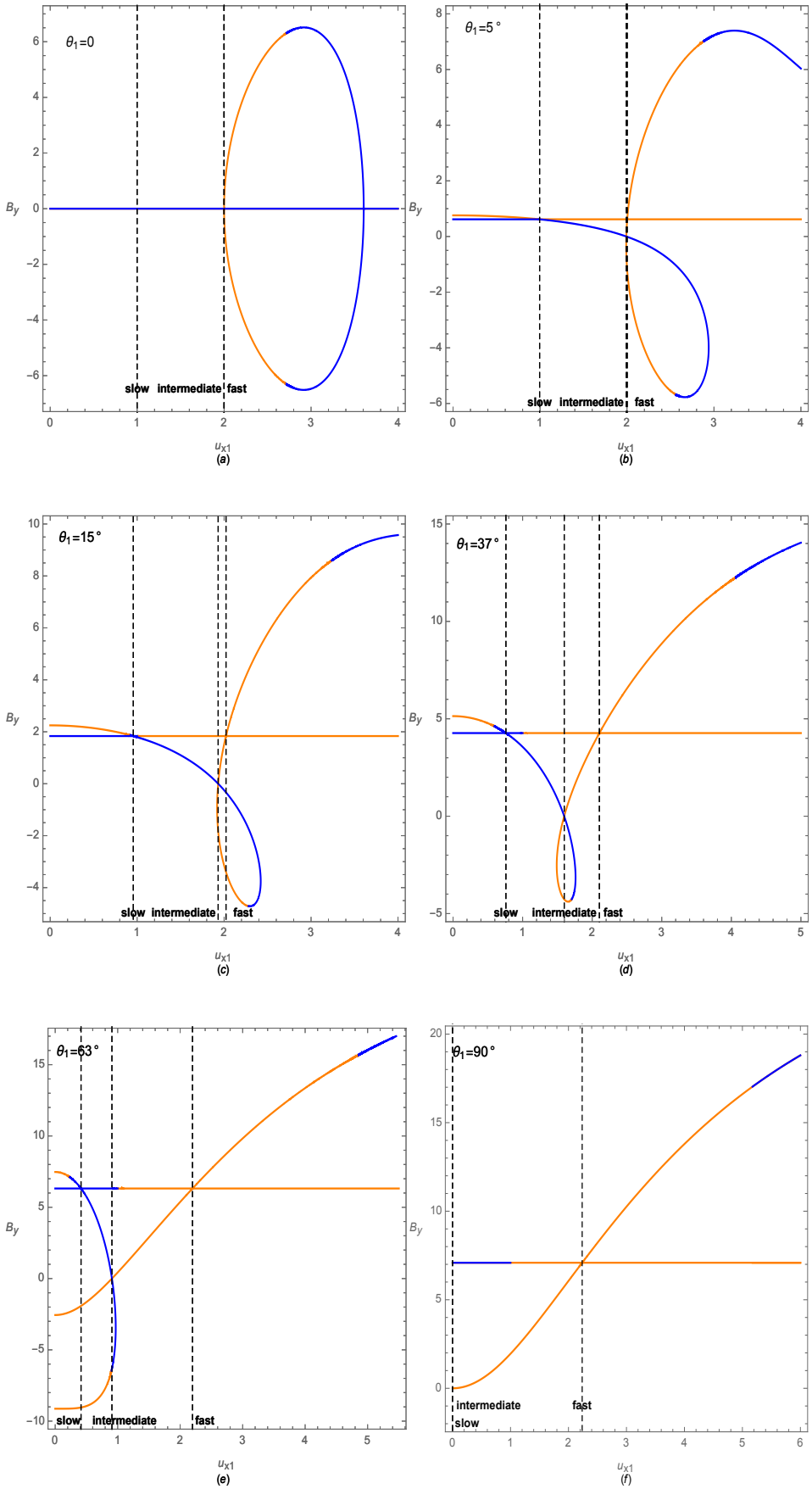

Figure 26:

B_y values of stationary points for each shock angle are the vertical intercepts at a given upstream speed, supersonic in orange, subsonic in blue. Horizontal line gives the upstream value of B_y. Speeds are in terms of the upstream sound speed; $\frac{b_1}{a_1} = 2$

5 Fast Shocks

In this chapter the structure of "stand alone" fast MHD shocks will be presented. These are fast shocks produced by upstream speeds greater than the Jouget speed, the latter being the maximum speed at which two downstream states can occur. In this case the MHD $B_y - B_z$ phase plane has only two stationary points, either two on the supersonic sheet or one each on the supersonic and subsonic sheet. The structure is determined by numerical integration of the first order ODEs given in Chapter 2, which will be simplified for the case of a fast shock since $B_z = 0$ throughout the shock. As in other chapters investigating shock structure, the numerical method used is the eighth order Runge-Kutta method of Dormand and Prince. As the upstream state is always supersonic the downstream state may be supersonic or subsonic, so there are $1^+ \to 2^+$ and $1^+ \to 2^-$ transitions. The distinction between supersonic and subsonic transitions is determined by the presence of the equisonic point in the flow regime where the downstream normal flow speed is equal to the downstream speed of sound. The location of this point where the downstream normal flow and sound speed curves cross, as shown in Figure 10 , is found by placing $a_2 = u_{x2}$ in (52) and solving the resultant quintic equation in u_{x2}. The corresponding upstream speed u_{x1} is then found by solving (46). For designatory purposes, as in earlier chapters, the supersonic state will be designated by the + superscript and the subsonic state by the - superscript.

5.1 Fast $1^+ \to 2^+$ Shocks

This section presents the structure of fast supersonic to supersonic shocks in the speed domain where intermediate shocks are not formed, the $B_y - B_z$ phase plane having only two stationary points. This will be done in two parts, presenting the structure of oblique and perpendicular fast shocks.

The oblique shock example presented here shows structures produced in the upstream speed domain of $v_{j1} < u_{x1} < v_{ef1}$. For the upstream conditions $a_1 = 1$, $b_1 = 2$, $\gamma = \frac{5}{3}$, $\rho_1 = 1$ and $\theta_1 = 15°$, as shown on Figure 10, the Jouget speed is given by $v_{j1} = 2.42108$, producing a downstream normal shock speed of 1.11101 and downstream sound speed of 1.5998. The fast domain equisonic speed for these upstream conditions is $v_{ef1} = 3.2375$ producing a downstream normal flow speed of 1.59793.

The perpendicular shock example is for the upstream conditions $a_1 = 1$, $b_1 = 2$, $\gamma = \frac{5}{3}$, $\rho_1 = 1$ and $\theta_1 = 90°$, the upstream-downstream speed relationship being shown on Figure 13. Fast supersonic to supersonic shocks are produced in the speed domain between $v_{f1} = 2.23607$ and the equisonic fast speed $v_{ef1} = 5.17456$. The downstream speed at the equisonic speed is 2.15385.

5.1.1 Oblique Shock Phase Space and Shock Structure

In this subsection vector fields and shock structures will be presented for the case when only fast shocks can form in the $B_y - B_z$ plane. This occurs when the upstream shock speed is greater than the Jouget and upstream fast speeds, the phase plane only having two stationary points between which a transition can be made.

For the set of upstream parameters $\{1, 2, \frac{5}{3}, 1, 15°, 2.7\}$, Figure 27 shows the vector fields with two supersonic stationary points, the upstream speed being less than the fast equisonic speed, $u_{x1} < 3.2375$. A trajectory in the phase plane can link with the downstream stationary point through a passage along the B_y axis, the transition having zero B_z component with $|B_{y2}| > |B_{y1}|$ and $B_{y2}B_{y1} > 0$. From Figure

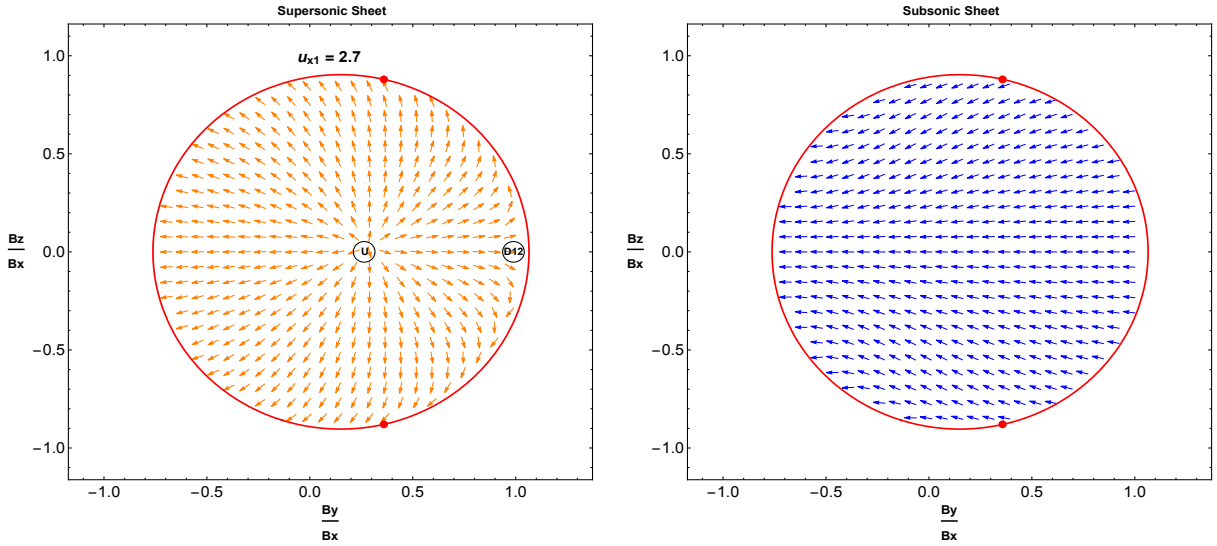

Figure 27: Phase plane vector fields having two stationary points on the supersonic sheet allowing a unique trajectory between them, a $1^+ \rightarrow 2^+$ shock; $\frac{b_1}{a_1} = 2$, $\theta_1 = 15°$, $\frac{u_{x1}}{a_1} = 2.7$

5(c) $v_{i2} < u_{x2} < v_{f2}$, the transition is designated as a supersonic to supersonic $1 \rightarrow 2$ shock fast shock, or more compactly as a $1^+ \rightarrow 2^+$ shock.

The structure of a fast oblique shock is the variation in its flow variables B_y, u_x, p and Δs between its upstream and downstream states. The variation in the upstream transverse magnetic field component B_y is obtained by numerically integrating an autonomous first order ODE (27) for $\frac{dB_y}{dx_\eta}$. The phase plane diagram in Figure 27 shows that a linkage between the upstream stationary point U and the downstream stationary point D12 is only possible via a passage in the direction of the vectors along the B_y axis. Numerically the linking trajectory is found by carrying out an integration along the B_y axis from a point close to the upstream source point to a point close to the downstream saddle, the arrows giving the direction of variation in B_y and B_z for increasing values of x.

The B_z magnetic field component and the u_z velocity component are both set equal to zero through the shock transition allowing equations (15) to (20) to be written for the case of oblique fast shocks as

$$\frac{B_y^2}{8\pi} + p + f_1 u_x = f_2, \tag{123}$$

$$-\frac{B_x B_y}{4\pi} + f_1 u_y = f_3, \tag{124}$$

$$B_y u_x - B_x u_y - \eta \frac{dB_y}{dx} = f_5, \tag{125}$$

$$\frac{1}{2} f_1 \left(u_x^2 + u_y^2\right) + \frac{\gamma}{\gamma - 1} p u_x + \frac{1}{4\pi} u_x B_y^2 - \frac{1}{4\pi} B_x B_y u_y - \frac{\eta}{4\pi} B_y \frac{dB_y}{dx} = f_7. \tag{126}$$

Eliminating p, u_y and u_x from (123) to (126) using x_η defined by $x_\eta = \frac{x}{\eta}$ and taking the positive branch of the square root as the integration is only carried out on the supersonic sheet gives

$$\frac{dB_y}{dx_\eta} = \frac{1}{8\pi\left(\gamma+1\right)f_1}\{-8\pi\left(\gamma+1\right)\left(B_x f_3 + f_1 f_5\right) - \gamma B_y^3 + B_y[8\pi\gamma f_2 - 2\left(\gamma+1\right)B_x^2]$$

$$+B_y\sqrt{64\pi^2\left[\gamma^2 f_2^2 + \left(\gamma^2-1\right)\left(f_3^2 - 2f_1 f_7\right)\right] + 32\pi\left(\gamma^2-1\right)\left(B_x f_3 + f_1 f_5\right)B_y + 4[-4\pi\gamma^2 f_2 + \left(\gamma^2-1\right)B_x^2]B_y^2 + \gamma^2 B_y^4}\ \}. \tag{127}$$

The constants f_1, f_2, f_3, f_5 and f_7 are determined for the numerical integration from (95)-(99) using the given upstream conditions.

Equation (127) was integrated numerically from the upstream point with speed of $u_{x1} = 2.7$ for the upstream conditions $a_1 = 1$, $b_1 = 2$, $\gamma = \frac{5}{3}$, $\rho_1 = 1$ and $\theta_1 = 15^\circ$ using a step-off in B_y of $+0.001$. The mass density ratio across the shock determined using the jump conditions is 1.553. The normal flow speed was found using (124) and (125) which was then used to calculate the gas pressure using (123). The results of the integration, presented in four plots showing $B_y - u_x$, $u_x - x_\eta$, $\frac{\Delta s}{c_v} - p/\frac{B_y^2}{8\pi}$ and $\frac{\Delta s}{c_v} - x$ are shown in Figure 28.

The transverse upstream magnetic field component undergoes a monotonic increase through the shock and the normal velocity flow component decreases monotonically through the shock. The magnetic pressure at all points through the shock is greater than the gas pressure. The change in specific entropy shows a monotonic increase through the shock. The dominance of the magnetic pressure over the gas pressure that occurs in this type of shock is not entirely due to the supersonic nature of the flow. In §5.2 on oblique supersonic to subsonic fast shocks, it will be indicated that the downstream magnetic pressure is greater than the gas pressure for a range of speeds from the equisonic point.

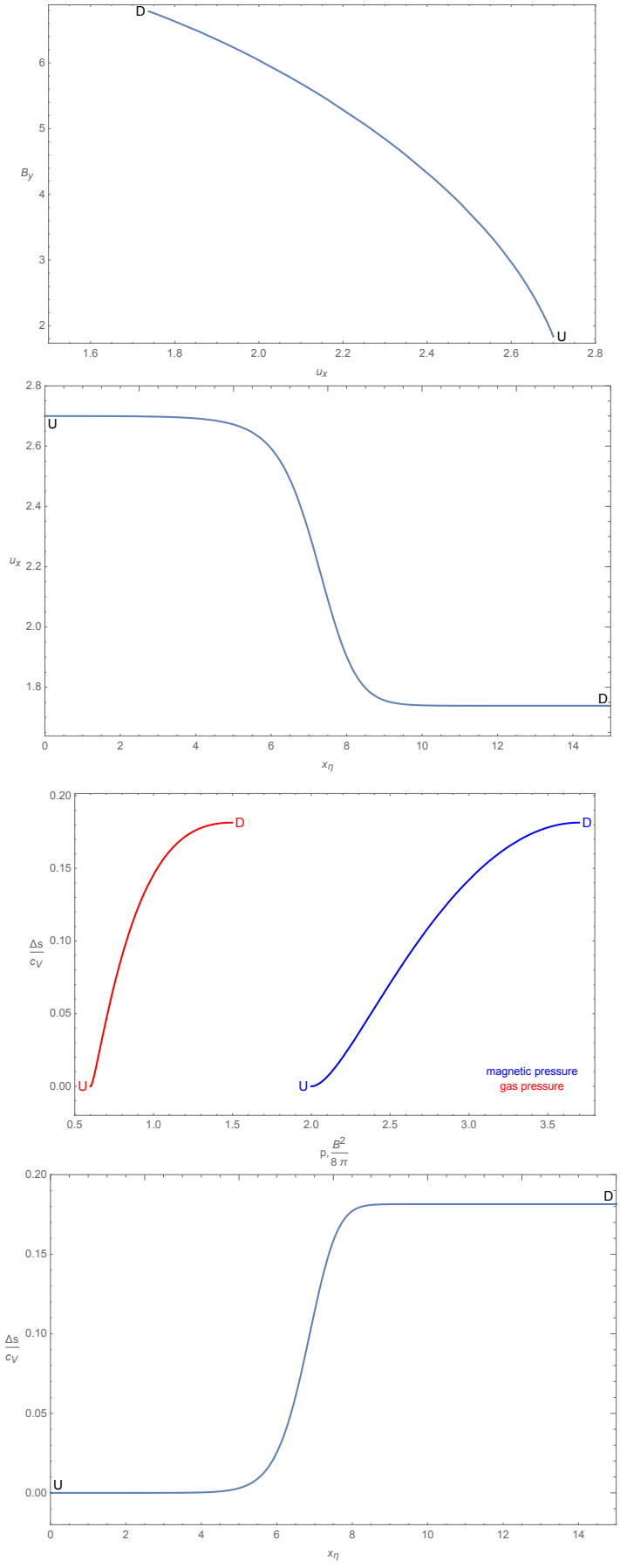

Figure 28: Variation in B_y, u_x, p and Δs through an oblique $1^+ \to 2^+$ shock. In this and all following fast shock plots $x_\eta = \frac{x}{\eta}$, $\rho_1 = 1$ and speeds are in terms of the upstream sound speed. In this plot $\frac{b_1}{a_1} = 2$, $\theta_1 = 15°$, $\frac{u_{x1}}{a_1} = 2.7$

5.1.2 Perpendicular Shock Phase Space and Shock Structure

For the upstream parameter set $\{1, 2, \frac{5}{3}, 1, 90°, u_{x1}\}$ Figure 26(f) shows that there are two stationary points in the $B_y - B_z$ phase plane for all upstream speeds. The downstream shock and sound speeds for this parameter set are shown in Figure 13.

Despite the existence of stationary points for all choices of u_{x1}, shock transitions are possible only when $u_{x1} > v_{f1}$. For $u_{x1} < a_1$ the upstream stationary point is a source on the subsonic sheet and the downstream point is a source on the supersonic sheet. From entropy and phase trajectory considerations a gas dynamic jump and passage to the stationary point is not possible. For $a_1 < u_{x1} < v_{f1}$ both stationary points are on the supersonic sheet, the upstream point being a saddle with a negative B_y eigenvalue and positive B_z eigenvalue, the downstream point being a source. Phase trajectories from the upstream point are unable to link along the B_y axis with the downstream point so a shock transition between the two stationary points is not possible. Figure 29 shows the phase plane vectors before a shock can form.

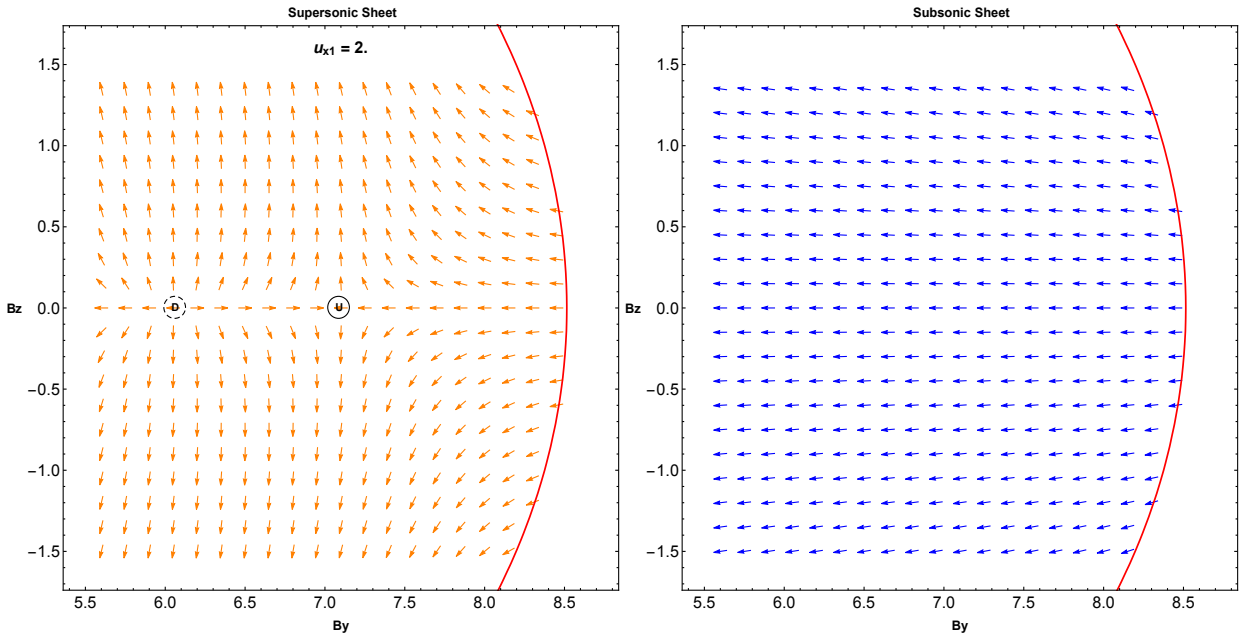

Figure 29: Phase plane vector fields with two stationary points before supersonic to supersonic perpendicular shock formation, trajectories from U being unable to reach D, $1 < \frac{u_{x1}}{a_1} < \frac{v_{f1}}{a_1}$; $\frac{b_1}{a_1} = 2$, $\theta_1 = 90°$, $\frac{u_{x1}}{a_1} = 2$

As the upstream shock speed increases the stationary points merge at the fast speed and swap roles, the upstream point becoming a source in structure and the downstream point a saddle. Figure 30 shows the phase plane structure for the case when $u_{x1} < v_{ef1}$, the equisonic speed in this case being 5.17456. Phase plane trajectories from U are able to link with the downstream stationary point by a passage along the B_y axis, the transition being a fast shock as $\frac{B_{y2}}{B_{y1}} > 1$. The upstream shock speed in this case produces a downstream to upstream mass density ratio of 2.

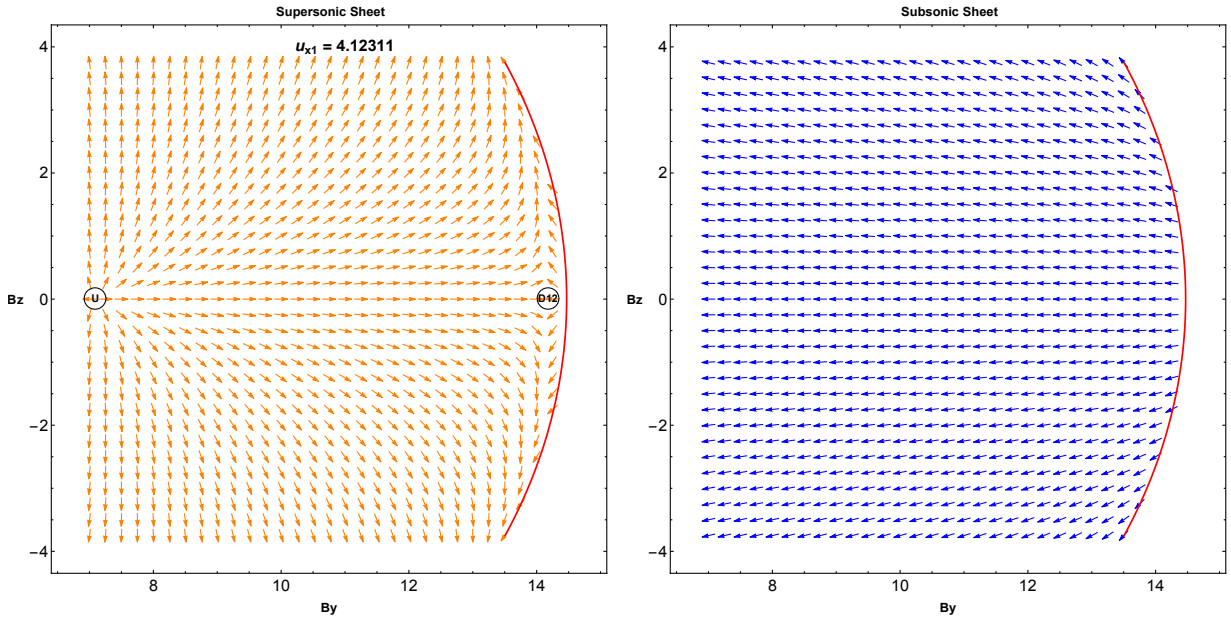

Figure 30: As for Fig 29, but $v_{f1} < u_{x1} < v_{ef1}$, a unique $1^+ \rightarrow 2^+$ shock links the upstream and downstream states ; $\frac{b_1}{a_1} = 2$, $\theta_1 = 90°$, $\frac{u_{x1}}{a_1} = 4.123111$

The structure of a perpendicular fast shock is found by formulating the steady state resistive MHD equations for the special case of $\theta_1 = 90°$ and numerically integrating the governing ODE. As the phase plane diagram in Figure 30 only allows a transition from the upstream source to the downstream saddle point by an integration along the B_y axis the structure equations for a perpendicular shock are found by placing $B_x = 0$ and $B_z = 0$ in (15) to (20)

$$\frac{B_y^2}{8\pi} + p + f_1 u_x = f_2, \tag{128}$$

$$B_y u_x - \eta \frac{dB_y}{dx} = f_5, \tag{129}$$

$$\frac{1}{2} f_1 u_x^2 + \frac{\gamma}{\gamma - 1} p u_x + \frac{1}{4\pi} u_x B_y^2 - \frac{\eta}{4\pi} B_y \frac{dB_y}{dx} = f_7. \tag{130}$$

Eliminating p and u_x from (128) to (130) and using $x_\eta = \frac{x}{\eta}$ gives for the case of supersonic flow

$$8\pi\left(\gamma+1\right)f_1\frac{dB_y}{dx_\eta} = -8\pi\left(\gamma+1\right)f_1 f_5 - \gamma B_y^3$$
$$+\ B_y\left\{8\pi\gamma f_2 + \sqrt{64\pi^2\left[\gamma^2 f_2^2 - 2\left(\gamma^2-1\right)f_1 f_7\right] + B_y\left[32\pi\left(\gamma^2-1\right)f_1 f_5 - 16\pi\gamma^2 f_2 B_y + \gamma^2 B_y^3\right]}\right\}. \tag{131}$$

Equation (131) was integrated numerically from the upstream point to the downstream point for the upstream speed of $u_{x1} = 4.12311$ for the upstream conditions $a_1 = 1, b_1 = 2, \gamma = \frac{5}{3}$ and $\rho_1 = 1$. The results of the integration, started using a step-off in B_y of $+0.001$ from the upstream stationary point are shown in Figure 31.

Figure 31 shows the transverse magnetic field component, the rate of change of mass density, the gas and magnetic pressure and the increase in specific entropy through the shock. All flow variables vary smoothly from the upstream to the downstream point as the entire transition occurs on the supersonic sheet. As the shock is classified as fast, $B_{y2} > B_{y1}$ with no change in sign. The mass density increases through the shock and the magnetic pressure is greater than the gas pressure at all stages. The transition is physically possible as the change in specific entropy between downstream and upstream is positive, its gradient being positive through the transition.

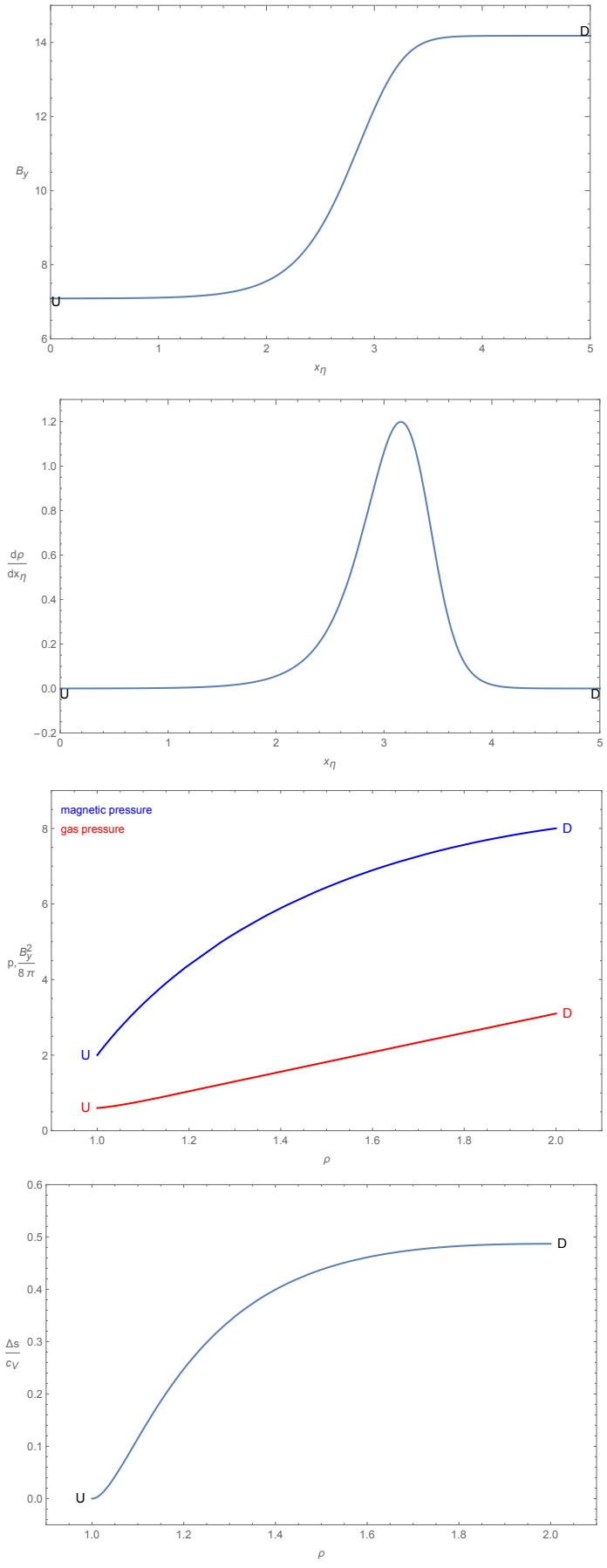

Figure 31: Variation in B_y, $\frac{d\rho}{dx_\eta}$, p, ρ and Δs through a perpendicular $1^+ \rightarrow 2^+$ shock; $\frac{b_1}{a_1} = 2$, $\theta_1 = 90°$, $\frac{u_{x1}}{a_1} = 4.12311$

5.2 Fast $1^+ \rightarrow 2^-$ Shocks

In this section the structure of fast supersonic to subsonic shocks, formed with only two stationary points in the $B_y - B_z$ phase plane, will be presented. It will be shown that the only path for the transition between the upstream and downstream source points is by passage along the B_y axis on the supersonic sheet followed by an isomagnetic jump to the downstream point on the subsonic sheet. The jump has an associated increase in specific entropy. As in the previous section, the presentation will be in two parts considering the oblique and perpendicular cases.

For the the upstream conditions $a_1 = 1$, $b_1 = 2$, $\gamma = \frac{5}{3}$, $\rho_1 = 1$ and $\theta_1 = 15^\circ$, as shown in Figure 10, the speed domain for $1^+ \rightarrow 2^-$ shocks is $u_{x1} > 3.2375$. For the upstream conditions $a_1 = 1$, $b_1 = 2$, $\gamma = \frac{5}{3}$, $\rho_1 = 1$ and $\theta_1 = 90^\circ$, as shown in Figure 13, the speed domain for a $1^+ \rightarrow 2^-$ shock is $u_{x1} > 5.17456$.

The shock structures that follow are typical, with one exception, for those in the speed domain $u_{x1} > v_{ef1}$. The exception is that the downstream gas pressure is greater than the downstream magnetic pressure for $u_{x1} > 3.72187$ in the case of the oblique shock and $u_{x1} > 6.76915$ for the perpendicular shock in the cases studied here.

5.2.1 Oblique Shock Phase Space and Shock Structure

When the upstream shock speed equals the equisonic speed the previous downstream saddle becomes a source on the subsonic sheet and the possible transonic transition point, denoted by the red disc in Figure 27, disappears at the B_y axis. Figure 32 shows the phase plane vector fields with a stationary point on each of the supersonic and subsonic surfaces, the upstream shock speed being greater than the fast equisonic speed. Trajectories from the upstream state can only reach the downstream source by a phase plane passage along the B_y axis followed by a gas dynamic jump to the downstream point on the subsonic sheet.

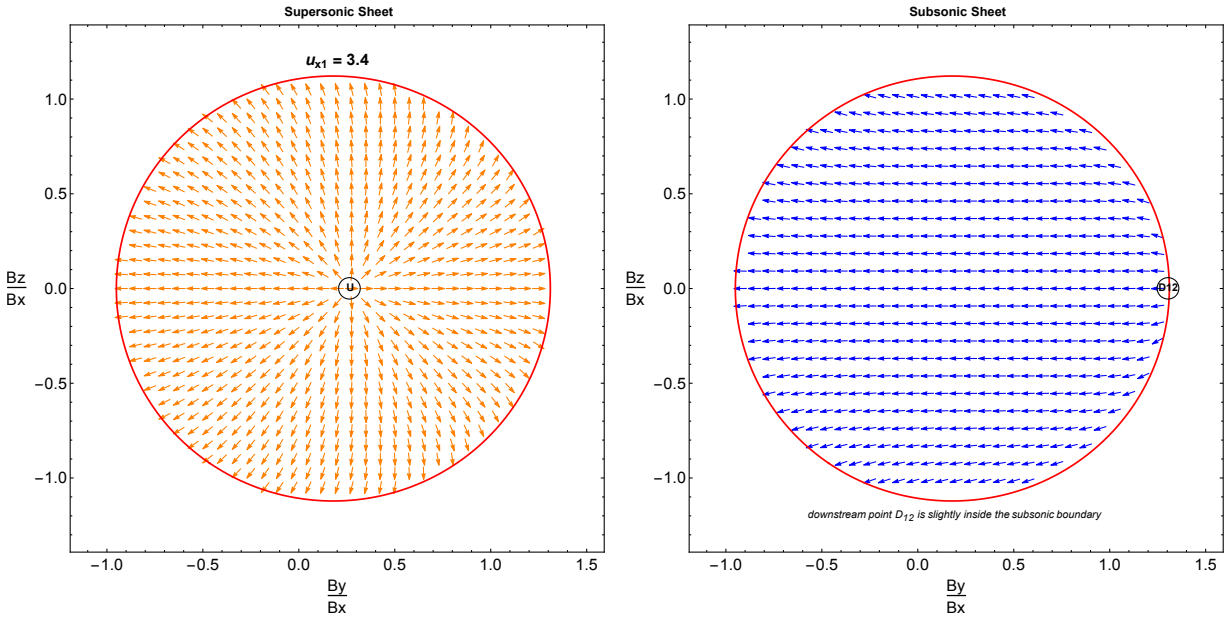

Figure 32: As for Fig 27, now with one stationary point on each sheet allowing a unique $1^+ \to 2^-$ shock having a gas dynamic jump to the downstream point, a $1^+ \to 2^-$ shock; $\frac{b_1}{a_1} = 2$, $\theta_1 = 15°$, $\frac{u_{x1}}{a_1} = 3.4$

The internal structure of the oblique fast supersonic to subsonic shock is determined using (128) to (130) after numerically integrating (131) along the B_y axis on the supersonic sheet with an isomagnetic jump to the subsonic sheet at the downstream point. The upstream shock speed is $u_{x1} = 3.4$ with the conditions $a_1 = 1$, $b_1 = 2$, $\gamma = \frac{5}{3}$, $\rho_1 = 1$ and $\theta_1 = 15°$. The numerical solution of (127) to determine the variation in B_y through the shock was started using a step-off of $+0.001$ in B_y and was terminated when $|B_y - B_{y2}| < 10^{-6}$. A gas dynamic jump occurred at the end of the integration to the downstream state to produce the structures shown in Figure 33. The increase in the value of $\frac{\Delta s}{c_v}$ between the pre-jump value and the downstream value is $+0.000497263$. For greater upstream speeds the difference in $\frac{\Delta s}{c_v}$ across the jump is greater, for example if $u_{x1} = 3.8$, the difference is $+0.0173081$. This is to be expected as in the limit at $u_{x1} = v_{ef1}$ the jump is at the common boundary is absent giving $\Delta s = 0$.

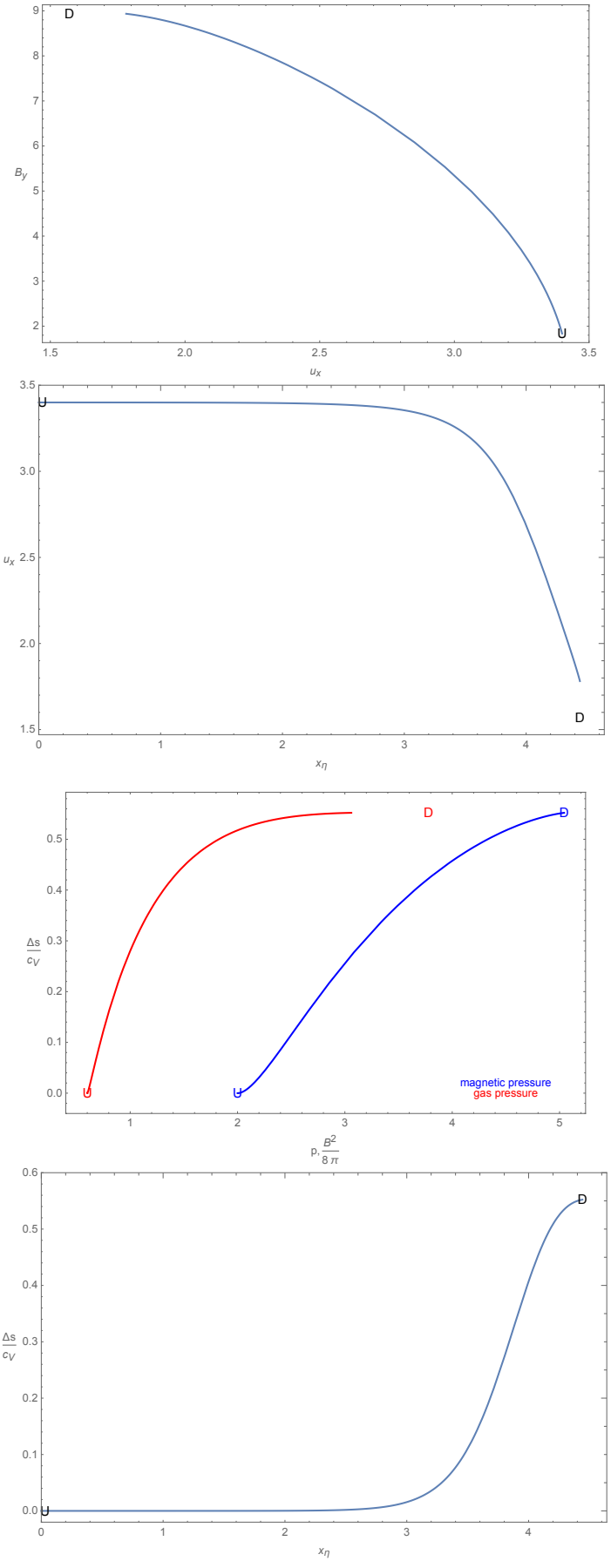

Figure 33: Variation in B_y, u_x, p and Δs through an oblique $1^+ \rightarrow 2^-$ shock. Gap between profile and D is due to a gas dynamic jump. In this and all following plots speeds are relative to the upstream sound speed; $\frac{b_1}{a_1} = 2$, $\theta_1 = 15°$, $\frac{u_{x1}}{a_1} = 3.4$

5.2.2 Perpendicular Shock Phase Space and Shock Structure

Figure 34 shows the phase plane for a supersonic to subsonic perpendicular shock transition with $u_{x1} > v_{ef1}$. The downstream stationary point is a source on the subsonic sheet, its B_y eigenvalue having reversed direction when it joined the subsonic sheet according to equation (121). Phase plane trajectories from the upstream point can only reach the downstream point after passage along the B_y axis on the supersonic sheet followed by a gas dynamic jump to the downstream point on the subsonic sheet. The upstream shock speed was chosen to produce a downstream to upstream mass density ratio of 3.

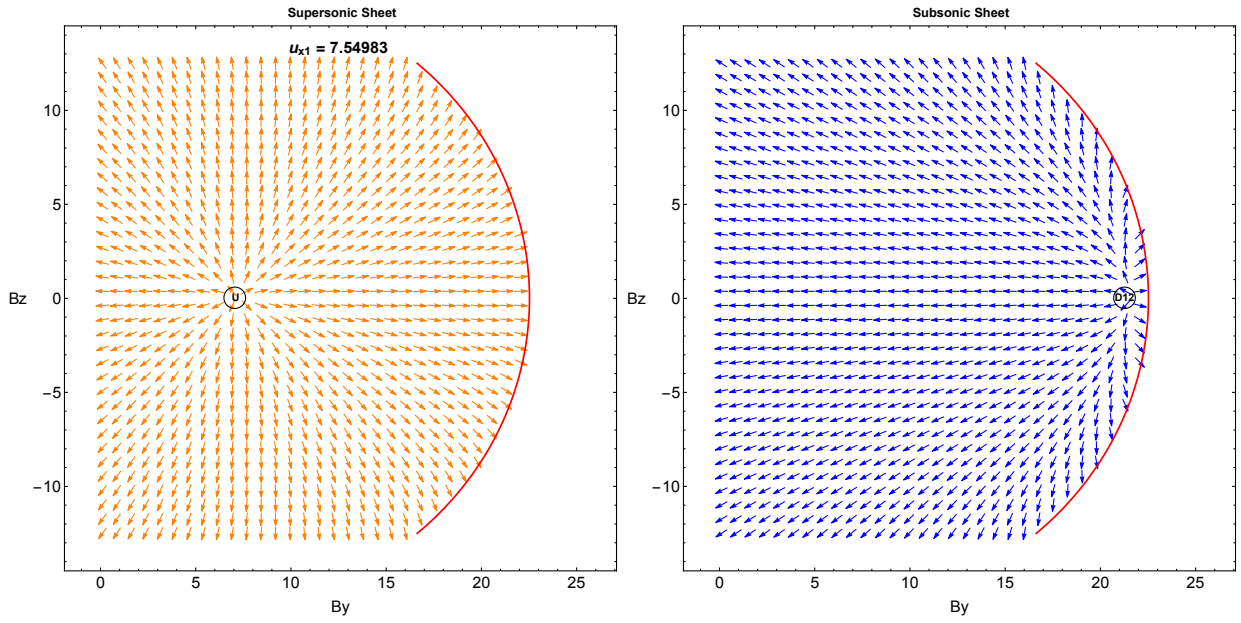

Figure 34: As for Fig 30, but with $u_{x1} > v_{ef1}$, a perpendicular $1^+ \rightarrow 2^-$ shock having a gas dynamic jump to the downstream point on the subsonic sheet; $\theta_1 = 90°, \frac{u_{x1}}{a_1} = 7.54983$

The variation of B_y through the shock from the upstream to the downstream state for the perpendicular supersonic to subsonic shock is determined by the numerical integration of (131) along the B_y axis in Figure 34 from the upstream source to $B_y = B_{y2}$ where an isomagnetic gas dynamic jump occurs to the downstream source on the subsonic sheet. The upstream shock speed is 7.54983 with upstream conditions $a_1 = 1$, $b_1 = 2$, $\gamma = \frac{5}{3}$, $\rho_1 = 1$ and $\theta_1 = 90°$. The step-off value in B_y to start the integration is +0.001 and the integration is carried out over a scaled length distance of 1.4506 before reaching the downstream point, the integration being terminated when $|B_y - B_{y2}| < 10^{-6}$. The structures produced by the integration with velocity and pressure determined using equations (129) and (128) respectively are shown in Figure 35. The change in $\frac{\Delta s}{c_v}$ across the gas dynamic jump to the subsonic sheet is +0.0460743. When upstream speeds closer to the equisonic speed are considered on Figure 13, the change in $\frac{\Delta s}{c_v}$ is smaller. If $u_{x1} = 6$ the change in $\frac{\Delta s}{c_v}$ is +0.00307424.

Summary

Fast shocks occur when the shock speed is greater than the fast MHD wave speed. Fast shocks have $|B_{y2}| > |B_{y1}|$ with $B_{y2} \times B_{y1} > 0$. The group of fast shocks considered in this chapter have two stationary points in the phase plane, this occurring when the shock speed is greater than the Jouget

speed. Fast shocks are of two types $1^+ \to 2^+$ and $1^+ \to 2^-$. Each of these has a unique structure, the $1^+ \to 2^+$ being smooth supersonic flow and the $1^+ \to 2^-$ being supersonic ending with an entropy increasing gas dynamic jump to the downstream subsonic state.

The next chapter considers the situation when two or four stationary points may be present in the phase plane, the transitions between two of the stationary points being a slow shock.

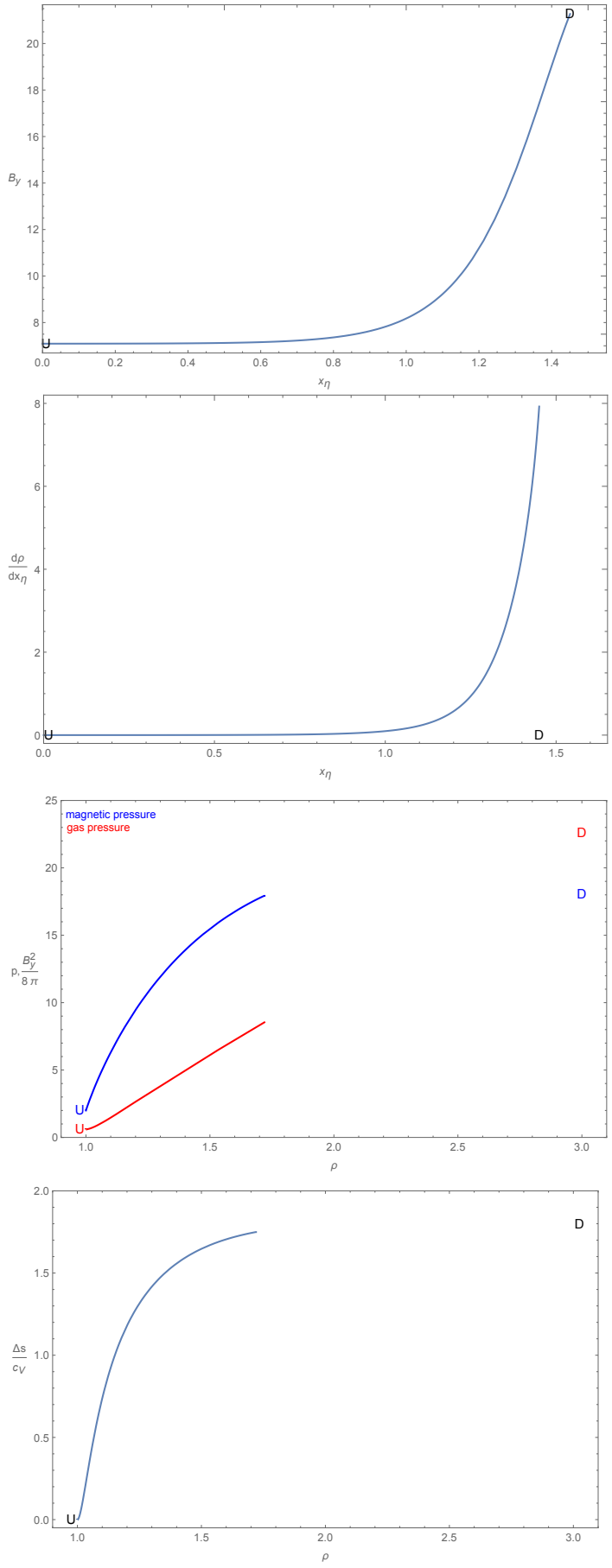

Figure 35: Variation in B_y, u_x, p, ρ and Δs through a perpendicular $1^+ \rightarrow 2^-$ shock. Gap between profile and D is due to a gas dynamic jump; $\frac{b_1}{a_1} = 2$, $\theta_1 = 90°$, $\frac{u_{x1}}{a_1} = 7.54983$

6 Slow Shocks

This chapter presents the phase space vectors and structures for slow shocks. Slow shocks are produced when $v_{s1} < u_{x1} < v_{i1}$ and $\theta_1 \neq 0^\circ$ or 90°. The downstream state is always subsonic so the trajectories linking the upstream and downstream points are either confined entirely to the subsonic sheet or start with a gas dynamic jump at the upstream point to the subsonic sheet in the case of a supersonic to subsonic slow shock. In both cases the general ODE (27) can be formulated for numerical integration of slow shock structure by placing $B_z = 0$ and choosing the negative branch of the square root corresponding to the subsonic sheet. Placing $x_\eta = \frac{x}{\eta}$ gives for the slow shock ODE

$$\frac{dB_y}{dx_\eta} = \frac{1}{8\pi\left(\gamma+1\right)f_1}\{-8\pi\left(\gamma+1\right)\left(B_x f_3 + f_1 f_5\right) - \gamma B_y^3 + B_y[8\pi\gamma f_2 - 2\left(\gamma+1\right)B_x^2]$$

$$-B_y\sqrt{64\pi^2\left[\gamma^2 f_2^2 + \left(\gamma^2-1\right)\left(f_3^2 - 2f_1 f_7\right)\right] + 32\pi\left(\gamma^2-1\right)\left(B_x f_3 + f_1 f_5\right)B_y + 4[-4\pi\gamma^2 f_2 + \left(\gamma^2-1\right)B_x^2]B_y^2 + \gamma^2 B_y^4}\ \}. \tag{132}$$

The constants f_1, f_2, f_3, f_5 and f_7 are determined from (95)-(99) by the specified upstream conditions. In Chapter 5 this was the governing ODE for fast shocks, but with the positive branch of the square root.

6.1 Slow $3^- \rightarrow 4^-$ Shocks

This section presents the phase space and structure of a slow subsonic to subsonic shock, which is produced when $v_{s1} < u_{x1} < a_1$ for $\theta_1 \neq 0^\circ$ and $\theta_1 \neq 90^\circ$.

Before giving examples of the phase space, it is informative to show the phase space at upstream speeds slightly less than the slow MHD wave speed, the slow speed being the minimum upstream disturbance speed to allow a transition between the upstream and downstream states.

For the set of upstream parameters $\left\{1, 2, \frac{5}{3}, 1, 15^\circ, u_{x1}\right\}$ the upstream slow speed is 0.955613. For these parameters a numerical solution of (120) shows that two stationary points occur in the phase plane when $u_{x1} < 1.9197$. Figure 36 (a) shows the $B_y - B_z$ phase plane structure for an upstream flow speed of 0.9, this being less than the value of u_{x1} at the intersection of the extended u_{x2} and a_2 curves in Figure 10, the intersection being at $u_{x1} = 0.913881$. When $u_{x1} = 0.9$ a stationary point is on each sheet, upstream trajectories being unable to leave the sink directly or by a gas dynamic jump due to the entropy change from the subsonic to supersonic sheet being negative. Figure 36 (b) shows the phase plane when the upstream shock speed is slightly less than the upstream slow speed. Both stationary points are on the subsonic sheet and an integral curve representing a shock transition is not able to link the upstream and downstream points due to direction of the vector fields.

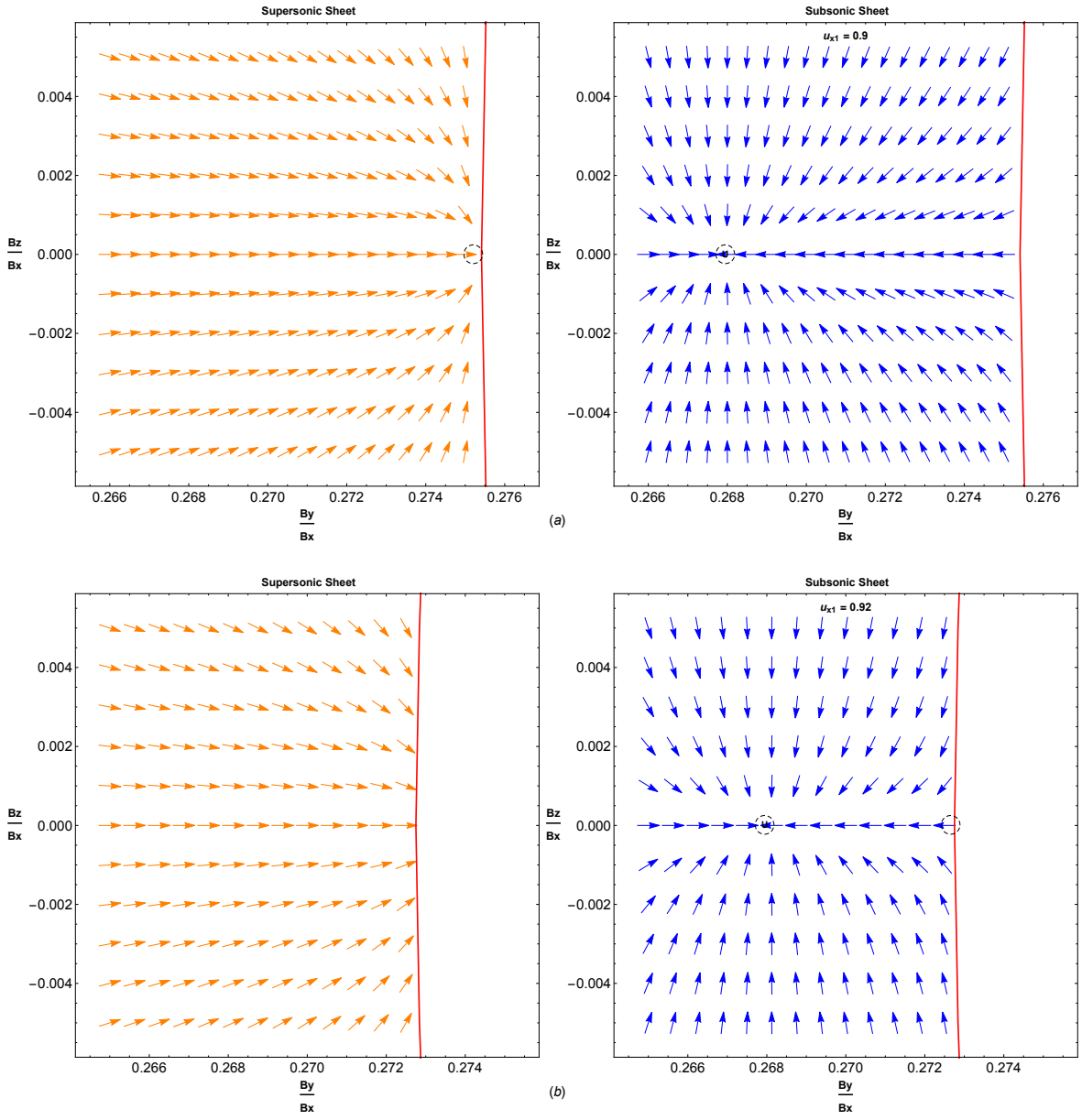

Figure 36: Phase plane vector fields before the formation of a slow shock, $u_{x1} < v_{s1}$, a trajectory is unable to link the stationary points; $\frac{b_1}{a_1} = 2$, $\theta_1 = 15°$, $\frac{u_{x1}}{a_1} = 0.9,\ 0.92$

6.1.1 Phase Space for $3^- \to 4^-$ Slow Shocks

For the set of upstream parameters $\left\{1, 2, \frac{5}{3}, 1, 15°, u_{x1}\right\}$ two stationary points occur when $u_{x1} < 1.9197$ and four stationary points occur when $1.9197 < u_{x1} < 2.42108$. The four stationary points are present in the interval between the vertical tangents to the downstream shock speed graph in Figure 10, the upper limit being the upstream Jouget speed, u_{j1}. As the upstream slow and intermediate speeds for these conditions are 0.955613 and 1.93185 respectively, two stationary points are present for most, 98.76%, of the slow shock speed domain.

Figure 37(a) shows the phase plane for the case of the upstream shock speed being slightly greater than the slow speed so that the upstream shock speed is subsonic. The upstream stationary point is now closer to the red subsonic boundary, inside of which the magnetic field derivatives are complex,

the downstream stationary point being further from the boundary. Figure 37(b) shows an enlarged view of the stationary points, the vector fields from the upstream saddle allowing a trajectory from the saddle to the downstream sink.

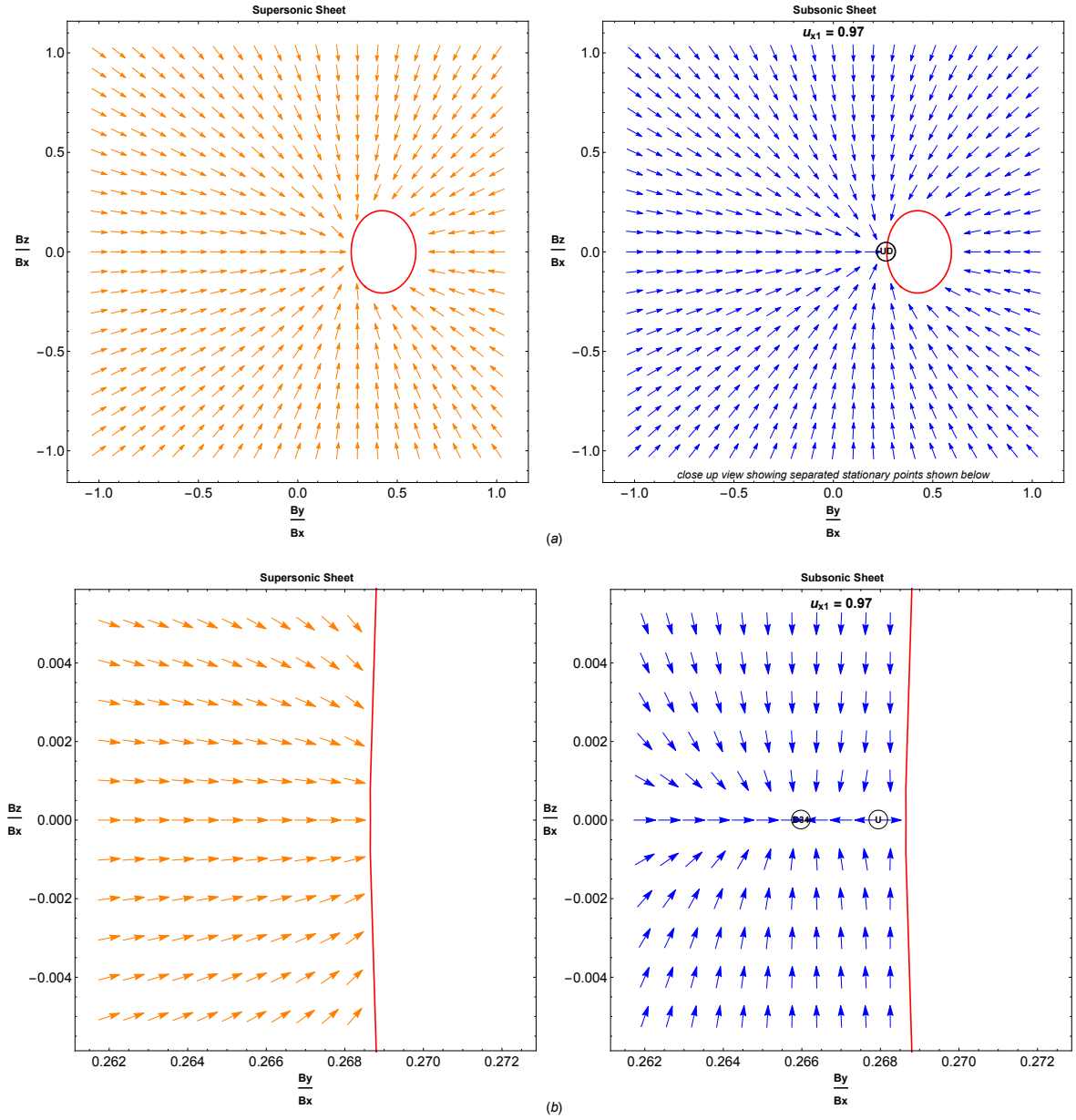

Figure 37: As for Fig 36, but for $v_{s1} < u_{x1} < a_1$. A unique trajectory, a $3^- \rightarrow 4^-$ shock, links the upstream and downstream states; $\frac{b_1}{a_1} = 2$, $\theta_1 = 15°$, $\frac{u_{x1}}{a_1} = 0.97$

6.1.2 Subsonic to Subsonic Slow Shock Structure from Numerical Integration

Representative slow shock structures are shown in Figure 38 for the set of upstream parameters $\{1, 2, \frac{5}{3}, 1, 15°, 0.97\}$. The first order ODE (132) was solved numerically by taking a step-off from the upstream stationary point of -1×10^{-7} in B_y with the integration direction being along the positive x direction. The small step-off was chosen to show the gradual change in the shock variables from the

upstream point. The numerical integration was terminated when $|B_y - B_{y2}| < 10^{-7}$.

The results of the integration, presented in four plots showing B_y vs u_x, u_x vs x_η, $\frac{\Delta s}{c_v}$ vs $p/\frac{B_x^2+B_y^2}{8\pi}$ and $\frac{\Delta s}{c_v}$ vs x are shown in Figure 38. In the slow shock case the downstream stationary point in the phase plane, as indicated in Figure 37 (b), is such that $B_{y2} < B_{y1}$, with both the same sign, the numerical integration showing that u_x is a monotonically increasing function of B_y. At all stages in the shock $\frac{d\rho}{dx_\eta}$ and $\frac{dp}{dx_\eta}$ are positive. The gas pressure undergoes a slight increase across the shock and the magnetic pressure undergoes a slight decrease, at all stages being greater than the gas pressure. The change in specific entropy through the shock profile shows a monotonic increase due to $\left(\frac{p}{p_1}\right)^\gamma < \frac{\rho}{\rho_1}$ through the transition, the difference being in the sixth decimal place at the downstream point.

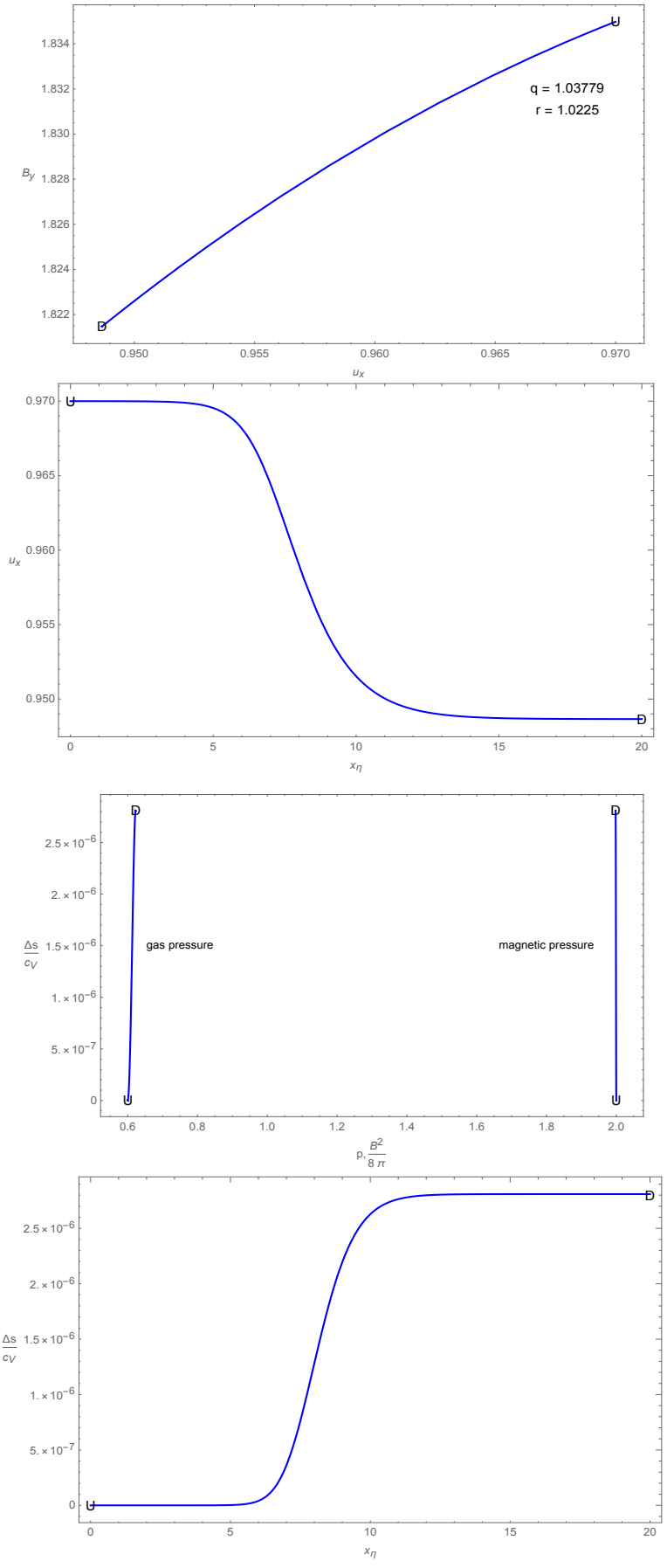

Figure 38: Variation in B_y, u_x, p and Δs through a $3^- \rightarrow 4^-$ shock. In this and all following slow shock plots speeds are in terms of the upstream speed of sound, $\rho_1 = 1$ and $x_\eta = \frac{x}{\eta}$. In this plot $\frac{b_1}{a_1} = 2$, $\theta_1 = 15$, $\frac{u_{x1}}{a_1} = 0.97$

6.2 Slow $3^+ \rightarrow 4^-$ Shocks

This section presents the phase space and structure of a slow supersonic to subsonic shock, which occurs when $a_1 < u_{x1} < b_1 \cos\theta_1$, $b_1 \cos\theta_1$ being the upstream intermediate speed, for $\theta_1 \neq 0°$ and $\theta_1 \neq 90°$.

6.2.1 Phase Space for $3^+ \rightarrow 4^-$ Slow Shocks

Figure 39 shows the phase plane structure for three shock speeds between a_1 and v_{k1} where v_{k1} is a speed slightly smaller than the intermediate speed. In this speed domain the phase plane contains only two stationary points. The speed designated as v_{k1} is the smaller positive solution of equation (53), the larger positive solution being the Jouget speed, v_{j1}. In Figure 39 (a) phase trajectories in the positive x direction are unable to leave the upstream sink in the supersonic plane, the only way to link to the downstream point being an immediate entropy increasing gas dynamic jump from the upstream state to the subsonic sheet with a phase trajectory leading to the downstream sink. At the downstream point B_{y2} has the same sign as B_{y1} and $|B_{y2}| < |B_{y1}|$. The supersonic boundary has a kidney bean shape with the red circles representing points where $\frac{du_x}{dx}$ has the indeterminate form of $\frac{0}{0}$. These points are first present when $u_{x1} = a_1$ and form on the B_y axis at the point on the boundary closest to the stationary points. When the upstream speed becomes supersonic the upstream saddle of the subsonic flow domain changes structure to a sink according to (121), the B_y eigenvalue changing direction across the upstream sound speed.

Figure 39 (b) and (c) show the effect of increasing the upstream shock speed on the phase plane structure. As the upstream shock speed is increased the kidney bean evolves into a sideways U shape, the U gradually enclosing the stationary points with finally the red circles meeting on the B_y axis when $u_{x1} = 1.84373$ to form an annular type region enclosing the stationary points. The inner boundary of this region in the $B_y - B_z$ plane is the common boundary of the supersonic and subsonic sheets inside of which the shock transitions occur. In the annular region the magnetic field derivatives are complex.

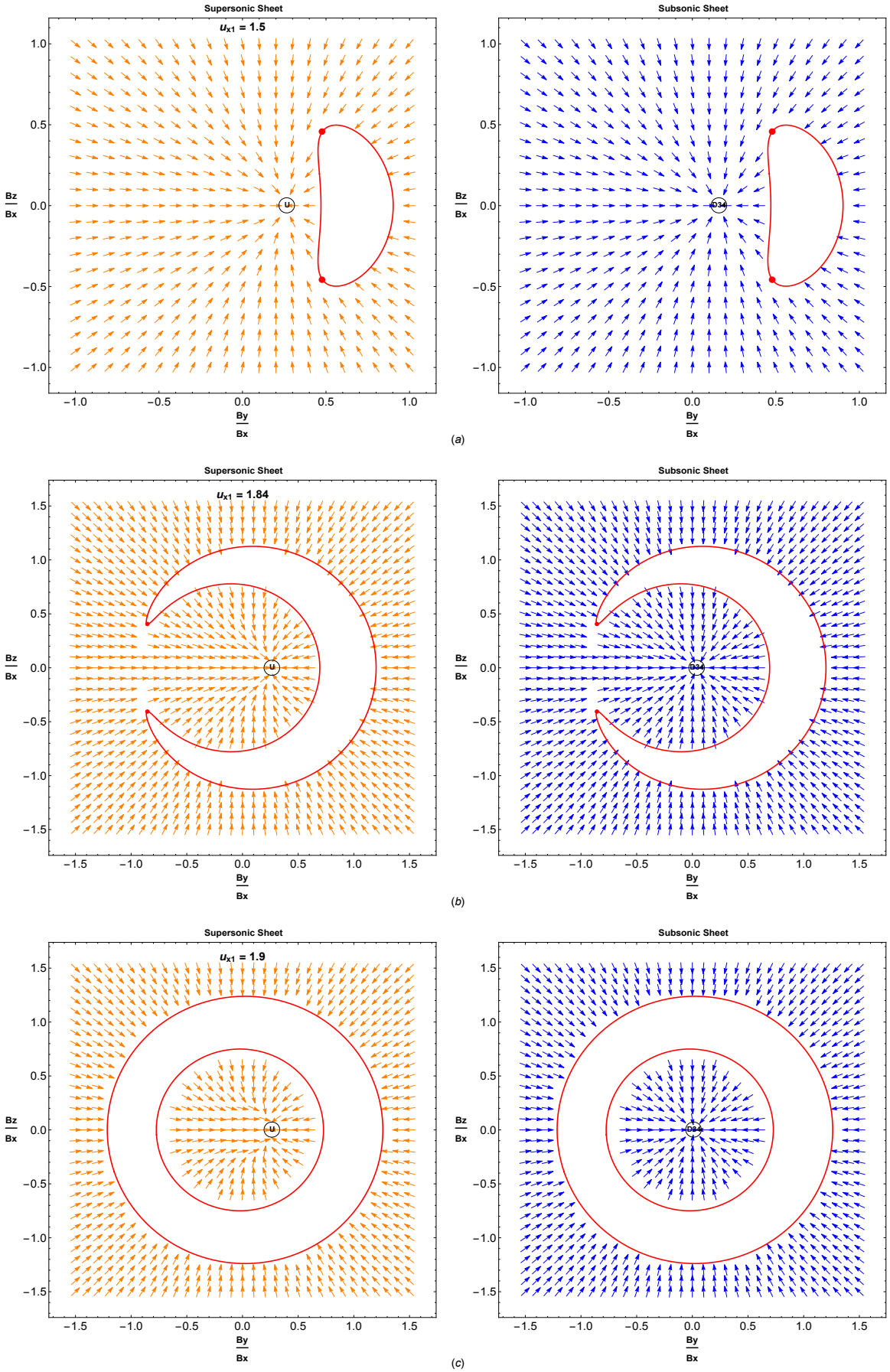

Figure 39: As for Fig 36, but $a_1 < u_{x1} < v_{k1}$. An immediate gas dynamic jump to the subsonic sheet is followed by a trajectory to the downstream point. This unique transition is a $3^+ \to 4^-$ slow shock. v_{k1} is the maximum shock speed to form two stationary points in the slow shock phase plane. $\frac{b_1}{a_1} = 2, \theta_1 = 15°, \frac{u_{x1}}{a_1} = 1.5, 1.84, 1.9$

The phase plane structure for upstream shock speeds slightly less than the intermediate speed v_{i1} will now be outlined. For the set of upstream parameters $\left\{1, 2, \frac{5}{3}, 1, 15°, u_{x1}\right\}$ four stationary points occur when $1.9197 < u_{x1} < 2.42108$, this interval covering 1.24% of the slow shock speed domain in Figure 10. Figure 40 (a) shows the presence of the four stationary points, two of the stationary points on the supersonic sheet not being accessible by trajectories from the upstream point. The only possible transition is a slow shock consisting of a gas dynamic jump at the upstream point to the subsonic sheet with the phase trajectory moving along the B_y axis to the downstream point, the downstream value B_{y2} being the same sign as B_{y1} with $|B_{y2}| < |B_{y1}|$.

Figure 40 (b) shows a closer view of the supersonic stationary points, the "unused" stationary points being a saddle and a source, both of these being unable to link with trajectories leaving the upstream source. In terms of entropy, transitions from the upstream point to the other two stationary points on the supersonic sheet involve a decrease in specific entropy and so are not possible. If the middle unused stationary point is taken as the upstream state and the other unused and current upstream state are downstream states a fast shock can occur from right to left between the former unused states. In this case an intermediate shock links the new and former upstream states. These transitions will be examined in the next chapter.

When the upstream shock speed excedes the upstream intermediate speed the upstream state changes from a sink to a saddle point due to the coefficient of δB_z in (122) changing from $-$ to $+$ across the intermediate speed.

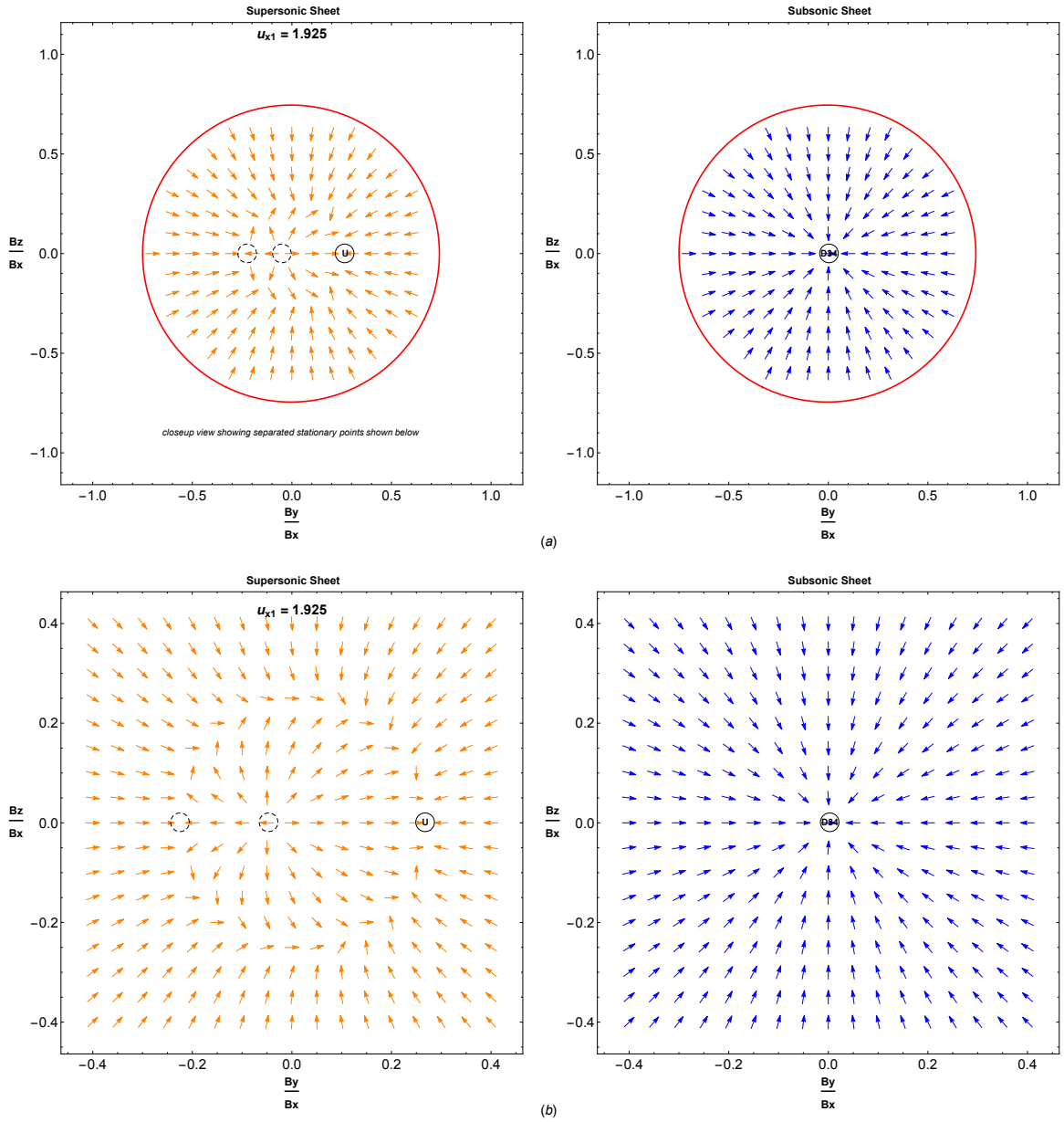

Figure 40: As for Fig 36 but $v_{k1} < u_{x1} < b_1 cos\theta_1$. A unique transition with a gas dynamic jump from U to the subsonic sheet followed by a trajectory to the downstream point. This unique transition is a $3^+ \rightarrow 4^-$ shock. $\frac{b_1}{a_1} = 2, \theta_1 = 15°, \frac{u_{x1}}{a_1} = 1.925$

When the upstream shock speed equals the upstream intermediate speed and the density ratio is greater than 1 (45) predicts that the downstream transverse magnetic field component is zero, yielding a switch-off shock. Equation (120) predicts that the stationary points on the B_y axis are $\{-B_{y1}, 0, 0, B_{y1}\}$ when $u_{x1} = v_{i1}$. The first solution belongs to a rotational discontinuity for which $r = 1$. In this case the transverse magnetic field component rotates through 180° across the discontinuity. One of the zero solutions is associated with an r value less than 1, this having an entropy decrease and so not being a viable shock transition. The other zero solution for B_{y2} on the subsonic sheet is the downstream value for a switch-off shock. For the upstream parameters $\left\{1, 2, \frac{5}{3}, 1, 15°, b_1 \cos\theta_1\right\}$ the phase plane vectors are shown in Figure 41. The switch-off shock is formed by a gas dynamic jump from the supersonic upstream point U in the $B_y - B_z$ phase plane to the subsonic sheet where the phase trajectory links

to the downstream point D.

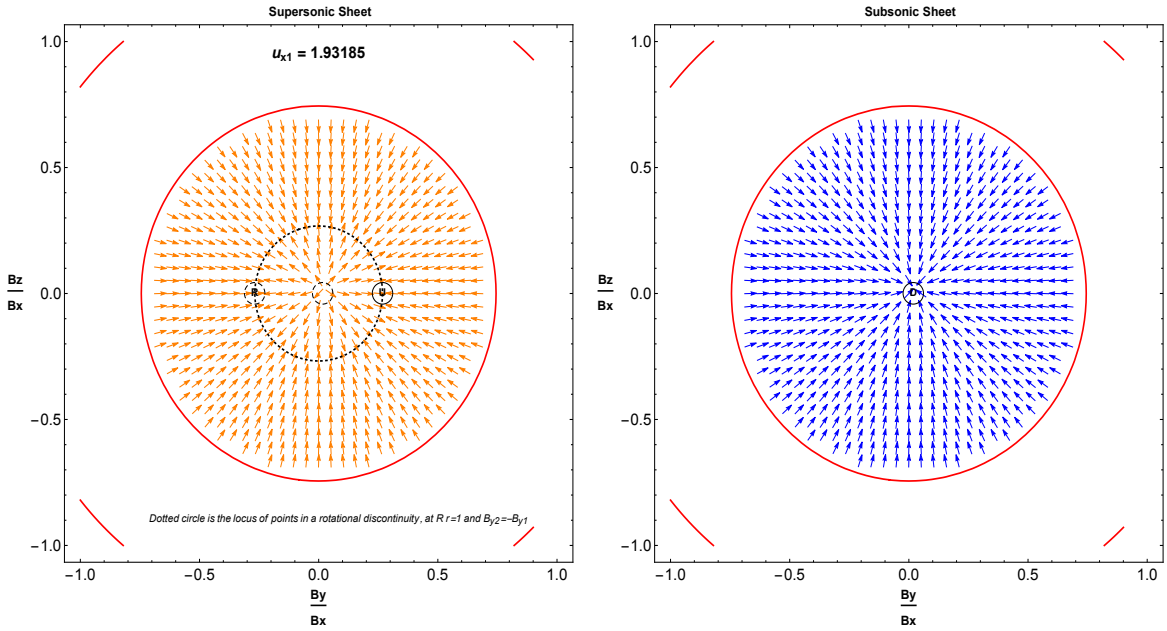

Figure 41: As for Fig 36, but $u_{x1} = b_1 cos\theta_1$. A switch-off shock being a transition with $B_{y2} = 0$. An initial gas dynamic jump from U is followed by a trajectory to the downstream point; $\frac{b_1}{a_1} = 2$, $\theta_1 = 15°$, $\frac{u_{x1}}{a_1} = 1.93185$

6.2.2 Supersonic to Subsonic Slow Shock Structure from Numerical Integration

This subsection presents the structure of a $3^+ \rightarrow 4^-$ slow shock as determined by numerical integration. For the set of upstream parameters $\{a_1, b_1, \gamma, \rho_1, \theta_1, u_{x1}\}$ a slow supersonic to subsonic shock is is produced when $a_1 < u_{x1} < b_1 \cos\theta_1$, $b_1 \cos\theta_1$ being the intermediate speed, for $\theta_1 \neq 0°$ and $\theta_1 \neq 90°$. The $B_y - B_z$ phase plane vector fields are shown in Figure 39. To determine the structure by numerical integration the upstream parameter set $\left\{1, 2, \frac{5}{3}, 1, 15°, 1.5\right\}$ will be used. The integration commences with a gas dynamic jump from the supersonic upstream point to the subsonic sheet and then follows the vector field to the downstream point as shown in Figure 39(a), the transition having zero B_z component. The results of the numerical solution of (132) are shown in Figure 42. The gas dynamic jump at the upstream point greatly reduces the normal velocity component of the shock causing a large increase in the gas pressure according to (21). An increase in the upstream shock speed has the effect of increasing the gas pressure in the subsonic state, the downstream gas and magnetic pressures being equal when $u_{x1} = 1.592$ and the gas pressure exceeding the magnetic pressure at all subsonic stages when $u_{x1} > 1.694$. As for the subsonic to subsonic slow shock, the change in specific entropy undergoes a monotonic increase through the shock transition.

In terms of mass density the slow shock in this example is compressive at all stages. The gas dynamic jump at the upstream point arrives in a zone in the subsonic $B_y - B_z$ plane where $\frac{d\rho}{dx_\eta} > 0$, the transition to D34 being through the compressive zone. Shercliff [37] states that slow shocks may have an expansive stage, but this was never seen in the cases for $b_1 > a_1$ examined by the author.

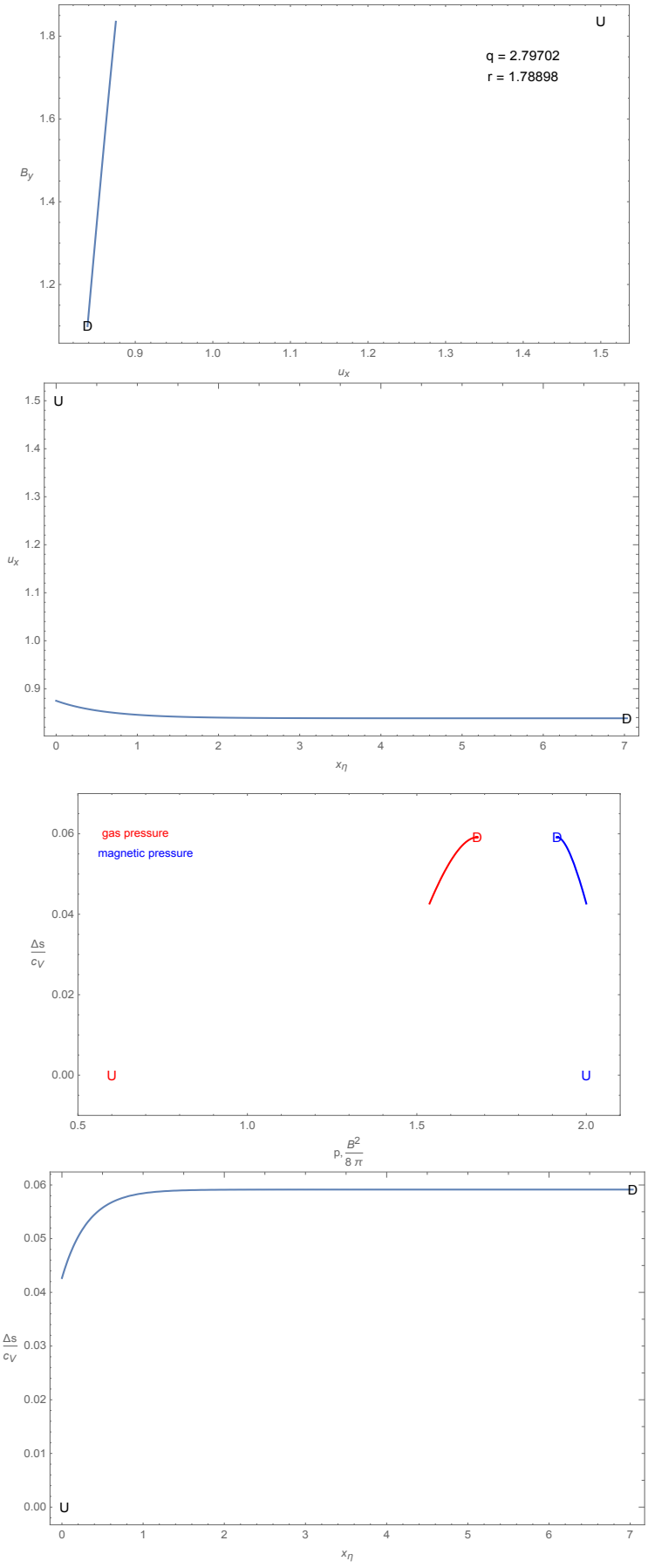

Figure 42: Variation in B_y, u_x,p and Δs through a $3^+ \rightarrow 4^-$ shock. Gap between U and profile is due to a gas dynamic jump; $\frac{b_1}{a_1} = 2, \theta_1 = 15°$, $\frac{u_{x1}}{a_1} = 1.5$.

A switch-off shock has a non-zero transverse magnetic field component upstream and a zero transverse magnetic field component downstream. A necessary condition for a switch-off shock is that $u_{x1} = v_{i1}$, as indicated by (45) or (94). For the set of upstream parameters $\left\{1, 2, \frac{5}{3}, 1, 15^\circ, 2\cos 15^\circ\right\}$ the $B_y - B_z$ phase plane shown in Figure 41 can produce a switch-off shock when a gas dynamic jump occurs from the upstream point to the subsonic sheet followed by passage of the phase trajectory to the downstream point. Figure 10 shows that when $u_{x1} = v_{i1}$ three values of u_{x2} are possible. The two largest values not corresponding to a shock solution. The largest has $B_{y2} = 0$ with $r < 1$ with an associated specific entropy decrease. The next has $B_{y2} = -1$ with $r = 1$ this being a rotational discontinuity with downstream normal shock speed, density and pressure being the same as the upstream values. The least of the three values of u_{x2} is associated with $B_{y2} = 0$ and $r > 1$, this being a switch-off shock. A switch-off shock is a slow shock with the downstream transverse magnetic field component being zero.

Figure 43 shows the structure of a switch-off shock determined by numerical integration of the structure ODE (132) with the upstream parameter set $\left\{1, 2, \frac{5}{3}, 1, 15^\circ, 2\cos 15^\circ\right\}$. The integration in phase space begins with a gas dynamic jump to the subsonic sheet and then proceeds directly along the B_y axis to the downstream point. The B_y component undergoes a monotonic decrease towards zero, the integration being stopped when $|B_y| < 10^{-7}$. The gas pressure is greater than the magnetic pressure at all stages in the shock transition after the gas dynamic jump and the change in specific entropy from the upstream point undergoes a monotonic increase with distance through the structure along the x axis. The change in specific entropy at the gas dynamic jump to the subsonic sheet in a switch-off shock has the maximum value for all gas dynamic jumps in the domain $a_1 < u_{x1} \leq v_{i1}$.

Summary

Slow shocks occur when the shock speed is between the slow MHD speed and the intermediate speed. In slow shocks $|B_{y2}| < |B_{y1}|$ with $B_{y2} \times B_{y1} > 0$. There are two distinct types of slow shock, $3^- \to 4^-$, having smooth subsonic flow throughout the transition and $3^+ \to 4^-$ having an initial gas dynamic jump followed by a smooth subsonic transition. Each type of slow shock has a unique structure. In the slow shock speed domain additional unreachable stationary points occur in the phase plane when the shock speed is close to the intermediate speed. One of these points corresponds to the upstream state of an intermediate and fast shock family and familes of these shocks are considered in the next chapter.

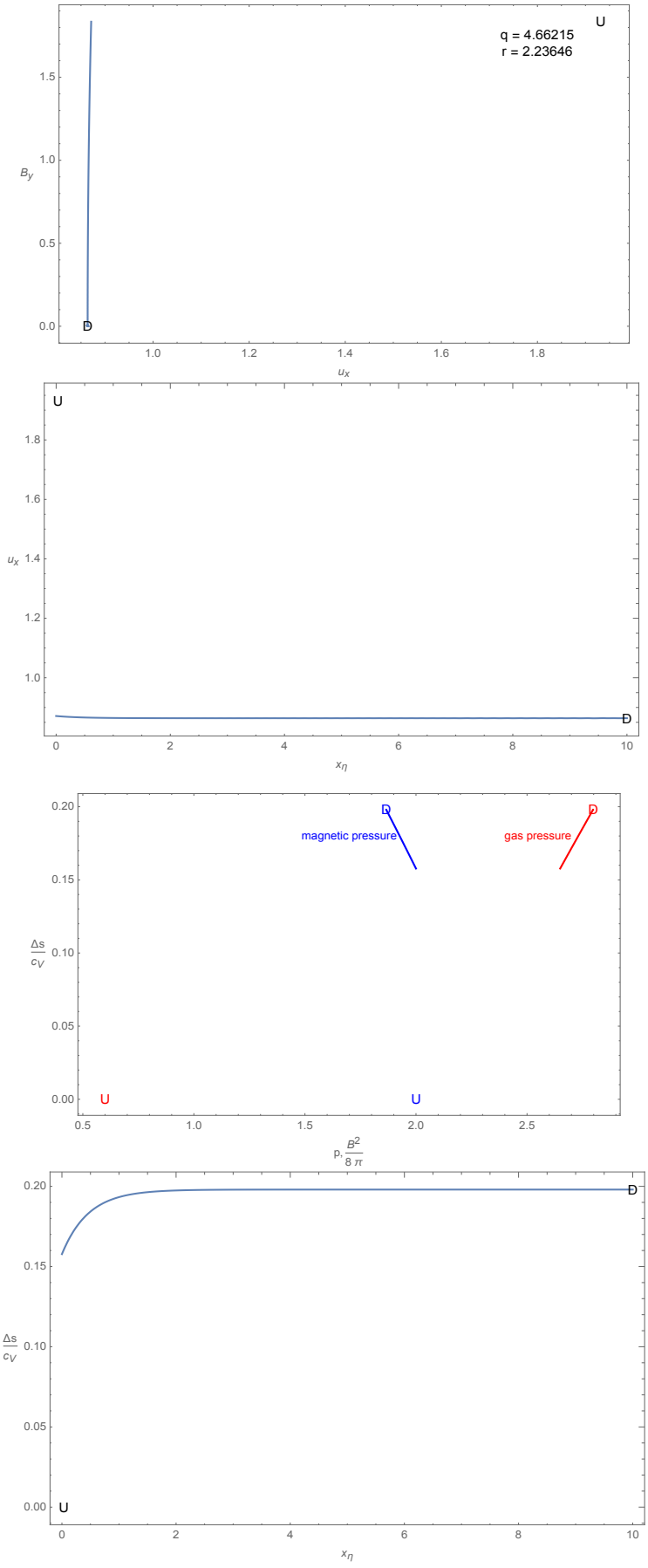

Figure 43: Variation in B_y, u_x, p and Δs through a supersonic to subsonic switch-off shock. Gap between U and profile is due to a gas dynamic jump; $\frac{b_1}{a_1} = 2$, $\theta_1 = 15°$, $\frac{u_{x1}}{a_1} = 1.93185$

7 Intermediate Shock Families

This chapter presents the $B_y - B_z$ phase plane and shock transitions in this plane when four stationary points are present in the phase plane and the upstream shock speed is greater than the intermediate speed. The four stationary points allow multiple transitions in the phase plane creating families of shocks possible for a given set of upstream parameters.

Intermediate shocks are defined as having their upstream normal shock velocity greater than the upstream intermediate speed, $u_{x1} > v_{i1}$, and downstream normal velocity component less than the downstream intermediate speed, $u_{x2} < v_{i2}$, the intermediate upstream and downstream speeds being given by $b_1 \cos\theta_1$ and $b_2 \cos\theta_2$ respectively. From (85), $v_{i2} = \frac{v_{i1}}{\sqrt{r}}$, allowing (45) to be written as

$$\frac{B_{y2}}{B_{y1}} = \frac{1}{r}\frac{u_{x1}^2 - v_{i1}^2}{u_{x2}^2 - v_{i2}^2}. \tag{133}$$

Equation (133) shows that for intermediate shocks the direction of the downstream transverse magnetic field component is the reverse of its upstream direction.

When intermediate shocks are present there are four stationary points representing potential upstream or downstream states, one in each of states 1, 2, 3 and 4. State 1 is always supersonic and 4 is always subsonic and depending on the choice of shock parameters there are three possibilities for states 2 and 3: both supersonic $(2^+, 3^+)$, one supersonic and the other subsonic $(2^+, 3^-)$ or both subsonic $(2^-, 3^-)$. Therefore the eight possible intermediate shock transitions are $2^+ \to 3^+$ or $2^+ \to 3^-$ or $2^+ \to 4^-$ and $2^- \to 3^-$ or $2^- \to 4^-$ and $1^+ \to 3^+$ or $1^+ \to 3^-$ or $1^+ \to 4^-$.

The intermediate shocks presented in this chapter exemplify the full range of intermediate shock properties and are calculated at upstream shock angles of 5°, 15°, 37° and 37° at the points indicated in the yellow and green zones of Figure 3. The examples in this chapter will be from an upstream state where $a_1 = 1$, $b_1 = 2$, $\gamma = \frac{5}{3}$ and $\rho_1 = 1$. In all numerical calculations in this chapter shock speeds are always considered relative to the upstream speed of sound and in all numerical integrations $x_\eta = \frac{x}{\eta}$.

As intermediate shock trajectories are two dimensional in the $B_y - B_z$ phase plane the thickness of an intermediate shock in terms of x_η is greater than those of a fast or slow shock. This is due to the greater accumulation of increments of Δx_η between neighbouring points on the two dimensional $B_y - B_z$ phase trajectory as it travels from the upstream to the downstream point.

The intermediate shocks presented in the first three sections of this chapter are $2 \to 3$ and $2 \to 4$ shocks. In this case, for the specified upstream conditions, only two stationary points are reachable by a trajectory from the upstream point.

The intermediate shocks presented in the last three sections of this chapter are $1 \to 3$ and $1 \to 4$ shocks. In this case three downstream points are accessible by integral curves from the given upstream stationary point. Two of the downstream stationary points can be reached by a trajectory that forms

an intermediate shock, either $1 \to 3$ or $1 \to 4$. The third downstream stationary point is reached by a trajectory representing a fast shock, a $1 \to 2$ transition. The properties of these associated fast shocks are the same as those presented in Chapter 5 and so are not considered here.

7.1 Intermediate $2^+ \to 3^+$ and Intermediate $2^+ \to 4^-$ Shock Family

This section presents the $B_y - B_z$ phase plane vector fields and the variation in the state variables in the transition from the upstream state to the downstream state as determined by numerical integration. The upstream parameter set that determines the family is $\{1, 2, \frac{5}{3}, 1, 15°, 2\}$, as for the slow $3^+ \to 4^-$ shock in §6.2 but now the upstream speed is greater than the intermediate speed. Equation (122) predicts that $\frac{dB_z}{dx_\eta}$ changes sign around the upstream stationary point, causing the upstream sink of the slow shock domain to becomes a saddle. A pair of trajectories trajectories can leave the upstream state in the B_z direction and link to a previously unconnected supersonic stationary point in the same plane creating a $2^+ \to 3^+$ transition, or leave in the B_z direction and undergo a gas dynamic jump at any point on the supersonic sheet to the subsonic sheet the trajectory then linking to the downstream sink as a $2^+ \to 4^-$ transition.

The example given in this section uses the upstream speed at the black dot on the 15° line in the yellow zone of Figure 3.

7.1.1 Phase Plane

Three stationary points lie on the supersonic sheet and one on the subsonic sheet. The upstream point is a saddle allowing a connection with the negative B_y value downstream saddle through the separatrix as shown in Figure 44(a), the transition being an intermediate $2 \to 3$ shock. The second stationary point with a positive value of B_y is a saddle and is unable to link by a phase trajectory with the upstream point as shown in Figure 44(b), a transition from U to this point would decrease entropy.

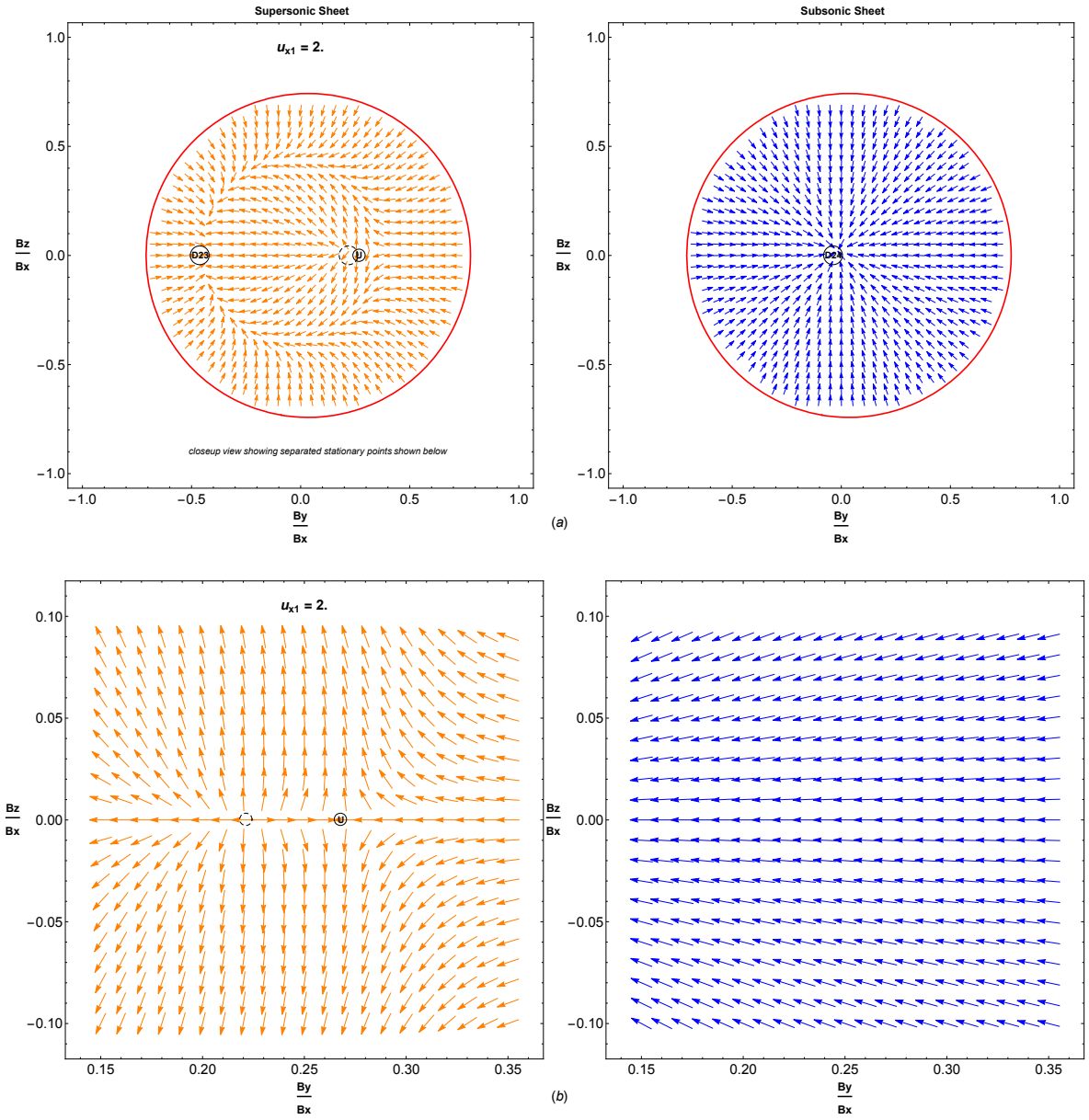

Figure 44: Phase plane vector fields having four stationary points allowing a unique $2^+ \to 3^+$ and a one parameter family of $2^+ \to 4^-$ intermediate shocks. First row shows the region inside the red transonic boundary where the flow derivatives have real values. Second row is a close up view of the region around the upstream point; $\frac{b_1}{a_1} = 2$, $\theta_1 = 15°$, $\frac{u_{x1}}{a_1} = 2$

7.1.2 $2^+ \to 3^+$ Shock Structure from Numerical Integration

For the upstream parameters in §7.1.1 the autonomous system of ODEs (27)-(28) was integrated numerically using the high order Dormand and Prince Runge-Kutta method from the upstream state to the downstream state using step-off values of ± 0.001 in B_z from the upstream point. The upstream point is a saddle point in the $B_y - B_z$ plane so there is one integral curve for $+B_z$ from the upstream saddle to the downstream sink and one for $-B_z$. The unique solution is along the separatrices linking the upstream and downstream point.

Figure 45(a) shows the variation in both magnetic field components, B_y and B_z, through the shock. The upstream magnetic field component B_{y1} undergoes a monotonic decrease through the shock to its downstream value B_{y2}. The B_z component starts and finishes at zero, reaching its maximum value slightly after $\frac{dB_y}{dx_\eta}$ has its lowest value. Figure 45(b) shows the two integral curves from the upstream point to the downstream point. As the right hand side of (28) is an odd function of B_z the integral curve is symmetric about the B_y axis. The dashed curve shows the boundary of the supersonic sheet, this being the locus of points where the normal flow velocity u_x equals the sound speed a. Inside this boundary the derivatives $\frac{dB_y}{dx_\eta}$ and $\frac{dB_z}{dx_\eta}$ are real, beyond the boundary they are complex. Figure 45(c) shows the shock transition from the upstream point to the downstream point in terms of B_y, B_z and u_x. The surface (B_y, B_z, u_x) of points where B_y and B_z have real first derivatives, u_x being the corresponding normal velocity flow value, is shown with a yellow top portion representing supersonic normal flow ($u_x > a$) and a blue lower portion representing points where a shock transition is subsonic ($u_x < a$). The $2 \to 3$ shock transition studied in this case is the black curve drawn on the supersonic surface from U to D23. The other downstream stationary point, D24, is on the lower blue subsonic surface.

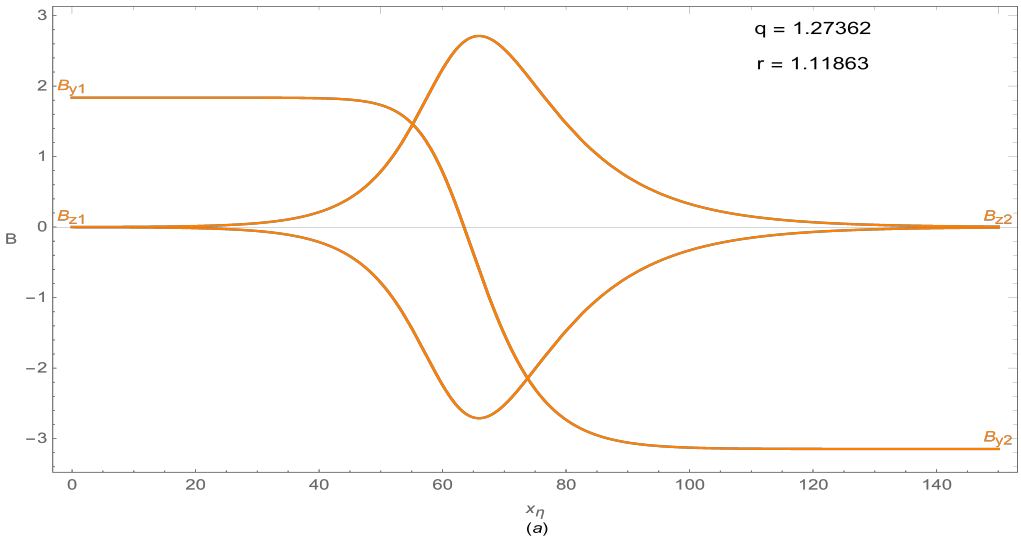

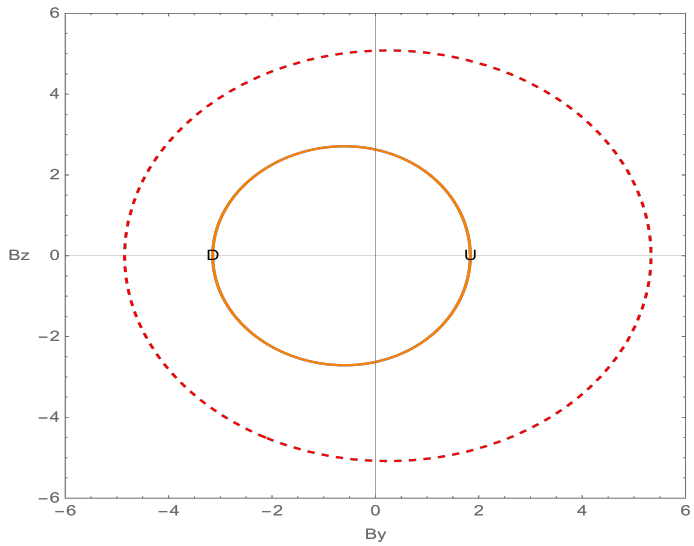

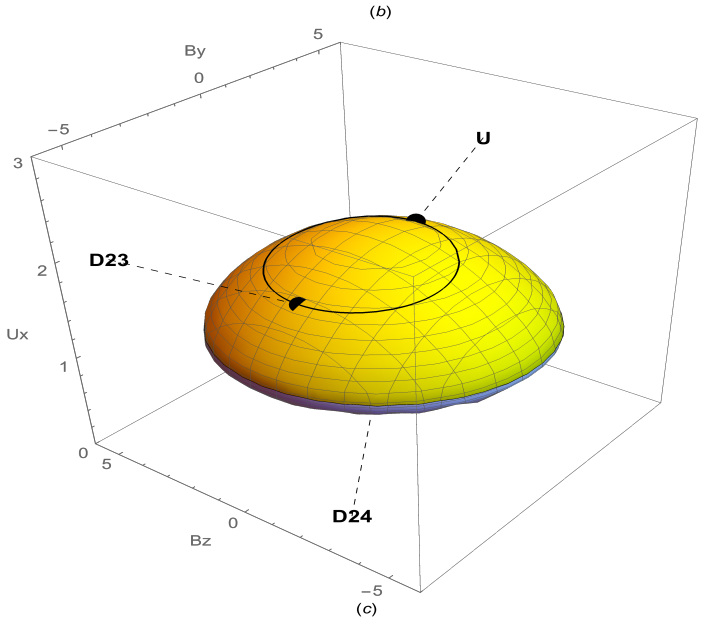

Figure 45: Variation of B_y, B_z and u_x through the pair of $2^+ \to 3^+$ shocks of the $2^+ \to 3^+ \& 2^+ \to 4^-$ family (a) B_y and B_z through the shock (b) two unique transitions from upstream saddle to downstream sink (c) shock trajectories on the $B_y - B_z - u_x$ supersonic surface; $\frac{b_1}{a_1} = 2$, $\theta_1 = 15°$, $\frac{u_{x1}}{a_1} = 2$

7.1.3 $2^+ \rightarrow 4^-$ Shock Structure from Numerical Integration

The integration of the ODEs starts in a similar manner to §7.1.2 and follows the separatrix out of the upstream saddle on the supersonic sheet. Before reaching the D23 point on the supersonic sheet the shock can undergo an isomagnetic jump to the subsonic sheet from where it proceeds to the sink on the subsonic surface. In this example presented here, the gas dynamic jump from the supersonic to the subsonic sheet is chosen to occur when $B_y = -3$.

Figures 46a and b shows the variation in magnetic field components through the shock. Figure 46c shows the shock in $B_y - B_z - u_{x1}$ space, the transition passing from the upstream point on the supersonic surface to a gas dynamic jump to the subsonic surface where the transition must pass to the sink, the only stationary point on the subsonic surface. For the given upstream conditions and shock speed the maximum increase in specific entropy occurs when the gas dynamic jump to the subsonic surface occurs at the upstream point and the least when the jump occurs at the D23 stationary point on the supersonic surface. A gas dynamic jump at the D23 point to the subsonic surface produces a slow shock transition to the D24 point.

In terms of mass density, the shock transition in this example is compressive at all stages. If the gas dynamic jump occurs at an angle less than 90° to the B_y axis a subsonic expansive stage occurs at the end as the trajectory tracks towards D24. D24 is at the left end of a small circular zone in the $B_y - B_z$ plane where transitions are expansive, the rest of the plane being compressive. Trajectories approaching D24 from the left avoid the expansive stage.

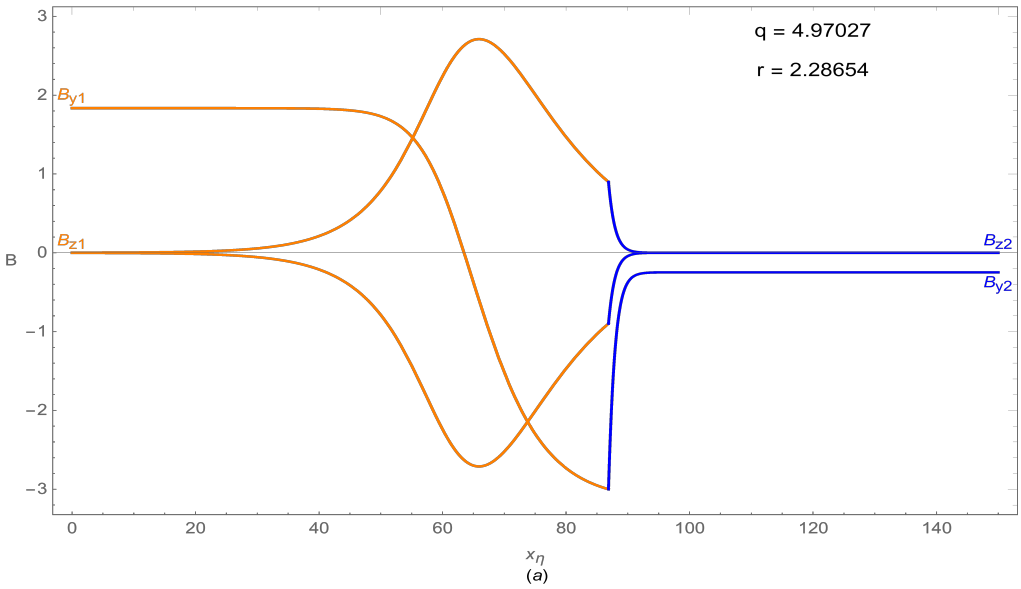

(a)

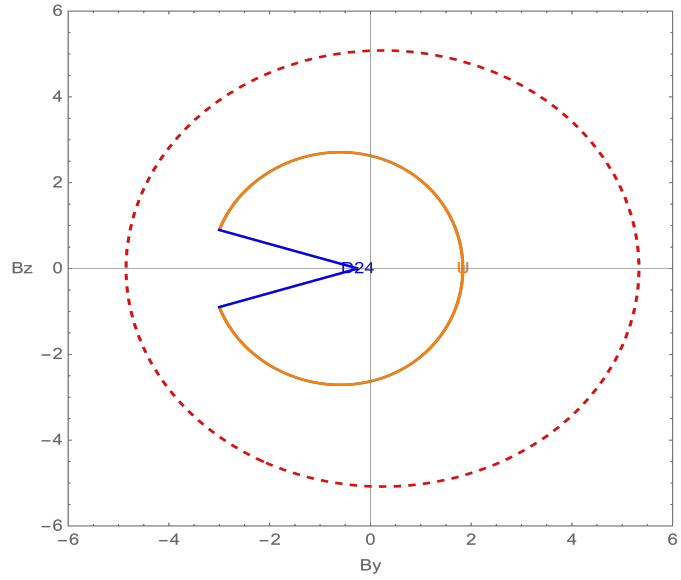

(b)

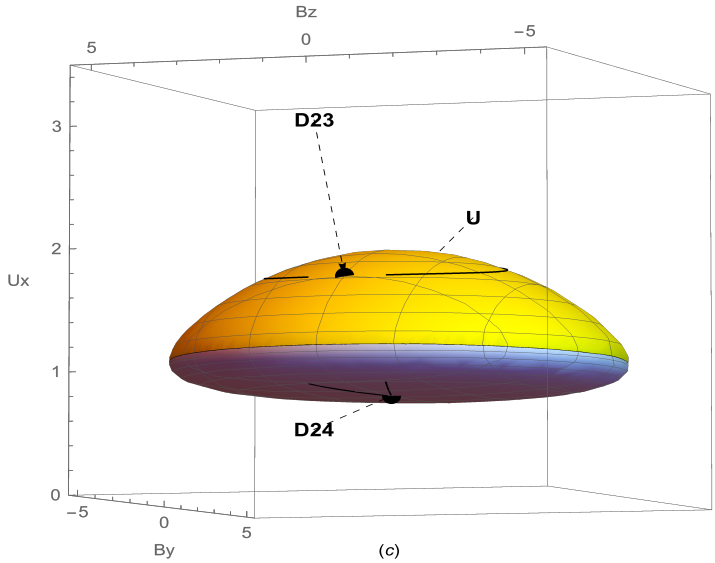

(c)

Figure 46: As for Fig 45, but for a $2^+ \to 4^-$ shock of the $2^+ \to 3^+$& $2^+ \to 4^-$ family. In this case a gas dynamic jump before D23 leads to the subsonic stationary point D24. The location of the jump is a degree of freedom, yielding a one-parameter family of solutions.

7.2 Intermediate $2^+ \rightarrow 3^-$ and Intermediate $2^+ \rightarrow 4^-$ Shock Family

The example given in this section uses the upstream speed at the black dot on the 37° line in the yellow zone of Figure 3. The $2^+ \rightarrow 3^-$ shock has transonic transition points present in its phase plane, a feature not present in the $2^+ \rightarrow 3^+$phase plane. The presence of the transonic flow point allows a smooth transition between the supersonic and subsonic sheets.

7.2.1 Phase Plane

Figure 47(a) shows the phase plane structure for the case of two stationary points on each of the supersonic and subsonic sheets, the upstream shock speed being $u_{x1} = 1.75$. The upstream saddle U can link to the downstream subsonic saddle D23 by the separatrix passing through the red circles, which are the transonic flow points, or U can link with the downstream subsonic sink through a gas dynamic jump to the subsonic sheet. The remaining stationary point (dashed circle) is at lower entropy and so is inaccessible.

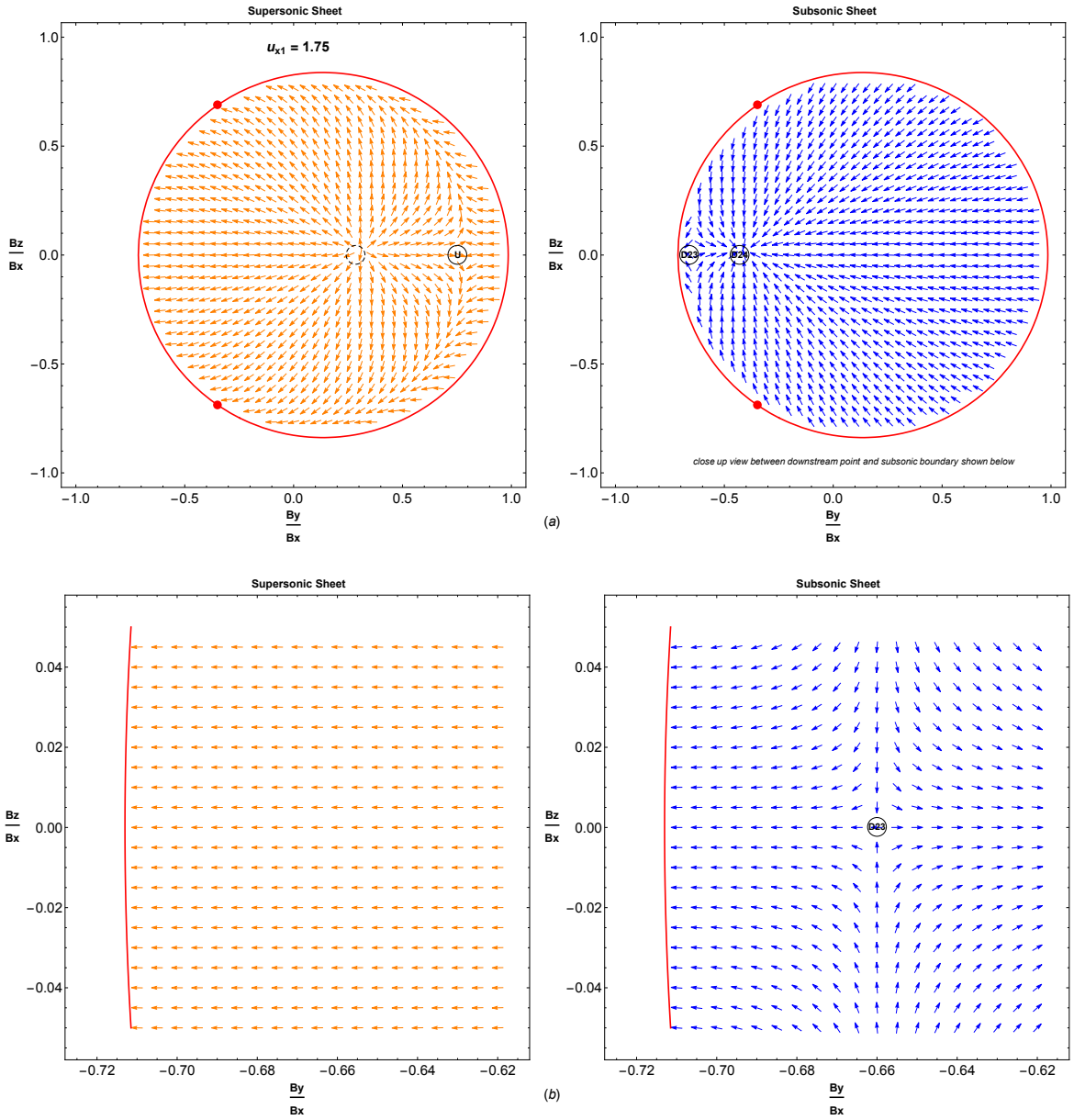

Figure 47: As for Fig 44, but with $\theta_1 = 37°$ and $\frac{u_{x1}}{a_1} = 1.75$. In this case this is a pair of $2^+ \to 3^-$ intermediate transitions through transonic points and a one-parameter family of $2^+ \to 4^-$ intermediate shocks

Figure 3 contains gray areas representing (u_{x1}, θ_1) values where a shock transition cannot occur. Such a gray area is encountered after passing through the yellow zone on the 37° line considered in this section so it is instructive to consider its phase space structure.

As the upstream shock speed increases the second stationary point on the supersonic sheet approaches U and the subsonic stationary points become closer together, the subsonic pair merging at the Jouget speed to form a double root and then absent at higher speeds until $u_{x1} > v_{ef1}$ when a subsonic stationary point appears.

When the upstream Jouget speed is less than the upstream fast speed an interval exists in which transitions from the upstream state to a notional downstream state a decrease in specific entropy. For

the upstream properties $\left\{1, 2, \frac{5}{3}, 1, 37^\circ, u_{x1}\right\}$, as shown in Figure 11, two stationary points occur when $u_{x1} > 1.76061$, both being on the supersonic sheet, the previous subsonic pair having merged at the Jouget speed. Figure 48(a) shows the supersonic and subsonic phase plane for an upstream speed $u_{x1} = 2$, this value being between the upstream Jouget and fast speeds. Figure 48(b) is a close up view of the supersonic stationary points indicating that trajectories from U are unable to link with the other stationary point.

As the upstream speed increases the supersonic stationary points approach, merging when u_{x1} is the upstream fast speed. Further increase in the upstream speed transforms the upstream point to a saddle, its B_y eigenvalue changing sign according to (121). The other supersonic stationary point also changes the direction of its B_y eigenvalue at the upstream fast speed due to the changes in signal speeds shown on Figure 6(d). A phase trajectory is now able to link the upstream source with the downstream saddle, the transition being a supersonic fast shock. The stationary points have effectively swapped their former roles, the upstream stationary point now being a source and the downstream point a saddle.

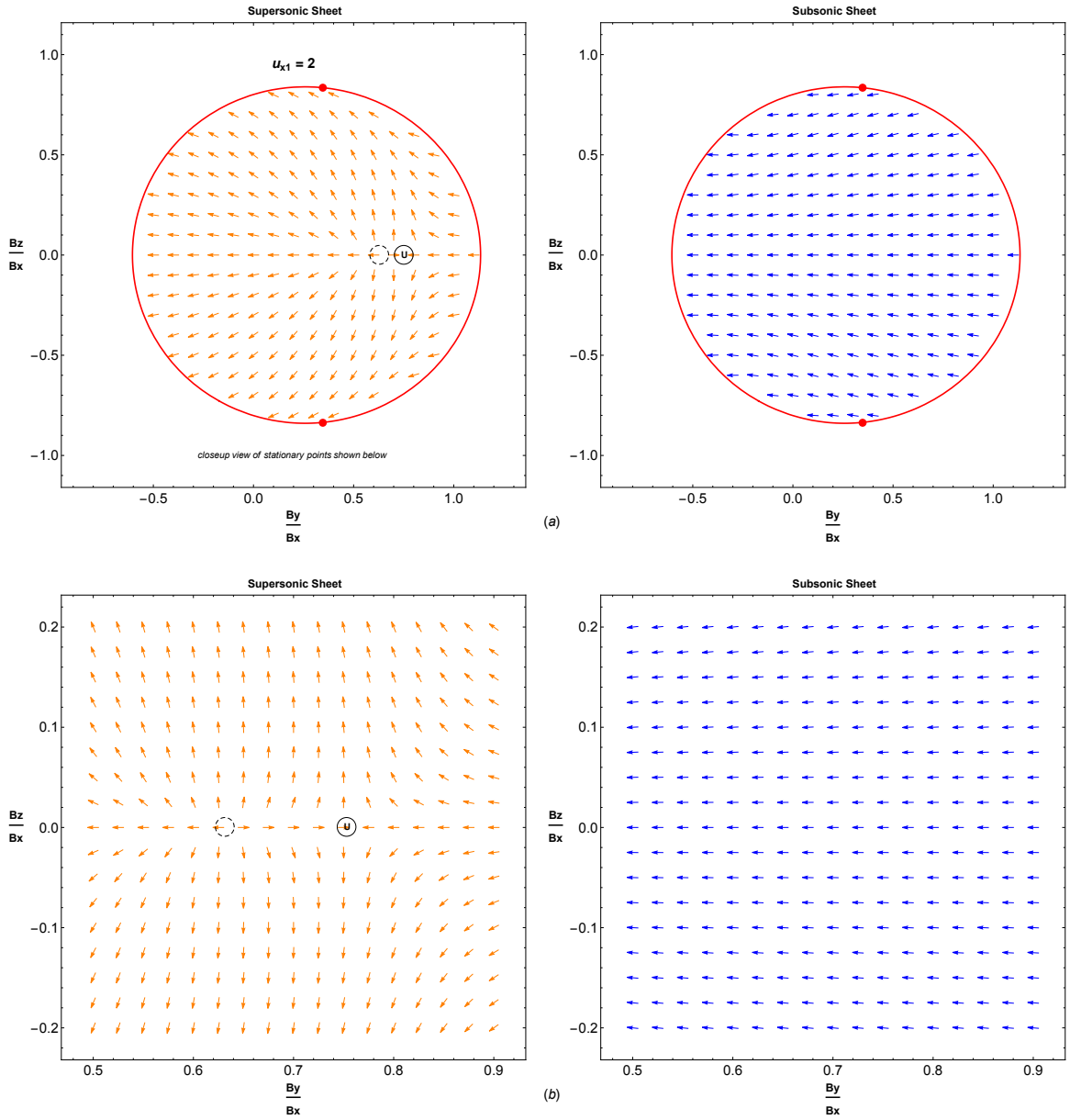

Figure 48: As for Fig 44, but with $\theta_1 = 37°$. In this case there are no allowed shock transitions. This occurring for upstream shock speeds in the interval between the Jouget speed and the fast speed when $v_{j1} < v_{f1}$.

7.2.2 $2^+ \to 3^-$ Shock Structure from Numerical Integration

This subsection presents the structure of the shock occurring in the transition with upstream parameters $a_1 = 1$, $b_1 = 2$, $\gamma = \frac{5}{3}$, $\rho_1 = 1$, $\theta_1 = 37°$ and $u_{x1} = 1.75$. The flow velocities and sound speed for these upstream conditions are shown on Figure 11 and the $B_y - B_z$ phase space structure is shown in Figure 47. The upstream and downstream points are both saddle points, the eigenvectors being in the opposite direction on the downstream subsonic saddle. Transonic flow points are present in the $B_y - B_z$ plane on the supersonic boundary at $(-1.974348432, \pm 3.900167662)$. The first derivatives of B_y and B_z at these points are -1.974348432 and $+3.900167662$ respectively. The normal flow velocity at this point and its two possible first derivatives deduced from l'Hopital's rule are $+1.295187638$,-0.2900380969 and -0.08781961392 respectively. Numerical integration shows that the larger of the two l'Hopital first

derivatives is appropriate for the $2^+ \rightarrow 3^-$ transition at the transonic flow point. The value applies for the case of a $1^+ \rightarrow 4^-$ transition in this phase plane where the upstream point is the "unused" stationary point of the $2^+ \rightarrow 3^-$ case.

Figure 49 shows the shock structure. In the two dimensional plots (a) and (b), a transition occurring on the supersonic sheet is drawn in orange and the supersonic stage of the shock is shown in blue. The transonic flow points, through which the transition passes smoothly with the same derivatives on each sheet, are shown as two small red circles on the junction of the supersonic and subsonic sheets which is shown by the red dashed boundary. In (b) the non applicable first derivative point is show as a small gray disk and the value to which the numerical integration approaches is shown as a small red disk at the join of the orange and blue integral curves.

The determination of the shock structure was carried out by the numerical solution of (27) and (28) in two stages. The first stage involved an integration out of the upstream point along the B_z axis using a step-off value in B_z of $\pm 0.0001 B_x$. The integration progresses in the positive x direction from $x = 0$ and follows the separatrix in $B_y - B_z$ space to the transonic point. The second stage involves integrating out of the downstream point, shown as $D23$ on Figure 47(b), with the same step-off. As the eigenvectors are entering the downstream point along the B_z axis the integration is carried out from $x = 0$ in the negative x direction and similarly follows the unique pathway along the separatrix to the transonic point. To obtain the functional variation of B_y and B_z through the shock a common distance x from the upstream point was used. For points on the subsonic sheet the distance of the sample point from the transonic point was added to the distance of the transonic point from the upstream point on the supersonic sheet to give a common distance x from the upstream point. A polynomial was then fitted to the B_y and B_z values in terms of the distance x from the upstream point.

Figure 49(a) shows the the relationship between the transverse components of the magnetic field. B_y is a monotonically decreasing function of x_η. Figure 49(b) shows the variation in $\frac{du_x}{dx_\eta}$ in terms of u_x. The normal flow velocity through the shock is found by eliminating u_z from (17) and (19) and placing f_4 and f_6 equal to zero

$$u_x = \frac{1}{4\pi f_1}\left(B_x^2 + \frac{4\pi f_1}{B_z}\frac{dB_z}{dx_\eta}\right), \tag{134}$$

the presence of the z magnetic field component allowing the transition to pass through $B_y = 0$, a property only shown by intermediate shocks. The first derivative, $\frac{du_x}{dx_\eta}$, on each side of the transonic point is found by applying (32) to the values of B_y, B_z and u_x on each side of the transonic point. An equivalent procedure, producing little difference in values close to the transonic point in this case, is to apply numerical differentiation to (134). The first derivative approaches the red circle in Figure 49(b) as the numerical integration proceeds from each stationary point. The gray circle is ignored by the numerical integration in the case of $2^+ \rightarrow 3^-$ shocks, it being the point towards which the integration proceeds for the $1^+ \rightarrow 4^-$ shock transition in this phase plane, having the unused stationary point as the upstream point, the upstream properties in this case being $a_1 = 0.8988059476$, $b_1 = 1.8749690733$, $\gamma = \frac{5}{3}$, $\rho_1 = 0.7846737467$, $\theta_1 = 15.9084861759^\circ$ and $u_{x1} = 2.2302262658$. The (q, r) value for this $1^+ \rightarrow 4^-$ shock is $(6.56905, 2.36055)$.

The similarity of the phase plane in the $2^+ \rightarrow 3^-$ and $1^+ \rightarrow 3^-$ cases will be shown in §7.6.3 where it will be seen that the intermediate $1^+ \rightarrow 4^-$ shock can pass through the transonic point when the phase trajectory leaves the upstream point at a particular angle. The numerical integration proceeds towards the gray circle of its first derivative for certain angles of departure from the upstream and downstream points, the red circle being reached by a unique integral curve which has higher order derivatives approaching their own particular l'Hopital values. An entropy analysis by expanding about the transonic point in a Taylor series expansion keeping up to third order terms gives positive entropy changes on the downstream side using the derivatives at both positions.

Figure 49(c) shows the passage of the shock in B_y, B_z, u_x space as a black curve from the upstream point U to the downstream point D23. The transonic transition point is the red disk on the junction of the supersonic (yellow) and subsonic (blue) surfaces.

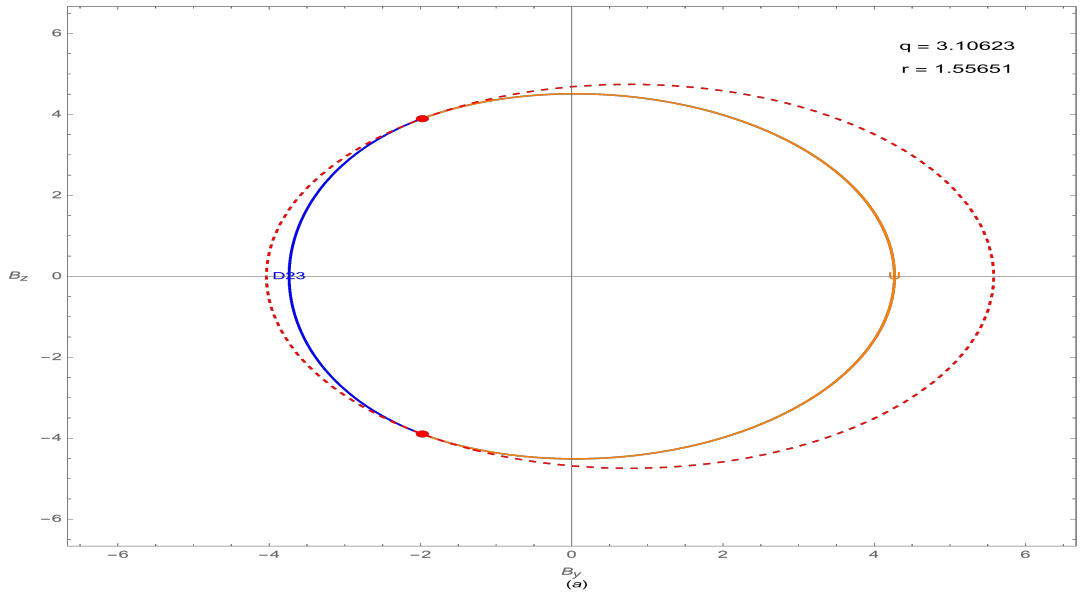

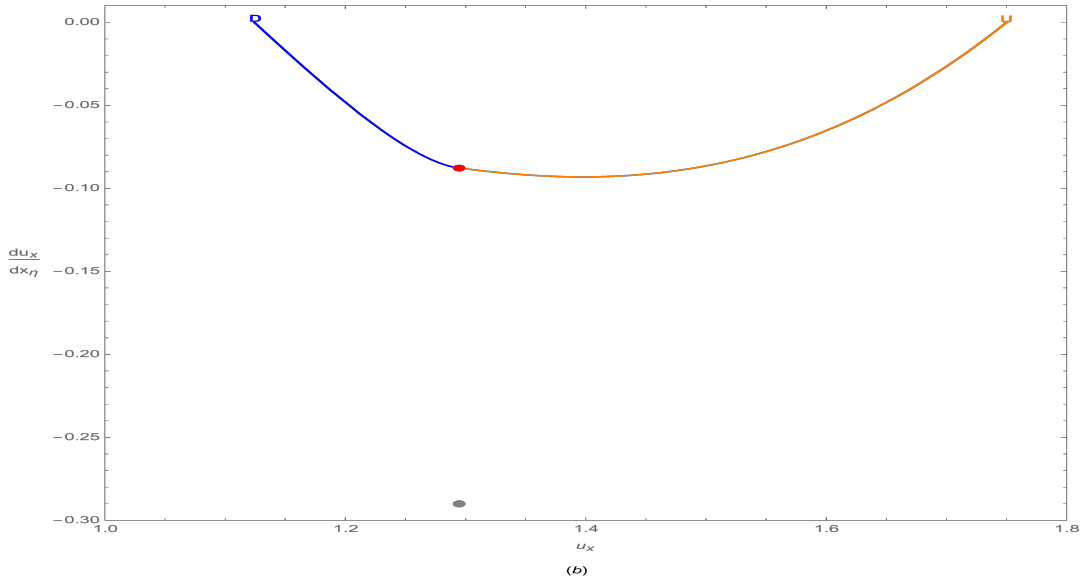

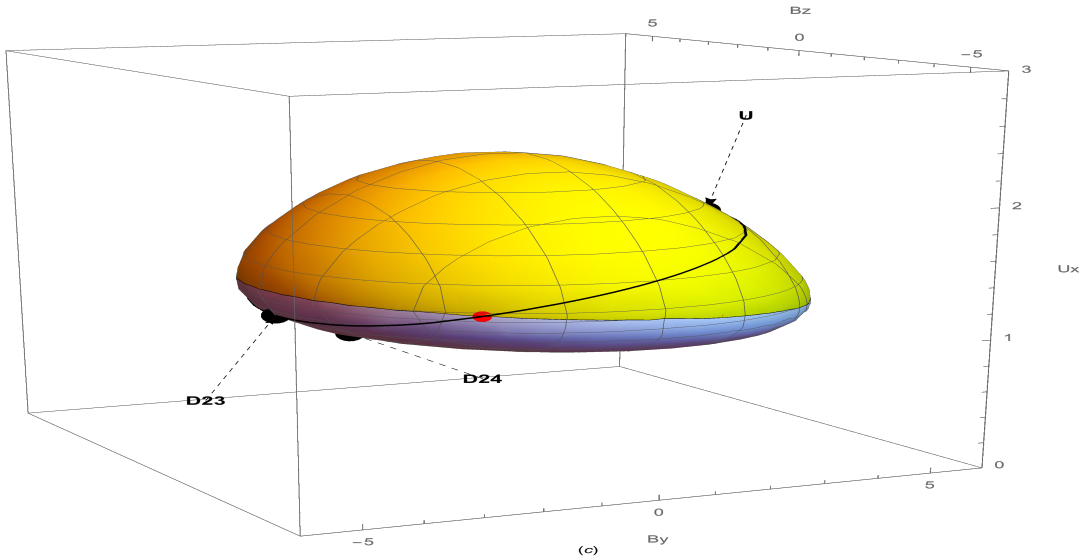

Figure 49: As for Fig 45, but with $\theta_1 = 37°$ and $\frac{u_{x1}}{a_1} = 1.75$. An intermediate $2^+ \to 3^-$ shock of the $2^+ \to 3^-\&2^+ \to 4^-$ family having a unique passage along separatrices and smoothly through the transonic transition points, shown as red circles (see text)

7.2.3 $2^+ \to 4^-$ Shock Structure from Numerical Integration

The $2^+ \to 4^-$ shock structure associated with the $2^+ \to 3^-$ shock in §7.2.2 is shown in Figure 50. The numerical integration from the upstream point follows the separatrix out of the upstream saddle point, as in the case of the $2^+ \to 3^-$ shock, and undergoes a gas dynamic jump to the subsonic surface prior to reaching the transonic flow point. In the case shown here, the jump occurs at $B_y = -1.13244$. On the subsonic sheet the vector field, as indicated in Figure 50(a), leads the integral curve to the downstream sink at D24.

To reach the downstream state the $2^+ \to 4^-$ shocks all involve a gas dynamic jump, either before the integral curve reaches a stationary point on the supersonic surface, as in §7.1.3, or before the integral curve reaches a transonic transition point, as in the example just given. The position of the gas dynamic jump represents a degree of freedom, so $2^+ \to 4^-$ shocks are a one-parameter family.

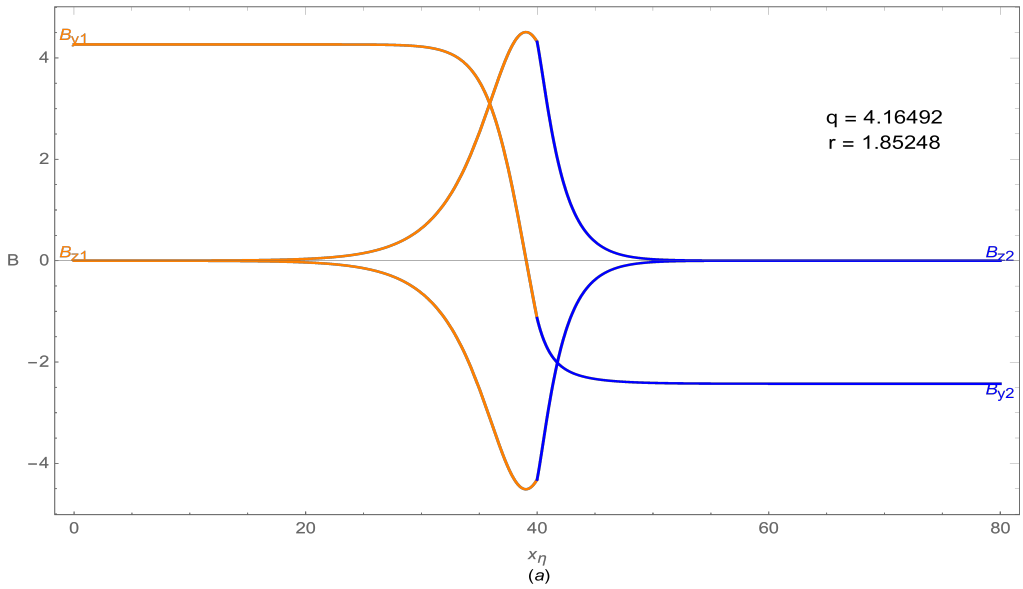

(a)

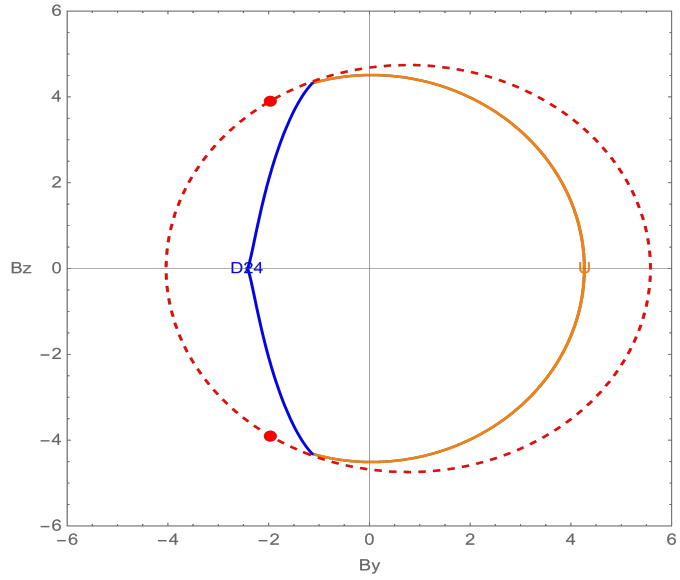

(b)

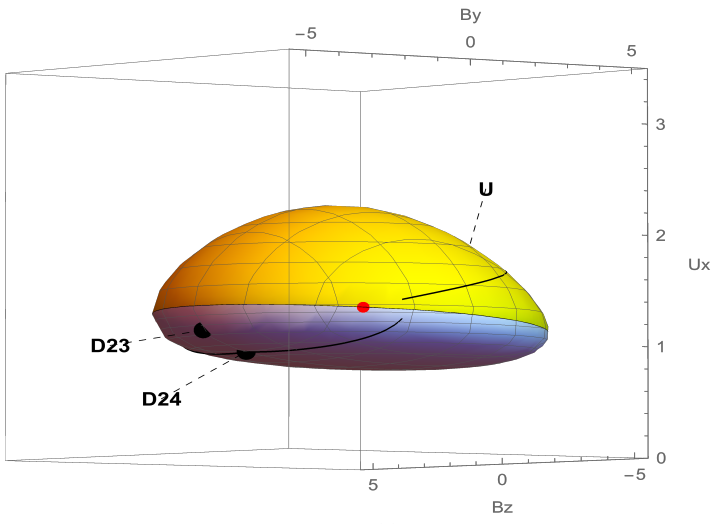

(c)

Figure 50: As for Fig 45, but with $\theta_1 = 37°$ and $\frac{u_{x1}}{a_1} = 1.75$. An intermediate $2^+ \to 4^-$ shock of a $2^+ \to 3^-$&$2^+ \to 4^-$ family. The location of the gas dynamic jump to the subsonic surface represents a degree of freedom yielding a one-parameter family of solutions.

7.3 Intermediate $2^- \rightarrow 3^-$ and Intermediate $2^- \rightarrow 4^-$ Shock Family

The example given in this section uses the upstream speed at the black dot on the 63° line in the yellow zone of Figure 3. A transonic transition point is not present in a $2^- \rightarrow 3^-$ and $2^- \rightarrow 4^-$ family as they are restricted to the subsonic sheet.

7.3.1 Phase Plane

For the set of upstream parameters $\left\{1, 2, \frac{5}{3}, 1, 63°, u_{x1}\right\}$ when $u_{x1} = 0.93$ three stationary points are found on the subsonic sheet and one on the supersonic sheet as shown in Figure 51(a) . In this case the upstream conditions are subsonic with phase trajectories unable to access the supersonic stationary point. Subsonic trajectories can link the upstream source U with the saddle D23 and the sink D24. Figure 51(b) and (c) show a close up view of the stationary points near the subsonic boundary. The upstream B_y eigenvalue is approximately 500 times that of the B_z eigenvalue producing vectors that are pointing dominantly in the B_y direction. Similarly the B_y eigenvalue at the saddle D23 has a magnitude approximately 60 times that of its B_z value producing arrows with a strong B_y component.

As the upstream shock speed increases the location of the supersonic stationary point shifts to increasing B_y and the subsonic stationary points with negative values of B_y approach each other to form a double root of (120) at the Jouget speed. As the upstream speed increases past a_1 (121) indicates that the upstream stationary point becomes a saddle on the supersonic sheet and the other supersonic stationary point gradually increases in its B_y value, shock transitions not being possible during this stage as U is a sink. When the upstream speed equals the upstream fast speed the supersonic stationary points merge forming a double root of (120). For upstream speeds greater than the fast speed (121) indicates that the upstream point behaves as a source and Figure 6(e) shows that the downstream supersonic stationary point becomes a saddle, allowing a supersonic fast shock trajectory from the upstream source to the downstream saddle.

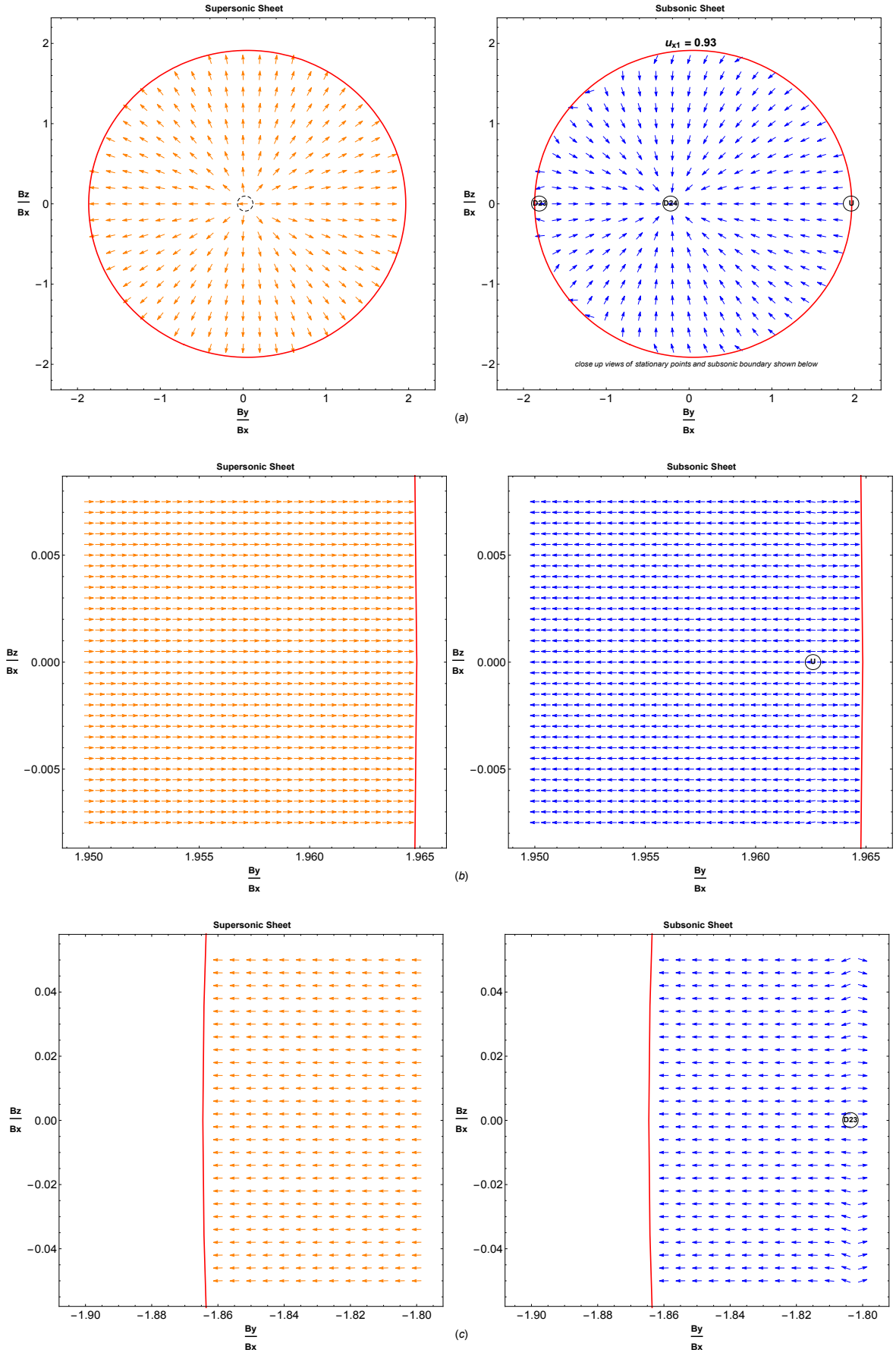

Figure 51: As for Fig 44, but with $\theta_1 = 63°$ and $\frac{u_{x1}}{a_1} = 0.93$. In this case there is a unique $2^- \to 3^-$ transition and a one-parameter family of $2^- \to 4^-$ transitions. The lower rows show expanded views of the stationary points.

7.3.2 $2^- \to 3^-$ Shock Structure from Numerical Integration

For the set of upstream parameters $\left\{1, 2, \frac{5}{3}, 1, 63°, 0.93\right\}$ the upstream and downstream points in the $B_y - B_z$ plane are a source and and a saddle respectively. A linear analysis about the upstream point gives eigenvalues of 21.9 and 0.0435 in the B_y and B_z directions respectively, as a result the B_z component around the upstream point is not apparent in Figure 51b. The downstream saddle point has B_y and B_z eigenvalues of 2.87 and -0.0474 respectively. As a result it is easier to integrate out of the downstream point along the x axis in the negative direction using a small step-off in the B_z direction as the B_z eigenvalue is relatively greater at the downstream point. Using a step-off of ± 0.001 in the B_z direction the ODEs were numerically integrated in the phase plane to produce the structures shown in Figure 52(a) and (b). The integral curve joining the upstream and downstream points represents a unique transition on the subsonic sheet. Figure 52(c) shows the transition from the upstream state to the downstream state in $B_y - B_z - u_x$ space. The subsonic surface on which the transition occurs is shown in blue.

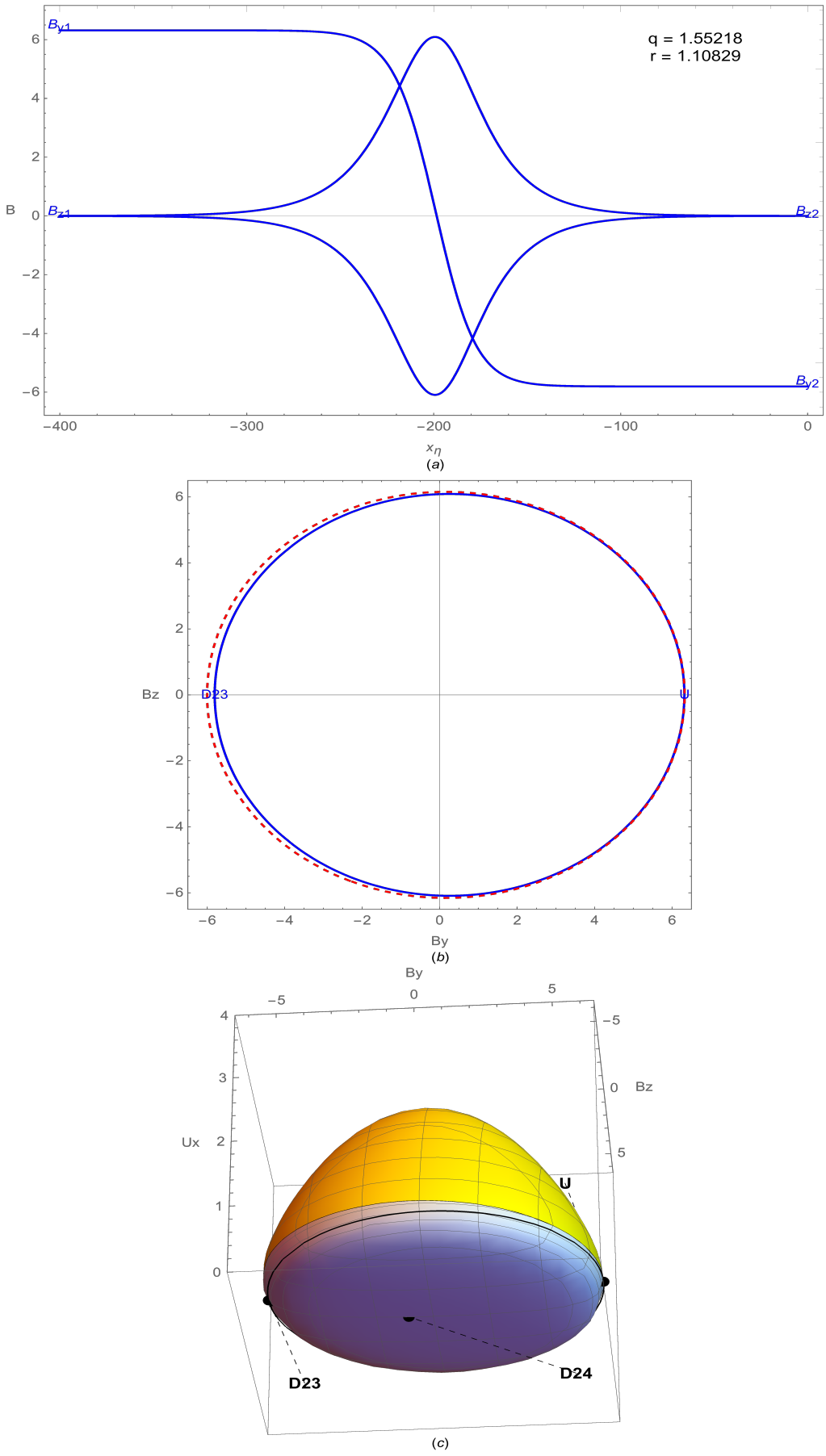

Figure 52: As for Fig 45, but with $\theta_1 = 63°$ and $\frac{u_{x1}}{a_1} = 0.93$. The $2^- \to 3^-$ shocks of the $2^- \to 3^- \& 2^- \to 4^-$ family. Diagrams show a pair of unique transitions from upstream source to downstream saddle.

7.3.3 $2^- \rightarrow 4^-$ Shock Structure from Numerical Integration

This subsection presents the structure of the $2^- \rightarrow 4^-$ shock. This structure is unusual as B_z decreases shortly after leaving the upstream point, the ratio $\left|\frac{B_z}{B_y}\right|$ being very small through the shock and in a particular case is equal to zero, a feature that is absent in other types of intermediate shocks.

The $2^- \rightarrow 4^-$ transition that follows is associated with the same set of upstream conditions as that given in the previous subsection. The $B_y - B_z$ phase plane structure is shown on Figure 51. The upstream and downstream points are a source and sink respectively. Linear analysis about these stationary points reveals that the upstream and downstream eigenvalues are $\{+21.9, +0.0435\}$ and $\{-0.384, -0.378\}$ respectively. To compute the integral curve it is necessary to begin by taking a small step-off from the upstream point at an angle to the B_y axis. The angle introduces a degree of freedom into the shock structure. The magnitude of the step-off was chosen as 0.0001 and illustrative directions were chosen to be 95° and 180° to the positive B_y axis.

The 95° step-off angle was selected to compare the variation in B_z with a step-off angle of 180° to the positive B_y axis. The 180° solution follows the vector field in Figure 51a and b directly from the upstream point U to the downstream point D24 with $B_z = 0$ throughout the transition.

The variation in density through the shock is shown in Figure 53b. The density undergoes a compressive stage to a maximum value and then an expansive stage to the downstream value. The presence of compressive and expansive zones in the phase plane was indicated in §4.3 and shown in Figure 25 for the case of $\theta_1 = 15°$. The specific entropy monotonically increases throughout the transition. Figure 53c shows the transition in $B_y - B_z - u_x$ space, the upstream point indicated by U being slightly inside the junction of the subsonic and supersonic surfaces. The shock is the transition, shown as a black line, across the blue subsonic surface to the downstream point D.

The $2^- \rightarrow 4^-$ shock has one degree of freedom, characterised here by the choice of the step-off angle from the upstream point in the $B_y - B_z$ plane.

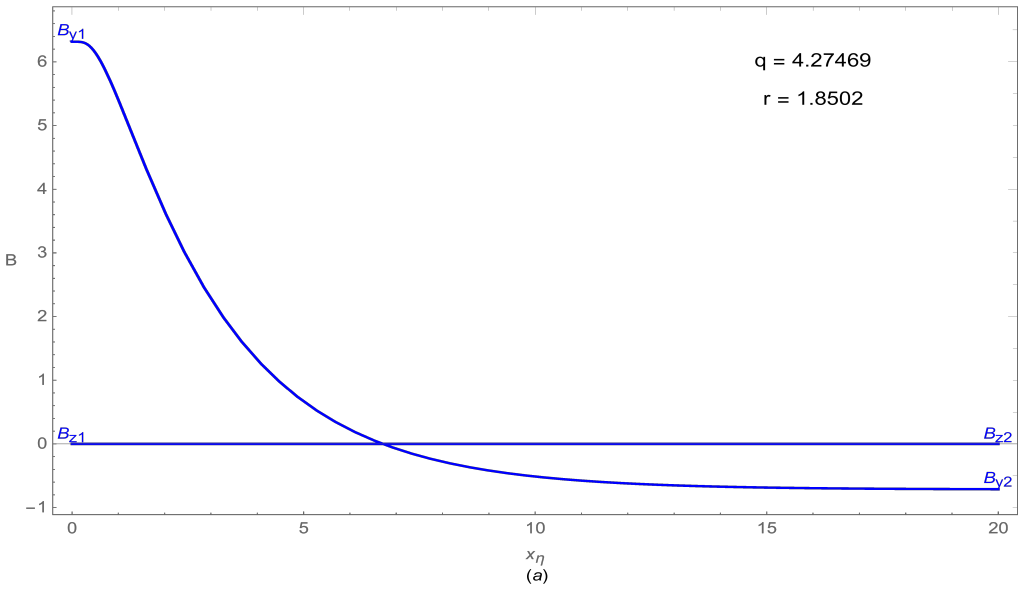

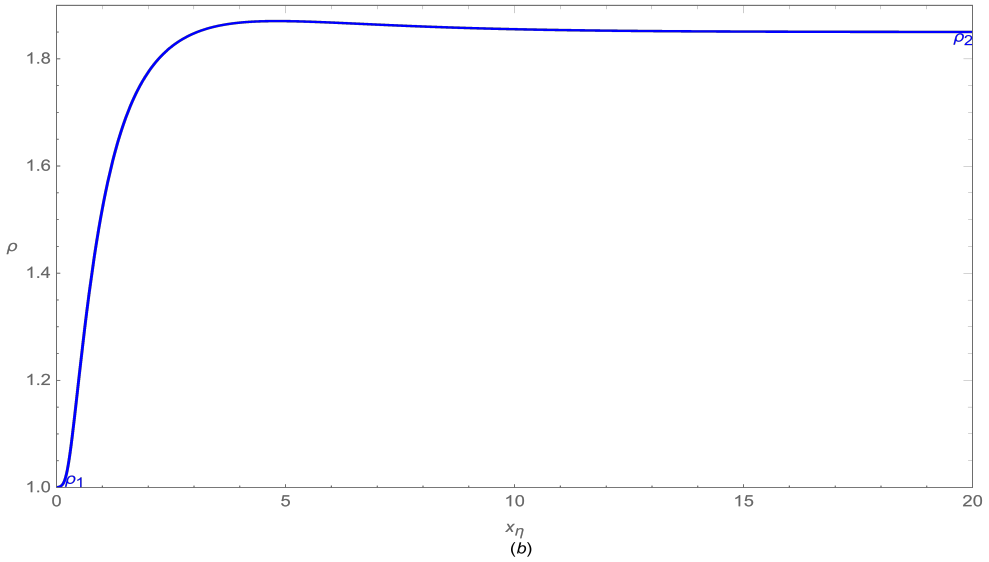

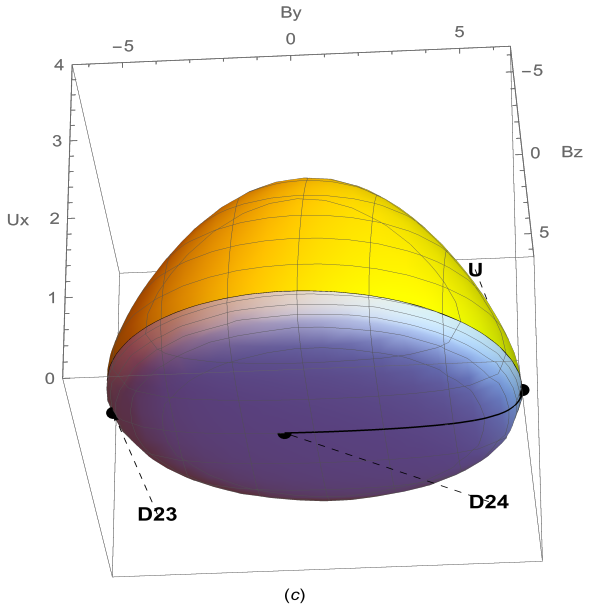

Figure 53: Behaviour of B_y, B_z, ρ and u_x in the $2^- \rightarrow 4^-$ shock of a $2^- \rightarrow 3^-$&$2^- \rightarrow 4^-$ family. (a) B_y and B_z through the shock, B_z rapidly approaches zero (b) ρ reaches a maximum and then decreases to the downstream value (c) passage from U to D24 on subsonic surface with $B_z \simeq 0; \frac{b_1}{a_1} = 2$, $\theta_1 = 63°$, $\frac{u_{x1}}{a_1} = 0.93$

7.4 Intermediate $1^+ \to 3^-$, Intermediate $1^+ \to 4^-$ and Fast $1^+ \to 2^-$ Shock Family

The example given in this section adopts the upstream state corresponding to the black dot on the 5° line in the green zone of Figure 3. This dot lies between the equisonic and Jouget curves in the green zone, where all three downstream stationary points are subsonic. Since at the location of the dot $u_{x1} > a_1$, the phase plane has a supersonic upstream stationary point and three subsonic downstream stationary points. As the black dot is outside of the region between the red equisonic curves smooth transonic transitions do not occur.

7.4.1 Phase Plane

Figure 54 shows the vector fields for the upstream shock speed of 2.92. The upstream source on the supersonic sheet allows trajectories to link with stationary points on the subsonic sheet after undergoing gas dynamic jumps. A trajectory can link with the greater B_y value stationary point by undergoing a gas dynamic jump at the downstream point, the transition being a fast shock. Upstream trajectories can also reach the downstream stationary points of negative B_y value by undergoing a jump on the B_y axis or in the plane to join a trajectory to the sink D14, or make a jump to the separatrix linking to the saddle at D13.

As the upstream shock speed increases the intermediate stationary points D13 and D14 merge when $u_{x1} = v_{j1}$ the only transition thereafter possible from the upstream point being a supersonic to subsonic fast shock to the D12 point.

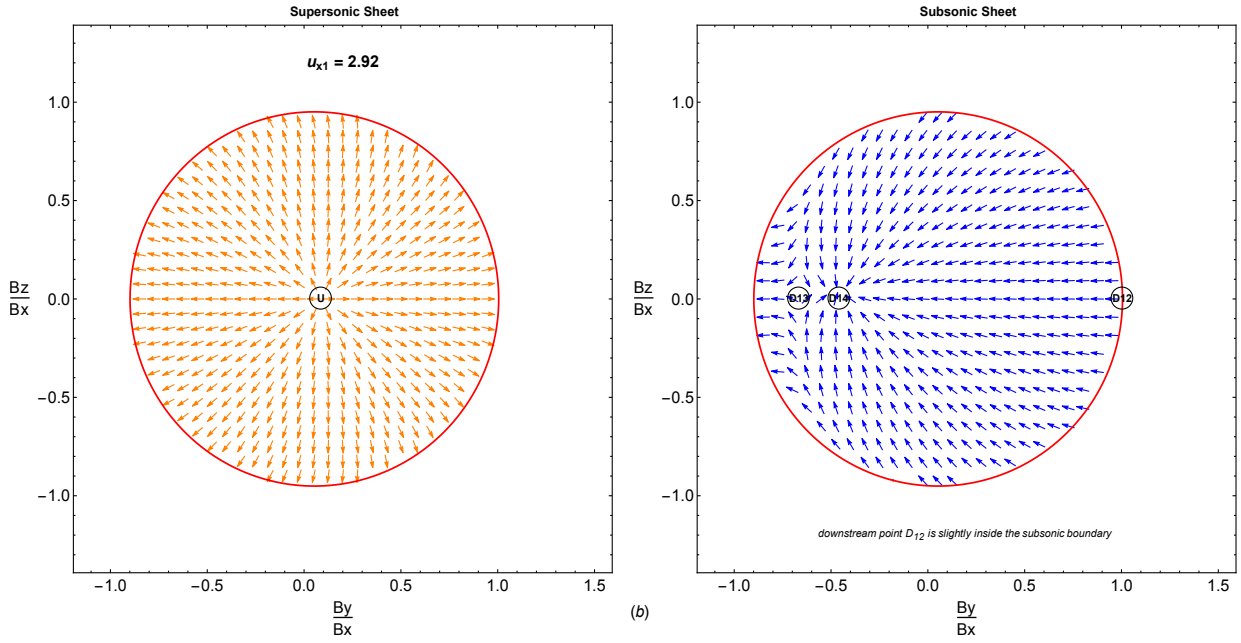

Figure 54: As for Fig 44, but with $\theta_1 = 5°$ and $\frac{u_{x1}}{a_1} = 2.92$. The upstream state lies on the supersonic sheet, with three downstream states on the subsonic sheet. There is a unique $1^+ \to 2^-$ shock, a one-parameter family of $1^+ \to 3^-$ shocks and a two parameter family of $1^+ \to 4^-$ shocks.

7.4.2 $1^+ \rightarrow 3^-$ Shock Structure from Numerical Integration

The $1^+ \rightarrow 3^-$ structure is determined by a trajectory leaving the upstream point on the supersonic sheet at an angle ϕ to the B_y axis and undergoing a gas dynamic jump over the exact point where the separatrix leads to the downstram saddle. Computationally, the structure is determined in reverse by a simultaneous numerical integration of the ODEs (27) and (28) from the downstream D13 saddle stationary point on the subsonic surface with a isomagnetic jump made to the supersonic surface at a designated point on the separatrix. The eigenvalues of the first order solution about the saddle point are $\{+0.219284, -0.205137\}$ as indicated by the direction of the vector fields in Figure 54. The integration is carried out in the negative x direction with a step-off in the B_z direction of size 0.0001. After the computational jump to the supersonic state the integration proceeds in the negative direction towards the upstream source as it is the only stationary point on the supersonic sheet. This procedure is chosen for computational ease due to the relative difficulty of shooting numerically from the upstream point to the exact value of the designated point on the separatrix to enable the structure to transition towards the D13 subsonic state.

For illustrative purposes six trajectories in the $B_y - B_z$ plane are presented in Figure 55. Reading clockwise from left to right in Figure 55b, the first structure is when the gas dynamic jump to the subsonic state occurs at the magnetic field values of the D13 point. This structure does not gain a B_z component during the transition. The next structure is when the jump occurs in the (B_y, B_z) plane at $(-4, \pm 3.20600)$. The next structure displayed is when the gas dynamic jump occurs at a point closer to the subsonic boundary in the (B_y, B_z) plane, at $(2, \pm 6.35245)$. In terms of structure, the last mentioned jump is a change from a fast $1^+ \rightarrow 2^-$ shock from the upstream point to an intermediate $2^- \rightarrow 3^-$ shock to D13 as given in §7.3.2. In Figure 55b the blue curve represents the phase plane trajectory from the D12 source point to the D13 saddle point.

Intermediate $1^+ \rightarrow 3^-$ shocks have one degree of freedom in their structure this being represented by the location of the isomagnetic jump point to the separatrix leading to the downstream saddle on the subsonic surface.

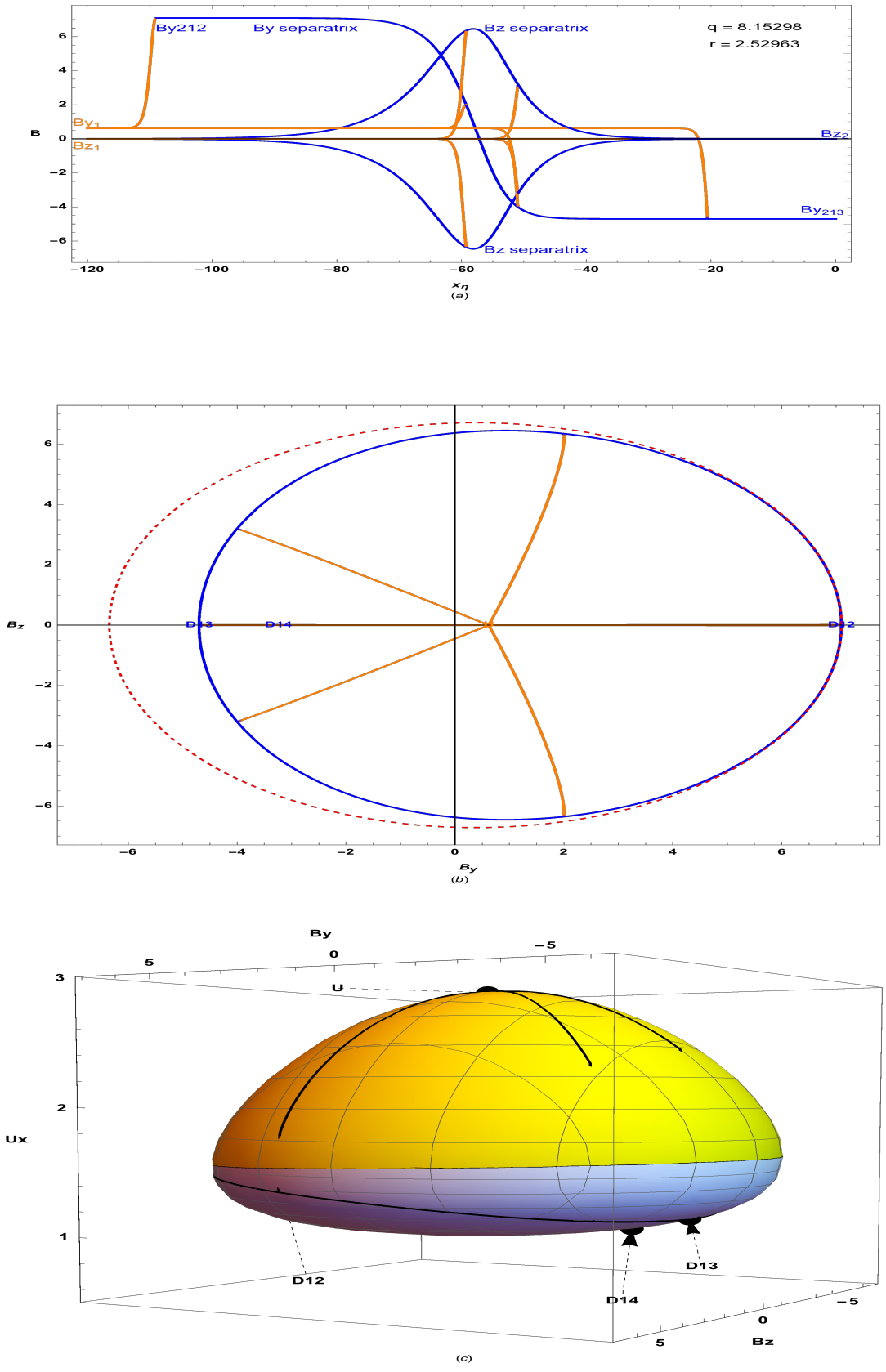

Figure 55: As for Fig 45, but $\theta_1 = 5°$ and $\frac{u_{x1}}{a_1} = 2.92$. Five $1^+ \to 3^-$ trajectories leave the upstream point and undergo a gas dynamic jump to the subsonic separatrices leading to the downstream point D13. The angle at which the trajectories leave U represents a degree of freedom yielding a one-parameter family of shock solutions.

7.4.3 $1^+ \to 4^-$ Shock Structure from Numerical Integration

The $1^+ \to 4^-$ structure in this family is determined by two free parameters, the angle at which the phase plane trajectory leaves the upstream point, ϕ, and the point on the trajectory where the gas dynamic jump occurs to the subsonic sheet before reaching the points.

Figure 56 shows representative shock structures for ϕ values of $0, \pm 40°, \pm 140°$ and $180°$. For $\phi = 0$ the jump can occur in the phase plane at any point between U and D14, and for $\phi = 180°$ the jump can occur between U and D12. In Figure 56 the jump points in the phase plane for these two cases are D14 and D12. For $\phi = \pm 40°$ the jumps occur in the $B_y - B_z$ phase plane at $(3, \pm 2.25485)$ and $(5.1, \pm 4.69022)$. For $\phi = \pm 140°$ the phase plane jumps are at $(-3, \pm 3.11062)$ and $(-3.7, \pm 3.66279)$.

The numerical solution of the ODEs (27) and (28) starts from the upstream point with a step-off of magnitude 0.0001 into the $B_y - B_z$ plane. The integration is carried out in the postive x direction as indicated by the outflowing vectors from U on the supersonic sheet in Figure 54. On reaching the designated jump point the integration restarts on the subsonic sheet, this being done using the negative branch of the square root in the ODEs. The profile of the magnetic field vectors in the shock transitions is shown in Figure 56(a) where supersonic flow is shown in orange and subsonic in blue. For clarity, only magnetic field component profiles for positive values of ϕ, with B_z being positive, are shown in Figure 56(a). The tallest peak in the profile belongs to the fast shock transition from U to D12 with a gas dynamic jump at D12 changing the shock transition to an intermediate $2^- \to 4^-$ transition, without a B_z component, on the subsonic sheet. Figure 56(b) shows the $B_y - B_z$ phase plane plot of the shock transitions. Phase plane trajectories approaching the separatrix from the saddle at D13 linking the source at D12 must undergo an isomagnetic jump to reach the sink D14 on the subsonic surface before the separatrix is reached. The separatrix is shown as the dashed blue curve, the supersonic and subsonic boundary is shown as the dashed red curve.

Figure 56(c) shows the shock structures in $B_y - B_z - u_x$ space. Trajectories reaching the blue subsonic surface at points other than on the subsonic separatrix curve towards the D14 point. If the isomagnetic jump is on the separatrix the transition is a $1^+ \to 3^-$ intermediate shock as described in §7.4.2.

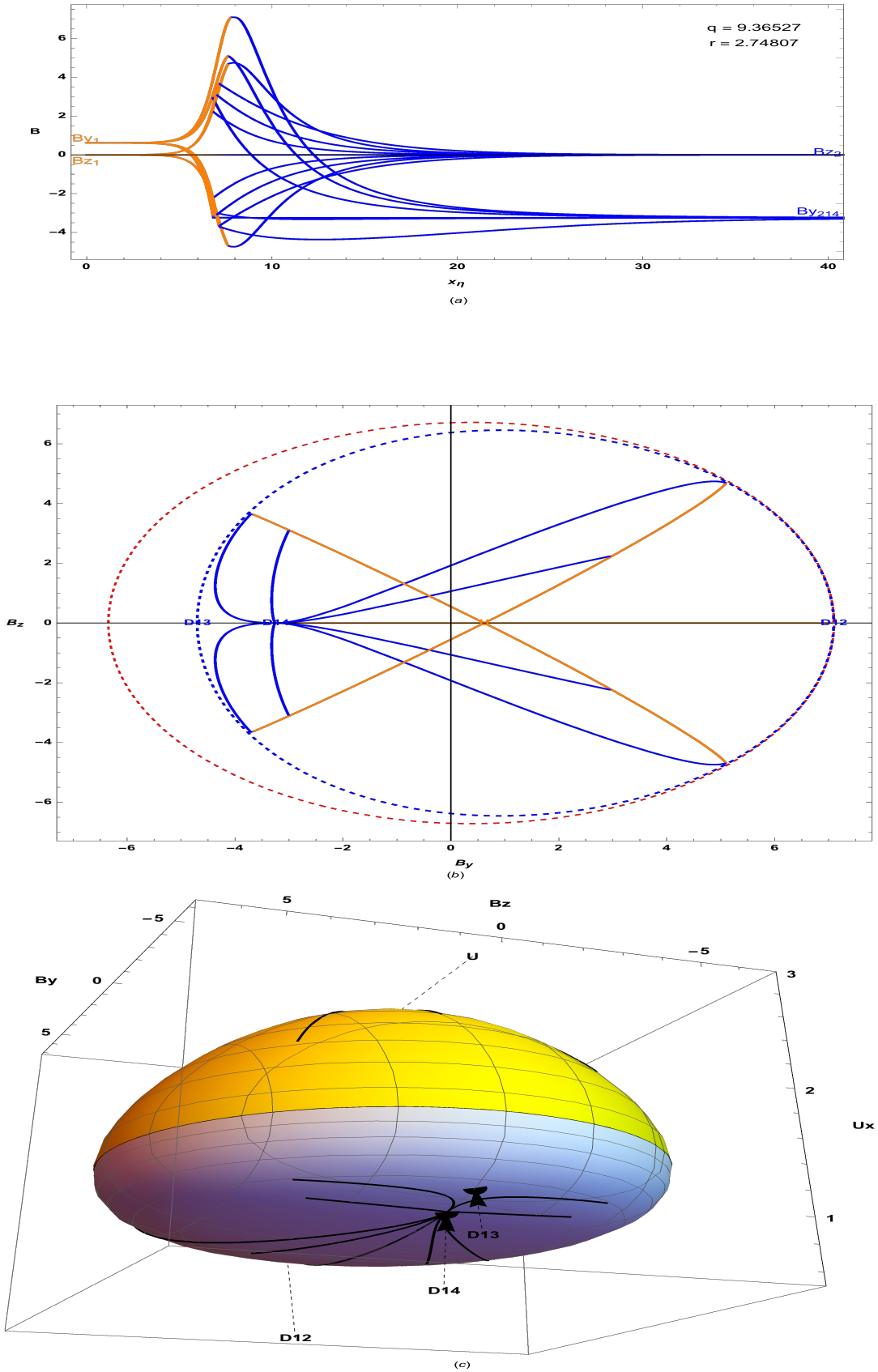

Figure 56: As for Fig 45, but with $\theta_1 = 5°$ and $\frac{u_{x1}}{a_1} = 2.92$. Trajectories leave the upstream point and undergo a gas dynamic jump to the subsonic sheet. Jumps not to a separatrix lead to the D14 point. The angle at which the trajectories leave U and the location of the jump give $1^+ \rightarrow 4^-$ trajectories two degrees of freedom this being a two-parameter family of shock solutions.

7.5 Intermediate $1^+ \to 3^+$, Intermediate $1^+ \to 4^-$ and Fast $1^+ \to 2^+$ Shock Family

Continuing the development of the phase plane structure associated with the upstream parameter set $\{1, 2, \frac{5}{3}, 1, 15°, u_{x1}\}$ considered in §5.1, §5.2, §6.1, §6.2 and §7.1, this section considers the upstream state at the first black dot in the green zone on the 15° line in Figure 3. This point is outside the region bounded by the red equisonic curves so that a transonic transition point on the boundary of supersonic and subsonic sheets cannot exist.

7.5.1 Phase Plane

Figure 57(a) and (b) shows phase plane structures with three and one stationary points on the supersonic and subsonic sheets respectively.

In Figure 57(a) the upstream shock speed, $u_{x1} = 2.2$, is less than the upstream intermediate equisonic speed, which in this case equals 2.28129, as shown on Figure 10. A transonic transition point is not produced by this upstream shock speed. A fast shock trajectory along the B_y axis links U to D12. Trajectories leaving U at an angle to the B_y axis can undergo a gas dynamic jump to the subsonic sheet and link to the subsonic sink D14 as an intermediate $1^+ \to 4^-$ shock. Alternatively, upstream trajectories from U can link to the supersonic stationary point of negative B_y value by a direct path along the negative B_y axis or by a trajectory in the plane that merges with the separatrix entering the downstream saddle. These transitions are classified as an intermediate $1^+ \to 3^+$ shock.

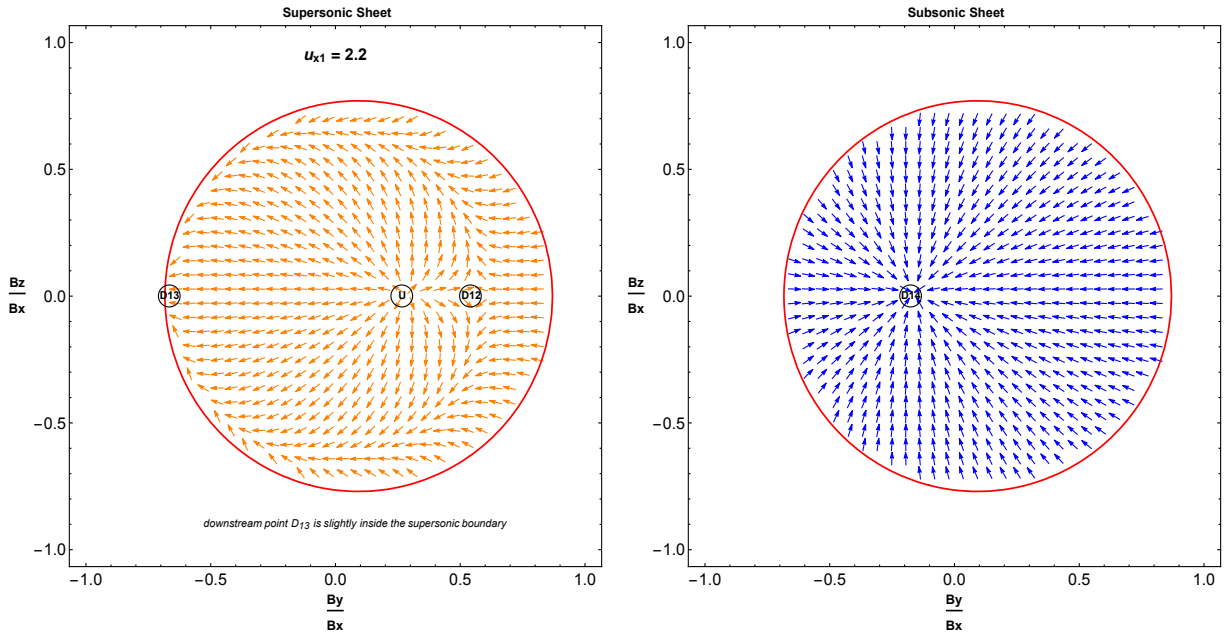

Figure 57: As for Fig 44, but with $\frac{u_{x1}}{a_1} = 2.2$. Three stationary states lie on the supersonic sheet and one on the subsonic. A unique fast shock trajectory links U and D12. Supersonic trajectories remaining in the plane merge with the separatrix leading to D13 producing a $1^+ \to 3^+$ shock. Trajectories from U may undergo a gas dynamic jump to the subsonic sheet giving a $1^+ \to 4^-$ shock.

7.5.2 $1^+ \to 3^+$ Shock Structure from Numerical Integration

This subsection presents $1^+ \to 3^+$ intermediate shock structure in the case where the upstream and downstream states are both supersonic as shown in Figure 57. The numerical solution of the ODEs (27) and (28) uses a step-off into the $B_y - B_z$ plane of magnitude 0.0001 from the upstream point at various angles ϕ to the positive B_y axis. Figure 58(a) shows the shock profiles in $B - x_\eta$ space for step-off angles 0°, 0.1°, 180° and 359.9°. The $\phi = 0°$ solution follows the direct path to the downstream saddle D12, the transition is a fast shock. The $\phi = 0.1°$ solution closely follows the initial path of the 0° solution gaining a positive B_z component due to the presence of the downstream saddle point causing the integral curve to bend sharply in $B_y - B_z - u_x$ space following the separatrix from the saddle point towards the downstream sink undergoing a reversal in the direction of its B_y component and so forming an intermediate $1^+ \to 3^+$ shock. The $\phi = 180°$ solution follows a direct path to the downstream sink, not gaining a B_z component over the transition, reversing the direction and increasing the magnitude of its B_y magnetic field component. The $\phi = 359.9°$ step-off produces the same solution, apart from B_z and v_z having opposite sign, as $\phi = 0.1°$ as (27) is an even function in B_z.

Figure 58(b) shows the paths in the $B_y - B_z$ plane. The $\phi = 0.1°$ and $\phi = 359.9°$ solutions are shown with another 32 integral curves from the upstream point with step-off angle at 11.25° increments from the positive B_y axis. Figure 58(c) shows the integral curves of (b) in $B_y - B_z - u_x$ space.

Intermediate $1^+ \to 3^+$ shocks have one degree of freedom in their formation producing non-unique structures in the transition from the upstream state to the downstream state.

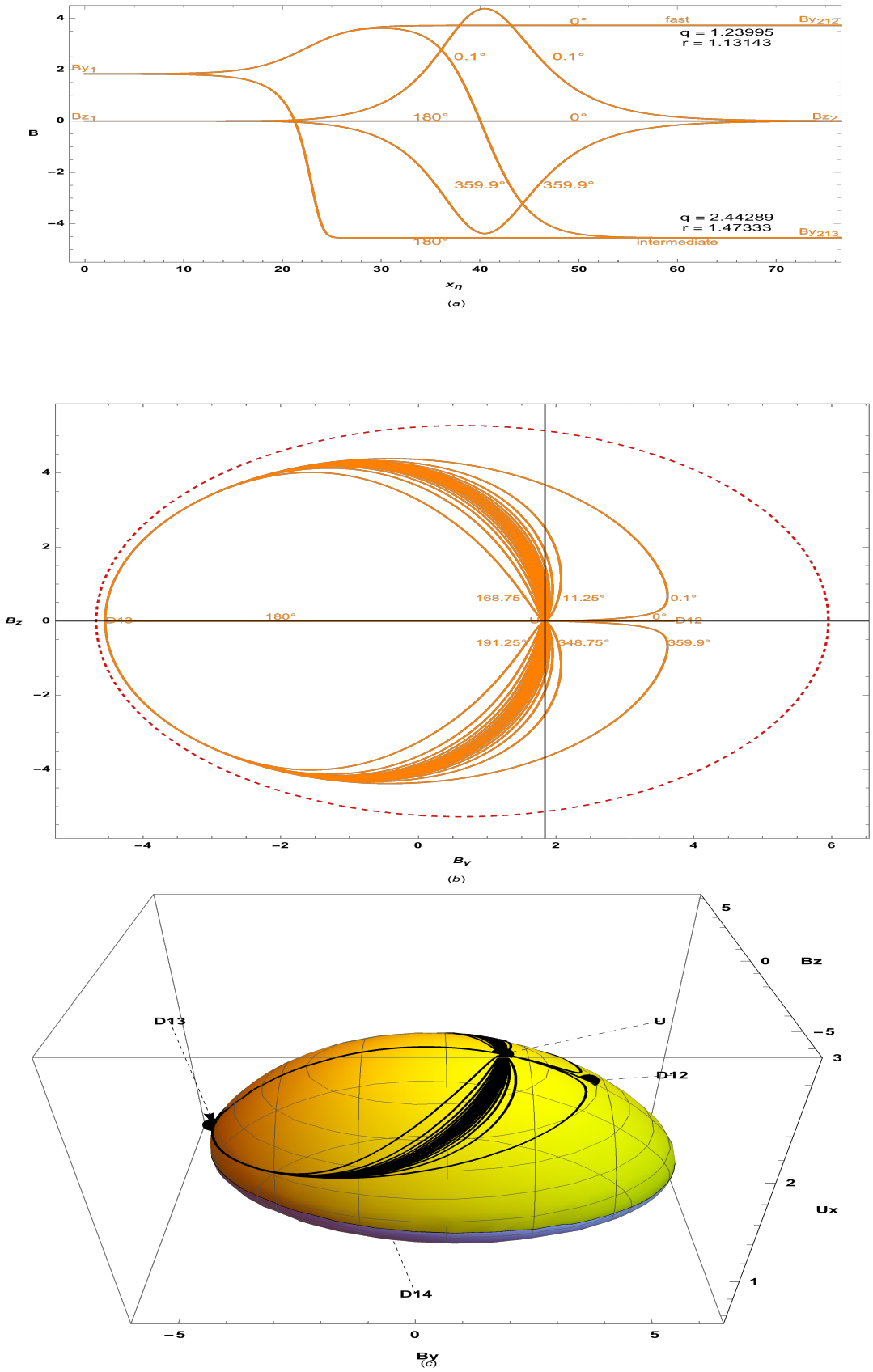

Figure 58: As for Fig 45, but $\frac{u_{x1}}{a_1} = 2.2$. Trajectories leave U and those remaining supersonic merge with the separatrices to reach D13. The angle at which the trajectories leave U gives these shocks one degree of freedom yielding a one-parameter family of $1^+ \rightarrow 3^+$ shocks.

7.5.3 $1^+ \rightarrow 4^-$ Shock Structure from Numerical Integration

To reach the final subsonic D14 state the shock must undergo a gas dynamic jump in which the magnetic field components B_x, B_y and B_z are unchanged but u_x decreases.

The numerical integration is started as in §7.5.2 and proceeds to the selected point in $B_y - B_z$ supersonic space where the gas dynamic jump occurs to an integral curve in subsonic $B_y - B_z$ space that leads to the downstream point D14. The jump point can be at any point along the supersonic integral curve as there is only one stationary point on the subsonic $B_y - B_z$ plane, introducing an additional degree of freedom. The latter transition structurally has a shock within a shock as initial $1^+ \rightarrow 3^+$ shock undergoes a gas dynamic reduction in normal flow velocity and an increase in mass density and gas pressure at the D13 point to become a slow shock to reach the final D14 state.

By way of example, the first jump point in the transition is chosen to be at $B_y = -0.5$. Figure 59a shows the shock profile. Magnetic field profiles are shown for three values of ϕ, $0.1°, 180°$ and $359.9°$. The B_y structure for the first and last step-off angles are identical. The separatrix from the saddle point D13 is shown as the dotted orange curve in Figure 59 b. All integral curves from the upstream point except those for $\phi = 0°$ and $\phi = 180°$ approach the separatrix. At the chosen jump point the 30 integral curves in the $11.25°$ increment set have not reached the separatrix and so produce differing subsonic shock structures. This is shown on Figure 59c.

Trajectories leaving the upstream point for $\phi > 90°$ undergo an initial expansive stage and then become compressive with a final expansive stage as they approach D14.

The second chosen jump point is $B_y = -4.5$, slightly before in the $B_y - B_z$ plane the D13 point as shown in Figure 60b and c. The magnetic field profiles for three values of ϕ as shown in Figure 60a. Figure 60c shows the 32 integral curves leaving the upstream point computed at ϕ increments of $11.25°$. These integral curves approach the separatrix from the upstream saddle linking the downstream supersonic sink. The separatrix is shown as the dotted orange curve. At the chosen jump point the thirty $11.25°$ incremental integral curves are close together and share an approximately common subsonic passage to the D14 point as shown on Figure 60c. The magnitude of the transverse magnetic field component decreases as the trajectory approaches the subsonic stationary point D14.

Transitions in the second example do not undergo an expansive stage as they approach the downstream point.

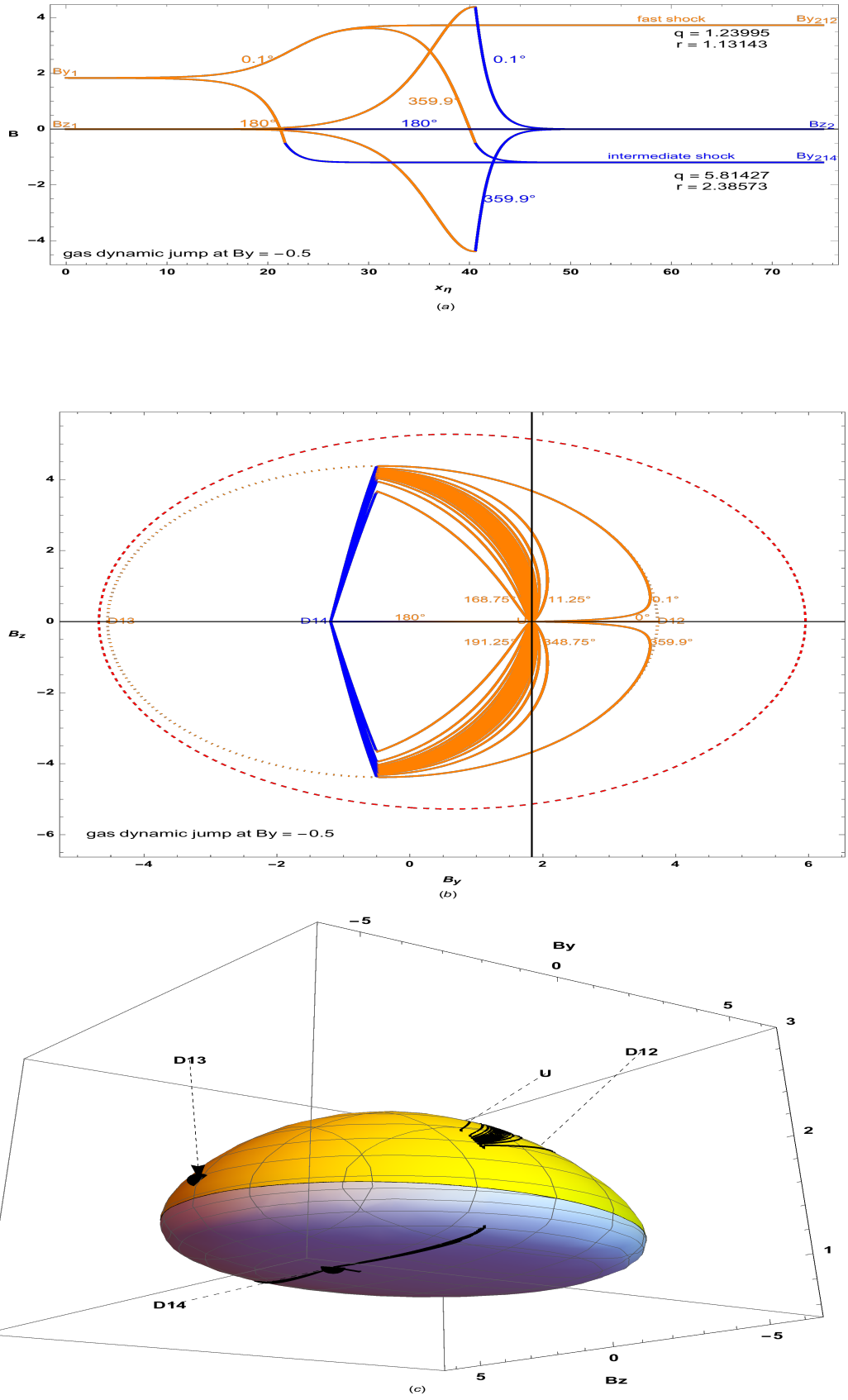

Figure 59: As for Fig 45, but $\frac{u_{x1}}{a_1} = 2.2$. Trajectories from U undergo a gas dynamic jump to the subsonic surface and then converge on the sink D14. For ease of visualisation, all trajectories jumped at a common B_y value. The angle at which the trajectories leave U and the location of the gas dynamic jump gives these shocks two degrees of freedom being a two-parameter $1^+ \to 4^-$ family of solutions.

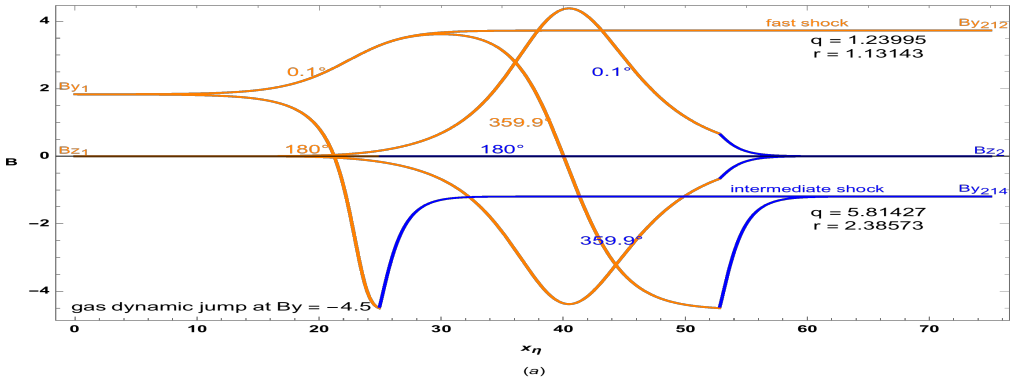

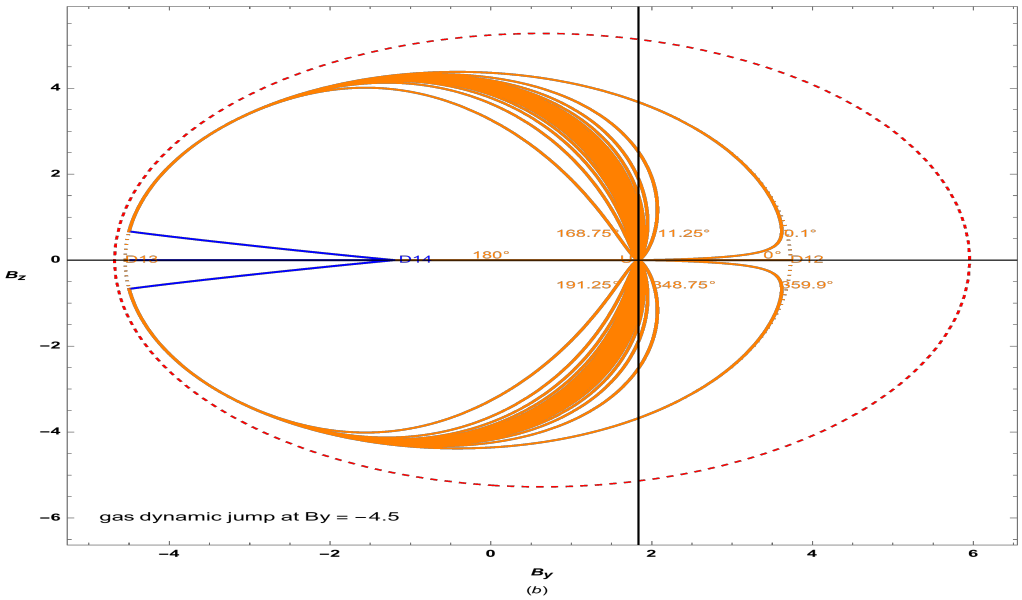

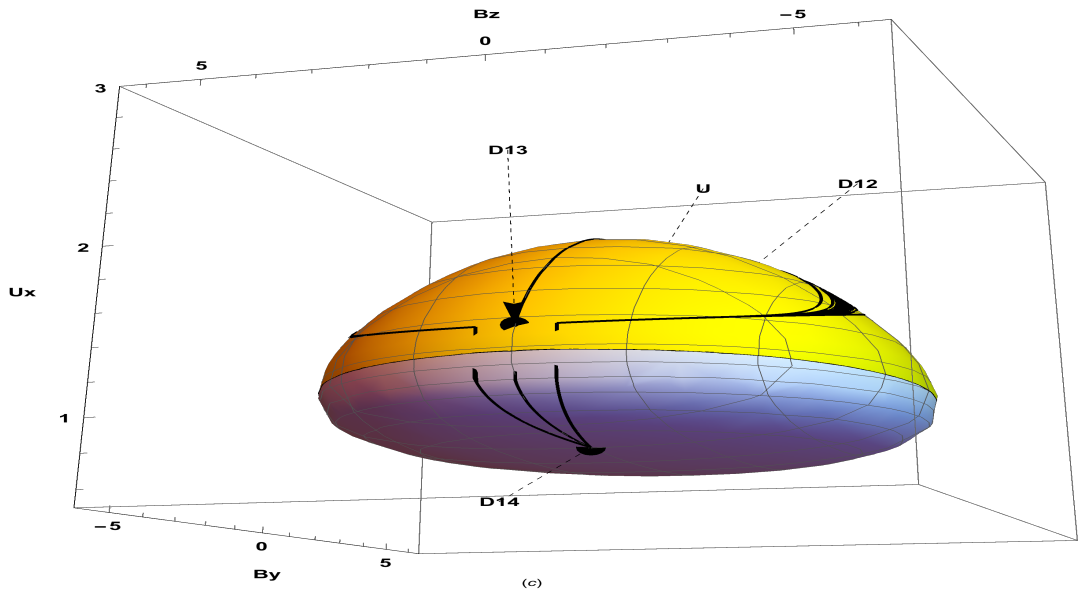

Figure 60: As for Fig 59, but now the gas dynamic jump occurs near the D13 point. $1^+ \to 4^-$trajectories now decrease in $|B_y|$ as they approach the subsonic sink D14.

7.6 Intermediate $1^+ \to 3^-$, Intermediate $1^+ \to 4^-$ and Fast $1^+ \to 2^+$ Shock Family

This section considers the upstream state at the second black dot in the green zone on the 15° line in Figure 3. For this choice, the D12 stationary point is on the supersonic sheet and D13 and D14 lie on the subsonic sheet.

7.6.1 Phase Plane

Figure 61 shows the phase plane with the locations of the two transonic transition points indicated on the boundary. A fast shock transition along the B_y axis links U to the D12 stationary point. Oblique trajectories can undergo a gas dynamic jump to the subsonic sheet and link with the sink as an intermediate $1^+ \to 4^-$ shock. If the gas dynamic jump occurs at a point in the $B_y - B_z$ plane on the separatrix connecting the supersonic and subsonic saddle points after the separatrix passes through the transonic transition point, the transition is an intermediate $1^+ \to 3^-$ shock. If the gas dynamic jump from the supersonic to the subsonic sheet occurs at the transonic flow point a smooth transition in terms of the magnetic field derivatives occurs this being a $1^+ \to 4^-$ shock. The separatrix from the D12 saddle point on the supersonic sheet passes through the transonic point on its way to the subsonic D13 saddle. This phase trajectory represents a $2^+ \to 3^-$ shock with D12 as its upstream point as in §7.2.

The point considered in Figure 3 is close to the Jouget curve. As the upstream shock speed increases the subsonic stationary points merge at the Jouget speed producing no subsonic stationary points for slightly greater upstream shock speeds as shown on Figure 26(c).

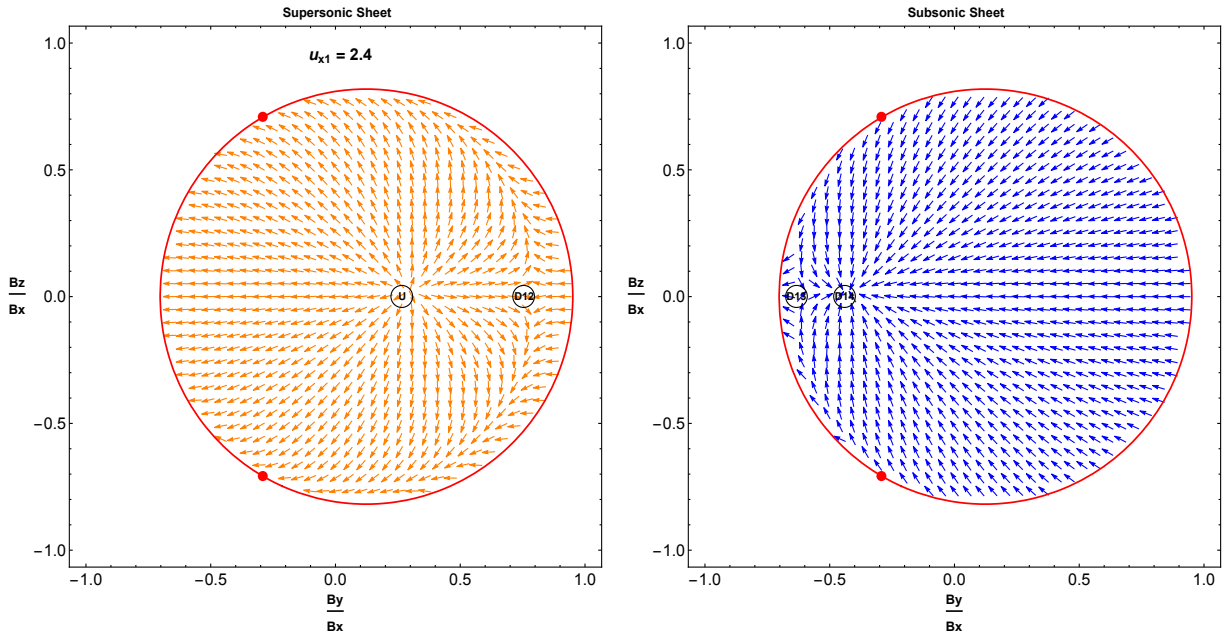

Figure 61: As for Fig 44, but $\frac{u_{x1}}{a_1} = 2.4$. Two stationary points are on each sheet and transonic transition points (red circles) are present. A unique fast shock links U and D12. Supersonic trajectories can undergo a gas dynamic jump to the separatrices and reach the subsonic saddle D13 forming a one parameter family of $1^+ \to 3^-$ shocks due to the departure angle from U. Supersonic trajectories may undergo a gas dynamic jump to the subsonic sheet and converge on the sink giving a two-parameter family of $1^+ \to 4^-$ shocks with parameters being the departure angle from U and the location of the jump. A smooth $1^+ \to 4^-$ transition can occur through the transonic transition point (see text).

7.6.2 Intermediate $1^+ \to 3^-$ Shock Structure from Numerical Integration

The computed structures in this example have upstream shock angle $\theta_2 = 15°$ and upstream shock speed $u_{x1} = 2.4$.

To reach the subsonic D13 point the integral curve from the upstream point must undergo a gas dynamic jump to reach the separatrix linking the supersonic D12 saddle point with the subsonic D13 saddle. The separatrix passes through the transonic transition point on the supersonic-subsonic boundary. The gas dynamic jump to reach the separatrix on the subsonic sheet can occur in $B_y - B_z$ space at a point where the separatrix is on the subsonic sheet.

As a point of comparison, the phase structure in the present example is the same, with different numerical values, to that of the $2^+ \to 3^-$ shock presented in §7.2. In the present example the upstream point is the "unused" stationary point of the $2^+ \to 3^-$ phase plane, the downstream fast shock stationary point is the previous upstream point and the linking separatrix is a unique $2^+ \to 3^-$ shock transition. The separatrix represents a $2^+ \to 3^-$ transition with upstream values $a_1 = 1.120434083$, $b_1 = 2.129566467$, $\gamma = \frac{5}{3}$, $\rho_1 = 1.294393387$, $\theta_1 = 37.12213862°$ and $u_{x1} = 1.854150388$ with $q = 2.94598$ and $r = 1.54847$.

Computationally, the first step is to determine the position of the gas dynamic jump in the $B_y - B_z$ plane. For a given step-off angle at the upstream point the phase trajectory in the $B_y - B_z$ supersonic plane is determined by numerical integration of (27) and (28) in the positive x_η direction. The trajectory is also computed from the D13 point using an integration in the negative x_η direction that

starts off at 90° to the B_y axis, this being the direction of the separatrix at the downstream point as determined by the eigenvectors of the linearised solution about the downstream point. A root finding algorithm is used to determine the B_y and B_z coordinates of the intersection point of the phase trajectories in phase space, this being the location of the gas dynamic jump from the supersonic state to the subsonic state. Using the upstream data in this example it was found using a shooting method that for $\phi > 128.8°$ upstream phase trajectories can undergo a gas dynamic jump to the subsonic separatrix.

The step-off angle ϕ at the upstream point is chosen to be $\pm 160°$, $\pm 170°$ and $180°$ and the size of the initial step off into the $B_y - B_z$ plane at each stationary point to start the integration is 0.0001. When $\phi = \pm 160°$ the gas dynamic jump is calculated to occur at $(B_y, B_z) = (-2.81898, \pm 4.21271)$, when $\phi = \pm 170°$ the jump occurs at $(-3.63141, \pm 3.07490)$ and when $\phi = 180°$ the jump is at the D13 point, $(-4.33572, 0)$.

Figure 62(a) shows the B_y and B_z variation through the shock in terms of x_η for the five sample step-off angles, the supersonic and subsonic stages being shown as unbroken orange and blue lines respectively. The dashed orange-blue line shows the limiting values of B_y and B_z in this particular transition. For $\phi = 180°$ the transition does not gain a B_z component and the jump occurs when B_y equals its value at the downstream point. This is the most negative value of B_y at which a jump can occur to the subsonic state with the subsequent phase trajectory reaching a stationary point. For example, if a jump were to occur in the phase plane at $(-4.6, 0)$, a point between the separatrix and the transonic boundary, the change in specific entropy is $+0.00525 c_v$ but the vector fields as indicated in Figure 61 in this region cause trajectories not to reach the stationary point.

Figure 62(b) shows the parametric plot of $B_y - B_z$ for the five values of the parameter ϕ. The dashed orange curve coming from the upstream point has a smooth continuous change in its B_y, B_z and u_x derivatives at the transonic transition point, the integral curve passing to the D14 point on the subsonic sheet. The shooting method used to find the ϕ value of this trajectory matched the first, second and third derivatives of u_x on each side of the sonic point to determine the value of $\phi = 128.8°$. For values of $\phi > 128.8°$ integral curves from the upstream point can make a gas dynamic jump to the subsonic separatrix and pass to the D13 point. For values of $\phi < 128.8°$ the trajectory leaving the upstream point does not join to the separatrix, coming close to it in the vicinity of the transonic point. These trajectories cannot pass through the transonic transition point as their u_x derivatives are not differentiable at the transonic point. These trajectories can only undergo a gas dynamic jump to the subsonic surface and then join an integral curve to the D14 point. In the $B_y - B_z$ plane only the separatrix linking the saddle points and the smooth transition to the D14 point can pass through the transonic transition point.

Figure 62(c) shows the shock transitions in $B_y - B_z - u_x$ space. Integral curves in the yellow supersonic state with a ϕ value greater than that of the dashed curve from the upstream point U can make a gas dynamic jump to the blue subsonic state at the correct point and join the unique separatrix towards D13. The dotted curve from D12 point is the integral curve making a smooth passage through the transonic flow point, indicated as a red circle, to the downstream stationary point D13.
The parameter ϕ gives the $1^+ \to 3^-$ shock a degree of freedom in its structure as it determines the jump point in $B_y - B_z - u_x$ space for each particular upstream trajectory to reach the unique separatrices that enter the D13 stationary point.

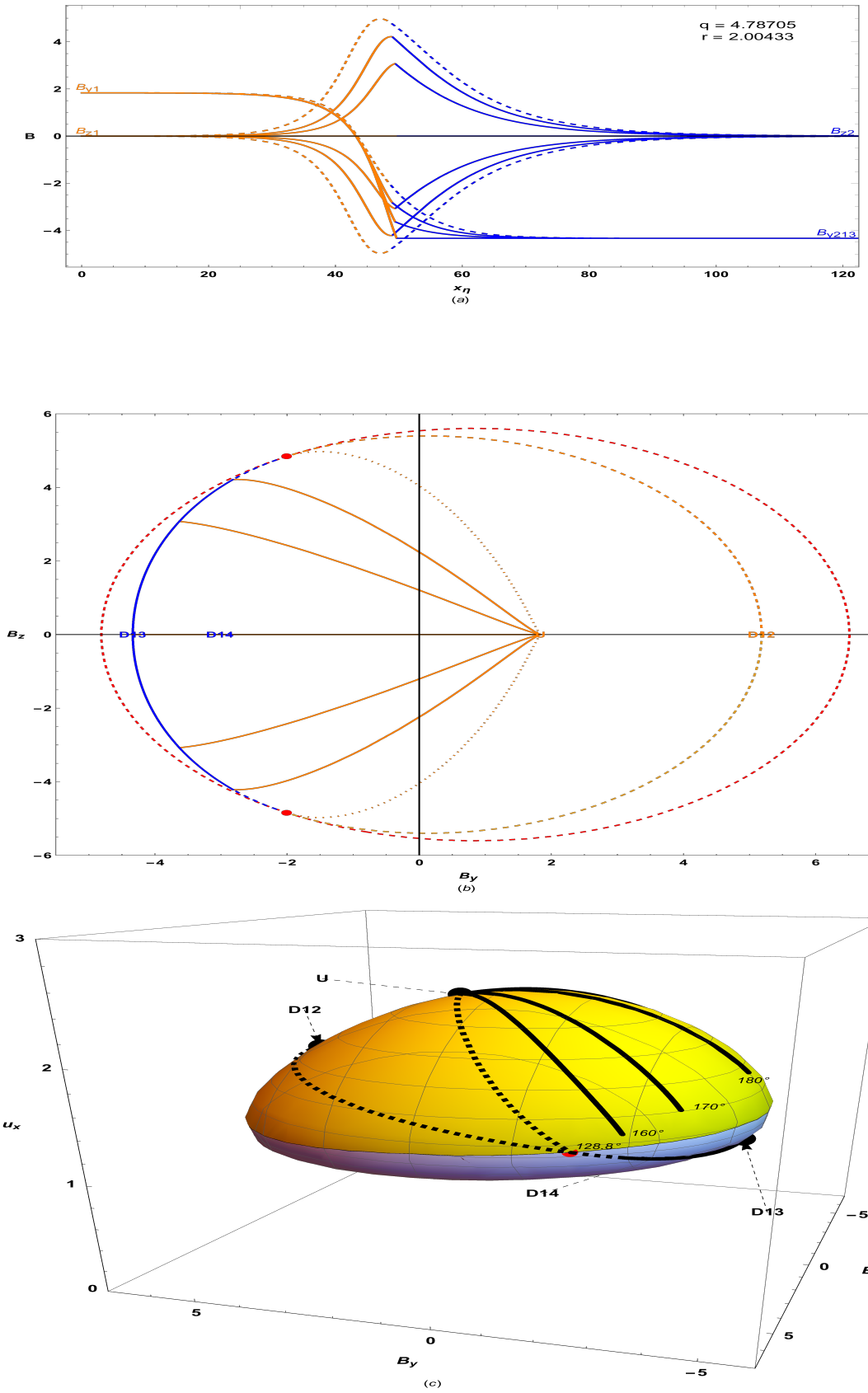

Figure 62: As for Fig 45, but $\frac{u_{x1}}{a_1} = 2.4$. Five trajectories leave the upstream point and undergo a gas dynamic jump to the subsonic separatrices leading to D13. The angle of departure from U is a degree of freedom giving a one-parameter family of $1^+ \to 3^-$ shocks.

7.6.3 Intermediate $1^+ \rightarrow 4^-$ Shock Structure from Numerical Integration

To show the representative shock structures present seven values of the upstream parameter ϕ are considered. These are $\pm 1°$, $\pm 128.8°$, $\pm 170°$ and $180°$. Intermediate $1 \rightarrow 4$ transitions all involve an ending in a subsonic state so an additional parameter is needed to specify the point in the $B_y - B_z$ plane where the gas dynamic jump to the subsonic state occurs. The second parameter is chosen as a particular value of B_y on the trajectory so that illustrative structures are produced. For $\phi = \pm 1°$ the jump is chosen to be at $B_y = 0$, for $\phi = \pm 128.8°$ the jump is at the transonic transition point $(-1.998811631, \pm 4.847571811)$, for $\phi = \pm 170°$ it is at $B_y = -3.4$ and for $\phi = 180°$ the jump is taken to occur at $B_y = -3.7$. The jump can occur at any point in the $B_y - B_z$ plane reached by the trajectory provided that the specific entropy change across the jump to the subsonic state is not negative. As indicated in §7.6.2, shocks are not formed in the region in the $B_y - B_z$ plane between the separatrices and the transonic boundary.

The numerical integration of the ODEs (27) and (28) from the upstream point is carried out in the positive x direction with an initial step-off of 0.0001 and proceeds on the supersonic sheet until the chosen jump point to the subsonic sheet is reached.

Figure 63(a) shows the $B_y - x_\eta$ and $B_z - x_\eta$ profiles. The B_y profile for $\phi = 1°$ approaches that of the associated supersonic fast shock with downstream transverse magnetic field component $B_{y2} = 5.18344$. Due to the increasing B_z component the intermediate phase trajectory approaches the separatrix from the saddle before undergoing a gas dynamical jump to a subsonic state. The B_y profile for $\phi = 128.8°$ from the upstream point passes through the transonic transition point with its first, second and third u_x derivatives equal to that of a phase trajectory leaving the downstream D14 point at $\phi = 176.56°$. These trajectories were determined by "shooting" from the upstream and downstream points and comparing the velocity derivatives, as given by equations (32), (34), (35) and (36) on each side of the transonic point. The "smooth" trajectory approaches the appropriate l'Hopital derivative at the transition point. The black trajectories from the downstream and upstream points in Figures 64 and 65(a), (b) and (c) respectively target the black dot, this being the derivative value for the smooth transition for the $1^+ \rightarrow 4^-$ transition. The grey dot represents the derivative values for the $2^+ \rightarrow 3^-$ transition in the phase plane.

The smooth transitions through the transonic points are shown passing through the red circles in Figure 63 (a), (b) and (c). Alternatively, the smooth transition can be computed by integrating the first oder ODEs out of the transonic point in the negative x direction on the supersonic sheet to reach the upstream source point and then integrating out of the transonic point in the positive direction on the subsonic sheet to reach the downstream sink. The solutions are then joined at the transonic point. Since the shock profiles shown in Figure 63(a) are computed with a common x scale using integrations out of the upstream stationary point at the same step-off the first described method was used to profile the smooth transition. Gas dynamic jumps at B_y values between those of the downstream subsonic stationary points are shown in Figure 63 (b) and (c), the trajectory on the subsonic surface being captured by the sink at D14. As previously indicated in §7.6.2 the D13 point can only be reached by a unique jump to the subsonic surface.

The trajectories from the upstream point at $\phi = 180°$, $\pm 170°$ and $\pm 128.8°$ pass through a region of the phase plane where the shock is expansive after leaving the upstream point, this region being the supersonic central red region in Figure 25b. The trajectory with $\phi = \pm 1°$ has an expansive stage as it passes through the subsonic red region in Figure 25b, before the trajectory reaches the D14 point.

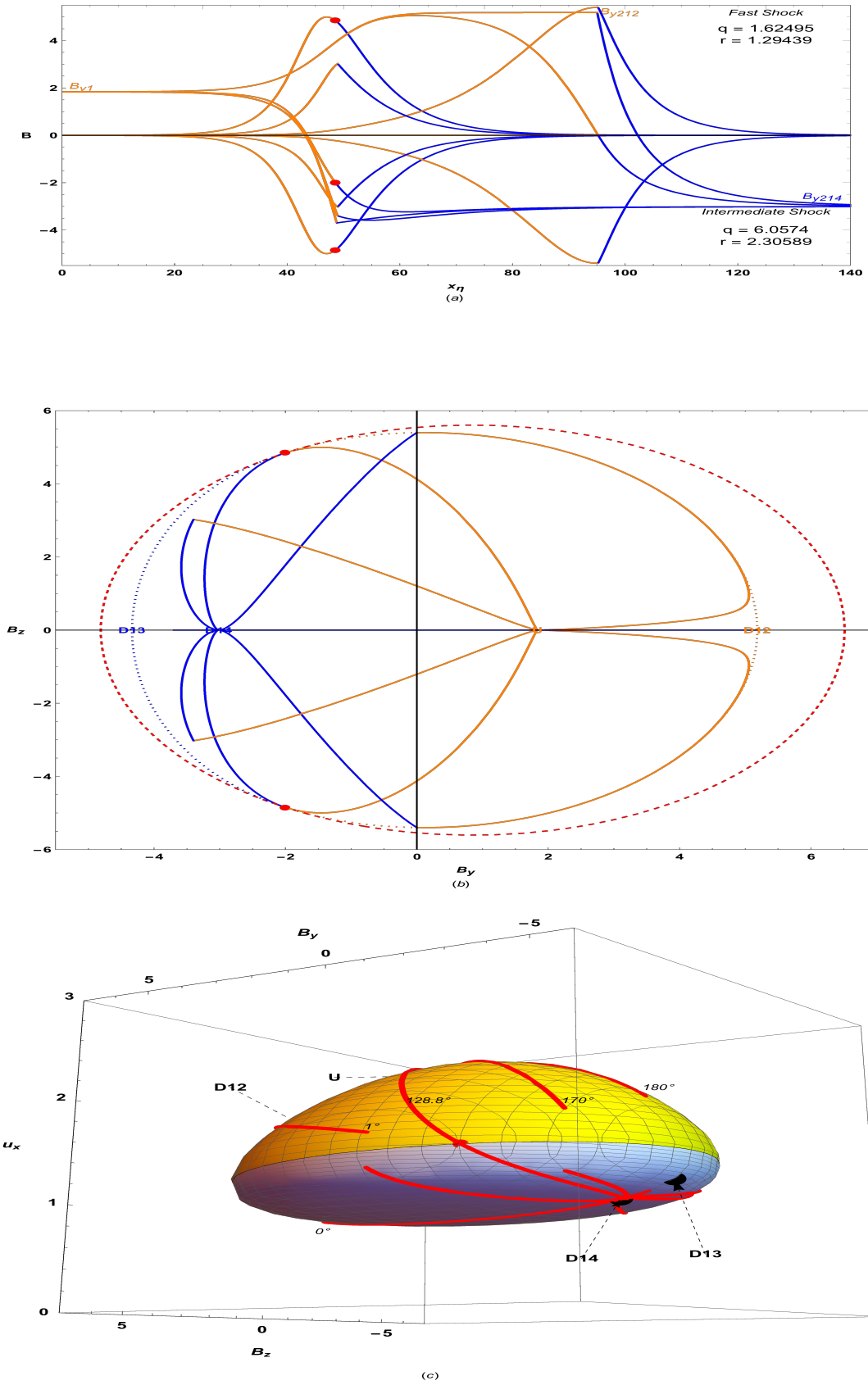

Figure 63: As for Fig 62 but showing trajectories undergoing a gas dynamic jump to points on the subsonic surface other than those on a separatrix. These trajectories then converge on D14. These trajectories have degrees of freedom in their departure angle from the upstream point and the location of the jump point giving a two-parameter family of $1^+ \rightarrow 4^-$ shocks. Also shown is the smooth transition through the transonic transition points.

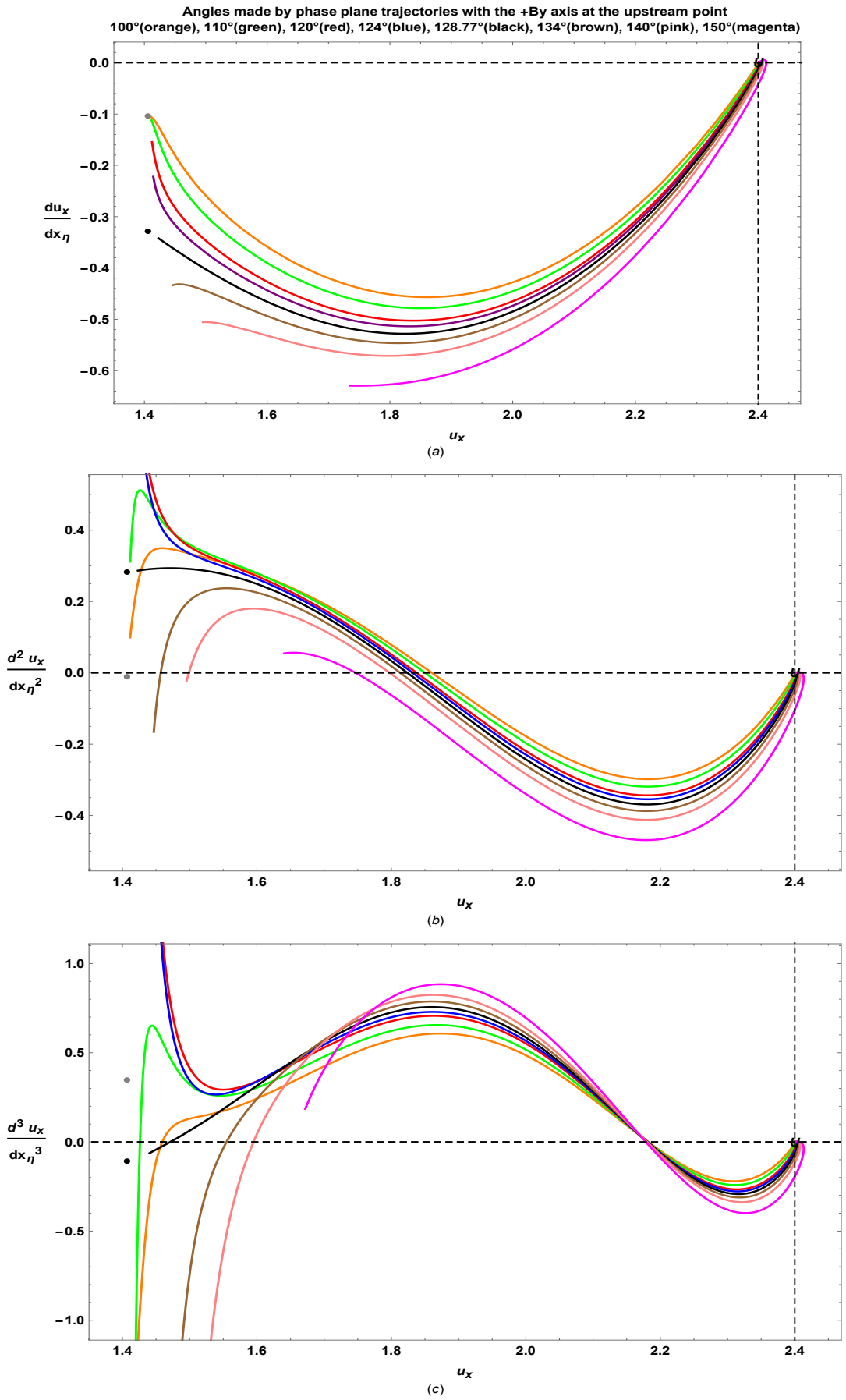

Figure 64: Velocity derivatives for trajectories from the upstream point, only one converges on a common value at the transonic point with trajectories coming from the downstream point; $\frac{b_1}{a_1} = 2$, $\theta_1 = 15°$, $\frac{u_{x1}}{a_1} = 2.4$

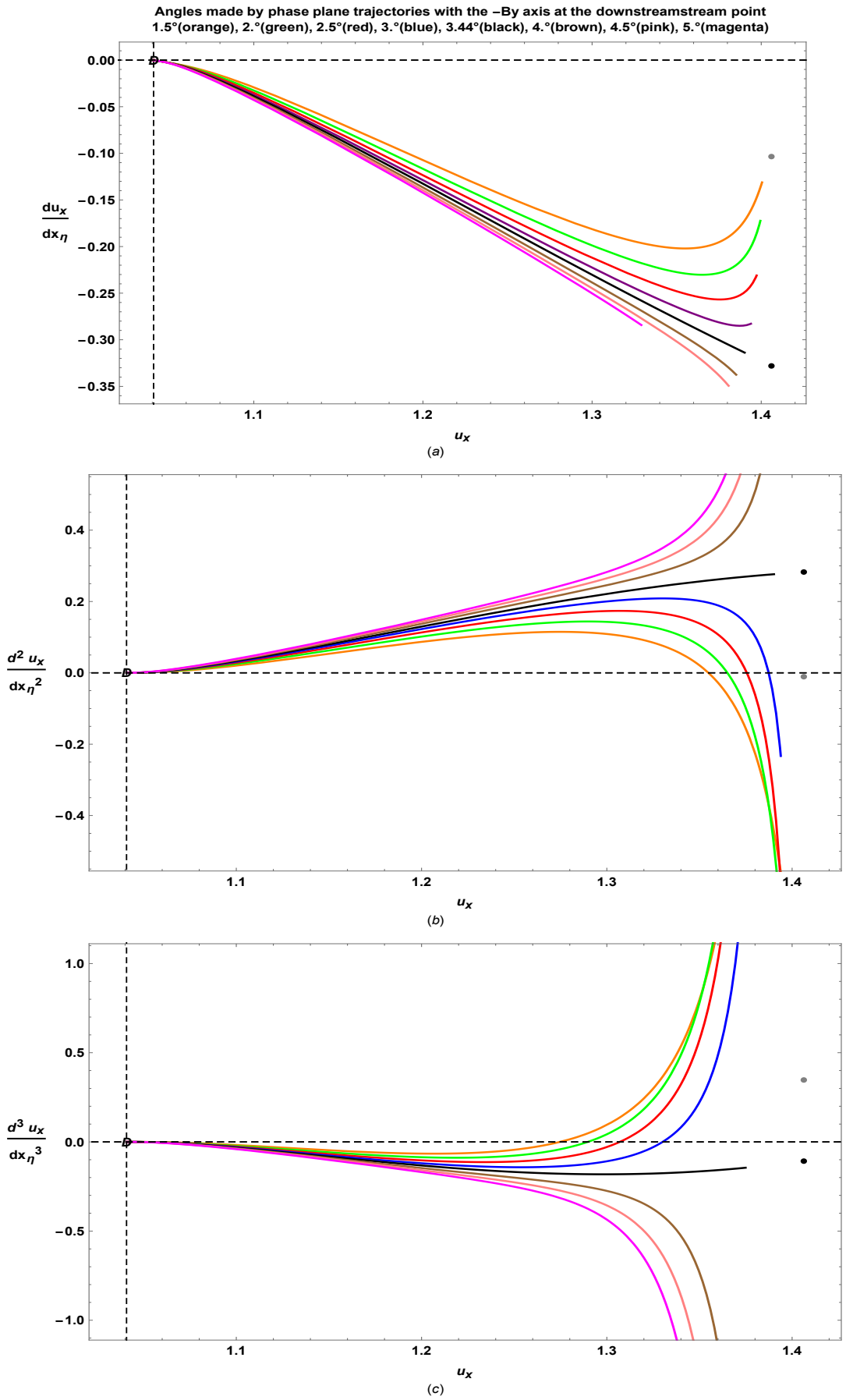

Figure 65: Velocity derivatives for trajectories from the downstream point, only one converges on a common value at the transonic point with trajectories coming from the upstream point; $\frac{b_1}{a_1} = 2$, $\theta_1 = 15°$, $\frac{u_{x1}}{a_1} = 2.4$

8 Switch-On Shocks

This chapter presents the phase plane and structure of MHD switch-on shocks, a special case of parallel shocks where $B_{y1} = 0$. The switch-on MHD shock has an upstream speed greater than the intermediate speed and a downstream normal speed equal to the downstream intermediate speed, as shown on Figure 5 (a). The switch-on shock is the limiting case ($\theta_1 = 0°$) of fast and intermediate shocks which emerge as distinct with an increase in the upstream shock angle. As the switch-on shock is a precursor for the formation of fast and intermediate shocks, occurring only when $\theta_1 = 0$ and $b_1 < u_{x1} < \sqrt{\frac{(\gamma+1)b_1^2 - 2a_1^2}{\gamma - 1}}$, the switch-on shock is presented as a separate chapter in this thesis.

For the set of upstream properties $\left\{1, 2, \frac{5}{3}, 1, 0°, u_{x1}\right\}$ the previously stated inequality predicts that two stationary points occur for $u_{x1} < 2$ and $u_{x1} > 3.60555$, the solutions of (120) being double roots for $B_y = 0$. Four stationary points occur when $2 < u_{x1} < 3.60555$, two of these being the double root $B_y = 0$, the other two solutions being of opposite sign representing the "switched-on" transverse magnetic field component having symmetry in space about the x axis. The upstream shock speed and the downstream sound and normal shock velocity component for this set of upstream properties is shown in Figure 7.

For $a_1 < u_{x1} < b_1$, Figure 66 shows the vector fields before the formation of the transverse switch-on magnetic field component. The two stationary points present allow a supersonic to subsonic transition in the form of a gas dynamic jump between the $B_y = 0$ stationary points on both sheets.

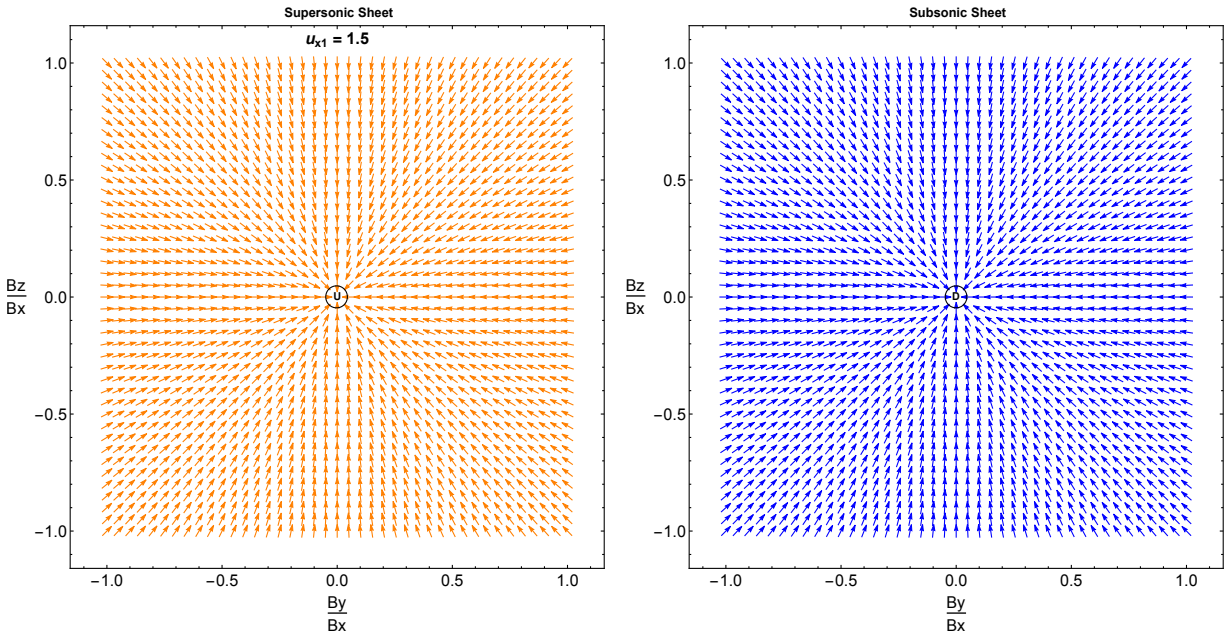

Figure 66: Phase plane vector fields for a parallel shock, $a_1 < u_{x1} < b_1$, gas dynamic supersonic to subsonic shock only possible; $\frac{b_1}{a_1} = 2$, $\theta_1 = 0^\circ$, $\frac{u_{x1}}{a_1} = 1.5$

8.1 Switch-On Supersonic to Supersonic Shocks

When the upstream shock speed just excedes the intermediate speed the upstream point in the $B_y - B_z$ phase plane becomes a source with an associated downstream sink with a 360° ring symmetry about the upstream point as shown in Figure 67. This reflects the axial symmetry of the upstream state about

the shock normal. As the upstream speed increases the ring expands, the vector fields inside the ring are directed radially outwards and between the ring and the supersonic boundary is directed radially inwards. The governing ODE is that of the fast shock (127) with B_y replaced by $|B_T|$, representing the magnitude of the transverse ¨switched-on¨ magnetic field. In previous analysis of shock structure the y axis direction was established due to the presence of the transverse upstream magnetic field component, B_y. Here, as the switch-on process occurs for parallel shocks defined by having $B_{y1} = B_{z1} = 0$, the y direction is not pre-defined.
Equation (74) gives the upstream shock speed when the downstream switch-on shock speed equals the downstream sound speed, showing that switch-on supersonic to supersonic shocks are produced in the upstream speed domain $b_1 < u_{x1} < \sqrt{\frac{\gamma\left[(\gamma-1)b_1^2-a_1^2\right]+\sqrt{\gamma\left[\gamma a_1^4+2(\gamma-1)b_1^2\left(b_1^2-a_1^2\right)\right]}}{\gamma(\gamma-1)}}$.

For the set of upstream parameters $\left\{1, 2, \frac{5}{3}, 1, 0^\circ, u_{x1}\right\}$ Figure 67(a) and (b) show the change in the phase plane vector field as the upstream shock speed increases within the switch-on supersonic to supersonic domain. The downstream gas dynamic and magnetohydrodynamic switch-on stationary points are shown as DG and DM respectively. The switch-on stationary points first form on the supersonic sheet when the downstream fast, Alfven and shock speeds are equal and increase in transverse $|B|$ value as the upstream shock speed increases. When the DM locus reaches the supersonic boundary it changes to the subsonic sheet and, as shown in Figure 26(a), $|B_T|$ continues to increase on the subsonic sheet before reaching its maximum value. This case is presented in the next section. Further increase in upstream shock speed decreases the transverse $|B|$ value finally zero when the downstream slow, Alfven and shock speeds are equal. The MHD signal speeds in the switch-on shock domain are shown on Figure 5(a) .

On the supersonic sheet the switch-on MHD shock transition is produced by phase plane trajectories from the source U being linked to the surrounding locus of downstream points.

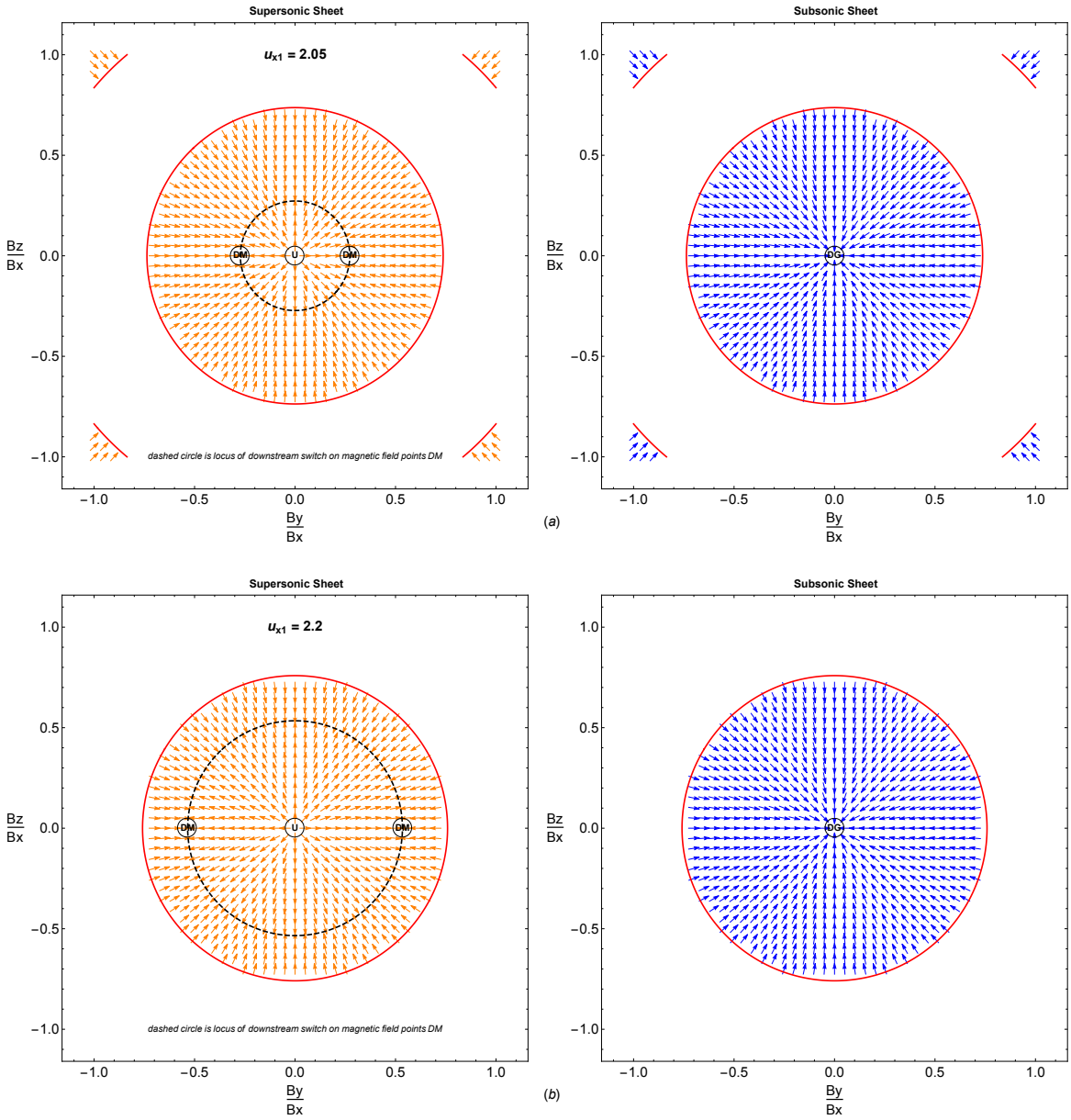

Figure 67: As for Fig 66, but when $\frac{u_{x1}}{a_1} = 2.05$ and 2.2. Switch-on MHD supersonic to supersonic shocks occur when $\theta_1 = 0°$ and $b_1 < u_{x1} < \sqrt{\frac{\gamma\left[(\gamma-1)b_1^2-a_1^2\right]+\sqrt{\gamma\left[\gamma a_1^4+2(\gamma-1)b_1^2\left(b_1^2-a_1^2\right)\right]}}{\gamma(\gamma-1)}}$. Any point on the dashed circle is a valid downstream state with a "switched-on" transverse magnetic field component.

The integration was started at the upstream stationary point on the supersonic sheet using a step off of in $|B_T|$ of +0.0001 in the phase plane shown in Figure 67(b). Following the direction of the vector field, the integration proceeds along the positive x direction to the downstream point.

Figure 68 shows the shock structure for the MHD switch-on shock. The rate of increase of the transverse magnetic field component with respect to the normal shock velocity is large at the upstream point compared to an oblique fast shock. The shock normal velocity shows a monotonic decrease through the shock and the magnetic pressure is greater than the gas pressure, the range of these pressures through

the shock being less than the case of an oblique fast shock. The change in specific entropy undergoes a monotonic increase from the upstream point through the transition.

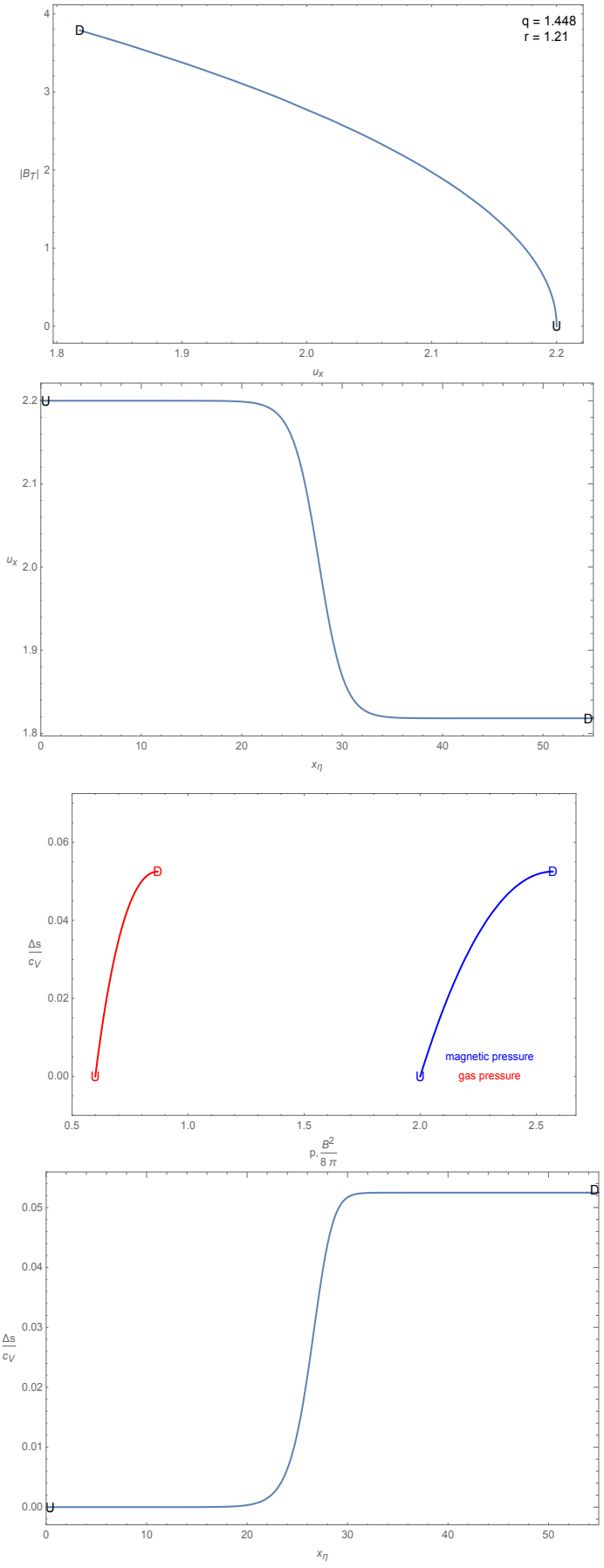

Figure 68: Variation in B_y, u_x, p and Δs through a supersonic to supersonic MHD switch-on shock. In this and the following switch-on plots $x = \frac{x}{\eta}$, $\rho_1 = 1$ and all speeds are in terms of the upstream sound speed. In this plot $\frac{b_1}{a_1} = 2$, $\theta_1 = 0°$, $\frac{u_{x1}}{a_1} = 2.2$.

8.2 Switch-On Supersonic to Subsonic Shocks

When $\sqrt{\frac{\gamma\left[(\gamma-1)b_1^2-a_1^2\right]+\sqrt{\gamma\left[\gamma a_1^4+2(\gamma-1)b_1^2\left(b_1^2-a_1^2\right)\right]}}{\gamma(\gamma-1)}} < u_{x1} < \sqrt{\frac{(\gamma+1)b_1^2-2a_1^2}{\gamma-1}}$ the downstream MHD stationary point is on the subsonic sheet and the switch-on transition is enabled by a phase trajectory from the supersonic upstream point undergoing a gas dynamic jump to the subsonic sheet on the locus of downstream points. This is shown in Figure 69.

For the set of upstream parameters $\left\{1, 2, \frac{5}{3}, 1, 0°, u_{x1}\right\}$ the upstream shock speed domain for the formation of supersonic to subsonic MHD shocks is $2.71729 < u_{x1} < 3.60555$. As indicated in §8.1, the maximum value of the switched on magnetic field component occurs when the downstream point is on the subsonic sheet, slightly inside the subsonic boundary, the value being $|B_T| = 6.51241$ occurring when $u_{x1} = 2.91548$.

Figure 69 (a) and (b) shows the change in the phase plane vectors as the upstream shock speed increases. The vectors in the annulus change direction as the downstream locus decreases, the direction of the vectors on the subsonic sheet having reversed direction following the switch-on stage. Figure 70 shows the supersonic and subsonic phase plane for $u_{x1} > \sqrt{\frac{(\gamma+1)b_1^2-2a_1^2}{\gamma-1}}$.

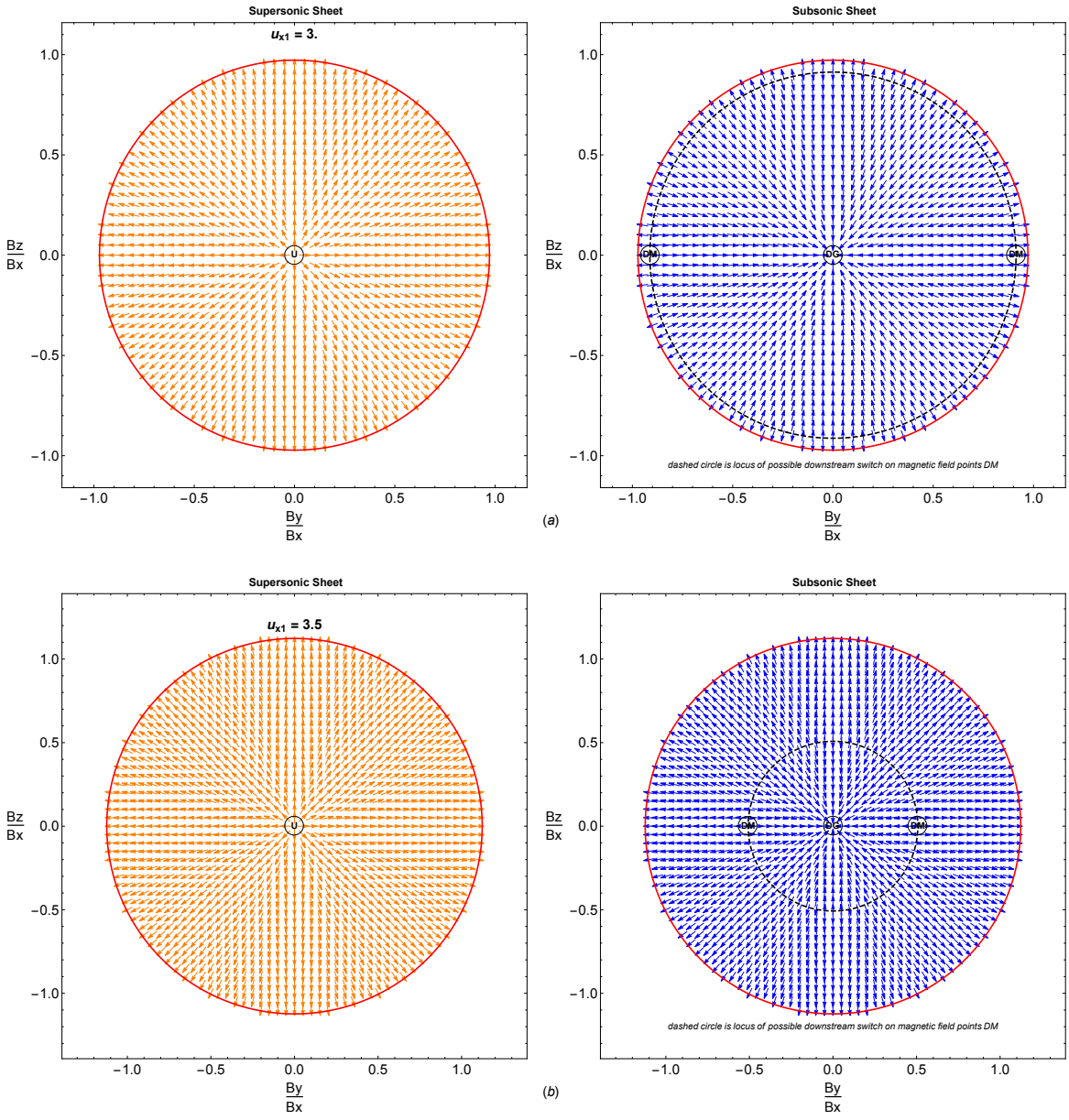

Figure 69: As for Fig 66, but when $\frac{u_{x1}}{a_1} = 3.0$ and 3.5. Switch-on supersonic to subsonic MHD shocks occur when $\theta_1 = 0°$ and $\sqrt{\frac{\gamma\left[(\gamma-1)b_1^2-a_1^2\right]+\sqrt{\gamma\left[\gamma a_1^4+2(\gamma-1)b_1^2\left(b_1^2-a_1^2\right)\right]}}{\gamma(\gamma-1)}} < u_{x1} < \sqrt{\frac{(\gamma+1)b_1^2-2a_1^2}{\gamma-1}}$. Points on the dashed ring are valid downstream states with a "switched-on" transverse magnetic field component.

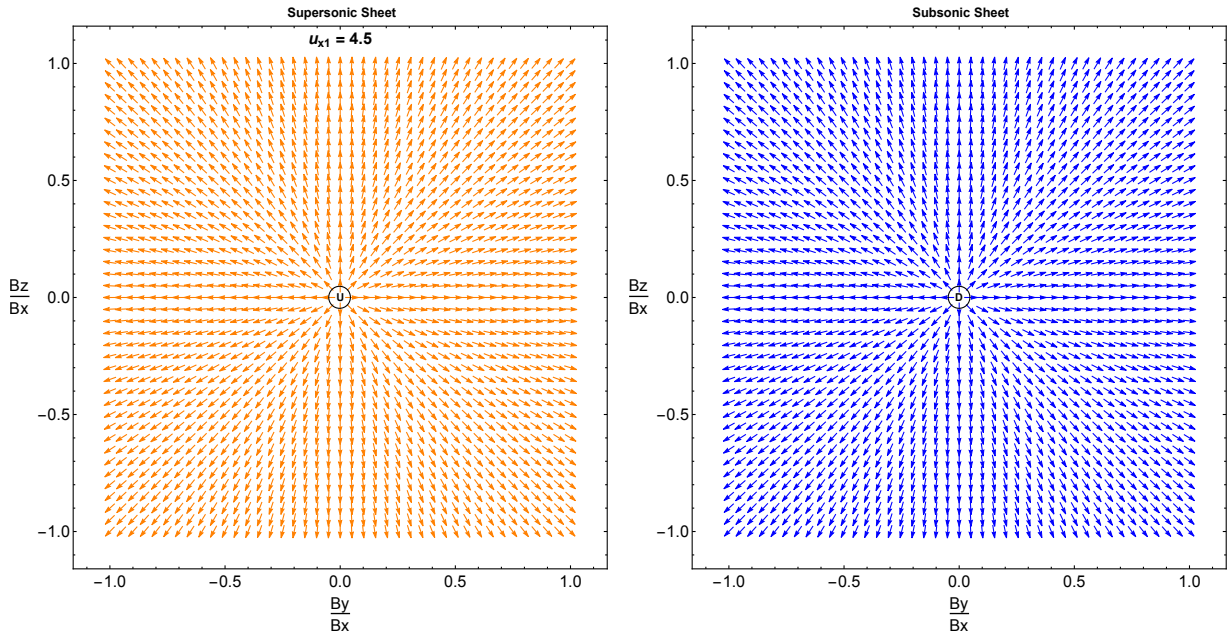

Figure 70: As for Fig 66, but when $u_{x1} > \sqrt{\frac{(\gamma+1)b_1^2-2a_1^2}{\gamma-1}}$. Only a gas dynamic supersonic to subsonic shock is possible;

The numerical solution of the ODE (127) for the upstream parameters $\left\{1, 2, \frac{5}{3}, 1, 0°, 3\right\}$ in the phase plane shown in Figure 69 (a) begins using a step off in $|B_T|$ of $+0.0001$ and continues on the supersonic sheet before making a gas dynamic jump to the subsonic sheet at the subsonic stationary point. The large increase in the gas pressure, made possible due to the reduction in normal flow speed, causes the downstream gas pressure to be greater than the downstream magnetic pressure, this first happening when the upstream shock speed is greater than 2.96.

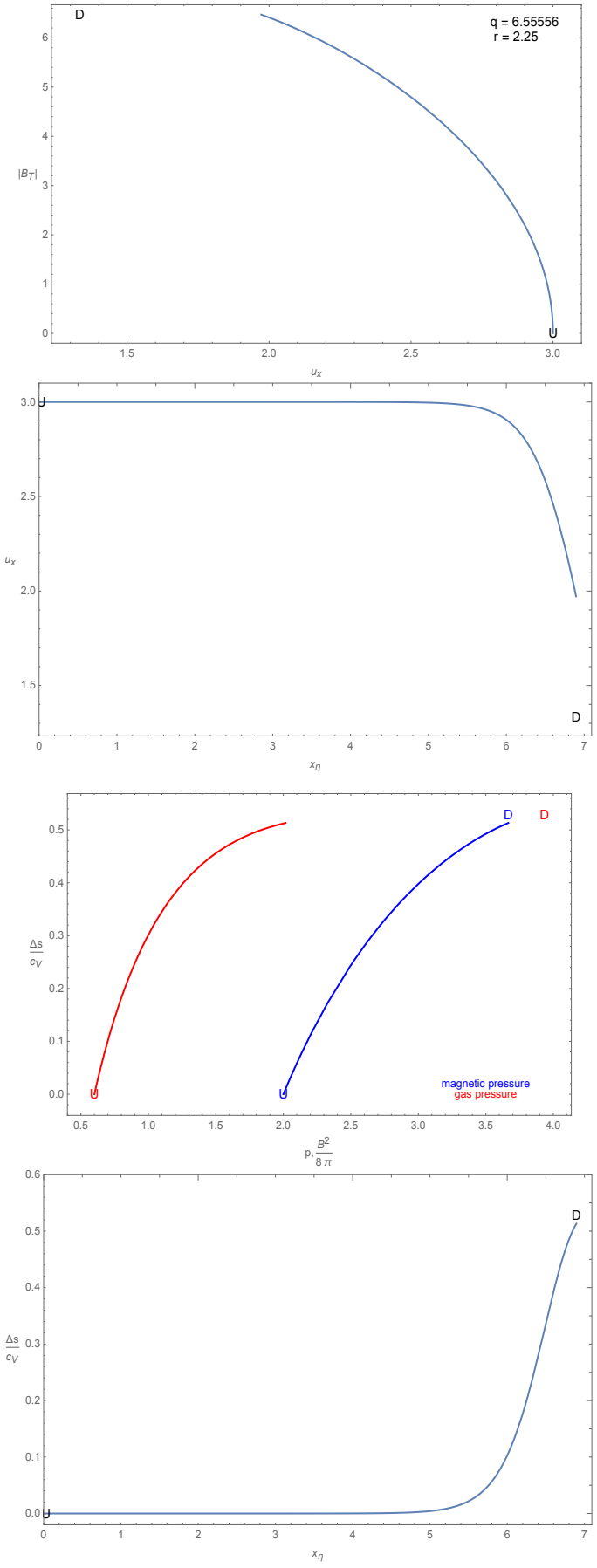

Figure 71: As for Fig 68, but with $\frac{u_{x1}}{a_1} = 3$. Gap between profile and D is due to a gas dynamic jump.

9 Summary and Discussion

The aim of the research presented in this thesis is to catalogue the various MHD shock waves that can arise with particular reference to intermediate shocks. Intermediate shocks all have a reversal of the direction of the transverse magnetic field component through the shock and are unusual in that in most cases the transition linking the pre-shock and post-shocked states is not unique, having degrees of freedom in their structure, a feature not shared by the well known and experimentally confirmed fast and slow shocks. Intermediate shocks were at first considered unphysical, being unable to adapt to perturbations and remain stable. The role of degrees of freedom within the structure as a means of allowing the shock to adapt to perturbations and become surviving was presented by the works of C.C. Wu [9] and the variety of possible transitions shown using the magnetic phase plane was given by the pioneering work of Hau and Sonnerup [24]. The former studied MHD shock structure using a simplified model in which some dissipative terms were not present.

This thesis attempts to clarify the rich variety of structures present in the phase plane and takes the analysis further than that of Hau and Sonnerup by giving a more detailed description of both the types of shocks possible and in the role of the speed of sound in determining various features in the phase plane. An original analysis involving higher derivatives of the smooth resistive supersonic to subsonic transition through the sonic point is presented, this being the point where the downstream sound speed and normal flow velocity are equal and have continuous derivatives in the normal flow velocity component.

The previous chapters presented a thorough study of the possible types of the steady shock transitions that can be produced by a disturbance moving through a magnetised conducting fluid when dissipation is due to ohmic heating. The shocks were assumed to be steady and planar and viscosity was neglected. In the steady state the physical principles embodied in the laws of conservation of momentum, magnetic flux and energy with ohmic heating reduce to two coupled first order ordinary differential equations in the magnetic field components B_y and B_z that describe the spatial shock structure. The approach taken allows the shock structure to be represented as a trajectory in the magnetic phase plane, this being a two dimensional (B_y, B_z) representation of the pathways linking the physical conditions existing at a given initial pre-shock stationary state and other points in the plane where the derivatives of the flow variables are zero, these being the downstream post shocked states. The phase plane gives a visual overview of families of shocks that appear as trajectories between stationary points in the plane. Trajectories can link stationary points either by a smooth transition in all flow variables and derivatives or by an entropy increasing gas dynamic jump within the transition where the normal velocity shock component undergoes a discontinuous decrease to a lower value in the absence of fluid viscosity.

In most situations there are only two stationary points in the magnetic phase plane, the transition between these two states being a slow shock if the downstream transverse magnetic field component is less than its upstream value, or a fast shock if the downstream transverse magnetic field component is greater than its upstream value. In both slow and fast shocks the pre-shock and post shock transverse magnetic field components are in the same direction.

In some situations there are four stationary points in the magnetic phase plane and in this case two or three downstream states are possible with two of these being linked by an intermediate shock, the intermediate shock being characterised by a reversal in direction of its post-shock transverse magnetic field component relative to its pre-shock direction. Four stationary points can be found in the magnetic

phase plane during the presence of slow shocks before the formation of a switch-off shock, the other two stationary points being unable to receive phase trajectories.

This thesis uses phase plane diagrams to show the variety of shock structures produced in the case where the upstream Alfven speed is greater than the upstream sound speed, this being equivalent to $\beta_1 < \frac{2}{\gamma}$, where β_1 is the upstream value of the ratio of the gas pressure to the magnetic pressure. This condition allows the emergence of the switch-on MHD shock, the progenitor of families of intermediate and fast shocks. Twelve families of MHD shocks, containing fourteen distinct individual transitions, obey the jump conditions with an associated entropy increase. Table 1 presents a summary of the shock families. The list in the table is given in order of increasing upstream shock angle as displayed in the plots in §3.2. In column 4 of the table u indicates that the phase plane transition linking the stationary points is unique, 1 and 2 indicate that there are these numbers of degrees of freedom, meaning free parameters in the set up of the phase trajectory linking the stationary points in the phase plane.

Table 1 shows that slow and fast shocks have unique internal structures and produce unique final results. This means that a given upstream disturbance can only produce one final state after the passage of the shock and the magnetic field, pressure and density vary uniquely as the shock passes.

According to the laws of fluid dynamics, electromagnetism and thermodynamics when conditions are such that an intermediate shock can form there are at least two possible end states that can form. Each end state has a different flow speed, magnetic field, pressure and density. An intermediate $2 \rightarrow 3$ shock, in its subsonic and supersonic forms, is unique. This means that this shock, for given starting conditions, only has one possible end state and the magnetic field, pressure and density change in one way only as the shock passes. The conditions that set up a $2 \rightarrow 3$ shock also set up a $2 \rightarrow 4$ shock having a different end state and having many ways of reaching this end state by varying one parameter. This parameter is the angle at which the trajectory leaves the upstream point on its journey towards its downstream point. The laws of physics in some situations allow three possible end states with two of these being associated with an intermediate shock and the other a fast shock. In this case the $1 \rightarrow 3$ transition is not unique, the trajectory can leave at various angles and reach the same downstream point; the $1 \rightarrow 4$ transition is also not unique and has two degrees of freedom in its structure, these being the angle at which the trajectory leaves the upstream point and the point in the phase plane where the trajectory undergoes a gas dynamic jump to become subsonic and link with its end point.

The presence of "freedom" in the angle at which the shock trajectory leaves its upstream point and "freedom" where the transition can undergo a gas dynamic jump to a subsonic state make intermediate shocks non-unique in their structure.

Family	Stationary Points	Transitions	Degree of Freedom, MHD Properties
switch-on $+ \to +$ gas $1^+ \to 4^-$	3	$(+,+) \to (-,)$	u, $P_{2_{SO}} < P_{2_{14}}$
switch-on $+ \to -$ gas $1^+ \to 4^-$	3	$(+,+) \to (+,)$	u, $P_{2_{SO}} < P_{2_{14}}$
$3^- \to 4^-$	2	$(+,-) \to (-,-)$	u, $0 < \frac{B_{y2}}{B_{y1}} < 1$
$3^+ \to 4^-$	2 or 4	$(-,-) \to (-,-)$ jump at start	u, $0 < \frac{B_{y2}}{B_{y1}} < 1$
$2^+ \to 3^+$ $2^+ \to 4^-$	4	$(-,+) \to (-,-)$ $(-,+) \to (-,-)$	u, $\frac{B_{y2_{23}}}{B_{y1}} < 0$, 1, $\frac{B_{y2_{24}}}{B_{y1}} < 0, P_{2_{23}} < P_{2_{24}}$ $\lvert B_{y2_{24}}\rvert < \lvert B_{y2_{23}}\rvert$
$2^+ \to 3^-$ $2^+ \to 4^-$	4	$(-,+) \to (+,-)$ $(-,+) \to (-,-)$	u, $\frac{B_{y2_{23}}}{B_{y1}} < 0$, 1, $\frac{B_{y2_{24}}}{B_{y1}} < 0, P_{2_{23}} < P_{2_{24}}$ $\lvert B_{y2_{24}}\rvert < \lvert B_{y2_{23}}\rvert$
$2^- \to 3^-$ $2^- \to 4^-$	4	$(+,+) \to (+,-)$ $(+,+) \to (-,-)$	u, $\frac{B_{y2_{23}}}{B_{y1}} < 0, \left\lvert\frac{B_{y2_{23}}}{B_{y1}}\right\rvert < 1$ 1, $\frac{B_{y2_{24}}}{B_{y1}} < 0, P_{2_{23}} < P_{2_{24}}$ $\lvert B_{y2_{24}}\rvert < \lvert B_{y2_{23}}\rvert$
$1^+ \to 2^-$ $1^+ \to 3^-$ $1^+ \to 4^-$	4	$(+,+) \to (+,+)$ $(+,+) \to (+,-)$ $(+,+) \to (-,-)$	u, $\frac{B_{y2_{12}}}{B_{y1}} > 1, P_{2_{12}} < P_{2_{13}}$ 1, $\frac{B_{y2_{13}}}{B_{y1}} < -1, P_{2_{13}} < P_{2_{14}}$ 2, $\frac{B_{y2_{14}}}{B_{y1}} < 0, \frac{B_{y2_{14}}}{B_{y2_{13}}} < 1$
$1^+ \to 2^+$ $1^+ \to 3^+$ $1^+ \to 4^-$	4	$(+,+) \to (-,+)$ $(+,+) \to (-,-)$ $(+,+) \to (-,-)$	u, $\frac{B_{y2_{12}}}{B_{y1}} > 1, P_{2_{12}} < P_{2_{13}}$ 1, $\frac{B_{y2_{13}}}{B_{y1}} < -1, P_{2_{13}} < P_{2_{14}}$ 2, $\frac{B_{y2_{14}}}{B_{y1}} < 0, \frac{B_{y2_{14}}}{B_{y2_{13}}} < 1$
$1^+ \to 2^+$ $1^+ \to 3^-$ $1^+ \to 4^-$	4	$(+,+) \to (-,+)$ $(+,+) \to (+,-)$ $(+,+) \to (-,-)$	u, $\frac{B_{y2_{12}}}{B_{y1}} > 1, P_{2_{12}} < P_{2_{13}}$ 1, $\frac{B_{y2_{13}}}{B_{y1}} < -1, P_{2_{13}} < P_{2_{14}}$ 2, $\frac{B_{y2_{14}}}{B_{y1}} < 0, \frac{B_{y2_{14}}}{B_{y2_{13}}} < 1$
$1^+ \to 2^+$	2	$(+,+) \to (-,+)$	u, $\frac{B_{y2}}{B_{y1}} > 1$
$1^+ \to 2^-$	2	$(+,+) \to (+,+)$ jump at end	u, $\frac{B_{y2}}{B_{y1}} > 1$

Table 1: Shock family summary table. The nature of the stationary points is given in column 3: $(+,+)$ indicates a source, $(-,-)$ a sink and $(+,-)$ or $(-,+)$ a saddle. Column 4 gives the number of degrees of freedom of the shock structure, u meaning unique. Also given are the upstream and downstream transverse magnetic field components and gas pressures.

The numerical integrations show that structures with dissipation due to ohmic heating linking the end points of each transition are obtainable either as an entirely smooth passage or as a combination of a smooth passage and a discontinuous entropy increasing jump. The calculations provide the groundwork for future study of the stability of each shock transition since before the stability of a dissipative shock transition can be investigated its steady state structure must be known.

The calculations presented here consider the case in a conducting fluid where the pre-shock Alfven speed is greater than the sound speed. This condition is met in many astrophysical situations. As seen by comparing Figures 3 and 4 a much greater variety of shock types arises in this case. A switch-on shock, being the progenitor of intermediate-fast shock families, can only arise if the pre-shock Alfven speed is greater than the sound speed.

The calculations consider the case of resistive MHD shocks, these arising when the energy dissipation in the fluid is due to ohmic heating. Other dissipative processes, such as viscous transfer and heat conduction, have not been considered. The addition of viscosity would smooth out the gas dynamic jump of purely resistive theory. With the inclusion of both electrical resistance and viscosity the phase plane for fast and slow shock trajectories is formulated in terms of B_y and u_x, the ODES for a perpendicular shock becoming

$$\frac{dB_y}{dx_\eta} = -f_5 + B_y u_x, \tag{135}$$

$$\frac{du_x}{dx_\eta} = \frac{3(\gamma-1)\xi}{4}\left(f_7 - \frac{f_5}{4\pi}B_y\right) + \frac{3\gamma\xi}{4}\frac{B_y^2}{8\pi} - f_2 + \frac{3\,(\gamma+1)\,\xi f_1}{8}u_x, \tag{136}$$

where the ratio of the magnetic diffusivity to the kinematic viscosity is given as ξ, this ratio being known as the reciprocal of the magnetic Prandtl number. Linearisation about the downstream point reveals a saddle point, the eigenvectors in this case not being mutually perpendicular as in the case of purely resistive MHD shocks. To illustrate a perpendicular shock structure with both resistive and viscous dissipation present, the ODEs (135) and (136) were numerically integrated out of the downstream point with the same magnitude step-off for three values of ξ for the resistive shock considered in §5.2.2. The results are shown in Figure 72. Figure 72(a) shows the case of a very small viscosity, the sudden transition to the downstream value becoming a gas dynamic jump in the limit as $\nu \to 0$. Figure 72(b) shows the case of equal resistive and viscous factors, the profile smoothly stretching out and Figure 72(c) shows the case where the viscosity is much greater than the magnetic diffusivity. In summary, the presence of viscosity in the equations controls the scale of the transition, which approaches a gas dynamic jump as $\nu \to 0$.

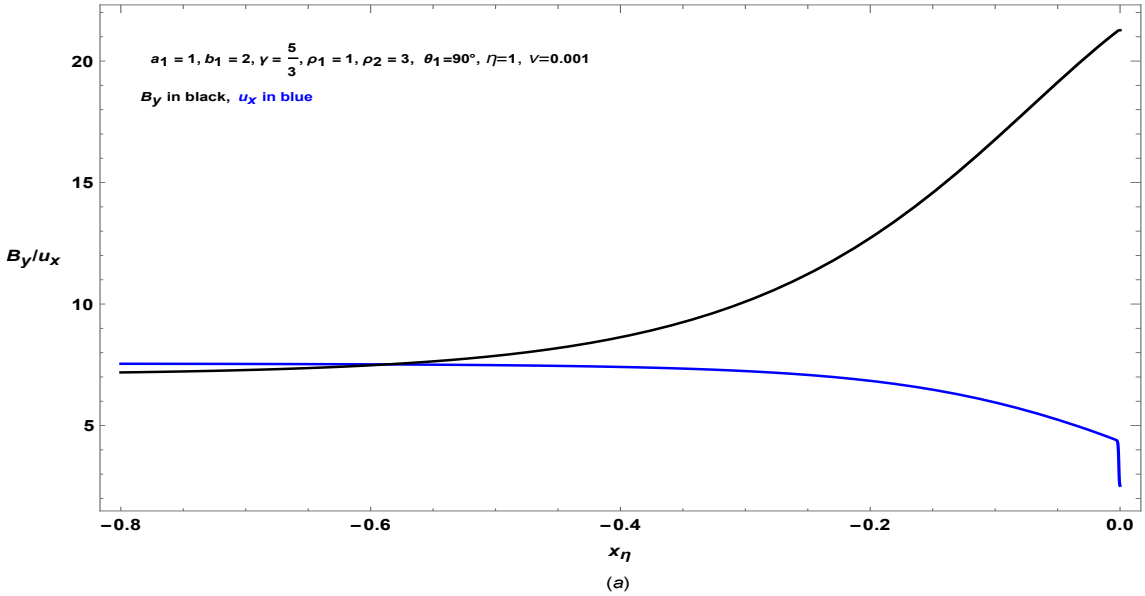

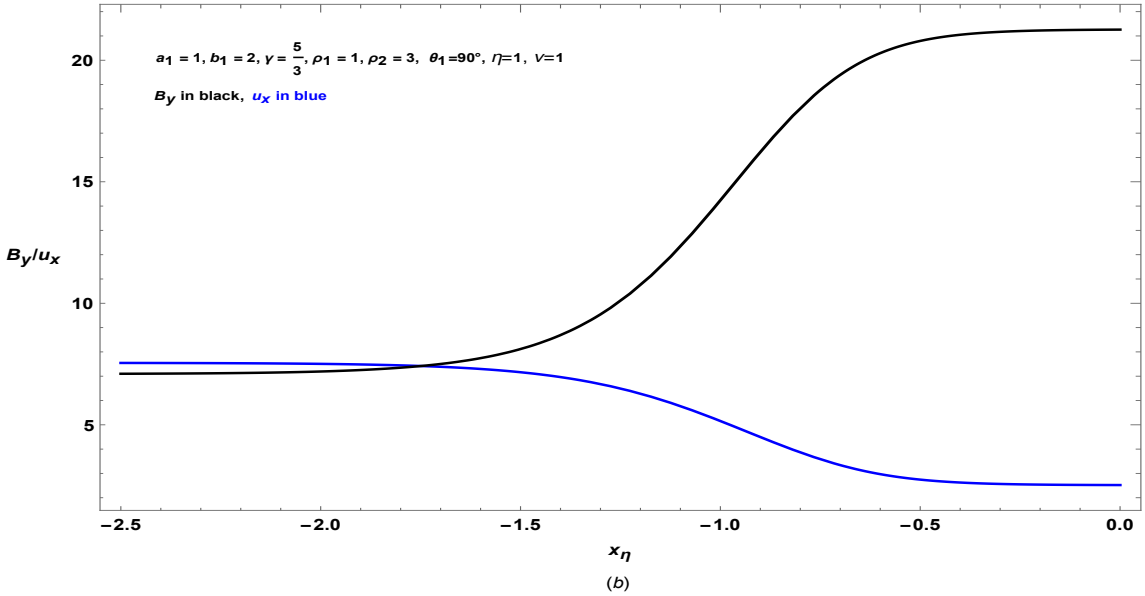

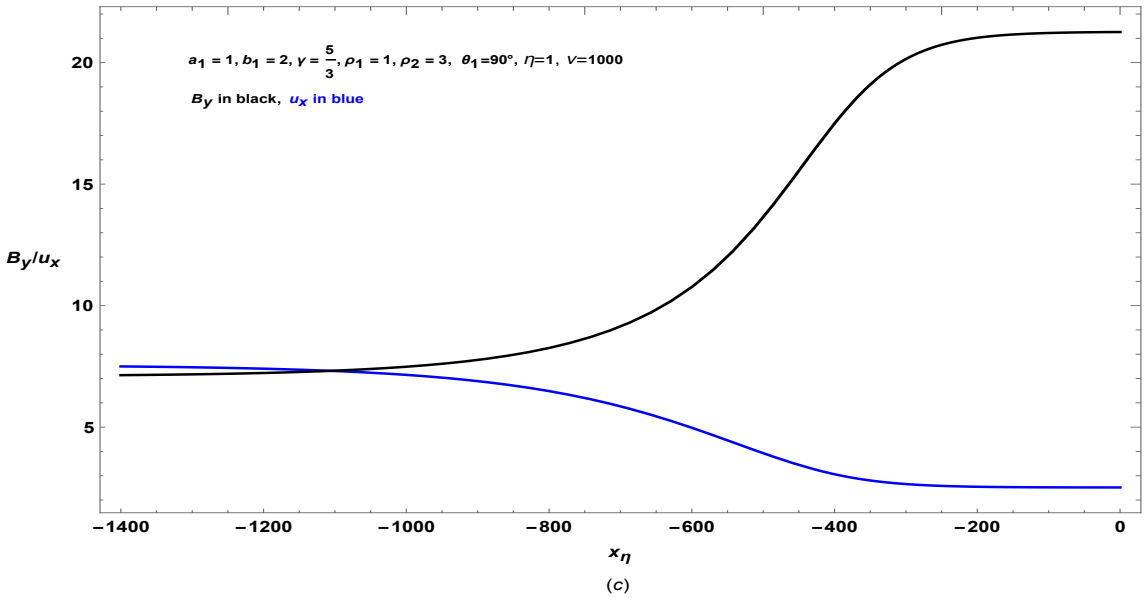

Figure 72: Perpendicular resistive shock profiles with kinematic viscosity ν. In this and all following plots in this chapter speeds are in terms of the upstream speed of sound, $\rho_1 = 1$ and $x_\eta = \frac{x}{\eta}$. In this plot $\frac{b_1}{a_1} = 2$, $\theta_1 = 90°$, $\frac{u_{x1}}{a_1} = 7.54983$

An important question is the existence of intermediate shocks and the consequences of the multiplicity of shock solutions. The calculations presented here show that there is one intermediate transition type with a unique structure, the $2 \rightarrow 3$ shock. Kennel et. al. [40] include the $2 \rightarrow 3$ shock with the $1 \rightarrow 2$ and $3 \rightarrow 4$ as physically realizable shocks. All other intermediate shock types possess one or two internal degrees of freedom in their structure. As demonstrated in this thesis, the degrees of freedom manifest the angle in which the phase space integral curve leaves the upstream point or the position in the magnetic phase plane where the hydrodynamic jump to the subsonic state occurs.

The traditional argument for the non-existence of $1 \rightarrow 3$, $1 \rightarrow 4$ and $2 \rightarrow 4$ shocks advanced by early authors as detailed by Akhiezer et. al. in [20] applies to non-dissipative systems with zero shock width. Stability was investigated by determining the response of the shock discontinuity to a disturbance by the seven small amplitude characteristic waves, these being the entropy wave moving with the discontinuity and the intermediate, slow and fast magnetoacoustic waves propagating normal to the plane of the shock. If a discontinuity responded in a determinable way by emitting a certain number of outgoing characteristic waves in response to the perturbation it was denoted as evolutionary, meaning that the structure survived the perturbation. Analysis of the hyperbolic system of MHD equations showed that the number of outgoing waves for an evolutionary discontinuity is 6 in the upstream and downstream directions. For $1 \rightarrow 2$ and $3 \rightarrow 4$ discontinuities there are 6 outgoing waves, making these evolutionary. For $2 \rightarrow 3$, $2 \rightarrow 4$, $1 \rightarrow 3$ and $1 \rightarrow 4$ discontinuities there are 6, 5, 5 and 4 outgoing waves respectively. Jeffrey and Taniuti [41] stated that the 6 outgoing waves alone a necessary condition and the sufficient condition involved 2 of these waves being intermediate waves. The additional restriction made the $2 \rightarrow 3$ discontinuity non-evolutionary as only 1 outgoing intermediate wave was released. Wu [42] stated that the extra degrees of freedom present in the structure of the $2 \rightarrow 4$, $1 \rightarrow 3$ and $1 \rightarrow 4$ transitions allows them to absorb a perturbation compensating for their deficit of outgoing waves in the linear evolutionary theory. In this thesis the analysis of trajectories in the phase plane and the calculation of shock structures using numerical integration show that intermediate shocks have the requisite number of degrees of freedom in their formation to confirm Wu's survivability requirement.

In summary, by calculating trajectories in the magnetic phase plane and computing shock structures by the numerical solution of the differential equations of hydrodynamics and electromagnetism with the calculation of associated entropy changes this thesis has demonstrated that the requisite number of degrees of freedom in the structure of MHD intermediate shocks are produced, supporting the view that intermediate shocks are physically realisable.

Particular points presented in this thesis are the use of the new parametric method to produce solutions to the MHD jump conditions, the establishment of the degrees of freedom in shock structure through the analysis of trajectories in the phase plane and a detailed analysis of the smooth passage of a shock trajectory through the transonic point in the case of $2^+ \rightarrow 4^-$ and $2^+ \rightarrow 3^-$ shocks.

The shock structures computed in this thesis provide the groundwork for ongoing stability analysis. As a first step, to test the hypothesis that the extra degrees of freedom in an intermediate shock can absorb small perturbations and produce a stable surviving shock structure a preliminary perturbation analysis was performed on the $2^+ \rightarrow 3^+$ intermediate shock studied in §7.1.2. The numerical method used here is an implementation of the analytical technique given by Inoue and Inutsuka [27]. Each shock variable is expressed in the form $q(x) = q_0(x) + \delta q(x) e^{-i\omega t}$ where $q_0(x)$ is the steady shock structure, $\delta q(x)$ is a small perturbation in $q(x)$ and ω is the frequency of the perturbation. The expression for the perturbed variables is substituted in the MHD equations and terms involving $\delta q(x)^2$ and

higher are neglected. The linearised equations are arranged into vector form involving a perturbation matrix $\Omega(x)$ whose components depend on ω and the steady shock structure, $\frac{d\delta q(x)}{dx} = \Omega(x)\delta q(x)$. The perturbation matrix was calculated for a range of values of ω, real and complex. The eigenvalues λ_j and eigenvectors v_j of the matrix where calculated for each value of ω and these were used to solve for the pertubation in each variable, $\delta q = \sum c_j v_j e^{\lambda_j x}$, where the c_j are constants.

The upstream perturbation matrix has 6 positive eigenvalues and 2 zero eigenvalues. Two of these eigenvalues have eigenvectors with components exciting perturbations along the z axis only, these decoupled solutions not affecting the other perturbed values. This means there are effectively 4 positive upstream eigenvalues contributing to solutions growing out of the upstream point. The downstream solution gave 2 positive eigenvalues and 2 zero eigenvalues. It was found that the coefficients of the growing downstream eigenvectors were minimised when two of the upstream eigenvectors were set equal to zero. The criterion to establish the minimisation of growth of the downstream perturbation was the minimisation of the ratio of the sum of the squares of the downstream coefficients of growing eigenmodes to the sum of the squares of all of the non z axis downstream coefficients. The growth ratio was calculated for a range of constants c_j and a shooting technique was used to determine c_j for the minimum growth ratio. It was found that $\omega = 0$, to within 0.1, gave the set of coefficients for the minimum growing eigenmodes, implying that the perturbed shock is steady to a small perturbation. Since the constants were now known the perturbation δq for each variable was then numerically integrated through the shock by solving the first order ODE. Figures 73-76 show the steady shock structure as a firm line and the structure produced by the perturbation as a dashed line. The diagrams indicate the response of a $2^+ \rightarrow 3^+$ shock to a small perturbation in the flow variables.

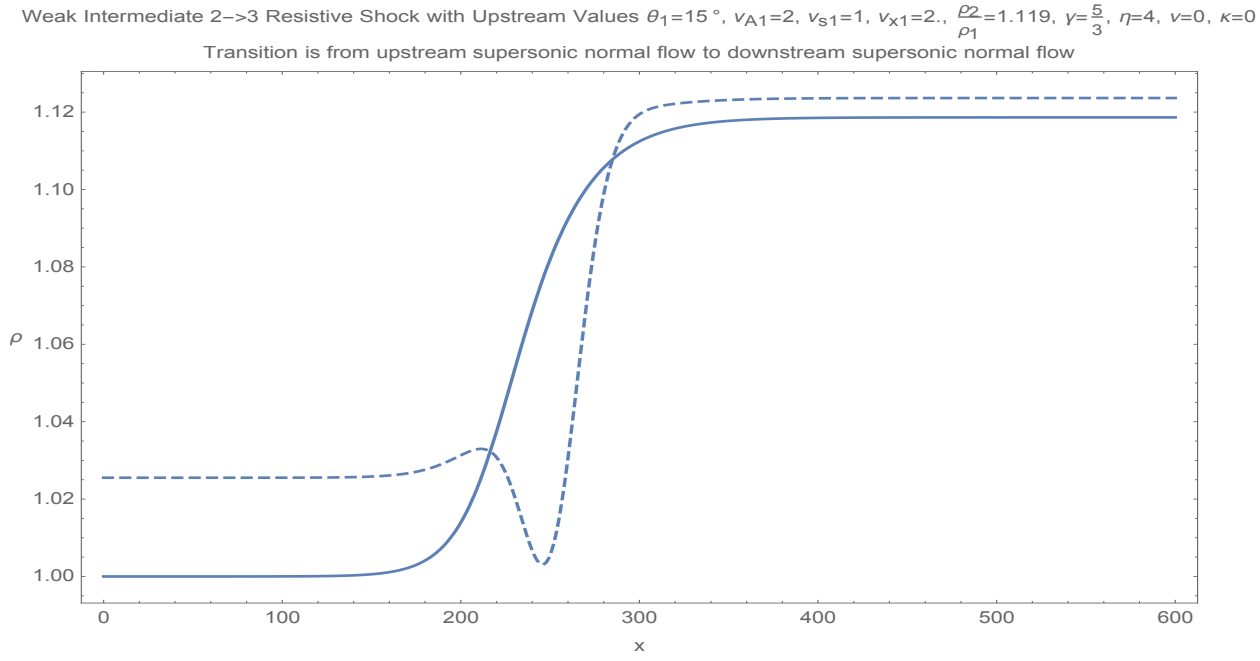

Figure 73: Steady and perturbed (dashed) upstream mass density spatial variation through a $2^+ \rightarrow 3^+$ shock, $\omega = 0$.

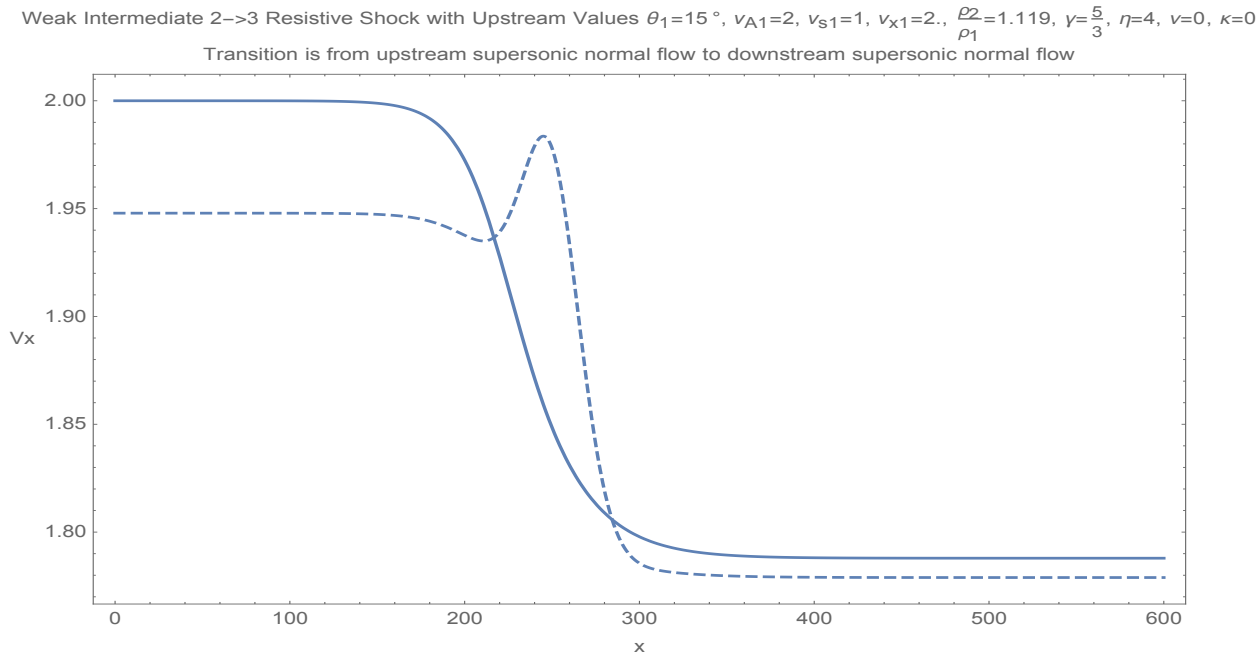

Figure 74: Steady and perturbed (dashed) upstream speed spatial variation through a $2^+ \rightarrow 3^+$ shock, $\omega = 0$.

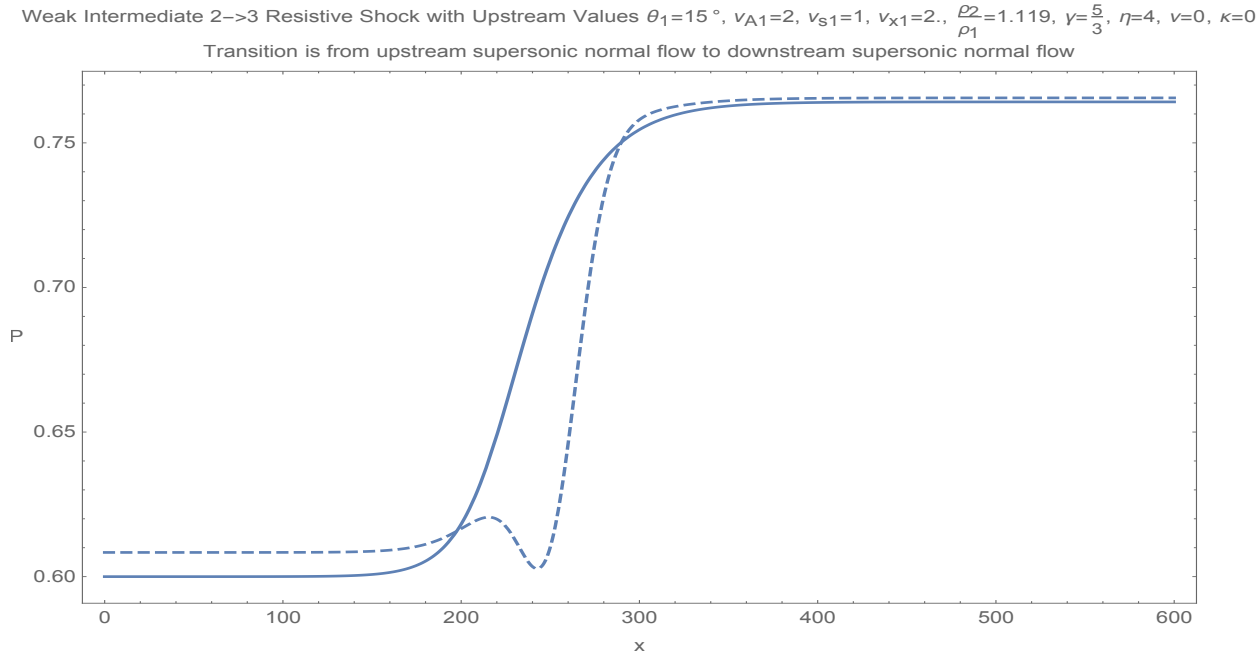

Figure 75: Steady and perturbed (dashed) upstream pressure spatial variation through a $2^+ \rightarrow 3^+$ shock, $\omega = 0$.

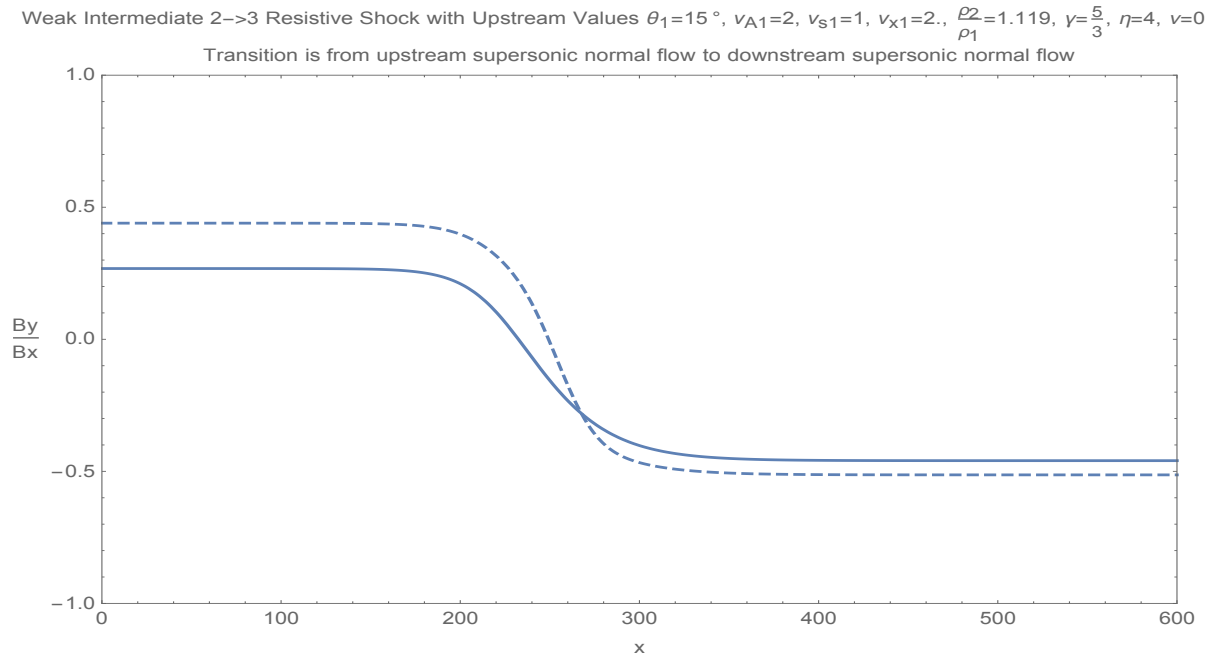

Figure 76: Steady and perturbed (dashed) upstream magnetic field spatial variation through a $2^+ \rightarrow 3^+$ shock, $\omega = 0$.

The plots in Figures 73-76 show the presence of a node in the density and pressure structure of the perturbed shock in its transition between its upstream and downstream perturbed states. After thesis submission during the correction stage a shooting technique through a range of the constants c_j was used to determine the presence of other solutions. The search found that a fundamental mode could be produced in the perturbed solution containing no nodes. In this case the density and pressure variation both undergo a monotonic change in their passage to the downstream state. Higher order overtones containing multiple nodes were not found in the discrete set of constants tested.

The next step is to apply the perturbation analysis of Inoue and Inutsuka [27] to the other varieties of intermediate shocks to confirm that the degrees of freedom of intermediate shocks do indeed control the stability of these structures.

References

[1] Paul Roberts in S. Molokov et al. (Ed.), *Magnetohydrodynamics-Historical Evolution and Trends,* Springer*, pp. 3-26, 2007*

[2] Carl-Gunne Falthammar, The discovery of magnetohydrodynamic waves, *J. Atmospheric Solar-Terrestrial Physics*, 69, 1604-1608, 2007

[3] N. Herlofson, Magneto-hydrodynamic waves in a compressible fluid conductor, *Nature*, 165, 1020, 1950

[4] F.de Hoffmann, E. Teller, Magneto-hydrodynamic shocks, *Phys. Rev.*, 80 (4), 692-703, 1950

[5] L.H. Helfer, Magneto-hydrodynamic shock waves, *Ap.J.*, 117, 177-199, 1953

[6] P.H. Roberts in G.L. Trigg (Ed.), *Encyclopedia of Applied Physics*, 9, VCH Publishers Inc., p 133, 1994

[7] A.I. Akhiezer, G.Ia. Liubarskii, R.V. Polovin, The stability of shock waves in magnetohydrodynamics, *Soviet Phys. JETP*, 35, (8), 3, 507-511, 1959

[8] R.V. Polovin, Shock Waves in Magnetohydrodynamics, *Soviet Phys. Uspekhi*, 3, 5, 677-688, 1961

[9] C.C. Wu, Formation,Structure and Stability of MHD Intermediate Shocks, *J. Geophys. Res.*, 95, (A6), 8149-8175, 1990

[10] J.K. Chao, L.H. Lyu, B.H. Wu, A.J. Lazarus, T.S. Chang, R.P. Lepping, Observations of an intermediate shock in interplanetary space, *J. Geophys. Res.*, 98, (A10), 17443-17450, 1993

[11] H. Feng, J.M. Wang, Observations of a $2 \rightarrow 3$ type interplanetary intermediate shock, *Solar Phys.*, 247, 195-201, 2008

[12] H.Q. Feng, Q.H. Li, J.M. Wang, G.Q. Zhao, Observations of an interplanetary intermediate shock associated with a magnetic reconnection exhaust, *Ap. J.*, 826:15 (5pp), 2016 July 30

[13] R.S. Steinolfson, A.J. Hundhausen, Coronal mass ejection shock fronts containing the two types of intermediate shocks, *J. Geophys. Res.*, 95, (A12), 20693-20699, 1990

[14] W. Marshall, The structure of magneto-hydrodynamic shock waves, *Proc. Roy. Soc.*, A, 233, 367-376, 1955

[15] G.B. Whitham, Some comments on wave propagation and shock wave structure with application to magnetohydrodynamics, *Comm. Pure App. Math.*, XII,113-158, 1959

[16] J.E. Anderson, *Magnetohydrodynamic Shock Waves*, MIT Press, 1963

[17] R.J. Bickerton, L. Lenamon, R.V.W. Murphy, The structure of hydromagnetic shock waves, *J. Plasma Physics*, 5 (2), 177-197, 1971

[18] V.A. Dixon, L.C. Woods, On the structure of oblique hydromagnetic shock waves, *Plasma Physics*, 18, 627-640, 1976

[19] A.E. Robson, J. Sheffield, *Oblique Hydromagnetic Shock Waves, Plasma Physics and Controlled Nuclear Fusion Research*, Proc. Conf. Novosibirsk, August 1968

[20] A.I.Akhiezer, I.A. Akhiezer, R.V. Polovin, A.G. Sitenko, K.N. Stepanov, *Plasma Electrodynamics*, Volume 1, *Linear Theory*, Pergamon, 1975

[21] C. C. Wu, On MHD intermediate shocks, *Geophys. Res. Lett.*, 14, 668-671, June 1987

[22] C.F. Kennel, R.D. Blandford, C.C. Wu, Structure and evolution of small amplitude intermediate shock waves, *Phys. Fluids B*, 2, 253, 1990

[23] P.S. Coppi, R.D. Blandford, C.F. Kennel, On the existence and stability of intermediate shocks, *Proceedings of the Joint Varenna-Abastumani International School & Workshop on Plasma Astrophysics*, Varenna, Italy, 24 Aug - 3 Sep 1988, *ESA SP-285*, Vol 1, Dec 1988

[24] L.-N. Hau, B.U.O. Sonnerup, On the structure of resistive MHD intermediate shocks, *J. Geophys. Res.*, 94, (A6), 6539-6551, 1989

[25] Tohru Hada, Evolutionary conditions in the dissipative MHD system; Stability of intermediate MHD shock waves, *Geophys. Res. Lett.*, 21, 2275-2278, October 1994

[26] S.A.E.G. Falle, S.S. Komissarov, On the existence of intermediate shocks, *12th Kingston Meeting: Computational Astrophysics ASP Conference Series*, Vol. 123, 66-71, 1997

[27] T. Inoue, S. Inutsuka, Evolutionary conditions in the dissipative MHD system revisited, *Prog. Theor. Phys.*, 118 (1), 47-58, 2007

[28] K. Takahashi, S. Yamada, Regular and non-regular solutions of the Riemann problem in ideal magnetohydrodynamics, *J. Plasma Physics*, 79, (3), 335-356, 2013

[29] K. Takahashi, S. Yamada, Exact Riemann solver for ideal magnetohydrodynamics that can handle all types of intermediate shocks and switch-on/off waves, *J. Plasma Physics*, 80, (2), 255-287, 2014

[30] M. Brio, C. C. Wu, An upward differencing scheme for the equation of ideal magnetohydrodynamics, *J. Comput. Phys.*, 75, 400-422, 1988

[31] L. D. Landau, E. M. Lifshitz, L. P. Pitaevskii, *Electrodynamics of Continuous Media*, 2nd edition, 1983

[32] Ya.B. Zel'dovich, Yu. P. Raizer, *Physics of Shock Waves and High-Temperature Hydrodynamic Phenomena*, Dover Press, 2001

[33] A. G. Kulikovskii, N. V. Pogorelov, A. Y. Semenov, *Mathematical Aspects of Numerical Solution of Hyperbolic Systems*, Chapman & Hall/CRC, 2001

[34] D. S. Jones, *The Theory of Electromagnetism*, Pergamon, 1964

[35] P. J. Prince, J. R. Dormand, Higher order embedded Runge-Kutta formulae, *J. Comp. Appl. Math.*, 7 (1), 67-75, 1981

[36] S. G. McAndrew, M.P.C., 24961, 1995APR15

[37] J. A. Shercliff, One-dimensional magnetogasdynamics in oblique fields, *J. Fluid Mech.*, 9, 481-505, 1960

[38] R. V. Polovin, V. P. Demutskii, *Fundamentals of Magnetohydrodynamics*, Consultants Bureau, 1990

[39] F.V. Coroniti, Dissipation discontinuities in hydromagnetic shock waves, *J. Plasma Physics*, 4 (2), 265-282, 1970

[40] C.F. Kennel, R.D. Blandford, C.S. Coppi, MHD intermediate shock discontinuities. Part 1 Rankine-Hugoniot conditions, *J. Plasma Physics*, 42 (2), 299-319, 1989

[41] A. Jeffrey, T. Taniuti, *Non-Linear Wave Propagation with Applications to Physics and Magnetohydrodynamics*, Academic Press, 1964

[42] C. C. Wu in M. Shearer (Ed), *Viscous Profiles and Numerical Methods for Shock Waves*, SIAM, pp. 209-226, 1990

APPENDIX A

$$k_6 = k_{66}u_{x1}^6,$$

$$k_4 = (k_{44} + k_{46}u_{x1}^2 + k_{48}u_{x1}^4)u_{x1}^4,$$

$$k_2 = (k_{22} + k_{24}u_{x1}^2 + k_{26}u_{x1}^4 + k_{28}u_{x1}^6 + k_{210}u_{x1}^8)u_{x1}^2,$$

$$k_0 = k_{00} + k_{02}u_{x1}^2 + k_{04}u_{x1}^4 + k_{06}u_{x1}^6 + k_{08}u_{x1}^8 + k_{010}u_{x1}^{10} + k_{012}u_{x1}^{12}.$$

	p_1^0	p_1^1	p_1^2	p_1^3	p_1^4
k_{66}	$1024\pi^4(\gamma+1)^2\rho_1^6 \times B_x^2$	0	0	0	0
k_{44}	$32\pi^2\gamma(\gamma-1)\rho_1^4B_x^2 \times[-2(\gamma+1)^2B_x^4 + (\gamma+1)(\gamma^2+3\gamma+6)B_x^2B_{y1}^2 + \gamma B_{y1}^4]$	$512\pi^3\gamma(\gamma-1)\rho_1^4 \times B_x^2[(\gamma+1)^2B_x^2 + \gamma B_{y1}^2]$	$2048\pi^4(\gamma - 1)\gamma^2\rho_1^4B_x^2$	0	0
k_{46}	$-256\pi^3\gamma(\gamma-1)\rho_1^5 \times B_x^2[-2(\gamma+1)^2 \times B_x^2 + (\gamma^3+2\gamma^2+3\gamma+4)B_{y1}^2]$	$-1024\pi^4\gamma(2\gamma^3 + 3\gamma^2+8\gamma-1)\rho_1^5B_x^2$	0	0	0
k_{48}	$-512\pi^4\gamma(\gamma-1)\rho_1^6 \times[2(\gamma^2+2\gamma+3) \times B_x^2 - (\gamma-2)(\gamma+1)^2B_{y1}^2]$	0	0	0	0
k_{22}	$\gamma^2(\gamma^2-1)^2\rho_1^2B_x^4 \times(B_x^2+B_{y1}^2)^3$	$-16\pi\gamma^2(\gamma-1)^2\rho_1^2 \times B_x^4(B_x^2+B_{y1}^2) \times[(\gamma+1)^2B_x^2 - (\gamma^2+3\gamma+1)B_{y1}^2]$	$64\pi^2\gamma^2(\gamma-1)^2\rho_1^2 \times B_x^4[(\gamma^2+1)B_x^2 + (\gamma^2+6\gamma+1)B_{y1}^2]$	$1024\pi^3(\gamma-1)^2\gamma^3 \times\rho_1^2B_x^4$	0
k_{24}	$-8\pi\gamma^2(\gamma-1)^2\rho_1^3B_x^2 \times(B_x^2+B_{y1}^2)^2[2(\gamma+1)^2B_x^2 + (\gamma^2+1) \times B_{y1}^2]$	$64\pi^2(\gamma-1)\gamma^2\rho_1^3B_x^2 \times[(3\gamma^3+3\gamma^2+5\gamma-3)^2B_x^4+(\gamma^3-5\gamma^2-15\gamma - 1)B_x^2B_{y1}^2 + (-2\gamma^3+\gamma^2-2\gamma+2)B_{y1}^4$	$-512\pi^3(\gamma-1)\gamma^2\rho_1^3 \times B_x^2[(\gamma^3-\gamma^2+9\gamma-1)B_x^2 + (\gamma^3+\gamma^2+\gamma-1)B_{y1}^2]$	$-4096\pi^4(\gamma-1)\gamma^4 \times\rho_1^3B_x^2$	0
k_{26}	$16\pi^2(\gamma-1)^2\gamma^2\rho_1^4 \times(B_x^2+B_{y1}^2)[2 \times(3\gamma^2+6\gamma+7)B_x^4+ 2(3\gamma^2-7)B_x^2B_{y1}^2 + \gamma(\gamma-2)B_{y1}^4]$	$-256\pi^3(\gamma-1)\gamma^2 \times\rho_1^4[(3\gamma^3 + 3\gamma^2 + 17\gamma - 7)B_x^4 + (2\gamma^3 - 7\gamma^2 - 8\gamma - 7)B_x^2B_{y1}^2 - \gamma(\gamma - 1)(\gamma-2)B_{y1}^4]$	$1024\pi^4\gamma^3\rho_1^4[(\gamma^3 - 2\gamma^2+17\gamma-4)B_x^2+ (\gamma-2)(\gamma-1)^2B_{y1}^2]$	0	0
k_{28}	$-128\pi^3\gamma^2(\gamma-1)^2 \times\rho_1^5[2(\gamma^2 + 2\gamma + 5)B_x^4 + (3\gamma^2+1) \times B_x^2B_{y1}^2 + (\gamma^2 - 2\gamma - 9)B_{y1}^4]$	$1024\pi^4(\gamma-1)\gamma^2 \times\rho_1^5[(\gamma^3 + \gamma^2 + 11\gamma-1)B_x^2+(\gamma^3 - 3\gamma^2+7\gamma-1)B_{y1}^2]$	0	0	0

Table 2: Coefficients for Calculation of Downstream Sound Speed

table continued next page.....

	p_1^0	p_1^1	p_1^2	p_1^3	p_1^4
k_{210}	$256\pi^4\gamma^2(\gamma-1)^2\rho_1^6[(\gamma^2+2\gamma+9)B_x^2+(\gamma^2-2\gamma+9)B_{y1}^2]$	0	0	0	0
k_{00}	0	0	$2(\gamma-1)^3\gamma^4B_x^6\times(B_x^2+B_{y1}^2)^2$	$-32\pi(\gamma-1)^3\gamma^4\times B_x^6(B_x^2-B_{y1}^2)$	$128\pi^2(\gamma-1)^3\gamma^4B_x^6$
k_{02}	0	$(\gamma-1)^2(\gamma^2-6\gamma+1)\gamma^3\rho_1B_x^4(B_x^2+B_{y1}^2)^3$	$-16\pi(\gamma-1)^2\gamma^3\rho_1\times B_x^4(B_x^2+B_{y1}^2)\times[(3\gamma^2-8\gamma+1)\times B_x^2+(6\gamma-1)\times B_{y1}^2]$	$64\pi^2(\gamma-1)^2\gamma^3\rho_1\times B_x^4[(7\gamma^2-10\gamma+1)B_x^2+(-3\gamma^2-6\gamma+1)B_{y1}^2]$	$-1024\pi^3(\gamma-1)^2\gamma^5\rho_1B_x^4$
k_{04}	$-2(\gamma-1)^3\gamma^3\rho_1^2\times B_x^2(B_x^2+B_{y1}^2)^4$	$-8\pi(\gamma-1)^2\gamma^3\rho_1^2\times B_x^2(B_x^2+B_{y1}^2)^2\times[2(\gamma^2-8\gamma+3)\times B_x^2+(\gamma^2+\gamma-4)B_{y1}^2]$	$32\pi^2(\gamma-1)\gamma^3\rho_1^2\times B_x^2[4(3\gamma-2)\times(\gamma^2-4\gamma+1)B_x^4+4(2\gamma^3-6\gamma^2+12\gamma-3)B_x^2B_{y1}^2-(3\gamma^3-12\gamma^2+4\gamma+4)B_{y1}^4]$	$-512\pi^3(\gamma-1)\times\gamma^4\rho_1^2B_x^2[2(2\gamma^2-5\gamma+1)B_x^2+(3-4\gamma)B_{y1}^2]$	$2048\pi^4(\gamma-1)\times\gamma^6\rho_1^2B_x^2$
k_{06}	$8\pi(\gamma-1)^3\gamma^3\rho_1^3\times(B_x^2+B_{y1}^2)^3\times(4B_x^2+B_{y1}^2)$	$16\pi^2(\gamma-1)^2\gamma^3\rho_1^3\times(B_x^2+B_{y1}^2)\times[2(3\gamma^2-30\gamma+11)B_x^4+2(3\gamma^2-10\gamma+11)B_x^2B_{y1}^2+(\gamma^2+8\gamma-8)B_{y1}^4]$	$-256\pi^3(\gamma-1)\gamma^3\times\rho_1^3[(5\gamma^3-27\gamma^2+15\gamma-1)B_x^4+(3\gamma^3-13\gamma^2+23\gamma-3)B_x^2B_{y1}^2-(\gamma-1)(\gamma^2+2\gamma-2)B_{y1}^4]$	$1024\pi^4\gamma^5\rho_1^3[(\gamma-3)(3\gamma-1)B_x^2+(\gamma-1)^2B_{y1}^2]$	0
k_{08}	$-96\pi^2(\gamma-1)^3\gamma^3\rho_1^4\times(B_x^2+B_{y1}^2)^2\times(2B_x^2+B_{y1}^2)$	$-128\pi^3(\gamma-1)^2\gamma^3\times\rho_1^4[2(\gamma^2-12\gamma+3)B_x^4+(3\gamma^2-23\gamma+16)B_x^2B_{y1}^2+(\gamma^2-\gamma+10)B_{y1}^4]$	$512\pi^4(\gamma-1)\gamma^4\rho_1^4\times[3(\gamma^2-6\gamma+1)B_x^2+2(\gamma^2-4\gamma+1)B_{y1}^2]$	0	0
k_{010}	$128\pi^3(\gamma-1)^3\gamma^3\rho_1^5\times(4B_x^4+7B_x^2B_{y1}^2+3B_{y1}^4)$	$256\pi^4(\gamma-1)^2\gamma^3\rho_1^5\times[(\gamma^2-14\gamma+1)B_x^2+(\gamma^2-10\gamma+1)B_{y1}^2]$	0	0	0
k_{012}	$-512\pi^4(\gamma-1)^3\gamma^3\times\rho_1^6(B_x^2+B_{y1}^2)$	0	0	0	0

APPENDIX B

$$l_{12} = l_{120}, \quad l_{10} = l_{102}a_2^2 + l_{100}, \quad l_8 = l_{84}a_2^4 + l_{82}a_2^2 + l_{80},$$

$$l_6 = l_{66}a_2^6 + l_{64}a_2^4 + l_{62}a_2^2 + l_{60}, \quad l_4 = l_{48}a_2^8 + l_{46}a_2^6 + l_{44}a_2^4 + l_{42}a_2^2 + l_{40},$$

$$l_2 = l_{26}a_2^6 + l_{24}a_2^4 + l_{22}a_2^2 + l_{20}, \quad l_0 = l_{04}a_2^4.$$

	p_1^0	p_1^1	p_1^2	p_1^3
l_{120}	$512\pi^4(\gamma-1)^3\gamma^3\rho_1^5 \times(B_x^2+B_{y1}^2)^2$	$-8192\pi^5(\gamma-1)^3\gamma^3\rho_1^5 \times(B_x^2-B_{y1}^2)$	$32768\pi^6(\gamma-1)^3\gamma^3\rho_1^5$	0
l_{100}	$-128\pi^3(\gamma-1)^3\gamma^3\rho_1^4 \times(B_x^2+B_{y1}^2)^2(4B_x^2+3B_{y1}^2)$	$-256\pi^4(\gamma-1)^2\gamma^3\rho_1^4 \times[(\gamma^2-22\gamma+17)B_x^4+2(\gamma+11)(\gamma-1)B_x^2B_{y1}^2+(\gamma^2+26\gamma-23)B_{y1}^4]$	$4096\pi^5\gamma^3\rho_1^4[(\gamma-1)^4B_x^2-(\gamma-1)^2(\gamma^2+8\gamma-5)B_{y1}^2]$	$-16384\pi^6\gamma^3(\gamma^2-1)^2\rho_1^4$
l_{102}	$-256\pi^4(\gamma-1)^2\gamma^2\rho_1^5 \times(B_x^2+B_{y1}^2)[(\gamma-3)^2B_x^2+(\gamma^2-6\gamma+1)B_{y1}^2]$	$4096\pi^5(\gamma-1)^2\gamma^2\rho_1^5[(\gamma-1)(\gamma-5)B_x^2-(\gamma^2-6\gamma+1)B_{y1}^2]$	$-16384\pi^6(\gamma-1)^2\gamma^2 \times(\gamma^2-6\gamma+1)\rho_1^5$	0
l_{80}	$96\pi^2(\gamma-1)^3\gamma^3\rho_1^3(B_x^2+B_{y1}^2)^3(2B_x^2+B_{y1}^2)$	$128\pi^3(\gamma-1)^2\gamma^3\rho_1^3(B_x^2+B_{y1}^2)[2(\gamma-1)(\gamma-3)B_x^4+(3\gamma^2+25\gamma-22)B_x^2B_{y1}^2+(\gamma^2+13\gamma-12)B_{y1}^4]$	$-1024\pi^4(\gamma-1)\gamma^3\rho_1^3 \times[(3\gamma^3+2\gamma^2-\gamma-2)B_x^4-(3\gamma^3+14\gamma^2-21\gamma+8)B_x^2B_{y1}^2-2(\gamma-1)(\gamma^2+4\gamma-3)B_{y1}^4]$	$8192\pi^5\gamma^4(\gamma^2-1)\rho_1^3[(\gamma+1)B_x^2+(\gamma-1)B_{y1}^2]$
l_{82}	$128\pi^3(\gamma-1)^2\gamma^2\rho_1^4(B_x^2+B_{y1}^2)[2(\gamma-1)(\gamma-5)B_x^4+(3\gamma^2-16\gamma+7)B_x^2B_{y1}^2+(\gamma^2-4\gamma+1)B_{y1}^4]$	$-1024\pi^4(\gamma-1)\gamma^2\rho_1^4 \times[(3\gamma^3-21\gamma^2+17\gamma-3)B_x^4-(3\gamma^3-17\gamma^2+5\gamma+1)B_x^2B_{y1}^2-2(\gamma-1)(\gamma^2-4\gamma+1)B_{y1}^4]$	$8192\pi^5(\gamma-1)\gamma^2\rho_1^4[(\gamma^3-7\gamma^2-\gamma-1)B_x^2+(\gamma-1)(\gamma^2-4\gamma+1)B_{y1}^2]$	0
l_{84}	$-512\pi^4(\gamma-1)\gamma\rho_1^5[(\gamma^3-4\gamma^2+13\gamma-6)B_x^4+2(\gamma^3-5\gamma^2+3\gamma-3)B_x^2B_{y1}^2+(\gamma-1)^2\gamma B_{y1}^4]$	$8192\pi^5(\gamma-1)\gamma\rho_1^5[(\gamma^3-3\gamma^2+7\gamma-1)B_x^2-(\gamma-1)^2\gamma B_{y1}^2]$	$-32768\pi^6(\gamma-1)^3\gamma^2\rho_1^5$	0
l_{60}	$-8\pi(\gamma-1)^3\gamma^3\rho_1^2(4B_x^2+B_{y1}^2)(B_x^2+B_{y1}^2)^4$	$-16\pi^2(\gamma-1)^2\gamma^3\rho_1^2(B_x^2+B_{y1}^2)^2[2(3\gamma^2+2\gamma+3)B_x^4+2(3\gamma^2+20\gamma-13)B_x^2B_{y1}^2+(\gamma^2+8\gamma-8)B_{y1}^4]$	$256\pi^3\gamma^3(\gamma-1)\rho_1^2[(3\gamma-1)(\gamma+1)^2B_x^6-2(2\gamma^3+4\gamma^2-7\gamma+2)B_x^4B_{y1}^2-(6\gamma^3+10\gamma^2-17\gamma+5) \times B_x^2B_{y1}^4-(\gamma-1)(\gamma^2+2\gamma-2)B_{y1}^6]$	$-1024\pi^4\gamma^5\rho_1^2[(\gamma+1)^2B_x^4+4(\gamma^2-1)B_x^2B_{y1}^2+(\gamma-1)^2B_{y1}^4]$
l_{62}	$-16\pi^2(\gamma-1)^2\gamma^2\rho_1^3(B_x^2+B_{y1}^2)^2[2(3\gamma^2-18\gamma+7) \times B_x^4+2(3\gamma^2-14\gamma+1)B_x^2B_{y1}^2+\gamma(\gamma-2)B_{y1}^4]$	$256\pi^3(\gamma-1)\gamma^2\rho_1^3[(3\gamma^3-21\gamma^2+5\gamma-3)B_x^6-2(2\gamma^3-8\gamma^2+\gamma+3)B_x^4B_{y1}^2-(6\gamma^3-26\gamma^2+9\gamma+3) \times B_x^2B_{y1}^4-\gamma(\gamma-1)(\gamma-2)B_{y1}^6]$	$-1024\pi^4\gamma^3\rho_1^3[(\gamma^3-8\gamma^2-3\gamma-2)B_x^4+4(\gamma-1)(2\gamma^2-7\gamma+1)B_x^2B_{y1}^2+(\gamma-2) \times(\gamma-1)^2B_{y1}^4]$	0
l_{64}	$512\pi^3\gamma(\gamma-1)\rho_1^4B_x^2[(\gamma^3-3\gamma^2+7\gamma-1)B_x^4+(2\gamma^3-7\gamma^2+6\gamma-2)B_x^2B_{y1}^2+(\gamma^3-3\gamma^2+\gamma-1)B_{y1}^4]$	$-1024\pi^4\gamma\rho_1^4B_x^2[(6\gamma^4-18\gamma^3+27\gamma^2-4\gamma+1)B_x^2-(\gamma-1)(5\gamma^3-7\gamma^2-7\gamma+1)B_{y1}^2]$	$16384\pi^5\gamma^3(\gamma-1)^2\rho_1^4B_x^2$	0

Table 3: Coefficients for Calculation of Downstream Normal Flow Speed

APPENDIX B (continued)

	p_1^0	p_1^1	p_1^2	p_1^3
l_{66}	$1024\pi^4 B_x^2\rho_1^5[(2\gamma^3-5\gamma^2+8\gamma-1)B_x^2-(\gamma-1)^2(\gamma^2+1)B_{y1}^2]$	$-16384\pi^5\gamma(\gamma-1)^2\rho_1^5 B_x^2$	0	0
l_{40}	$2\rho_1\gamma^3(\gamma-1)^3B_x^2(B_x^2+B_{y1}^2)^5$	$8\pi\rho_1(\gamma-1)^2\gamma^3B_x^2(B_x^2+B_{y1}^2)^3[2(\gamma+1)^2B_x^2+(\gamma^2+5\gamma-2)B_{y1}^2]$	$-64\pi^2(\gamma-1)\rho_1\gamma^4B_x^2\times(B_x^2+B_{y1}^2)[(\gamma+1)^2B_x^4-4(\gamma^2+\gamma-1)B_x^2B_{y1}^2-(2\gamma^2+2\gamma-3)B_{y1}^4]$	$512\pi^3\rho_1\gamma^6B_x^2B_{y1}^2[(\gamma+1)\times B_x^2+(\gamma-1)B_{y1}^2]$
l_{42}	$8\pi\gamma^2(\gamma-1)^2\rho_1^2B_x^2(B_x^2+B_{y1}^2)^3[2(\gamma^2-6\gamma+1)B_x^2+(\gamma^2-4\gamma-1)B_{y1}^2]$	$-64\pi^2(\gamma-1)\gamma^2\rho_1^2B_x^2\times(B_x^2+B_{y1}^2)[(\gamma^3-7\gamma^2-\gamma-1)B_x^4-2(2\gamma-1)(\gamma^2-4\gamma-1)B_x^2B_{y1}^2-(2\gamma^3-8\gamma^2+3\gamma+1)B_{y1}^4]$	$512\pi^3\rho_1^2\gamma^4B_x^2B_{y1}^2[(5\gamma^2-14\gamma+3)B_x^2+(\gamma-1)(\gamma-3)B_{y1}^2]$	0
l_{44}	$-32\pi^2(\gamma-1)\gamma\rho_1^3B_x^2(B_x^2+B_{y1}^2)[2(3\gamma^3-7\gamma^2+9\gamma-1)B_x^4+(7\gamma^3-18\gamma^2+7\gamma-4)B_x^2B_{y1}^2+(\gamma-2)(\gamma^2+1)B_{y1}^4]$	$512\pi^3\gamma^2\rho_1^3B_x^2[(3\gamma-1)\times(\gamma-1)^2B_x^4+(-2\gamma^3+11\gamma-3)B_x^2B_{y1}^2-(\gamma-1)\times(\gamma-2)B_{y1}^4]$	$-2048\pi^4(\gamma-1)\gamma^4\rho_1^3B_x^4$	0
l_{46}	$-512\pi^3\gamma\rho_1^4B_x^4[2(\gamma-1)^2\times B_x^2-(\gamma-2)(\gamma^2+1)B_{y1}^2]$	$4096\pi^4(\gamma-1)\gamma^2\rho_1^4B_x^4$	0	0
l_{48}	$-2048\pi^4(\gamma-1)\rho_1^5B_x^4$	0	0	0
l_{20}	0	$-\gamma^3(\gamma^2-1)^2B_x^4(B_x^2+B_{y1}^2)^4$	$-16\pi(\gamma^2-1)\gamma^5B_{y1}^2B_x^4\times(B_x^2+B_{y1}^2)^2$	$-64\pi^2\gamma^7B_x^4B_{y1}^4$
l_{22}	$-\rho_1\gamma^2(\gamma-1)^2(\gamma^2-6\gamma+1)B_x^4(B_x^2+B_{y1}^2)^4$	$-16\pi\rho_1(\gamma-1)(\gamma-5)\gamma^4\times B_{y1}^2B_x^4(B_x^2+B_{y1}^2)^2$	$-64\pi^2\rho_1\gamma^5B_{y1}^2B_x^4[4(\gamma-1)B_x^2+(\gamma-4)B_{y1}^2]$	0
l_{24}	$16\pi(\gamma-1)\rho_1^2\gamma^2B_x^4(B_x^2+B_{y1}^2)^2[2(\gamma-1)^2B_x^2+(\gamma^2-2\gamma-1)B_{y1}^2]$	$-64\pi^2\gamma^3\rho_1^2B_x^4[2(\gamma-1)^2\times B_x^4-(\gamma-1)(\gamma+7)\times B_x^2B_{y1}^2+(5-2\gamma)B_{y1}^4]$	0	0
l_{26}	$64\pi^2\gamma\rho_1^3B_x^4[2(\gamma-1)^2B_x^4-(\gamma-1)(\gamma^2-\gamma+4)B_x^2B_{y1}^2-(\gamma-2)B_{y1}^4]$	0	0	0
l_{04}	$-2\rho_1\gamma^2(\gamma-1)^3B_x^6(B_x^2+B_{y1}^2)^3$	0	0	0

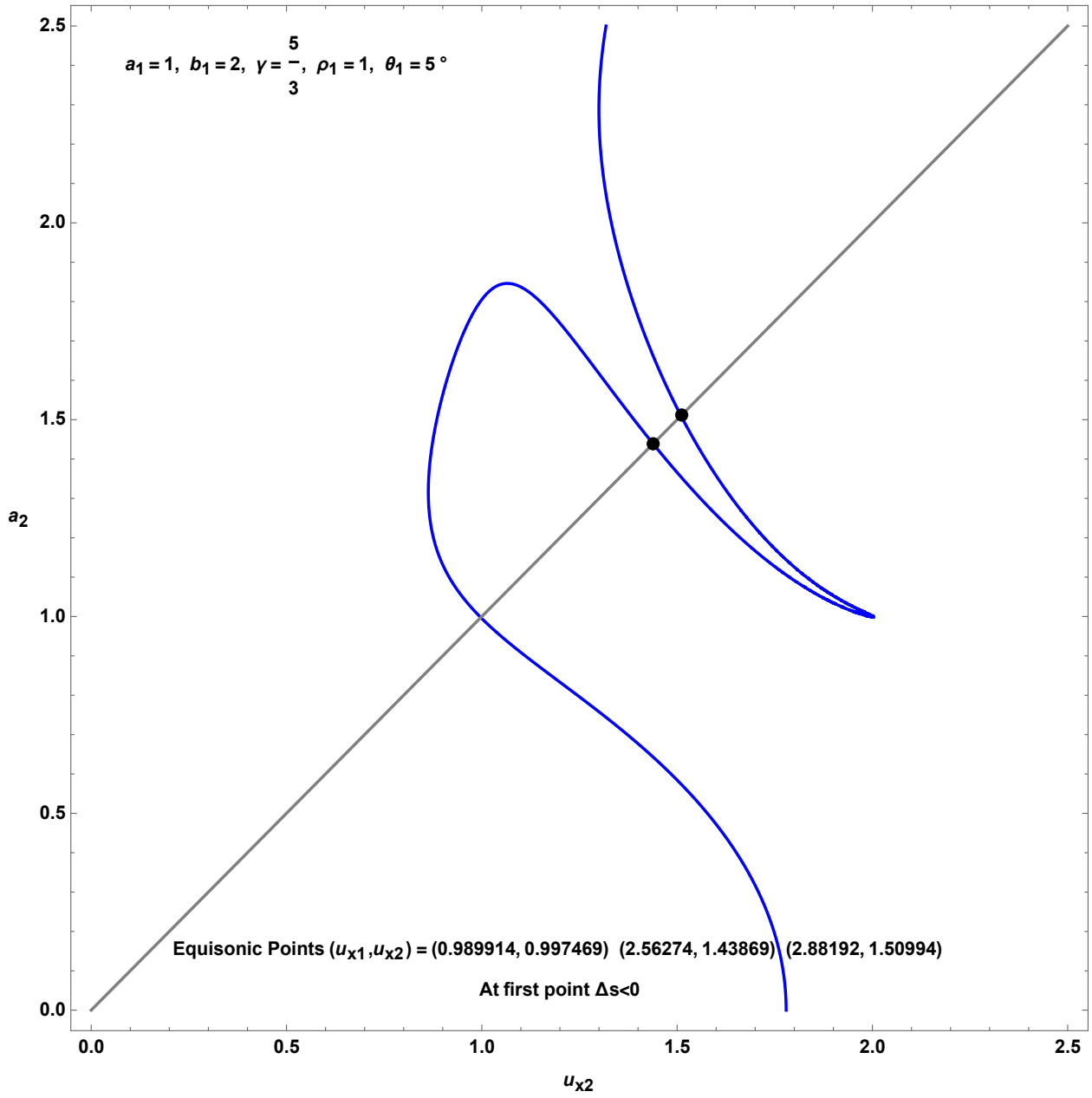

Figure 77: Equisonic point calculation $a_1 = 1$, $b_1 = 2$, $\gamma = \frac{5}{3}$, $\rho_1 = 1$, $\theta_1 = 5°$

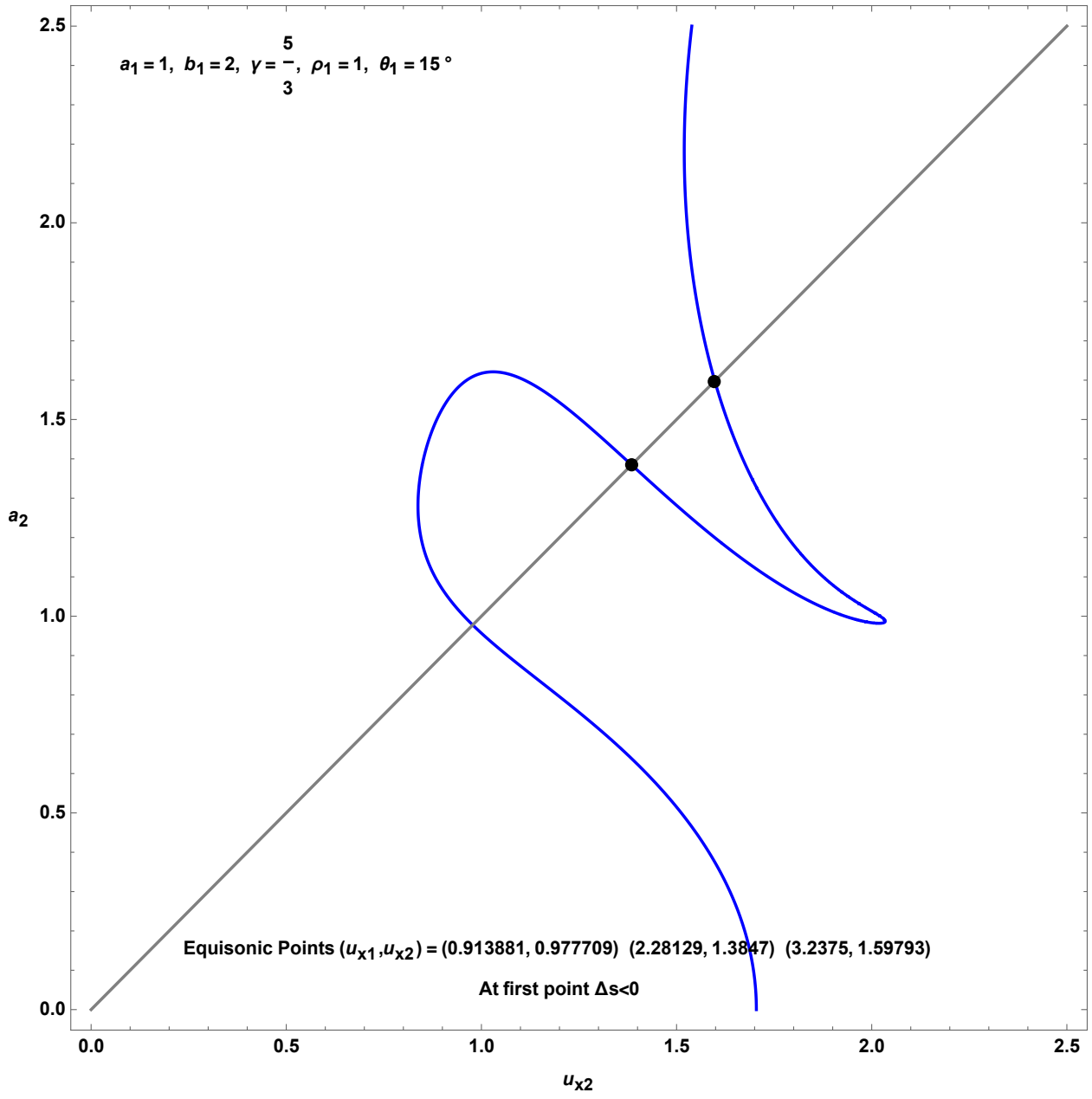

Figure 78: Equisonic point calculation $a_1 = 1$, $b_1 = 2$, $\gamma = \frac{5}{3}$, $\rho_1 = 1$, $\theta_1 = 15°$

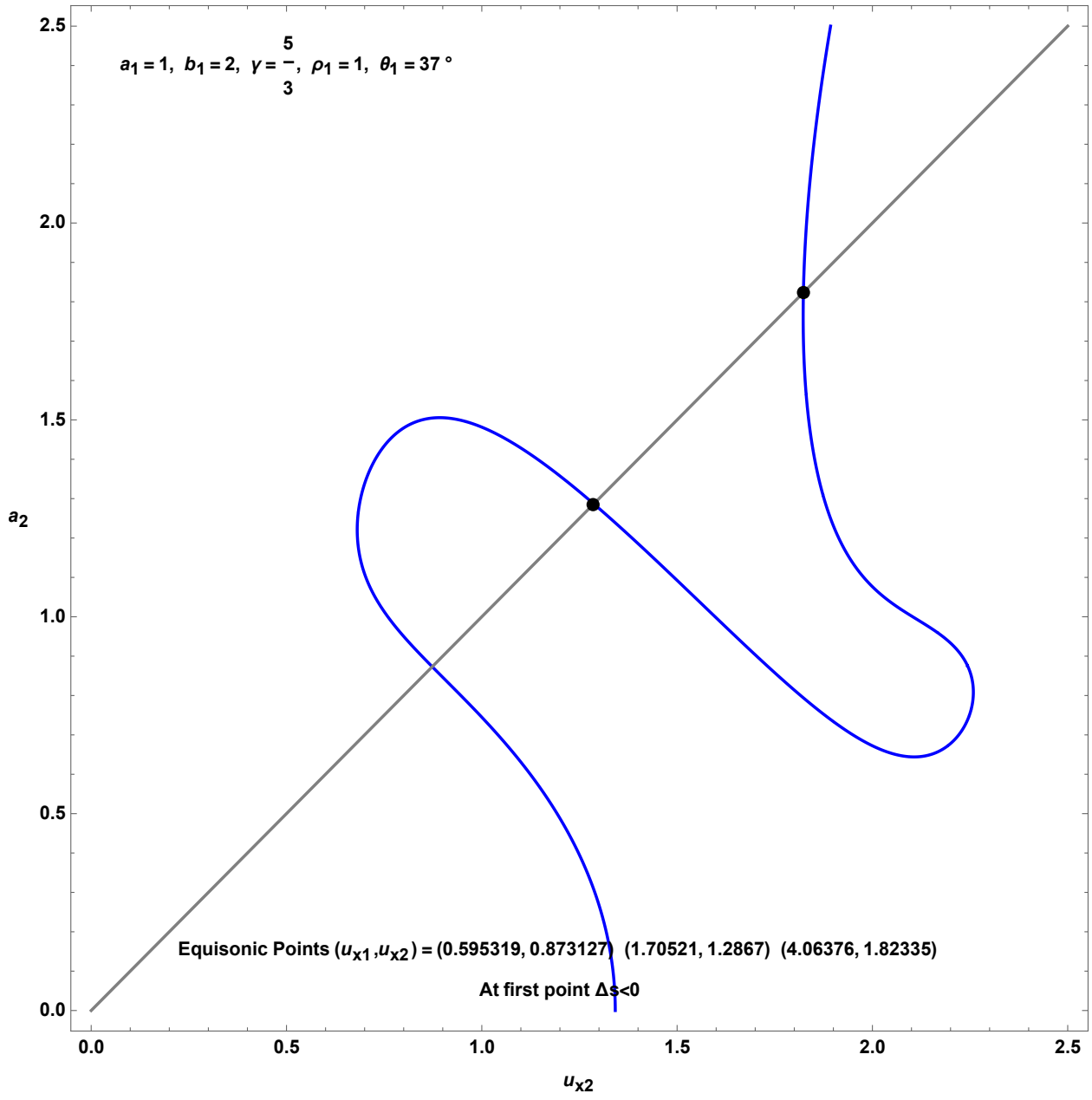

Figure 79: Equisonic point calculation $a_1 = 1$, $b_1 = 2$, $\gamma = \frac{5}{3}$, $\rho_1 = 1$, $\theta_1 = 37°$

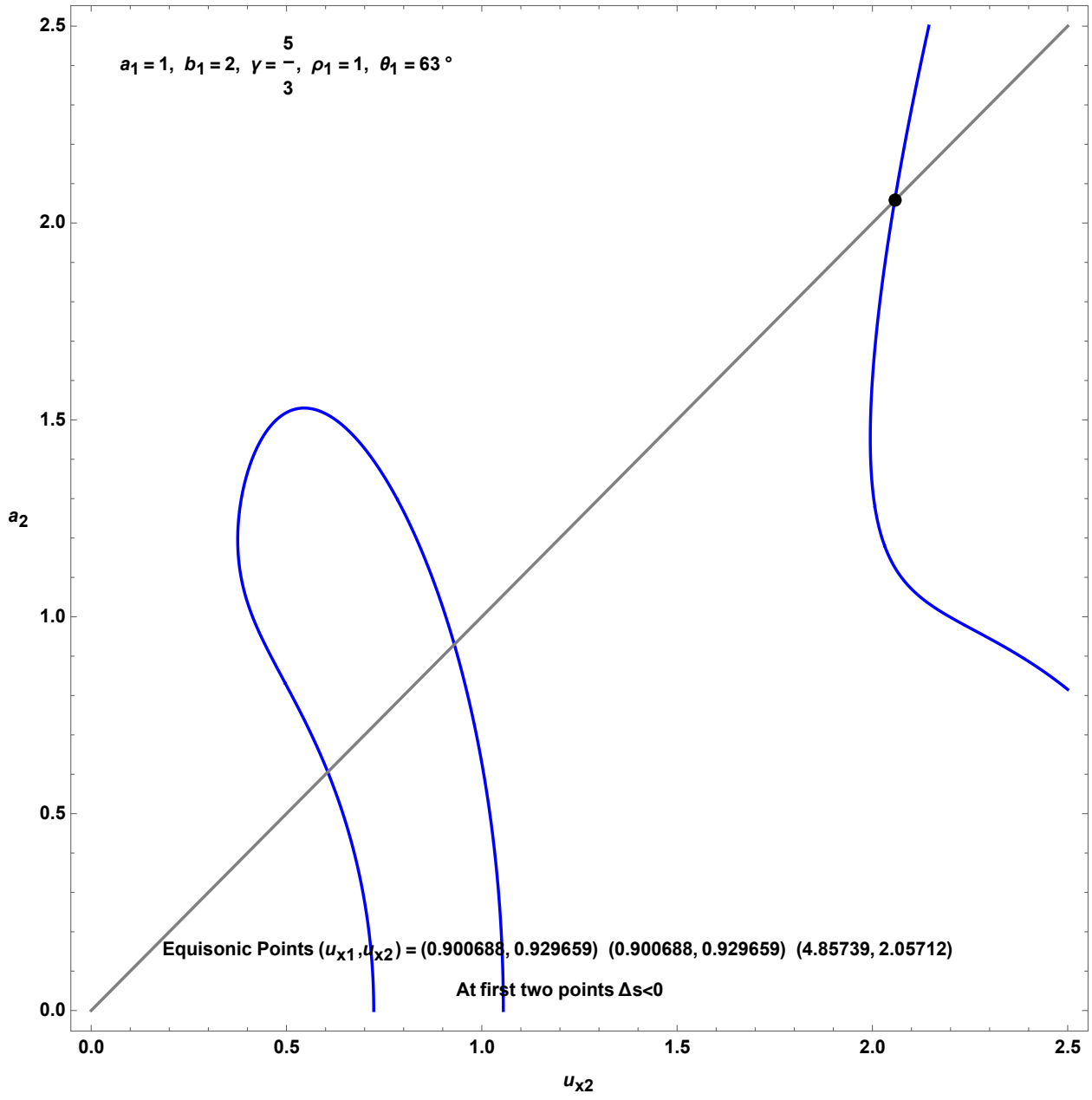

Figure 80: Equisonic point calculation $a_1 = 1$, $b_1 = 2$, $\gamma = \frac{5}{3}$, $\rho_1 = 1$, $\theta_1 = 63°$